THE UNIVERSITY *of* EDINBURGH

Real-time bioimpedance measurements of stem cell-based disease models-on-a-chip

Wesam Gamal

A thesis submitted for the degree of Doctor of Philosophy

The University of Edinburgh

2015

Abstract

In vitro disease models are powerful platforms for the development of drugs and novel therapies. Stem-cell based approaches have emerged as cutting-edge tools in disease modelling, allowing for deeper insights into previously unknown disease mechanisms. Hence the significant role of these disease-in-a-dish methods in therapeutics and translational medicine.

Impedance sensing is a non-invasive, quantitative technique that can monitor changes in cellular behaviour and morphology in real-time. Bioimpedance measurements can be used to characterize and evaluate the establishment of a valid disease model, without the need for invasive end-point biochemical assays. In this work, two stem cell-based disease models-on-a-chip are proposed for acute liver failure (ALF) and age-related macular degeneration (AMD).

The ALF disease model-on-a-chip integrates impedance sensing with the highly-differentiated HepaRG cell line to monitor in real-time quantitative and dynamic response to various hepatotoxins. Bioimpedance analysis and modelling has revealed an unknown mechanism of paracetamol hepatotoxicity; a temporal, dose-dependent disruption of tight junctions (TJs) and cell-substrate adhesion. This disruption has been validated using ultrastructural imaging and immunostaining of the TJ-associated protein ZO-1.

Age-related macular degeneration (AMD) is the leading cause of blindness in the developed world with a need for disease models for its currently incurable forms. Human induced pluripotent stem cells (hiPSCs) technology offers a novel approach for disease modelling, with the potential to impact translational retinal research and therapy. Recent developments enable the generation of Retinal Pigment Epithelial cells from patients (hiPSC-RPE), thus allowing for human retinal disease *in vitro* studies with great clinical and physiological relevance. In the current study, the development of a tissue-on-a-chip AMD disease model has been established using RPE generated from a patient with an inherited macular degeneration (case cell line) and from a healthy sibling (control cell line).

A reproducible Electric Cell-substrate Impedance Sensing (ECIS) electrical wounding assay was conducted to mimic RPE damage in AMD. First, a robust and reproducible real-time quantitative monitoring over a 25-day period demonstrated the establishment and maturation of RPE layers on microelectrodes. A spatially-controlled RPE layer damage that mimicked cell loss in AMD was then initiated. Post recovery, significant differences in migration rates were found between case and control cell lines. Data analysis and modelling suggested this was due to the lower cell-substrate adhesion of the control cell line. These findings were confirmed using cell adhesion biochemical assays. Moreover, different-sized, individually-addressed square microelectrode arrays with high spatial resolution were designed and fabricated in-house. ECIS wounding assays were performed on these chips to study immortalized RPE migration. Migration rates comparable to those obtained with ECIS circular microelectrodes were determined.

The two proposed disease-models-on-a-chip were then used to explore the therapeutic potential of the antioxidant N-Acetyl-Cysteine (NAC) on hiPSC-RPE and HepaRG cell recovery. Addition of 10 mM NAC at the end of a 24h paracetamol challenge caused a slight increase in the measured impedance, suggesting partial cell recovery. On the other hand, no effect on case hiPSC-RPE migration has been observed. More experiments are needed to examine the effect of different NAC concentrations and incubation periods. The therapeutic potential of electrical stimulation has also been explored. A preliminary study to evaluate the effect of electrical stimulation on RPE migration has been conducted. An externally applied direct current electric field (DC EF) of 300 mV/mm was found to direct the migration of the immortalized RPE cell line (hTERT-RPE1) perpendicular to the EF. The cells were also observed to elongate and to realign their long axes perpendicular to the applied EF.

The proposed tissue-on-a-chip disease models are powerful platforms for translational studies. The potential of such platforms has been demonstrated through revealing unknown effects of acetaminophen on the liver as well as providing deeper insights into the underlying mechanisms of macular degeneration. Combining stem cell technology with impedance sensing provides a high throughput platform for studying patient-specific diseases and evaluating potential therapies.

Declaration of Authorship

I hereby declare that the research presented in this thesis and the thesis itself was composed by myself based on work done at the School of Engineering at The University of Edinburgh. The work done in collaboration has been stated.

This thesis has not entirely or in part been submitted for any other degree or professional qualification.

Wesam Gamal

10 August 2015

Acknowledgments

First of all, I would like to express my deepest gratitude to my PhD supervisors. I sincerely thank Dr. Stewart Smith for all his help and support and for giving me the opportunity to work on such an exciting project; Professor Ian Underwood for his constant encouragement and guidance; and Dr. Pierre Bagnaninchi, thank you for always being there to help, motivate and push me beyond my limits. I could not have wished for a better mentor.

I would like to thank Dr. Christina Holmes, whom I was so lucky to meet while she was visiting from Canada, for teaching me all about cell culture, for her patience and for being such a great person to be around in the lab. I also deeply thank Dr. Vlastimil Srsen for all his help around the culture lab. He was always around to teach, help and advise me on what to do and how to do it. It would not have been the same without you.

Working on this multidisciplinary project, I got to meet and work closely with many exceptional scientists. I would like to deeply thank our collaborators: Professor Baljean Dhillon and Dr. Shyamanga Borooah for introducing me to the exciting world of regenerative medicine and for guiding me through all the biological processes involved in our work. I would also like to thank Professor Colin McCaig for giving me the opportunity to visit his labs at Aberdeen University and for enlightening me with his immense knowledge. Many thanks go to all members of the Hepatology Lab. specially, Dr. Leonard Nelson, Dr. Philipp Treskes and Katie Morgan. Thank you for your endless research ideas and for being the most motivated, enthusiastic research group that could ever be. It has been so much fun to work, and have lots of coffee, dinners, drinks, with you all.

I would like to thank everyone who has helped me design and fabricate my devices. I thank all members of the Scottish microelectronics centre, Professor Anthony Walton, Professor Tom Stevenson, Professor Ron Pethig, Dr. Yifan Li, Dr. Jonathan Terry, Dr. Adam Stokes, Dr. Peter Lomax, Constantine Talalaev and Aleksandr Tabasnikov. I would also like to thank Dr. Andrew Bunting for teaching me everything I know about microfabrication. I thank the electrochemistry group, Dr. Andrew Mount, Dr. Damion Corrigan, Dr. Ilka Schmeuser and Dr. Richard Perry for allowing me to occupy their lab and teaching me how to use their equipments. I would also like to thank Dr. Colin Campbell for providing me with RPE cells. I deeply thank Steve Gourlay, Andrew Garrie and all the technicians at the SMC clean rooms, the mechanical workshop and the electronics workshop for their help and for always being so efficient in getting the job done. I also sincerely thank the late Mrs. Susan Kivlin for being so friendly, helpful and allowing me to use her lab and borrow anything I needed at any time. She will be truly missed. I also thank Dr. Christian Renken and Ms. Catherine Toniatti-Yanulavich from Applied Biophysics for providing me with all the technical information I needed.

I would like to thank all my colleagues and friends for all the discussions, lunches, dinners, coffees and drinks that we had. Giuseppe Schiavone, Ilka Schmeuser, Enrico Mastropaolo, Jeremy Murray, Katie Morgan, Kat Srsen, Tao Chen, Helen Cope, Dimitris Tsikritsis, Ewen Blair, Andreas Tsiamis, Aleksandr Tabasnikov, Colin Chung, thank you for all the great times.

Finally, I would like to thank my family for everything. I thank my husband for simply being in my life, calming me down when I was panicking and always believing in me even when I did not believe in myself. Without your endless support, love, and cooking, I could not have done it. You are truly my rock. I want to thank my mum for always being the kindest, most supportive and most loving mother anyone could ask for. And finally, my dad for being the sound of reason that I always turn to, for always being there for me and pushing me for years to get a PhD. I dedicate this thesis to you.

Table of Contents

List of Figures

List of Tables

Glossary

8W1E	8 wells, 1 electrode/well
8W1DD	8 wells, 1 different diameter electrode/well
8W10E^{+}	8 wells, 10 interdigitated electrodes/well
96W20idf	96 wells, 20 interdigitated fingers/well
AC	Alternating current
ADD	HepaRG medium additives
ADRs	Adverse drug reactions
ADSCs	Adipose-derived stem cells
Ag/AgCl	Silver/silver chloride
ALF	Acute liver failure
AMD	Age-related macular degeneration
AO/EB	Acridine Orange/Ethidium bromide
AP	Apoptotic appearance
APAP	Acetyl-para-aminophenol
ATP	Adenosine triphosphate
Au	Gold
BC	Bile canalicular lumen
BEC	Biliary-like epithelial cells
Ca^{2+}	Calcium ion
CE	Counter electrode
CH	Cholangiocyte
CI	Cell index
CO_2	Carbon dioxide
CPE	Constant phase element
Cr	Chromium

CsA	Cyclosporine-A
CYP450	Cytochrome P450
DAPI	4', 6-diamidino-2-phenylindole
DC	Direct current
DI	De-ionized water
DILI	Drug induced liver injury
DMEM	Dulbecco's modified eagle medium
DMG	Dense mitochondrial granules
DMSO	Dimethyl sulfoxide
ECIS	Electric Cell-Substrate Impedance Sensing
ECM	Extracellular matrix
EF	Electric field
EGCG	Epigallocatechin gallate
EMT	Epithelial-to-mesenchymal transition
ESCs	Embryonic stem cells
FAK	Focal adhesion kinase
FBS	Fetal bovine serum
FCS	Fetal calf serum
FDA	Food and drug administration
FDM	Finite difference modelling
FEA	Finite element analysis
FLF	Fulminant liver failure
GPS	General purpose seeding medium
GSH	Glutathione
H	Hepatocyte
H_2O_2	Hydrogen peroxide
HBSS	Hank’s balanced salt solution

HEKa	Adult human epidermal keratinocytes
HEPES	(4-(2-hydrxyethyl)-1-piperazineethanesulfonic acid)
hESCs	Human embryonic stem cells
HIM	Hepatocytes induction medium
hiPSCs	Human induced pluripotent stem cells
HLCs	Human hepatocyte-like cells
hMSCs	Human mesenchymal stem cells
hTERT	Human telomerase reverse transcriptase
HTS	High throughput screening
IBCA	Impedance- based cellular assay
IHP	Inner Helmholtz plane
K^+	Potassium ions
LORMD	Late onset retinal macular degeneration
MDS	Molecular devices
MEA	Microelectrode arrays
MET	Mesenchymal-to-epithelial transition
MFT	ECIS multiple frequency mode
MMM	Metabolic maintenance medium
Mt	Mitochondria
MTT	(3-(4,5-dimethlthiazol-2-yl)-2, 5-diphenyl tetrazolium bromide)
N	Cell nucleus
Na^+	Sodium ions
NAC	N-acetyl-cysteine
NACA	N-acetyl-cysteine amide
NAPQI	N-acetyl-p-benzo-quinoneimine
NH	Necrotic appearance
NPCs	Neural progenitor cells

NSCs	Neural stem cells
Nu	Cell nucleolus
OHP	Outer Helmholtz plane
PBS	Phosphate buffered saline
PCB	Printed circuit board
PDMS	Polydimethylsiloxane
PECVD	Plasma enhanced chemical vapour deposition
PEDF	Pigment epithelium derived factor
PHH	Primary human hepatocytes
PI3k	Phophoinositide 3-Kinase
PKC	Phosphokinase c
PMA	Phorbol-12-myristate-13-acetate
PSC	Pluripotent stem cells
Pt	Platinum
qPCR	Quantitative PCR
RDM	Retinal differentiation medium
RIF	Rifampicin
ROS	Reactive oxygen species
RPE	Retinal Pigment Epithelium
RT-CES	Real-time cell electronic sensing
RT-PCR	Reverse transcription polymerase chain reaction
SAM	Self-assembled monolayer
SFT	ECIS single frequency mode
SiO_2	Silicon dioxide
Si_3N_4	Silicon nitride
Ta	Tantalum
TBH	Tetriary-butyl hydroperoxide

TCRP	Time-dependent cell response profiles
TEM	Transmission electron microscope
TEP	Transepithelial potential
TER	Transepithelial resistance
Ti	Titanium
TiN	Titanium nitride
TJ	Tight Junction
UV	Ultra violet
WE	Working electrode
ZO-1	Zona occuldens protein 1

List of Symbols

α	Cell-electrode adhesion
A	Area of the culture chamber
C	Capacitance
C_{64kHZ}	Capacitance at 64 kHz
C_{cl}	Capacitance of the apical and basal membrane
$C_{cell\text{-}covered}$	Capacitance of the electrode covered with cells
$C_{cell\text{-}free}$	Capacitance of the cell free electrode
C_{dl}	Double layer capacitance
C_m	Cell membrane capacitance
f	Frequency
h	Distance between cells and electrode
I_o, I_1	Modified bessel functions
I_e	Current of ECIS working electrode
$I(t)$	Current as a function of time
J_e	Current density of working electrode
L	Length of the culture chamber
m	Cell migration rate
ϕ	Phase shift between voltage and current
Q_e	Electric charge of working electrode
ρ	Resistivity
R	Resistance
R_{4kHz}	Resistance at 4 kHz
R_b	Cell-cell barrier resistance
r_c	Cell radius

$R_{cell\text{-}covered}$	Resistance of the electrode covered with cells
$R_{cell\text{-}free}$	Resistance of the cell free electrode
R_{ct}	Charge transfer resistance
R_s	Solution resistance
t	Time
Θ	Orientation angle
$V_{applied}$	ECIS applied voltage
V_e	Voltage of ECIS working electrode
V_m	Voltage at the cell membrane
$V(t)$	Voltage as a function of time
ω	Angular frequency
Z	Complex impedance
Z'	Real part (Z), i.e. Resistance
Z''	Imaginary part (Z), i.e. capacitance
Z_{cell}	Cell impedance
$Z_{cell\text{-}covered}$	Impedance of the electrode covered with cells
$Z_{cell\text{-}free}$	Impedance of the cell free electrode
Z_e	Impedance of ECIS working electrode
Z_m	Impedance of apical and basal cell membranes
Z_w	Warburg impedance

List of Publications

W. Gamal, S. Borooah, S. Smith, I. Underwood, V. Srsen, S. Chandran, P.O. Bagnaninchi, B. Dhillon. 'Real-time quantitative monitoring of hiPSC-based model of macular degeneration on Electric Cell-substrate Impedance Sensing microelectrodes', 2015, Biosensors and Bioelectronics, 71, 445–455.

W. Gamal, P. Treskes, K. Morgan, C. Chesne, V. Shevchenko, J.N. Plevris, P.O. Bagnaninchi, L.J. Nelson ' Mechanistic insight into acetaminophen-induced hepatic tight junction disruption using a human hepaRG- based liverbiochip impedance biosensor', 2015, The 50th international Liver Congress, April 22-26, Vienna, Austria.

L.J. Nelson, P. Treskes, K. Morgan, W. Gamal, C. Chesne, J.N. Plevris, P.O. Bagnaninchi, 'Investigating paracetamol toxicity in HepaRG-based 3D human hepatic organotypic models with non-invasive optical coherence phase microscopy (OCPM)' ,2015, The 50th international Liver Congress, April 22-26, Vienna, Austria.

A. Kozlowska, W. Gamal, K. Morgan, P. Treskes, P. C. Hayes, J. N. Plevris, P. O. Bagnaninchi, L. J. Nelson, 'Mechanistic Insight into Chlorpromazine-induced Hepatic Tight Junction Disruption Using a Human HepaRG-based Liverbiochip Impedance', 2015, UEG Week, October 24-28, 2015, Barcelona – Spain.

W. Gamal, P. Treskes, C. Chesne, J.N. Plevris, P.O. Bagnaninchi, L.J. Nelson, 'Human hepatic HepaRG co-culture model as a sensitive and non-invasive toxicological platform using Electrical Cell-substrate biosensors',2014, The International Liver Congress , 49th annual meeting, April 9-13, London.

W. Gamal, P. Treskes, C. Chesne, J.N. Plevris, P.O. Bagnaninchi, L.J. Nelson. 'Human hepatic HepaRG co-culture model as a sensitive and non-invasive toxicological platform using ECIS biosensors',2014, VII Falk Gastro-Conference, October 8-11, Freiburg, Germany.

W.Gamal, S.Smith, I.Underwood, P.O. Bagnaninchi, 'Microelectrode Array System for Electrically Driven Cell Migration Studies',2013, 2nd conference on Impedance-based cellular assays (IBCA), August 21-23, Budapest, Hungary.

Chapter 1

Introduction

1.1. Disease-in-a-dish: A new promise for stem cells

In 1998, James A. Thomson and his colleagues at the University of Wisconsin–Madison succeeded in creating human embryonic stem cells (hESCs) in a lab for the first time [1]. These cells could renew themselves, providing an unlimited supply, and could differentiate into any other cell type. Using these stem cells to create transplants to cure almost all diseases was a possibility that intrigued researchers, clinicians and most of all, patients with incurable diseases. Unfortunately, these stem cells had to be derived from the inner cell mass of developing embryos [2]; an ethical issue that led President George W. Bush to announce in 2001 that the US would not fund embryonic stem cell research, except for that using already existing stem cell lines [3]. In addition to ethical concerns, controlling the stem cell differentiation process was not easy with almost all initial trials failing to derive other cell types from stem cells [3]. This however changed in 2002 when Hynek Wichterle et al. managed to derive motor neurons from embryonic stem cells [4]. This was considered a milestone, allowing researchers and clinicians to develop new stem cell-based therapies to treat patients with incurable brain or spinal cord conditions. Soon other researchers started to realize that there was another promise for the use of stem cells: creating a disease-in-a-dish. It was thought that this new role for stem cells in disease modelling would allow for the study of incurable diseases or reveal unknown mechanisms underlying curable ones, and would be a groundbreaking

technique in drug discovery [5]. However, the ethical issues surrounding embryonic stem cells remained, hindering the progress of such research.

In 2006, a major breakthrough in stem cell research was achieved when Shinya Yamanaka was able to derive embryonic-like stem cells from human adult cells (somatic cells). This process of transforming adult cells back into stem cells was called 'reprogramming' and the cells were known as induced pluripotent stem cells (iPSCs) [6]. iPSCs shared the self renewal properties of ESCs and the ability to differentiate into other cell types, without the ethical concerns surrounding ESCs.

Recent recognition of the importance of the series of breakthroughs in stem cell research was acknowledged with the awarding of the 2012 Nobel prize for medicine and physiology to Sir John Gurdon, who first demonstrated the cloning of an adult frog, and Shinya Yamanaka [2]. Generating human iPSCs (hiPSCs) from patients is revolutionizing the field of regenerative medicine and disease modelling, with the potential to model almost any disease or genetic disorder [7].

1.2. Stem cells and drug development

The development cost of marketable drugs is continuing to grow reaching billions of pounds, with almost 90% of the drugs failing to get approved after clinical trials or are withdrawn from the market due to safety concerns [8]. The pharmaceutical industry therefore needs toxicity assays that can accurately evaluate the toxic/therapeutic potential of a drug during its development phase. Stem cells provide innovative tools for drug high-throughput screening (HTS) [8]. The ability to generate patient-specific human induced pluripotent stem cells also shows a great potential in individualizing drug testing [9]. However, in such stem cell-based toxicity assays, validation is essential in order to establish a reliable platform that can evaluate drug metabolism and investigate possible side effects.

1.3. Impedance sensing and stem cells: Quantifying stem cell research

The need for a non-invasive, quantitative technique that can monitor the differentiation process, growth kinetics and quality of stem cells is essential for determining the validity of stem cell-based disease models and drug screening platforms. Usually biochemical assays, including reverse transcription polymerase chain reaction (RT-PCR), western blotting and immunofluorescence assays, are used to determine the suitability of stem cells for disease modelling and to make sure that the required differentiation path is reached [10, 11]. However, these assays are end-point, invasive and time-consuming procedures. There is therefore a need for a non-invasive technique that can monitor stem cell-differentiation in real-time and validate stem cell-based disease models.

Electric Cell-substrate Impedance Sensing (ECIS) is a non-invasive method that can quantitatively characterize cells and monitor changes in their cellular behaviour/morphology in real-time [12]. In this technique, a small alternating current (AC) is driven between a sensing (measuring) electrode and a larger counter electrode, and impedance measurements are recorded using a lock-in amplifier. As cells grow on top of the sensing electrode, they impede current flow resulting in an increase in the measured bioimpedance. Hence, any change in cell physiology can be interpreted from the impedance measurements. The impedance can also be analyzed and translated into biologically-relevant parameters describing cell-cell junctions, cell-electrode adhesion and cell membrane capacitance [13].

Due to this non-invasive, real-time, quantitative nature, impedance sensing is increasingly being used to evaluate and characterize stem cell-based models [14, 15]. Impedance based cellular assays (IBCAs) are therefore an emerging technology in drug discovery, providing a

high-throughput screening approach that can monitor cellular response to a test compound in real-time [16-18].

1.4. The proposed disease models-on-a-chip: Aims and objectives

The main aim of this research is to develop a platform, combining impedance spectroscopy with stem cells, to quantitatively model and examine disease kinetics and underlying mechanisms; and evaluate the therapeutic potential of drugs and new therapies. In the current study, two stem cell-based disease models are proposed to investigate underlying mechanisms of drug-induced acute liver failure (ALF) and age-related macular degeneration (AMD). The non-invasive, real-time Electric Cell-substrate Impedance Sensing (ECIS) platform formed the basis of these disease models-on-a-chip; providing a quantitative method for the characterization of the diseases as well as the evaluation of therapeutic approaches.

The first disease model-on-a-chip presented in this work, employs a liver biochip approach where HepaRG cells, a bipotent human hepatic progenitor cell line, self-organize for 8 days, until they form a liver-like structure, directly on ECIS microelectrodes. The liver biochip has been used to monitor in real- time, via impedance measurements, dynamic changes in structural tight junctions and cell-substrate adhesions in response to the introduction of drugs and test compounds during the conducted hepatotoxicity studies.

The second disease model-on-a-chip is for age-related macular degeneration. AMD is the main cause of blindness in the developed world affecting 500,000 patients in the UK alone [19, 20]. Hence the need for disease models to fully investigate AMD incurable forms. An hiPSC-based disease model has been developed on ECIS microelectrodes. Induced pluripotent cells have been successfully derived from a patient with macular degeneration and one unaffected sibling. Patient's fibroblasts were expanded and reprogrammed to a pluripotent state before being differentiated to retinal pigment epithelial cells (RPE). Cells were plated on ECIS microarrays

before being allowed to mature for an additional period of 3 weeks. Final RPE maturation was completed on the microelectrode arrays before investigating the regenerative abilities of the affected (case) and control cell lines using electrical wound healing assays. Figure 1.1 shows the basic steps towards the establishment of the AMD disease model on ECIS chips.

The therapeutic potential of antioxidants and electrical stimulation on cell recovery has also been investigated. Moreover, microelectrode arrays, with different-sized, individually-addressed electrodes with a higher spatial resolution than that of ECIS commercial electrodes, have been designed and fabricated in-house.

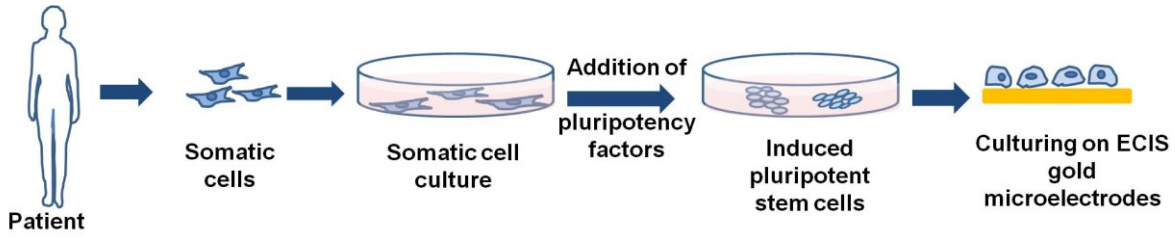

Figure 1.1: Establishment of the hiPSC-based AMD model-on-a-chip. Patient's fibroblasts were expanded and reprogrammed with Yamanaka factors to a pluripotent state before being differentiated to RPE. Cells were then plated on ECIS microarrays and allowed to mature. Figure modified from [2].

This thesis is divided into six main chapters and is organized as follows:

Chapter 2: Literature Review

This chapter provides the theoretical background behind this work. Advances in stem cell-based disease models and therapeutic approaches are discussed. A brief description of the two diseases modelled in the current study is provided. Moreover, basics of electrical impedance spectroscopy and Electric Cell-Substrate Impedance Sensing are explained. Finally, microelectrode design considerations and fabrication methods are described.

Chapter 3: Materials and Methods

The methods, materials and culturing protocols used in this work are described. Microelectrode designs and fabrication processes are also illustrated.

Chapter 4: Drug-induced injuries: Acute liver failure disease model-on-a-chip

This chapter introduces a disease model-on-a-chip for drug-induced acute liver failure. The model integrates impedance sensing with the progenitor HepaRG cell line and is used to examine the kinetics behind drug-induced hepatotoxicity. Finally, differences between sub-populations of the hepatic co-culture as reflected by impedance measurements are discussed.

Chapter 5: Electrically-induced Injuries: An in vitro model-on-a-chip for AMD and degenerative diseases

This chapter focuses on the study of cell migration and regeneration following an electrically-induced injury. Electrical wound healing assays are employed to mimic the damage of retinal pigment epithelial cells in age-related macular degeneration. Electrical wounding is also used to investigate the migration abilities of the hepatic cell lines, HepaRG and C3A, in order to gain more insight into hepatocytes regeneration. Finally, the use of in-house fabricated microelectrode arrays, with different-sized, individually-addressed electrodes for ECIS measurements is demonstrated.

Chapter 6: Towards a new therapy: Stimulation of wound healing

This chapter examines the potential of two therapeutic approaches; drug-stimulation and electrical stimulation, on cell recovery and wound healing. The effect of antioxidants on cell recovery in drug-induced acute liver failure is explored. The potential of electrical stimulation as a new therapy for age-related macular degeneration is then exmained. Finally, a new design

allowing for radial electrical stimulation and integrating the stimulation platform with impedance sensing is proposed.

Chapter 7: Discussion

This chapter discusses the results obtained in this work. Some considerations and limitations surrounding the measurements are described.

Chapter 8: Conclusions and Perspectives

This chapter provides a summary of the current work and describes areas for future development, followed by a few concluding remarks.

Chapter 2

Theoretical Background

This chapter provides the theoretical background behind this work. Advances in disease modelling and therapeutics are discussed together with a brief description of the two diseases modelled in the current study: acute liver failure and age-related macular degeneration. The theory of electrical impedance spectroscopy, employed in this thesis to quantitatively monitor disease kinetics, is also described. Finally, a few design considerations and microelectrode fabrication methods are discussed.

I. Advances in disease modelling

In the current study, two stem cell-based disease models-on-a-chip are proposed to investigate underlying mechanisms of drug-induced acute liver failure (ALF) and age-related macular degeneration (AMD). This section describes advances in disease modelling and therapeutics. A brief description of ALF and AMD is also provided.

2.1. Stem cell-based disease models

Disease models have become essential tools for investigating underlying mechanisms of diseases, making them a vital platform for drug development and novel therapies [9]. Animal-based disease models have been widely used for many years. However, many diseases are species-specific and animal models cannot fully reflect the human behaviour in these cases [7]. The failure of various treatments in humans despite the success achieved in animal models

has been attributed to this behavioural difference [9]. Ethical issues are also associated with animal studies, especially when toxicity assays and drug development are involved. *In vitro* cell-based disease models overcome these problems allowing for relevant models and, with the exception of embryonic stem cells, without the surrounding ethical issues [7, 21]. Primary human cells are still the preferred cell type for physiologically relevant disease models. However, primary cells are limited, expensive and difficult to obtain and culture [2]. For that reason, immortalized cell lines have predominated cell-based disease models, despite that in many cases they do not accurately reflect the *in vivo* behaviour [2, 9].

Due to their self-renewal properties, their ability to differentiate into various physiologically relevant cell types and their unlimited proliferation capacity, stem cells play a major role in therapeutic and regenerative medicine [2, 22]. Recently, stem cells have been widely used in disease modelling as an alternative to primary human cells, animal cells and transformed cells [22, 23]. In 2006, a breakthrough in regenerative medicine was achieved when the Nobel laureate, Shinya Yamanaka [6], was able to reprogramme somatic (adult) cells, transforming them back into stem cells. Generation of patient-specific human induced pluripotent stem cells (hiPSCs) offers a new paradigm for disease modelling and for individualizing drug testing [9].

In this work, two stem cell based-disease models are proposed for acute liver failure and age-related macular degeneration. The general mechanisms underlying these two diseases are explained in the following sub-sections.

2.1.1. Acute liver failure

Acute liver failure (ALF) is a rare but life-threatening critical illness that occurs most often in patients who do not have a pre-existing liver disease [24]. Drug-induced liver injury (DILI) is the most common cause of ALF in the developed world. Paracetamol (also known as

acetaminophen and acetyl-para-aminophenol (APAP)) toxicity was found to be the leading cause of drug induced ALF [25]. Well-described biochemical endpoint assays of APAP overdose show various intrinsic pathophysiological mechanisms from the depletion of the high-enegry phosphate (Adenosine triphosphate, ATP) that is required for many cellular processes, to mitochondrial dysfunction and oxidative stress. This eventually results in an unprogrammed (necrotic) cell death through physical disruption of cellular and liver architecture [26, 27].

Normal liver architecture is maintained by establishment of functional hepatic polarity arising from spatial structural and functional differences between apical and basolateral membranes as illustrated in Figure 2.1 and described in more detail in Appendix A [28, 29]. Cell-cell junctions and cell-substrate adhesion play a crucial role in preserving such polarity. Hepatic tight junctions (TJs) maintain the structural polarity essential for bile secretion, drug transporters and the expression of the detox enzymes cytochrome P450 (CYP450) [30]. Cell adhesion sites on the other hand connect the cytoskeleton to the extracellular matrix (ECM), and serve to modulate many aspects of cell behaviour including survival/apoptosis, differentiation, and polarity [31, 32]. Moreover, chemical disruption of adhesion sites can also have profound effects on the functioning of the liver. Cholestatic drugs, which induce leaky TJs, can generate toxic mechanisms (similar to APAP) in HepaRG cells [33, 34]. For instance, chlorpromazine has been shown to destabilize intercellular TJs; while phorbol-ester is known to disrupt TJ integrity and cell polarity in the hepatic cell line HepG2 [35]. Despite of the vital roles played by TJs and cell adhesion in sustaining many hepatic functions, temporal and quantitative effects of direct APAP toxicity on adhesion structures have not been previously explored, hindered by a lack of non-invasive, real-time and quantitative enabling technologies.

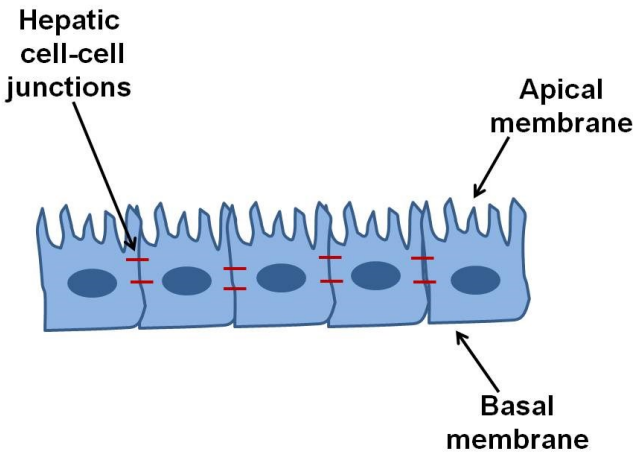

Figure 2.1: Hepatic Polarity. A schematic diagram showing the structural differences between hepatic apical and basal membranes. The red lines represent the hepatic cell-cell tight junctions.

Conventional 2D cultures for drug safety testing using rodent or human immortalized hepatic cell lines such as HepG2, Fa2N4 or HuH7 lack the functionality of primary human hepatocytes (PHHs) and are not representative of normal liver tissue. Although PHHs are still preferred for *in vitro* prediction of drug hepatotoxicity, they rapidly lose polarity and exhibit phenotypic instability, besides their limited supply [36]. Human hepatocyte-like cells (HLCs) generated using pluripotent stem cell (PSC) technologies have been put forward as potential hepatic models for drug discovery [37]. However, current PSC-differentiation protocols produce monolayers of HLCs with fetal phenotype. Also, compared with PHHs, HLCs exhibit reduced hepatic gene expression and CYP450 enzyme levels [38]. An alternative to PHHs increasingly used in hepatotoxicity testing, is the hepatic HepaRG progenitor (tissue-specific stem cells) cell line, which is able to differentiate to HLCs and biliary-like epithelial cells (BECs) [31, 39, 40]. HepaRGs are a uniquely stable, highly-differentiated hepatocyte:cholangiocyte co-culture model, which maintain *in vivo*-like liver-specific functions, including drug metabolism, lipid metabolism, and mitochondrial phenotype for several weeks [38, 41]. HepaRGs are used in this work to model ALF and investigate the underlying mechanisms of drug- induced hepatotoxicity.

2.1.2. Age-related macular degeneration

Age-related macular degeneration (AMD) is the most common cause of blindness in the developed world [19, 42]. The disease usually affects patients in their seventh and eighth decades resulting in the loss of functionally important central vision. There are two main forms of the disease; wet AMD, in which sub-retinal vascular leakage predominates and dry AMD in which the formation of drusen (lipid and fatty protein deposits) and cell degeneration are the primary disease processes [42]. Although treatments have recently been developed for wet AMD, there is currently no effective treatment for dry AMD.

The Retinal Pigment Epithelium (RPE) is a pigmented, polygonal monolayer of cells found directly below the photoreceptor layer in the retina (for more detail on the retinal structure and RPE functions, see Appendix B [43-45]). The primary role of the RPE is in maintaining photoreceptor homeostasis. RPE dysfunction, degeneration and reduced repair are implicated in the AMD disease process [46, 47]. In normal ageing, RPE cell loss is compensated for by increasing cell size and migration of neighbouring RPE [48]. In AMD however, healing is hampered leading to problems such as incomplete RPE coverage and the consequent death of overlying photoreceptors.

Late onset retinal macular degeneration (LORMD) is a rare form of macular degeneration. It is an autosomal dominant disease in which the abnormal gene dominates, i.e. the patient can get the disease even if the abnormal gene is inherited from only one parent [49]. LORMD results from a mutation in the gene encoding the protein C1QTNF5 [50]. The complete function of C1QTNF5 is currently unknown. However, it is suggested to play a role in cell adhesion between the RPE layer and the underlying basement membrane [51]. LORMD shares key clinical and pathological features with AMD including dark adaptation delay, drusenoid retinal changes prior to sub-retinal deposit, RPE cell loss and neuro-retinal atrophy. Therefore,

it has been proposed as a good model for AMD [52].

In vitro RPE models are required to investigate the underlying mechanisms associated with AMD. Primary human RPE cell lines will be the cells of choice in many research labs due to their physiological behaviour if not for their previously mentioned difficulties to obtain and culture. Hence immortalized cell lines are still predominant in AMD research. Recent developments enable the generation of RPE cells derived from patients (hiPSC-RPE) [53, 54], thus allowing *in vitro* studies of human retinal disease that have a great clinical and physiological relevance. In the macular degeneration disease model proposed in this work, hiPSC-RPE case and control cell lines, used to model RPE loss accompanying the disease, have been derived from a patient with LORMD and one of his unaffected siblings respectively [55].

2.2. Automated quantitative assays for disease modelling

While biochemical assays remain the gold standard for detecting, quantifying and studying various cellular behaviours, the invasive nature of these assays results in the destruction of the sample under investigation. These traditional methods are normally performed at one time point, missing any changes in cellular behaviour over time. Impedance sensing overcomes these problems. Being a label-free, non-invasive technique allows for measurements to be performed on live cells. The measurements are also done in real-time and for long periods. Impedance sensing can therefore monitor kinetics of cellular behaviour and changes in morphology over time and is in that sense particularly useful to monitor processes like wound healing, stem cell differentiation and cytotoxicity assays [56]. Impedance sensing has been employed in this study to establish fully automated, quantitative stem cell-based disease models for acute liver failure as well as age-related macular degeneration. Impedance-based assays for

drug-induced liver injuries and electrically-induced retinal injuries have been used to model the two diseases.

2.2.1. Drug-induced injuries

Adverse drug reactions (ADRs) are a major issue for the pharmaceutical industry and public health, and are a frequent cause of both failure of drug approval and withdrawal. As the liver is bound to be the most affected during drug metabolism, drug-induced-liver-injury (DILI) is the most prominent reason for a drug to be withdrawn from the market [17, 18, 57, 58].

During the drug development process, cell-based assays are a key tool to support the selection of safe drug candidates before entering animal testing [57, 59]. Biochemical methods, such as the MTT (tetrazolium dye) assay [60], the neutral red uptake assay [61], and ATP (adenosine triphosphate) measurement [62], are widely used in hepatotoxicity screening assays. However, these traditional biochemical assays are time consuming, requiring complex steps with multiple reagents at every prescheduled time point. Moreover, the information provided is usually limited to the time points investigated, disregarding the kinetics of the effects [63]. Impedance-based cellular assays (IBCAs) can overcome this problem. IBCAs are an emerging technology in drug discovery due to their high sensitivity, non-invasive and quantitative nature. An impedance-based assay could provide a high-throughput screening (HTS) approach that can monitor changes in cell morphology and behaviour in response to a test compound in real-time [16-18]. Impedance measurements can therefore be used to examine the temporal interaction of the tested compounds with cells; creating distinct profiles for drug kinetics and toxicity mechanisms [64]. In a study by Kustermann *et al*. [59], impedance-based time-dependent cell response profiles (TCRPs) were used to establish different impedance profiles allowing for the differentiation between cytostatic and cytotoxic drugs through recording and analyzing temporal kinetics of different compound-effects on NIH 3T3 fibroblasts.

Commercial as well as non-commercial impedance-based systems have been employed for cytotoxicity assays with many of them focusing on hepatotoxicity studies [65, 66]. Platforms like xCELLigence [67] and Electric Cell-Substrate Impedance Sensing (ECIS) [66] have been used to investigate the effects of various drugs and compounds on different cell types including hepatocytes [17, 57], cardiomycocytes [67], fibroblasts [68, 69] and cancerous cells [70]. Further drug effects have been explored using the Bionas platform. Ehret et al. [71] for instance demonstrated the effect of APAP on decreasing metabolism, the increase of acidification rates and decrease in oxygen consumption in liver cells using the Bionas Discovery device. The working principles behind some commercial platforms are described in Section 2.7.

It has to be mentioned that the majority of impedance-based toxicity studies have not made use of the full capability of impedance measurements. A decline in impedance, or cell index as measured by the xCELLigence system, is not necessarily a reflection of cell death, but could be due to a disruption of tight junctions, cell adhesion or a change in morphology. Using mathematical models, similar to the ECIS built-in model (Section 2.7.1.1), to further analyze the measurements, allows for a more accurate data interpretation and a deeper insight into the mechanisms of drugs/compounds.

In this study, an impedance-based liver-on-a-chip model has been developed. The highly-differentiated human hepatic cell line HepaRG has been combined with impedance sensing microelectrode arrays to profile real-time changes in the cellular impedance in response to model hepatotoxins. Moreover, the impedance measurements were deconvolved into parameters defining tight junctions, cell-substrate adhesion and cell membrane capacitance using ECIS modelling.

2.2.2. Electrically-induced injuries

Degenerative diseases are characterized by loss of cell regenerative abilities leading to a deterioration of tissue structure. In macular degeneration for instance, the loss of RPE ability to regenerate and heal after wounding is a characteristic symptom of the disease [46]. There is therefore a pressing need for wound healing and cell migration models for cell regenerative studies, to allow for a better understanding and uncover unknown mechanisms underlying degeneration.

There are various *in vitro* cell migration assays for wound healing and regenerative studies [72, 73]. The most commonly used is the traditional mechanical, scratching, assay where usually a fine pipette tip is used to scratch (wound) the cell layer before allowing the cells to migrate and recover [74, 75]. Scratching however does not produce a highly repeatable wound; a disadvantage that can be overcome by stamping. Stamping is another mechanical wounding assay where a physical stamp of defined geometry is used to create the wound [76]. Stamping, as well as scratching, can however disrupt the ECM layer as well as form debris that might affect the migration process.

Fencing, also known as gap closure assays, can be used to produce cell free regions where cell migration can be monitored after removing a solid [77], liquid [78] or gel barrier [79]. Cells grow around the physical barrier and then start migrating once it is removed. However, the lack of signalling from wounded cells as well as the absence of ECM proteins in the cell free regions does not really reflect what happens *in vivo*. Other wounding techniques include chemical [80] and optical methods [81, 82]. Recently, microfluidic channels have also been used for migration assays by using chemicals to produce a wound in a cell monolayer or through defining migration paths for the cells [78]. Zhang et al. combined microfluidics with a physical barrier technique to monitor the migration of human gastric cells as well as that of

mesenchymal stem cells towards tumor cells [83]. However, most of the above methods require extensive manipulation of the cell layer during both wounding as well as repair processes. Moreover, problems of quantification and reproducibility occur due to the difficulty of controlling the wounded areas.

Studies combining electrical wounding with impedance spectroscopy overcome this problem; as electrical wounding can produce well-defined repeatable wounds, while impedance sensing provides a quantitative, high throughput, real-time measurement of the healing process. Electric Cell-substarte Impedance Sensing (ECIS) is an impedance-based platform where cells are directly cultured on ECIS microelectrodes and the changes in impedance measurements are recorded in real-time. Because biological cells act as insulators, attachment of cells on top of ECIS arrays is accompanied by an increase in impedance. ECIS measurements are therefore a reflection of changes in cell behaviour or morphology (See Section 2.7.1).

In ECIS wounding assays, an elevated current pulse (0.1 mA- 3 mA) is used to wound the confluent cell monolayer through severe irreversible electroporation. The system then switches back to its normal operation where a small (1 μA) non-invasive current is used and the impedance is monitored while cells migrate to repopulate the electrodes [84]. The wound healing/migration rate represents the time taken by the cells to repopulate the electrode and is calculated according to Equation (3.1) described in Chapter 3. Figure 2.2 shows the basic principles of ECIS measurements and wounding healing assays.

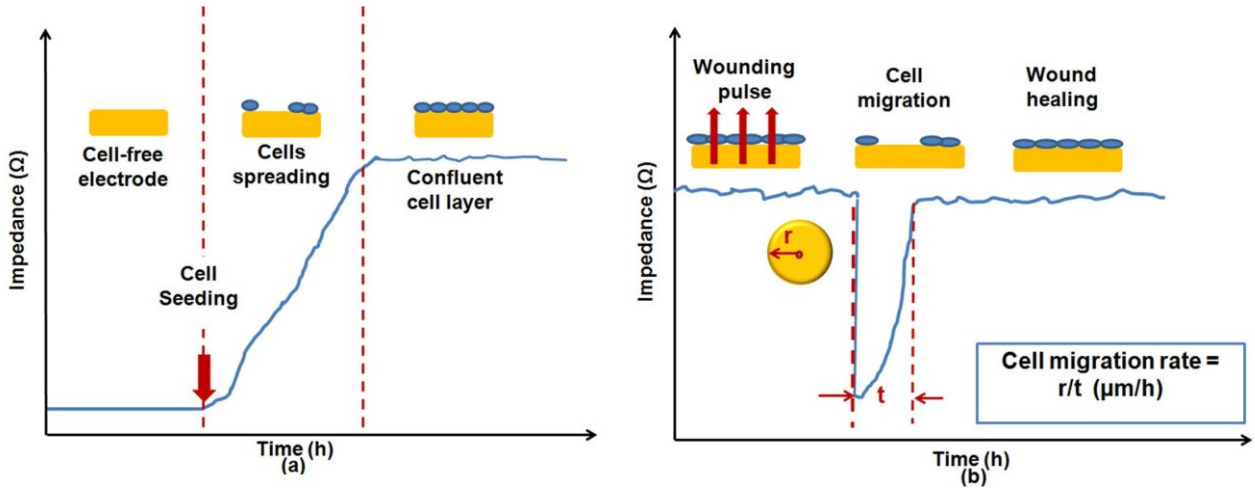

Figure 2.2: ECIS wound healing assay. (a) A schematic diagram showing the basic principle behind ECIS impedance measurements. Impedance (represented by the blue graph) increases when cells (blue) attach and spread onto the electrode (gold), reaching a plateau when a confluent layer is formed. (b) A schematic diagram describing the change in impedance measurements with ECIS electrical wounding. When a wounding pulse (red arrows) is applied to the confluent cell layer, the impedance drops to that of the cell-free level. With cell recovery, the impedance increases to reach a plateau when healing is achieved after a healing time (*t*).

The huge potential of ECIS electrical wounding assays in cell migration studies is undeniable. However, an efficient migration assay depends to a great extent on the wounding parameters used. A major drawback of ECIS electrical wounding is that arriving at such parameters is normally achieved through trial and error experiments, during which electrode damage or incomplete cell death and detachment might occur.

The ECIS platform has introduced another technique for cell migration studies known as the electric fence. This method is in essence similar to gap closure assays. Instead of using physical barriers to create a cell-free region, high electric pulses are applied before cell inoculation to prevent cell growth over the electrodes while cells spread and form a confluent layer in the rest of the culture well. This produces a clean electrode on which the cells can migrate and repopulate once the "electric fence" is switched off (Figure 2.3). Although the electric fence method has the advantage over electrical wounding of not requiring trial and error experiments, one can argue that cell migration assays based on electric fencing, like with any gap closure assay, might lack some of the signals and cues that are normally associated with *in vivo* injuries.

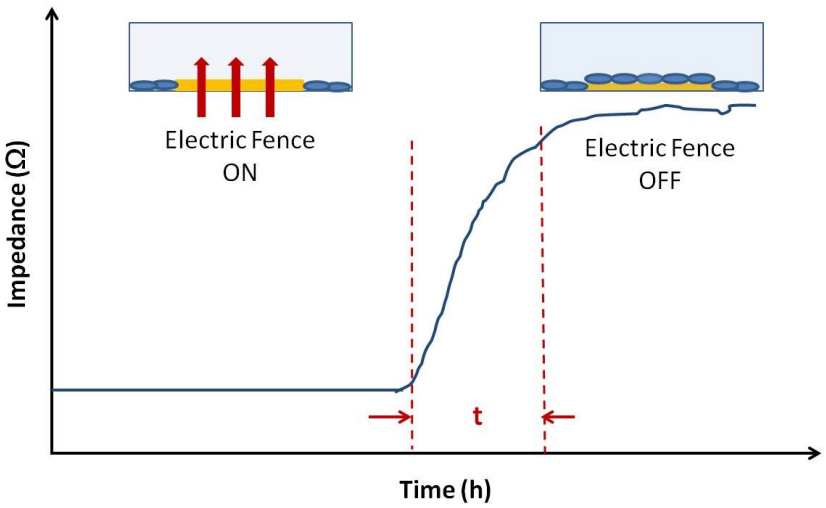

Figure 2.3: ECIS electric fence. A schematic diagram showing the principle underlying electric fencing. Elevated current pulses (red arrows) are applied to the electrodes before cell seeding. Cells (blue) grow around the electrode (gold) but not on top of it, creating an area empty of cells in the culture well (light blue rectangle). When the fence is off, the cells start to spread onto the electrode. The graph represents the changes in the impedance measurements accompanying the fencing process. *t* represents the time taken for cells to migrate after switching off the fence until a confluent cell layer is formed, reflected by the steady plateau formation.

Initially, ECIS cell migration studies used direct current (DC) wounding pulses [85, 86]. However, using a DC signal for wounding was a challenging, uncontrollable process as reported by Giaever and Keese [84]. These limitations were behind the present use of alternating current (AC) in ECIS electrical wounding. Keese et al. were the first to use AC pulses to perform wound healing assays on BS-C-1 (African green monkey kidney cells), NRK (normal rat kidney cells) and MDCK (Madin–Darby canine kidney cells) [84]. Ever since this study, ECIS has been intensively used to study wound repair as well as to investigate the effects of various factors on the healing process. The effects of various cytokines, kinases, adhesion proteins and signalling pathways on cell migration [87-93] and wound healing in the eye [94, 95], the airway epithelium [96-100], chronic wounds [101, 102], and cancer metastasis [103-112] have all been investigated. Moreover, there have been studies on the effect of negative pressure [113], radiation therapy [114] and specific medicines on migration and angiogenesis using nanoparticles [115] and microspheres [116] for drug encapsulation.

In the current study, the need for a physiologically relevant *in vitro* model of RPE layer repair that can be investigated quantitatively and reproducibly has been addressed through developing a tissue-on-a-chip approach. After establishing the hiPSC-RPE model on ECIS microelectrode arrays, an electrical wound healing assay was used to mimic RPE cell damage in both control and diseased hiPSC-RPE cell lines to study differences in cell migration abilities and repair.

2.3. Quantitative stem cell research

The need for a non-invasive, quantitative technique that can monitor the differentiation process, growth kinetics and quality of stem cells is essential for determining the validity of stem cell-based disease models. Whether the stem cells under investigation are embryonic (ESCs) or induced-pluripotent stem cells (iPSCs), with multi- or tissue specific- potency (progenitor cells) [117], quality control measures are required to define suitability for disease modelling [118, 119]. Biochemical assays including reverse transcription polymerase chain reaction (RT-PCR), western blotting and immunofluorescence assays, are usually used to make sure that the required differentiation path is reached [10, 11]. However, these assays are labour intensive, time consuming, end-point invasive procedures that destroy the cells under investigation. Due to its non-invasive, real-time, quantitative, automated nature, impedance sensing is increasingly used in the validation and characterization of stem cell-based models [14, 15].

Cho and Thielecke [120] were the first to use impedance spectroscopy to study and characterize growth of human mesenchymal stem cells (hMSCs). Following this study, impedance spectroscopy has been used to explore different aspects of stem cell research with many studies focusing on the kinetics of stem cell differentiation. Differentiation of stem cells is associated with a change in cell morphology, proliferation capacity and dielectric properties [121]. Impedance spectroscopy can detect these changes, defining distinctive impedance profiles for different differentiation paths. Hildebrandt et al. have reported an increase in resistance

measurements with the differentiation of human mesenchymal stem cells (hMSCs) towards osteoblasts [11], using a planar 1mm diameter platinum electrode-based chip. This rise in resistance was accompanied by a change in morphology from fibroblastic-like to a cuboidal morphology. Commercial platforms have also been used to monitor adipogenic vs. osteogenic differentiation. Angstmann et al. [122] used the two commercial systems ECIS and xCELLigence to examine differences in early phases of MSCs differentiation towards adipocytes and osteoblasts, while Kramer et al. have used xCELLigence to study adipogenesis of the preadipocytes 3T3-L1 cells [123]. In agreement with the previous studies, there was a drop in the measurements with adipogenesis while differentiation towards osteoblasts showed an increase in the measured values.

There are several factors that lead to the changes in impedance measurements during stem cell differentiation, including cell size and morphology changes. Differentiation towards certain cell types is associated with a decrease in size. In this case, a decrease in the measured impedance is expected simply because more gaps are expected to occur between adjacent cells where the current can pass through. However, in the case of osteogenic differentiation there is a significant increase in impedance associated with a decrease in cell size [11]. This can be attributed to mineralization and to the tight cell-cell junctions, forming a barrier that impedes the applied current [122, 124].

Another factor affecting impedance measurements during stem cell differentiation is cell-substrate adhesion. Changes in cell adhesion mechanisms and the amounts of secreted ECM proteins have been shown to affect cell morphology and function, which could in turn affect the differentiation process [125, 126]. Maercker et al. [127] have developed live cell chips to monitor cell adhesion as a marker of MSC differentiation. Cells were grown on electrode arrays for impedance measurements that reflected changes in cell adhesion. After stem cell differentiation towards human cardiac fibroblasts and human umbilical vein endothelial cells

was achieved, biochemical assays showed that the adhesion proteins had increased and translocated within the cells.

Cell-adhesion, cell-cell tight junctions as well as the integrity of cell plasma membranes can all be non-invasively assessed through further analysis and modelling of impedance data. Impedance modelling can therefore be used to provide further differentiation markers without the need for any biochemical assays. Bagnaninchi and Drummond [124] have used ECIS modelling to distinguish between osteogenic and adipogenic differentiation of adult stem cells (ADSCs). They reported an increase in the impedance measurements with the osteo-induced ADSCs that was also accompanied by an increase in tightness of the cell-cell junctions as indicated by the ECIS built-in model. On the other hand, the adipo-induced cells showed a drop in the impedance measurements and looseness in cell-cell junctions. A variation in dielectric properties between the two differentiation paths was also monitored as indicated by the higher cell membrane capacitance measured for the adipo-induced cells. Changes in dielectric properties accompanying stem cell differentiation towards adipocytes was also reported by Lee et al. [15]. They reported that a change in the average dielectric constant of adipocytes occurred during the differentiation process, which was related to lipid vacuoles accumulation.

It is worth noticing that impedance sensing is not entirely well-suited to monitor the differentiation process of all stem cell types. The use of impedance sensing to monitor neuronal and human embryonic stem cells differentiation has proven to be challenging. Neurons do not reach confluence when forming neuronal networks [128] and there will always be parts of the network not sensed by the electrodes. hESCs are known to grow in flat colonies [129], making the measurement impossible if the cells are away from the electrodes. In these cases, it is recommended to use interdigitated electrodes [10, 130] due to their ability to cover a wider area of the culture well. The measurements will then represent an average for the cultured cell population.

In the current study, the maturation of the HepaRG cell line and the establishment of a co-culture has been confirmed using impedance measurements before any hepatotoxicity assays were conducted. In the proposed AMD model, ECIS has been used to distinguish between the differentiation and maturation kinetics of the case and control hiPSC-RPE cell lines.

2.4. Therapeutic approaches

In this work, the proposed disease models-on-a-chip has been used to investigate therapeutic approaches to stimulate cell recovery. This section describes the two approaches used; namely drug stimulation and electrical stimulation.

2.4.1. Drug stimulation

Oxidative stress occurs due to the imbalance between reactive oxygen species (ROS) production and antioxidant defences, causing damage to a wide range of molecular species such as lipids, proteins and nucleic acids [131]. Oxidative stress has been implicated in different diseases including chronic wounds, neurodegenerative diseases, diabetes and cancer [131, 132]. Oxidative damage has also been linked to hepatotoxicity and liver failure caused by acetaminophen as well as other cholestatic drugs [133].

The retina is particularly susceptible to oxidative stress because of its high consumption of oxygen and its exposure to visible light [134]. Moreover, the amount of antioxidants present in the retina was found to degrade with age giving rise to high concentrations of ROS [135]. Hence, the role of oxidative stress in age-related retinal diseases like AMD [136, 137].

Antioxidants have attracted a wide interest recently, with many studies focusing on their protective and therapeutic potentials of ROS-dependent diseases. N-acetylcysteine (NAC), an ROS scavenger and the precursor of the detoxifying enzyme glutathione (GSH), has been widely used for the treatment of liver toxicity [133]. Furthermore, in 2006, the use of NAC was

approved by the Food and Drug Administration (FDA) for treatment of acetaminophen overdose. The use of NAC is not limited to the treatment of paracetamol toxicity though. In a study on citreoviridin cytotoxicity, Liu et al. [138] have indicated that citreoviridin-induced cell death was ROS-dependent and that pre-treating hepatocytes (HepG2) with NAC, reversed citreoviridin toxic effects. In a different study, NAC was shown to have an anti-inflammatory effect preventing apoptosis and completely abolishing acute fulminant liver failure (FLF) in mice [139].

NAC has also shown a promising effect on treating retinal diseases as it minimized the oxidative stress associated with diabetic retinopathy and AMD [140]. The novel thiol antioxidant, *N*-acetylcysteine amide (NACA), has been reported to be more effective than its parent compound, NAC. This was attributed to the increased ability of NACA to permeate cell membranes and the blood brain barrier due to its neutral carboxyl group. *In vitro* and *in vivo* experiments on rodents and human cells suggested that NACA may be a novel treatment for AMD and other retinal diseases [136].

In the current study, NAC has been used in an attempt to stimulate cell recovery after paracetamol-induced injuries in HepaRGs. The effect of oxidative stress on hiPSC-RPE migration followed by NAC treatment has also been explored.

2.4.2. Electrical Stimulation

2.4.2.1. Endogeneous Electric Fields

The existence of endogenous direct current electric fields (DC EF) within biological tissues has been known for more than two centuries [141]. In the late 1700s, Galvani's experiments on frog preparations provided proof for the existence of what he termed animal electricity, and is now referred to as bioelectricity [142-144]. In 1794, Galvani also demonstrated the existence of the injury potential in frogs by showing that the cut end of a leg sciatic nerve caused the

other leg to contract upon touching [142-144]. Based on this pioneering work, Matteucci measured injury potentials at the cut end of nerves and muscles using a galvanometer in 1831 [142]. Twelve years later, Emil Du-Bois Reymond, the founder of modern electrophysiology, was able to measure a current of 1μA flowing out of a cut in his own finger, another evidence for the existence of injury potentials [145].

DC electric fields exist within tissues due to spatial variations in the functioning of ion pumps, or leaks across individual cells or layers of cells, such as an ion-transporting epithelium. The resulting ionic gradients drive extracellular ionic current flow, establishing the voltage gradients [141, 146]. How the cells sense these gradients and how they respond to the corresponding electric fields is a complicated, not fully understood process. The immediate target of electric fields is likely to be the plasma membrane [145, 147, 148]. The EF has been proposed to redistribute integrins, charged lipid and protein molecules within the plasma membrane or modify the membrane potential at the ends of the cell facing the poles of the electric field [145]. It is suggested that electric fields also cause a redistribution of receptors and activate polarized signaling pathways specially of PI3K (Phosphoinositide 3-kinase), which was found to have a critical role in mediating EF-directed cell migration [149-151]. Ca^{2+} is known to regulate processes such as signal transduction, cytoskeletal reorganization, cell orientation, migration, cell differentiation and proliferation [148]. A significant increase in Ca^{2+} concentration in the presence of an externally applied EF has been reported suggesting a role for Ca^{2+} in EF-induced cellular responses [145, 152].

2.4.2.2. Mimicking Bioelectricity: Set ups and techniques

Vibrating probes and glass microelectrodes have been used to measure and confirm the presence of endogenous EFs *in vitro* [141, 145, 147]. *In vivo,* microneedle arrays have been used to measure transdermal skin potentials [153], while the detection and visualization of

electric potential at skin surface with no direct skin contact have been reported using the Bio-Electric Imager [154].

Electrotaxis chambers, also known as galvanotaxis chambers, are *in vitro* systems that apply external EFs and investigate their effects on various cellular processes [145]. The name refers to the electrotaxis phenomenon where an electric field is used to direct cell migration. In this set up (Figure 2.4), cells are usually cultured inside a petri-dish and glass coverslips are used to form a lid creating a thin chamber (~ 400 μm deep) of well-defined geometry. This allows for an accurate calculation of the imposed EFs, while the small volume allows for fast heat dissipation keeping Joule heating inside the chamber at a minimum [155]. EF application is performed using a DC power supply and agar salt-bridges in order to connect the metal electrodes to the culture medium while keeping any harmful electrode products away from the cells [145, 155].

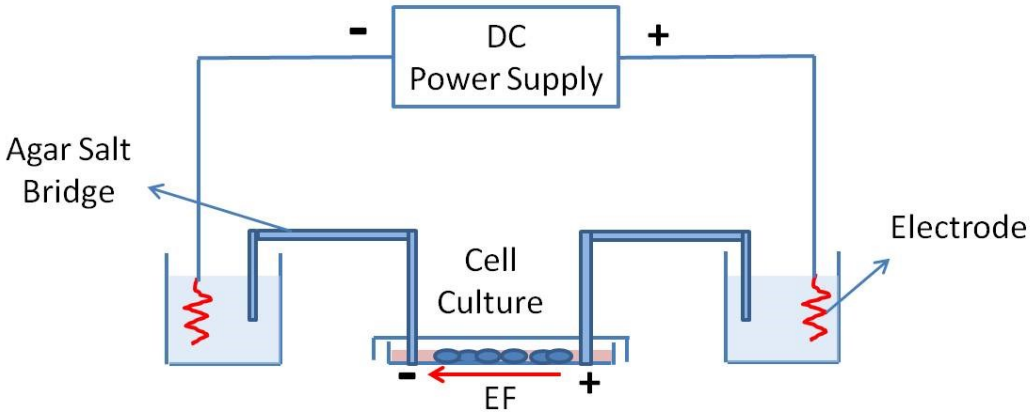

Figure 2.4: Electrotaxis chamber. A schematic diagram showing the general set up of an electrotaxis (galvanotaxis) chamber. The set up consists of a DC power supply, 2 metal electrodes, 2 beakers filled with a conductive salt solution, 2 agar salt bridges and a petri-dish where the cells are cultured. The agar bridges are used to connect the EF to the cell culture while keeping the cells away from any possible harmful electrode products. Figure modified from [145].

Recently, microfluidic channels have replaced petri-dishes of the traditional galvanotaxis chambers [95, 152, 156-161]. Moreover, complex microfluidic networks with interconnecting segments have been used to create multiple electric field strengths while providing a uniform flow field on the same chip [162]. In this work, a commercial microfluidic channel has been used to investigate the effects of an externally applied DC EF on RPE migration. Ag/AgCl has been used as the electrode material while agar bridges connected the EF to the cell culture inside the microchannel.

2.4.2.3. EF physiological role

Bioelectricity plays a major role in various cellular processes from cell cycle, cell division, differentiation, cell proliferation and migration to the establishment of left-right body asymmetry in fetal development [141, 145, 147, 148]. Endogenous EFs therefore affect multiple cell behaviours including embryonic development [163], wound healing [147, 164], nerve sprouting [165, 166], spinal-cord repair [167, 168], as well as cancer cell migration in metastasis [169-172].

i. EFs and Wound Healing

An injury potential is a DC voltage gradient that is induced within the extracellular and intracellular spaces by current flowing into and around an injury [145]. In epithelia, a transepithelial potential (TEP) occurs due to the directional transportation of ions causing a difference in net charge between the apical and basal epithelial sides. This is also coupled with the high resistance established by the sealing action of cell-cell tight junctions. As shown in Figure 2.5, in wounded epithelia, the potential drops at the wound site while remaining the same at distant areas. Potential gradients drive the electric current flow towards the wound from the surrounding tissue and then out from the wound, thus forming a laterally orientated

wound EF [147]. Injury potential gradients are normally in the order of tens of millivolts. EFs varying from 42 mV/mm in cornea wounds to 140 mV/mm at skin wounds in humans have been reported [141, 145, 147, 148]. It is worth mentioning that the measured injury potentials were found to vary both spatially and temporally [147]. The current flowing out of a wound varies spatially, having the strongest magnitude at the wound edge. The magnitude of the electric current changes with time as well. Currents at skin and cornea wounds were found to gradually increase during the first 1-2 hours after wounding and persist during the healing process before decreasing again when healing is achieved [173-175].

Injury EFs act as a directional cue directing cells to migrate into the wound during the healing process, thus playing a major role in wound repair [5, 145, 147]. Song et al. have demonstrated the importance of endogenous EFs in healing. Through inhibiting the transportation of ions using ouabain, benzamil and furosemid, a significant decrease in TEP, and in turn the induced wound EF, was monitored. This led to a delay in wound healing in a dose dependent manner illustrating the strong relationship between injury EFs and the repair process [176].

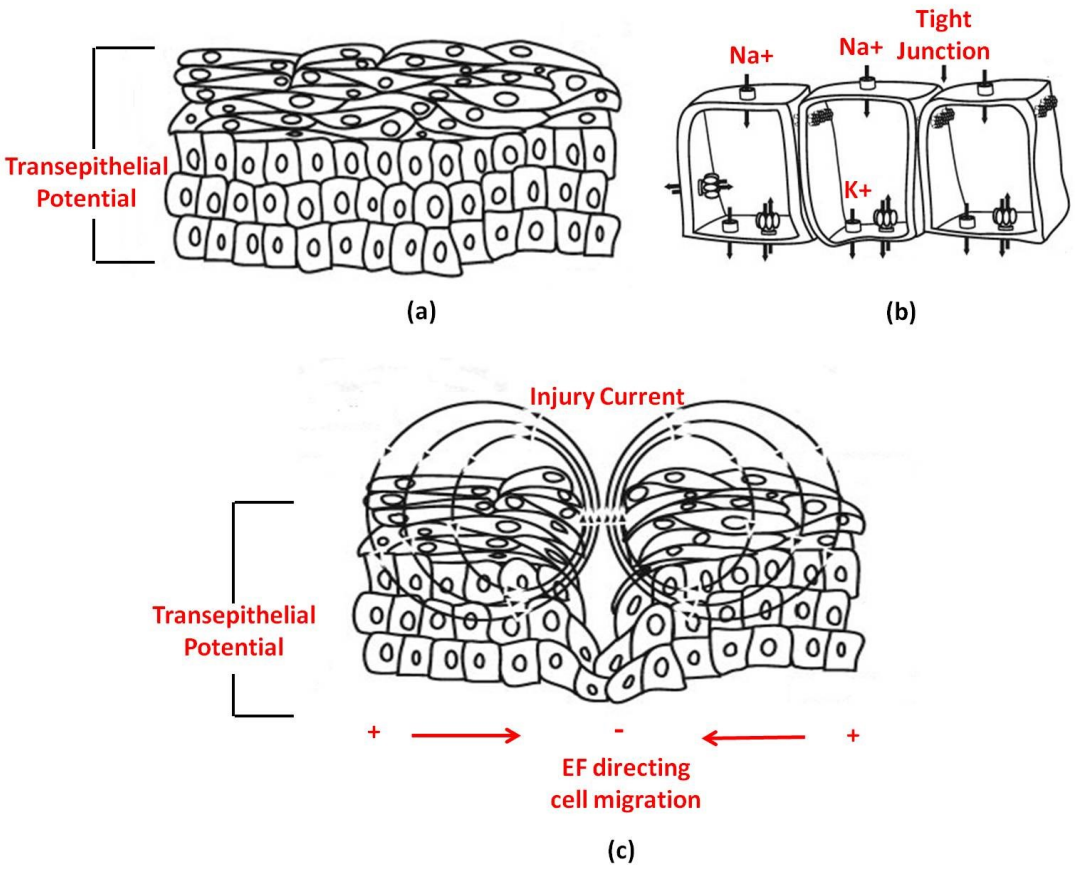

Figure 2.5: Transepithelial and injury potentials. (a) A schematic diagram showing the presence of a transepithelial potential between the apical and basal layers of an epidermal epithelium. (b) A cross section of the basolateral cuboidal layer showing the directional transportation of Na^+ and K^+ ions, causing a difference in net charge and coupled with the sealing action of cell-cell junctions to maintain TEP. (c) In injured epithelia, a low resistance path is created allowing Na^+ ions to flow outside of the wound, short-circuiting the TEP and generating an injury current. The TEP is not affected away from the wound however, and therefore an EF is established directing cell migration into the wounded area. Figure modified from [177].

EFs are suggested to play an overriding guidance role in directing cell migration in epithelial wound healing. Zhao et al. [173] have investigated the effect of applied EFs on wound healing in the presence of other co-existing chemical cues. It was found that EFs of physiological strengths were able to direct cell migration overriding other cues. According to the polarity of the applied EF, wound healing was either enhanced or impaired if applied in the opposite direction to that of the healing vector. EFs as low as 25 mV/mm with reverse polarity caused the wound to open up as cells migrated directionally away from the wound under the influence of the EF ignoring other co-existing cues.

Cell division, nerve sprouting and endothelial migration are all important elements in wound healing. Electric fields have been shown to control and direct these behaviours. Song et al. [178] have used drugs to manipulate ion transport affecting endogenous wound EFs. They demonstrated that an increase in these EFs caused an increase in cell division in wounded corneal epithelium by almost 40% with more nerves sprouting towards the wound. On the other hand, reducing the endogenous EFs decreased the rate of cell division as well as the directional nerve sprouting towards the wound edge [178].

Immune cell migration is a fundamental process in wound healing that could be compromised in chronic wounds. The effect of applied EFs on immune cell migration has been investigated by Li et al. In one of their studies on lymphocytes [179], they used microfluidic devices with integrated on-chip electrodes to demonstrate the cathodal migration of human blood T-cells when activated by antibodies. In another study, they showed the consistent electrotactic cathodal T-cell migration even in complex co-existing electrical and chemical guiding cues [180]. Electrotaxis can therefore be used as a guiding tool to direct migration of immune cells and assist in the wound healing process.

Impaired re-epithelialization due to defective cell migration into the wound is a characteristic symptom of chronic wounds associated with diabetic and pressure ulcers, as well as degenerative diseases [181]. The application of electrical signals to promote cell migration in such cases could form a new therapeutic platform. The role of EFs in retinal injury and retinal degeneration has been the subject of many studies. Migration of human and immortalized retinal pigment epithelium cell lines has been thoroughly investigated by various groups. Gamboa et al. have studied the effect of different field strengths (50-600 mV/mm) on the migration of wounded RPE cell layers as well as single cells [182]. In their studies, RPE cells were shown to realign their long axes perpendicular to the EF as they migrated towards the

anode. While the same RPE reorientation behaviour was noticed by other groups, the direction of the reported RPE migration varied. For instance, Sulik et al. [183] and Han et al. [184] reported the cathodal migration of human RPE. Different cell types exhibit varying migration capabilities and the different electrotactic response between different cell lines and even between cells originating from the same tissue has been reported. Cells derived from the same tissue have been found to migrate in opposite direction or even fail to migrate directionally at all [185, 186]. These opposite responses indicate that the effects of EFs on cells are cell-type and species specific, and therefore cell electrotactic response needs to be established experimentally on an individual basis.

ii. EFs and Stem cell research

Stem cells have a great potential in the treatment of several degenerative diseases [187]. However, directing and homing of transplanted stem cells towards the targeted organ is key to a successful therapy [161]. Using externally applied EFs to guide the migration of stem cells could be a solution to such a problem; especially after the reports on successful trials in directing stem cell migration [161].

Due to their huge promise in neuroregenerative studies and the repair of the central nervous system, a lot of research has been dedicated towards guiding the migration of neural stem and progenitor cells [188, 189]. Neural stem cells (NSCs) as well as neural progenitor cells (NPCs) have both been shown to possess a galvanotactic behaviour in the presence of a DC EF [146]. Feng et al. [190] have shown that even a small DC EF as low as 16 mV/mm induced a significant directional migration of human NSCs towards the cathode. They also demonstrated that this electrotactic response was time and voltage dependent, and that reversing the polarity of the applied EF reversed the direction of migration. Other studies have also reported the

cathodal migration of NPCs in externally applied DC EFs [188, 191]. The electrotactic behaviour of other stem cell types has also been reported [161].

2.4.2.4. Electrical stimulation therapeutic potential

Electrical stimulation has shown promising results in *in vivo* treatment of various diseases including cancer [192-195], chronic wounds [196] and spinal cord injuries [167, 168, 197].

In 2002, electrical stimulation was approved in the United States, for the treatment of chronic wounds and ulcers that do not respond to standard wound healing strategies [196]. Direct currents [198-200], high- or low-voltage pulsed currents [201], alternative currents [202], and low-intensity currents (less than 1mA) [196], have all been used in the treatment of diabetic, pressure and other chronic ulcers [203]. Reversal of polarity of the applied current has also been studied [198, 201]. Varying successes have been reported and more trials are still needed to arrive at accepted protocols for applying electrical stimulation for wound healing.

In this work, preliminary results show that electrical stimulation can direct the migration of RPE cells as well as control their alignment. The potential of using electrical stimulation to enhance cell recovery in AMD is discussed.

II. Impedance Spectroscopy of Adherent cells

2.5. Dielectric properties of biological tissues

The dielectric properties of cells and biological tissues are mainly attributed to interfacial polarization [204, 205]. This form of polarization, often referred to as the Maxwell-Wagner effect, occurs due to the accumulation of charges between interfaces with different dielectric properties as shown in Figure 2.6 [206, 207]. Cell membranes play a major role in interfacial polarization due to their extremely low conductivity that is considerably less than that of the

cytoplasm and the external medium [204, 207].

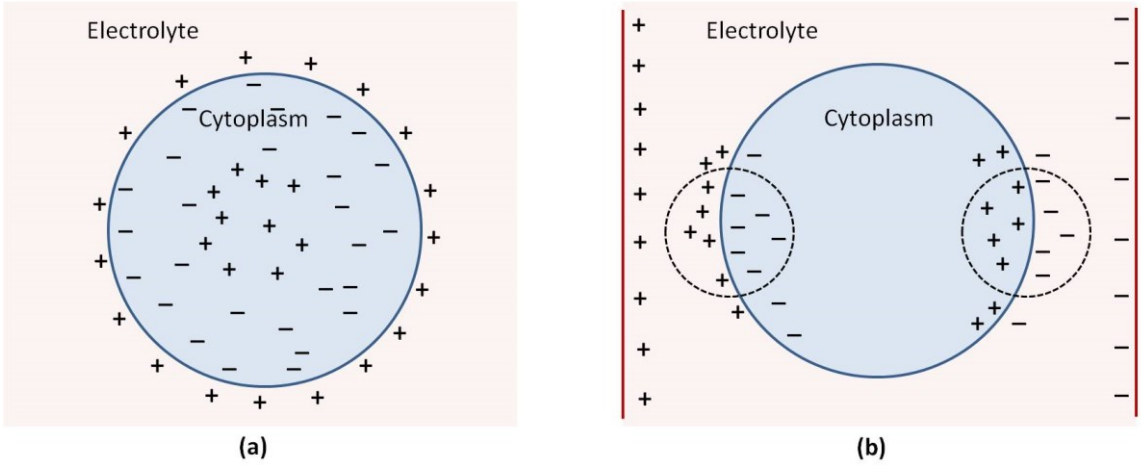

Figure 2.6: Maxwell Wagner effect. (a) A model of a cell (light blue) immersed in an electrolyte (pink). Charges in the conductive cytoplasm are separated from those in the extracellular medium (electrolyte) by the non-conducting membrane. (b) Applying an external electric field (red plates) causes the re-distribution of charges and results in dipole formation (dotted circles). Figure modified from [207].

Cell models are used to analyze the cellular dielectric properties of cells in suspension. These models consider cells as spherical and ellipsoidal shells represented by analytical equations that relate the electric parameters of the cell components to the dielectric spectrum [204, 208, 209]. However, due to the complex cellular structures, numerical simulation techniques, such as Finite Difference Modelling (FDM) and Finite Element Analysis (FEA), are required to better characterize cell-cell tight junctions and other complex structures [210-212].

The dielectric properties of cells and biological tissues are frequency dependent. The conductivity of cellular structures increases with frequency leading to less charge accumulation. This change in cellular permittivity and conductivity takes place through a serious of steps known as frequency dispersions [206, 207, 213]. Three main dispersion regions were described by Schwan in 1957: the α-, β- and γ-dispersions [205]. At low frequencies (centred at about 100 Hz), the α-dispersion region occurs due to ionic diffusion and is normally correlated with the tangential flow of ions across charged cell surfaces. The β-dispersion (10

kHz-10 MHz) takes place due to the change in interfacial polarization of the cellular plasma membranes. The γ-dispersion, first described by Foster and Schwan in 1989 [214], is centred at 10 GHz and depends on the aqueous content of the biological species and the presence of small molecules. An additional sub-dispersion δ, lying between the β and γ regions, was first described by Pethig in 1984 and is attributed to the dipolar moments of large molecules such as proteins [215]. Impedance spectroscopy of biological tissues is usually confined to the α and β regions. The different dispersion regions are illustrated in Figure 2.7.

2.6. Electrical Impedance Spectroscopy

2.6.1. Theory

Electrical Impedance Spectroscopy (EIS) is an electrochemical technique originally used for corrosion studies and coating evaluations, however, it has been recently widely used in biotechnology, cell culture monitoring and disease modelling [56, 216]. Impedance spectroscopy is based on applying an AC excitation signal and measuring the complex impedance, *Z,* of a system [217]. The measurements are scanned through a range of frequencies to define the impedance spectrum, hence the term spectroscopy [218]. The excitation current or voltage signal is normally very small allowing for a non-invasive measurement, which is the main reason behind the wide use of impedance spectroscopy in biological applications [219-221].

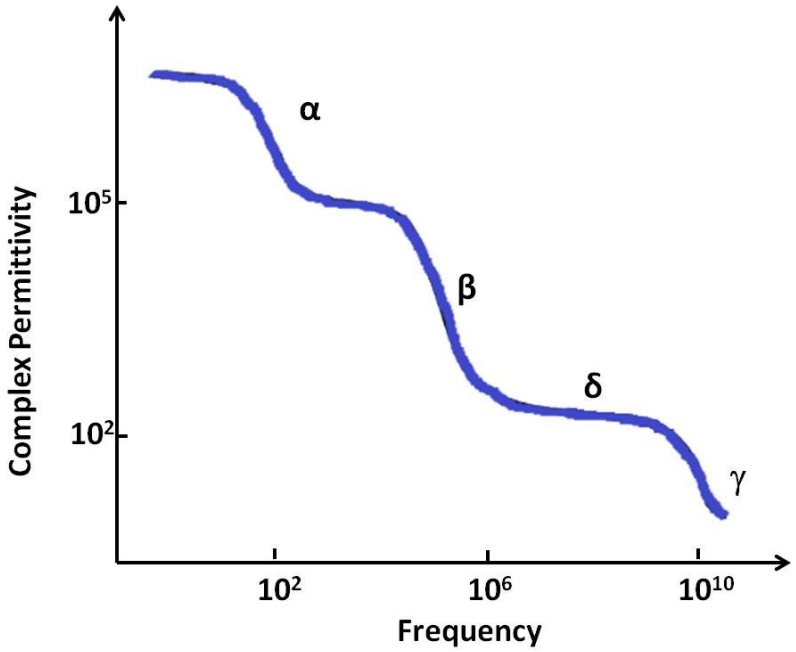

Figure 2.7: Dispersion regions. The change in cellular permittivity with frequency through different regions known as the α-, β-, δ- and γ- dispersions. Figure modified from [206]

The measured complex impedance represents the ratio between voltage and current according to Equation (2.1):

$$Z = \frac{V(t)}{I(t)} = \frac{V_o \sin(\omega t)}{I_o \sin(\omega t - \phi)} \quad (\Omega) \tag{2.1}$$

Where; *V(t)* is the voltage as a function of time, *I(t)* is the current as a function of time, ω is the angular frequency ($\omega = 2\pi f$) and ϕ is the phase shift between the voltage and the current [218]. The voltage and current are only in phase if the system is purely resistive. However, for cellular assays this is usually not the case as the cell capacitive properties will cause a phase shift between the applied voltage and measured current. Since cellular dielectric properties are frequency dependent, a spectrum of impedances measured at different frequencies would provide more information on cell properties than single frequency measurements [218].

There are various ways of plotting the complex impedance *Z*, the simplest of which is shown in Figure 2.8. In such a plot, *Z* can be plotted as a vector in a complex plane where the length

of the impedance vector indicates the magnitude $|Z|$ and the angle between the vector and the x-axis is the phase shift ϕ.

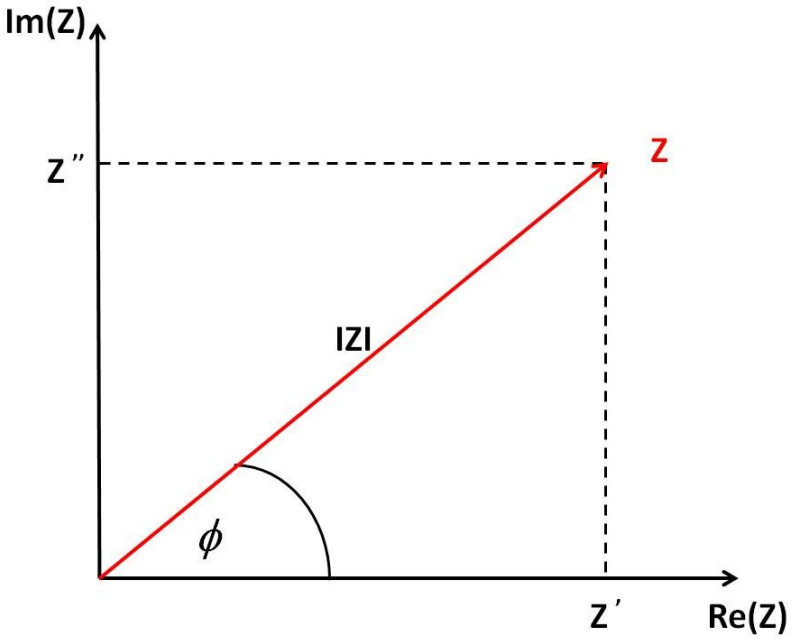

Figure 2.8: Complex impedance plot. A plot defining the complex impedance by its magnitude $|Z|$ (red vector) and the phase shift ϕ (angle between the x-axis and the impedance vector). Z' represents the real part of the impedance (resistance) while Z'' represents the imaginary part (capacitance). Figure modified from [218].

Nyquist plots are also a very common representation of the complex impedance [218, 222-224]. In Nyquist representations, the impedance real component is plotted on the x-axis against the imaginary component on the y-axis. However, the measurement frequencies cannot be extracted from such plots, a drawback that is overcome by Bode plots. In Bode plots, the impedance magnitude or its phase is plotted on the y-axis against frequency on the x-axis in logarithmic scale [218, 222, 223]. For more detail on Nyquist and Bode plots of simple RC circuits, see Appendix C [218, 224]. For further analysis, equivalent circuits and data fitting are used to model the impedance allowing for a deeper insight into different cellular properties and kinetics [218, 223]. Basic equivalent circuits and impedance elements are discussed in the following section.

2.6.1.1. Impedance elements and Equivalent circuits

When a metal is in contact with an electrolyte, a potential arises due to the unequal distribution of charges at the electrode-electrolyte interface. A double layer of charges is formed at the interface with one layer at the electrode surface and the other layer, with opposite polarity, just inside the electrolyte. This double layer behaves as a capacitor and is known as the double-layer capacitance (C_{dl}) as suggested by Helmholtz [225]. The Helmholtz planes at the electrode-electrolyte interface are shown in Figure 2.9. In situations where an electrochemical reaction takes place, some charges will leak through the double layer into the electrolyte. The transfer of these charges experiences a charge transfer resistance R_{ct} representing the speed of the charge transfer reaction. An ionic diffusion process also takes place where ions diffuse from the bulk of the electrolyte to the interface and a diffusion impedance, known as the Warburg impedance, Z_w , arises. For infinite diffusion, the Warburg impedance appears on a Nyquist plot as a diagonal line with a slope of 45°. However, when the diffusion is limited, the finite Z_w appears as a semi-circle at very low frequencies [218, 225].

C_{dl} often shows a non-ideal behaviour which may occur due to various reasons including surface roughness, slow adsorption reactions or non-uniform current distribution [225]. This non-ideal capacitor is normally referred to as a constant phase element (CPE) and its impedance can be expressed as:

$$Z_{CPE} = 1/((j\omega)^n C) \tag{2.2}$$

Where; Z_{CPE} is the impedance of the constant phase element, $j^2 = -1$, ω is the angular frequency and n is a constant that defines the behaviour of the CPE. When n=1, a purely capacitive behaviour is observed. With decreasing n-values, resistive behaviours start to appear with a pure resistive behaviour occurring at n=0 [218, 225, 226].

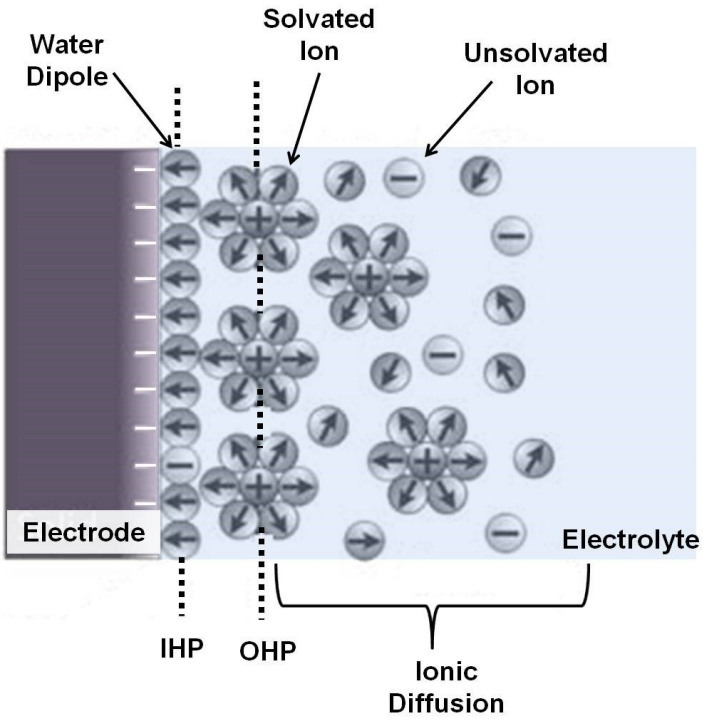

Figure 2.9: Electrode/electrolyte interface. A schematic diagram showing the ionic charge distribution and diffusion at an electrode/electrolyte interface. A double layer capacitor is formed between the inner Helmholtz layer (IHP) at the electrode site and the outer Helmholtz layer (OHP) inside the electrolyte. Ionic diffusion and charge transfer occur from the bulk electrolyte to the electrode and vice-versa. The figure is modified from [221].

The simplest equivalent circuit used to model the impedance of the electrode-electrolyte interface was developed by Randles in 1947 [227] and is shown in Figure 2.10. The main components of this circuit are the double layer capacitance C_{dl} and the charge transfer resistance R_{ct} connected in parallel. At low frequencies where the effect of diffusion is more pronounced, the Warburg impedance Z_w is introduced in series to R_{ct}. Moreover, the solution resistance R_s is connected in series to this parallel circuit and dominates the overall impedance at very high frequencies. R_s can be determined on the Nyquist plot at the intercept of the semicircle on the Z_{Re}-axis [218, 224]. R_s depends on the solution resistivity as well as the area of the solution chamber (Equation (2.3)). It is also affected by the ionic concentration, type of ions and temperature.

$$R_s = \rho \frac{l}{A} \tag{2.3}$$

Where, R_s is the solution resistance, ρ is the resistivity of the solution in a chamber with area A and length l [228].

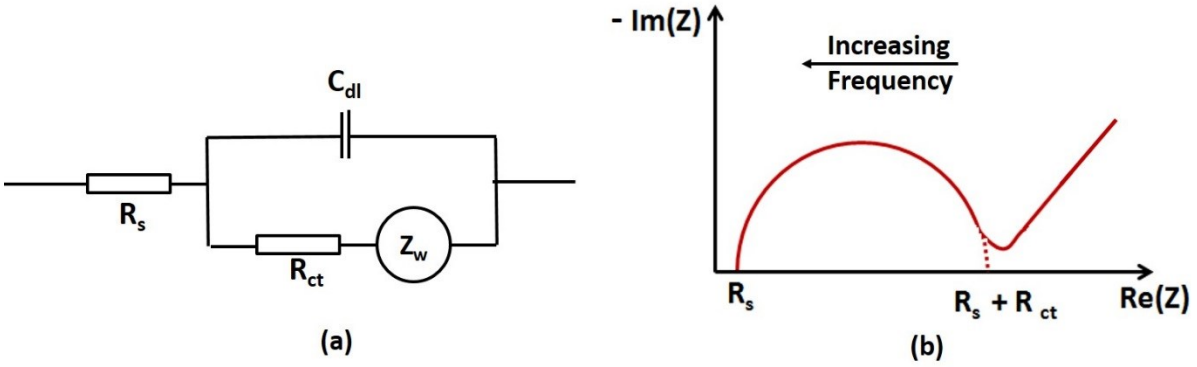

Figure 2.10: Randles equivalent circuit. (a) Randles model of the electrode-electrolyte interfacial impedance. The double layer capacitance (C_{dl}) is connected in parallel with the faradaic process elements (charge transfer resistance (R_{ct}) and the Warburg impedance (Z_w)). The solution resistance R_s is connected in series with the parallel circuit. (b) Nyquist plot of Randles circuit. The 45° line represents Z_w. Figure modified from [218, 225].

In this work, the small amplitude of the AC current (1μA) and the range of frequencies used for impedance spectroscopy (4 kHz- 64 kHz), should prevent redox reactions from taking place. The effects of charge transfer and diffusion can therefore be neglected and the interfacial impedance can then be simplified to C_{dl} (or the non-ideal CPE) in series with R_s. When biological cells are immobilized on top of the electrodes, they impede the current flow due to their previously mentioned insulating properties. In such cases, the cell impedance (Z_{cell}), is added in series to the equivalent circuit (Figure 2.11).

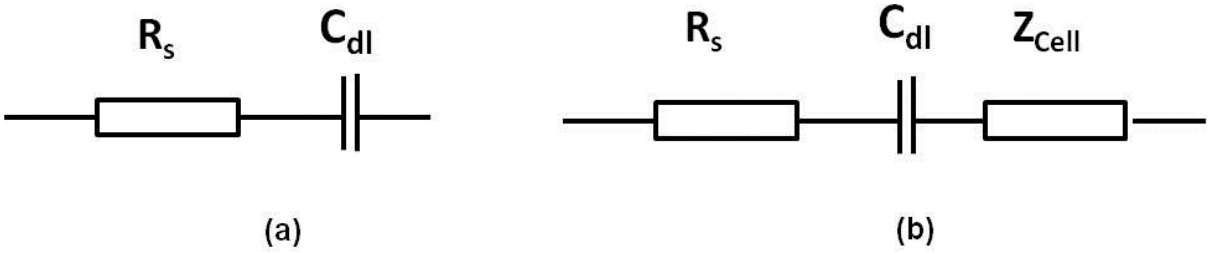

Figure 2.11: Simplified equivalent circuit for cell-based impedance spectroscopy. (a) Simplified Randles circuit neglecting the effect of charge transfer and ionic diffusion. The circuit is simplified into the solution resistance (R_s) connected in series with the double layer capacitance (C_{dl}). (b) The effect of immobilizing biological cells on top of the metal electrode. An impedance due to the cultured cells (Z_{cell}) appears and is connected to the previous circuit in series.

2.7. Impedance-based cellular assays

Giaever and Keese [229] were the first to employ impedance spectroscopy for cellular studies. Their system was commercialized in 1991 under the name Electric Cell-substrate Impedance Sensing (ECIS), which is described in more detail in the next section. Their initial design was different than the current commercial electrode arrays though. In their first experiments, mammalian fibroblasts were cultured onto four small working microelectrodes (3x 10^{-4} cm^2) and one large counter electrode (2 cm^2). The electrodes were fabricated by evaporating gold onto a petri-dish while using red wax for insulation. A single frequency of 4 kHz was used and a lock-in amplifier was used for the impedance measurements. Using their system, they were able to monitor cell attachment and spreading. Further fluctuations in the impedance measurements attributed to cell micromotion were also monitored.

After this pioneering work, impedance spectroscopy has been extensively used for various biological assays including cell proliferation [12, 230-232], cytotoxiciy [66, 69, 233, 234], wound healing [84, 93, 235], cell signalling [236, 237], cell invasion [238] and blood-brain barrier permeability studies [239]. Different electrode designs have been used from single to

several electrodes/well, either individually or collectively addressed. Radial electrode arrangements, widely used for impedance tomography, have been adopted for some impedance sensing studies. In a study by Rahman et al., 8 gold working electrodes arranged in a radial pattern were used to study the anchorage-dependent cell behaviour of ovarian cancer cells (Ovca429) [230] as well as the electrical properties of Human Vein Endothelial cells (HUVECs) [240]. In 2008, Wang et al. [241] developed an on-chip migration assay, combining self-assembled monolayers (SAMs) with cellular impedance sensing. SAMs inhibited cell attachment and were therefore used to create an area devoid of cells, representing a wound in the cell layer. After the desorption of SAMS from the electrodes by applying an electrical DC signal, cells were able to migrate with the circular arrangement of the electrodes producing a spatial average measurement of cell migration.

After their introduction for cell-based impedance studies in 1997 by Ehret et al., interdigitated electrodes were adopted for various cellular assays [242]. The relatively large area covered by the interdigitated electrodes means that the collective behaviour of a large number of cells is recorded as opposed to that of a few cells in the case of smaller sensing electrodes. For that reason, interdigitated electrodes are usually used for cytotoxicity assays and studies where the behaviour of a cell population is under investigation.

Recently, contactless measurement has been used for cellular impedance studies [243, 244]. In such set ups, the electrodes are covered with a passivating material and are therefore not in direct contact with the cells or the culture medium, resulting in the disappearance of the reactions at the electrode-electrolyte interface. However, in order to capacitively couple through the passivation, high frequencies have to be used and any interesting effects occurring at lower frequencies cannot be monitored [245, 246].

2.7.1. Electric Cell-Substrate Impedance Sensing

Electric Cell-substrate Impedance Sensing (ECIS) is a real-time, label-free monitoring technology pioneered by Giaever and Keese [13, 229] in which a small non-invasive AC current (1 μA) is applied through gold microelectrodes. ECIS uses a two-electrode set-up onto which adherent cells are directly grown on top of the planar microelectrodes. A 1V AC signal is applied through a 1MΩ resistor and the changes in the time-course complex impedance associated with cellular events are monitored through in-phase and out-of-phase measurements using a lock-in-amplifier [13]. The measured in-phase and out-of-phase current is converted to the real ($Z'(f)$) and imaginary ($Z''(f)$) parts of the complex impedance representing the resistive and capacitive components respectively. The basic ECIS set up is shown in Figure 2.12.

In order for the measured impedance to be dominated by that of the working (sensing) electrode, the impedance of the working electrode has to be much higher than that of the counter electrode and the solution resistance [247]. In order for the working electrode to have a higher impedance than the counter electrode, the area of the working electrode (typically 0.05 mm^2 in standard ECIS arrays) is made significantly smaller than that of the counter electrode (18 mm^2). The impedance contribution of the large counter electrode to the total impedance in that case is below one percent and can therefore be neglected [239]. The difference between working and counter electrode sizes as well as the close proximity between adherent cells and the electrode surface provide the high sensitivity of ECIS measurements [13, 247].

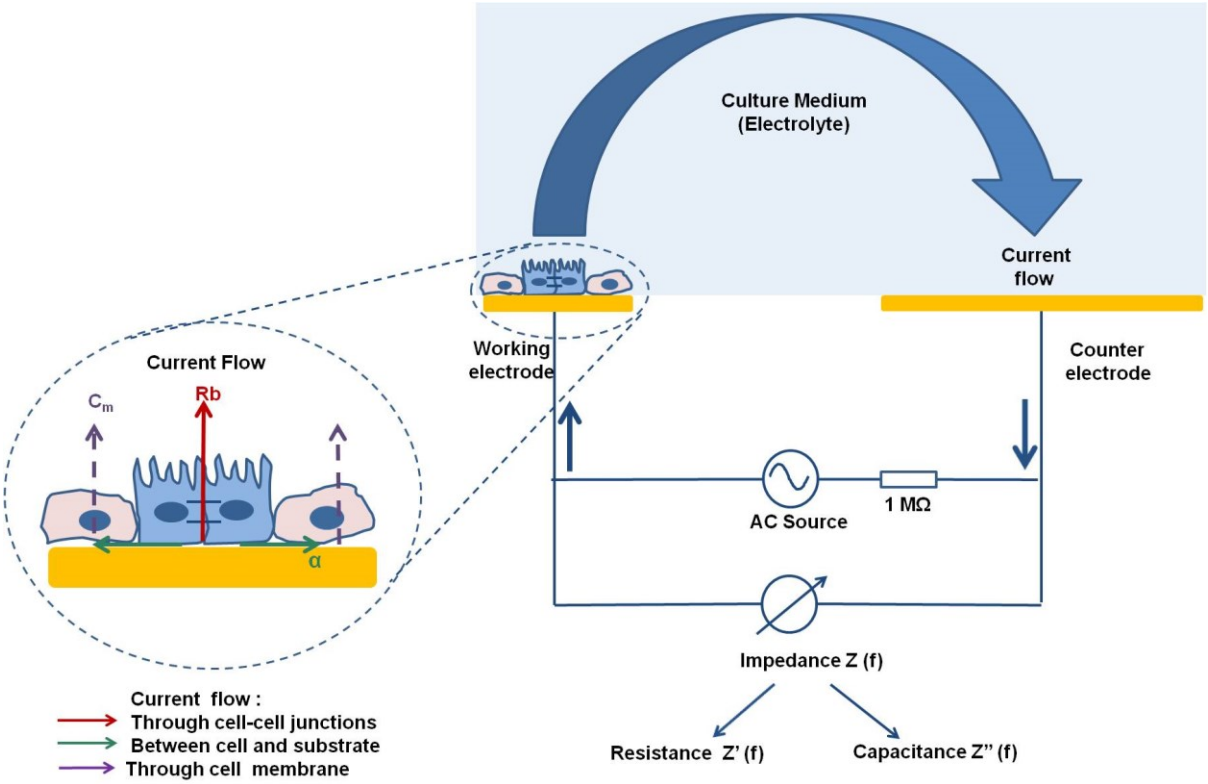

Figure 2.12: ECIS basics. A schematic diagram showing ECIS basic set up. ECIS mainly consists of a small (working) and a large (counter) electrode, an AC source and a lock-in amplifier. 1V AC signal is applied between the working and counter electrodes before the impedance is measured using a lock-in amplifier. The complex impedance *Z(f)* is analyzed into its two components: $Z'(f)$ (real part, i.e. resistance) and $Z''(f)$ (imaginary part, i.e. capacitance). The current pathways can be analyzed to reveal data on cell-cell junctions (R_b), cell-substrate adhesion (α) and cell membrane capacitance (C_m) using the ECIS built-in model.

When cells are cultured on top of the microelectrodes, they alter the current pathways due to the insulating properties of the cell plasma membranes. The measured impedance increases with cell growth until it reaches a plateau as the cells form a confluent monolayer on top of the electrodes. At low frequencies, the current is forced to flow under and in-between neighbouring cells and the measured impedance in this case is directly related to the properties of cell-substrate adhesion and cell-cell tight junctions. Only at high frequencies, the current can capacitively couple through the plasma membrane and the impedance can give an insight into the integrity and the dielectric properties of the cell membrane [12, 248].

ECIS has found many applications from cell attachment and spreading [12, 232], signal transduction [236], cytotoxicity [66, 233], electroporation [249] to metastasis [238] and more

recently regenerative medicine [124]. ECIS migration assays also allow the combination of electrical wounding and impedance spectroscopy to quantitatively and reproducibly measure cell migration rates and changes in cell morphology accompanying wound healing [84]. ECIS has also found a niche application in blood-brain barrier permeability studies [239], where the ECIS model has provided real-time quantitative monitoring of the establishment or loss of cell-cell tight junctions. It has to be noted that ECIS method of quantifying tight junctions is fundamentally different than the transepithelial electrical resistance (TER) measurement techniques. In these types of measurements, cells are usually cultured on permeable membranes between two chambers filled with the conductive medium. Electrodes are immersed in the two chambers and the measured impedance can then be used to assess cell-cell junctions and permeability. This set up is commonly known as the Ussing chamber [250-252]. ECIS however uses a built-in model to evaluate the resistance arising due to cell-cell tight junctions. The basics underlying this model are described in the next section.

2.7.1.1. ECIS Model

A major advantage of the ECIS platform over other commercial system is its built-in mathematical model that is able to deconvolve the impedance into its biologically relevant components. The impedance is scanned through various frequencies to recognize the different current pathways and translate it into data on cell-cell junctions (R_b), cell-electrode adhesion (α) as well as the cell membrane capacitance (C_m) [13]. At low frequencies (< 10 kHz), the current flows underneath and in-between the cells and therefore the measured impedance is an indication of how tight the cell-cell junctions are and how well-adhered the cells are to the electrodes. At high frequencies (> 40 kHz), the current can capacitively couple through the cells revealing data on the intracellular properties and the integrity of the cell plasma membrane [12, 13]. In this model, the overall impedance of a cell-free electrode can be represented by the

solution resistance in series with the impedance at the electrode-electrolyte interface (Z_e). For a cell-covered electrode, an impedance Z_{cell} is added in series to the previous cell-free equivalent circuit (Figure 2.13). Resistive contributions due to the membrane ion channels and ion leakage are usually neglected and are not taken into consideration in this model. It has to be mentioned that in order for ECIS model to be valid, the cell layer under investigation has to be confluent.

In order to arrive at a function describing the total impedance of the system, Giaever and Keese assumed cells as circular disks with radius r_c, hovering above the electrodes at a distance h in a medium with resistivity ρ [13]. The specific impedance (the impedance for a unit area) for the cell-free electrode was defined as $Z_e(f)$, representing the impedance at the electrode-electrolyte interface. The specific impedance for the cell was defined as $Z_m(f)$ and is mainly the capacitance of the upper and lower membranes in series, according to the equation:

$$Z_m = \frac{1}{j\omega C_{cl}} \tag{2.4}$$

where, C_{cl} is the capacitance of the apical and the basal cell membrane capacitances, and $C_m = 2C_{cl}$ (μF/ cm^2). In all their calculations, C_m was set as 1 μF/ cm^2.

It was assumed that the current flew radially in the space between the electrode and the hovering cells, and that the current density under the cells did not change in the z-direction. The electrode potential was defined as V_e while the electrolyte above the cell monolayer was assumed to have a constant potential of V_m.

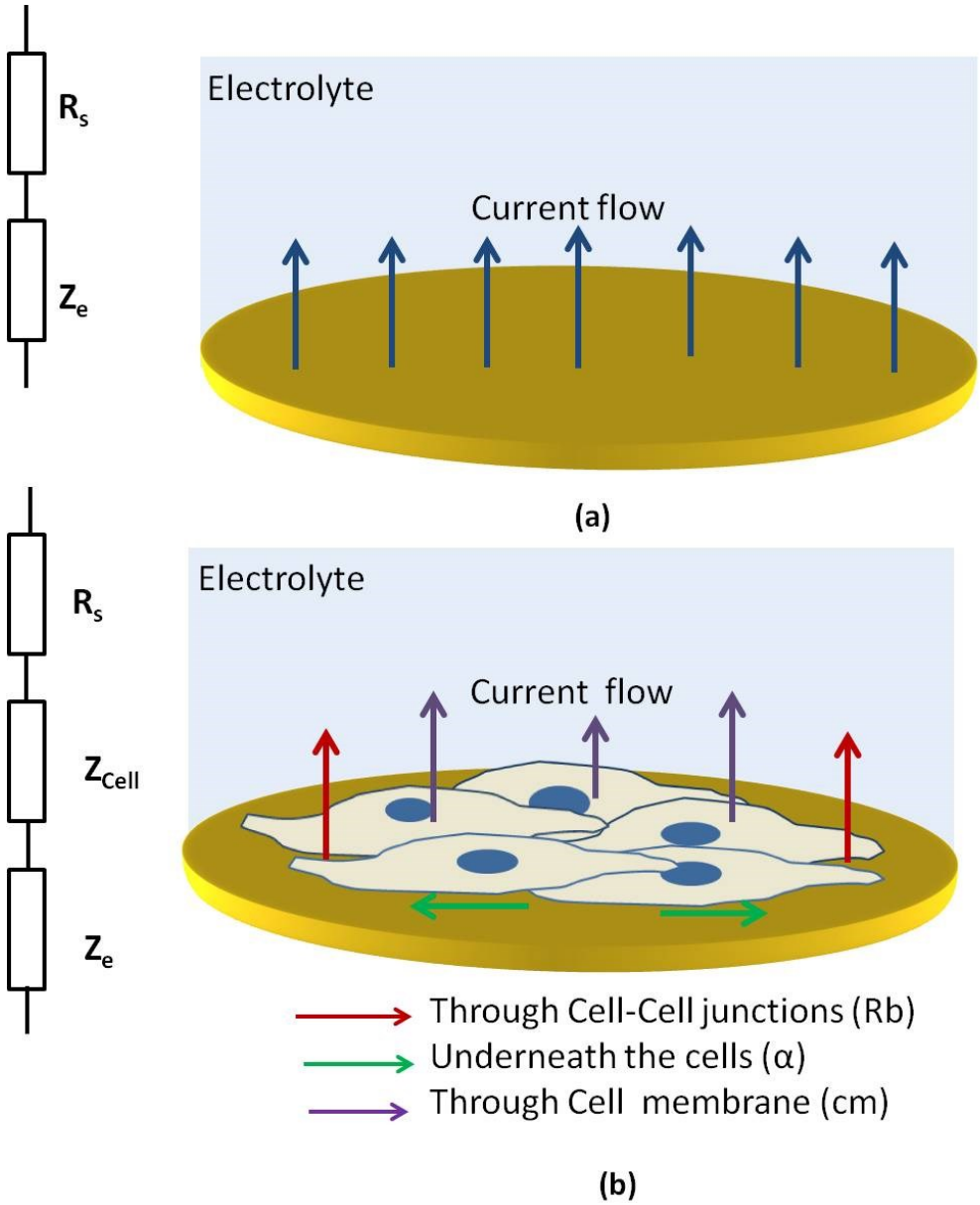

Figure 2.13: ECIS model. (a) A cell-free electrode with current flowing freely through the electrolyte (right). The equivalent circuit of a cell-free electrode is represented by the impedance at the electrode/electrolyte interface in series with the solution resistance (left). (b) Cells covering the electrode will impede current flow. Current can either pass in between (red arrows) or under the cells (green arrows). At high frequencies, current can capacitively couple through the cells (purple arrows). Current pathways are analyzed to deconvolve the impedance into the model parameters (R_b, α, C_m) (right). The equivalent circuit of a cell-covered electrode introduces an impedance Z_{cell} connected in series with the cell-free circuit (left).

By analyzing the different current pathways, Giaever and Keese derived four differential equations in order to arrive at a transfer function (Equation (2.5)) that described the overall impedance of the system [12, 253]. The derivation of this function is described in more detail in Appendix D [13, 254].

$$Z_{total} = \left[\frac{1}{Z_e} \left(\frac{Z_e}{Z_e + Z_m} + \frac{\frac{Z_m}{Z_e + Z_m}}{\frac{j\gamma r_c}{2} \frac{I_o(\gamma r_c)}{I_1(\gamma r_c)} + 2R_b \left(\frac{1}{Z_e} + \frac{1}{Z_m} \right)} \right) \right]^{-1} + R_s \qquad (2.5)$$

Where, I_0 and I_1 are modified Bessel functions of the first kind of the order zero and one. Z_e is the impedance at the electrode-electrolyte interface, and $\gamma^2 = \frac{\rho}{h}\left(\frac{1}{Z_e} + \frac{1}{Z_m}\right)$ with h representing the cell-electrode distance while ρ is the solution resistivity.

Once the total impedance has been determined, it can then be deconvolved into three biologically relevant parameters (R_b, α and C_m). The parameter R_b ($\Omega.cm^2$) is a measure of the resistance against current flow in the intercellular clefts and is thus a reflection of the tightness of cell-cell junctions. The parameter α is a measure of the impedance to current flow in the subcellular clefts which represents the level of cell-substrate adhesion. According to Equation (2.6), α depends on the cell radius r_c, the cell-electrode distance h and the electrolyte resistivity ρ, it has units of $\Omega^{0.5}$cm.

$$\alpha = r_c \sqrt{\frac{\rho}{h}} \qquad (2.6)$$

The cell membrane capacitance parameter C_m depends on the plasma membrane properties and morphology and can be determined from the membrane impedance Z_m. In practice, the parameters are retrieved through fitting the measured, experimental, impedance to the model transfer function using non-linear regression as described by Wegener et al [255].

It is worth mentioning that determining a frequency range of high sensitivity is key to accurate ECIS data interpretation. Figure 2.14 shows a typical impedance spectrum for the impedance magnitude $|Z|$ of a cell-free and a cell-covered electrode as a function of frequency. At low frequencies ($< 10^3$ Hz), the impedance is dominated by the electrode

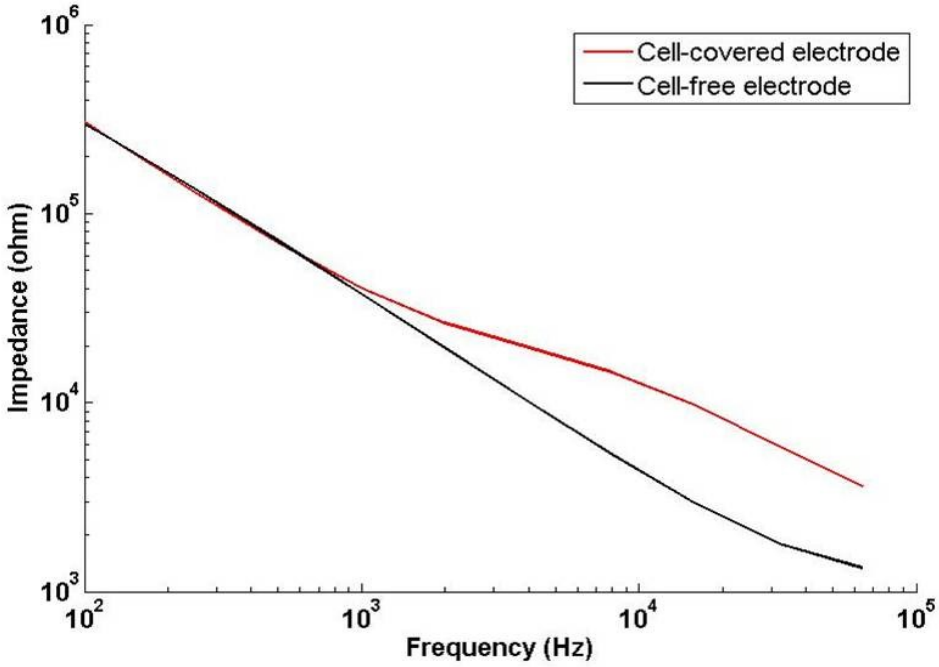

Figure 2.14: Impedance Spectrum. Graph showing the difference in impedance spectrum between a cell-free and a cell-covered electrode. As cells attach to the electrode, impedance increases in a characteristic way within a certain frequency range. This will be the range of frequency providing the highest measurement sensitivity.

capacitance as indicated by a linear decrease with increasing frequencies. At high frequencies ($> 10^5$ Hz), the impedance of the cell-free electrode approaches the value of the electrolyte resistance. A cell layer covering the electrode surface increases the electrode impedance in a characteristic way within a certain frequency range. Monitoring cellular behaviours should therefore be performed within this range of frequencies. Usually, 4 kHz is the frequency of choice for cell morphology, adhesion and tight junction studies, whereas 40 kHz is used for studying cell coverage and the membrane dielectric properties [12]. Recording ECIS measurements at a frequency of 4 kHz has been reported to accurately reflect changes in cell motility and morphology with high sensitivity. Even slight alterations in cell-cell junctions and cell-substrate adhesion have been detected at this frequency [248, 256]. At higher monitoring frequencies, intercellular and subcellular resistive components do not contribute to ECIS measurements as much as they do at 4 kHz. In the higher frequency range (typically $\geq$ 40 kHz),

however, capacitive contributions arising from the cell membranes are detected with high sensitivity as a big fraction of the current can couple through the membranes. Cell membrane capacitances of the cell layer add to the electrode capacitance in a reciprocal manner following Kirchhoff's laws, decreasing the electrode capacitance values with cell coverage [12, 253].

The sensitivity of a monitoring frequency can also be extracted from normalized presentations where the ratio of *Z, R* or *C* of a cell-covered electrode to that of a cell-free electrode ($Z_{cell\text{-}covered}$ / $Z_{cell\text{-}free}$, $R_{cell\text{-}covered}$ / $R_{cell\text{-}free}$, $C_{cell\text{-}covered}$ / $C_{cell\text{-}free}$), is plotted as a function of frequency. From these plots, the frequency range exhibiting a high sensitivity is normally the one providing a maximum normalized value [253].

2.7.2. Other commercial systems

Following the pioneering work of Giaever and Keese and the commercialization of ECIS, other commercial systems for impedance-based cellular assays have been developed. The xCelligence system (previously known as Real-Time Cell Electronic Sensing, RT-CES) by Roche Applied Science [257] has found many applications including cell adhesion and spreading [258], cell invasion [259], blood-brain barrier function [260], cytotoxicity [59], cardiology [261], cell signalling [262] and co-culture studies [263]. In this system, cells are cultured on top of gold interdigitated electrodes usually at the bottom of a 96-well plate and the cell behaviour is reflected by a cell index (CI). This index represents the relative change in impedance between the cell-free and cell-covered electrodes averaged over three measurement frequencies of 10, 25, and 50 kHz [264]. However, the CI has been reported to not always accurately reflect cell behaviour specially in cell toxicity assays where a decrease in CI was not always associated with cell death [265].

More specialized systems were also developed. The CellKey system by Molecular Devices (MDS), Inc. is a benchtop device that also uses interdigitated electrodes in 96- or 384- well

plates to measure changes in impedance. It mainly monitors cellular changes stimulated by ligand-receptor interaction, making it a good platform for drug screening assays [266, 267].

A slightly different device for cell-based assays is the Bionas Discovery. Besides impedance measurements, it uses sensors for acidity and oxygen concentration providing information on the metabolic activity, allowing for a more comprehensive insight into cellular properties and mechanisms [268, 269]. The impedance is however measured at a fixed frequency of 10 kHz.

2.8. Microelectrode Arrays: Design and Fabrication

In this work, different sized, individually addressed microelectrode arrays have been designed and fabricated for ECIS measurements. This section introduces some design considerations and the basic microfabrication techniques.

2.8.1. Design Considerations

Microelectrode arrays (MEA) are formed in essence from a conducting layer (usually metal) placed between two insulating layers, namely the substrate and the passivation layer. Small openings are then made in the passivation layer, exposing the metal in specific areas to define the measuring microelectrodes that will be in contact with the biological cells [221].The design, number, size and arrangement of these microelectrodes all depend on the application they are used for [270, 271].

Depending on the properties of the cells under investigation, an appropriate microelectrode size could be determined. For single cell studies for instance, the size of the sensing microelectrode should be in the range of 10-30 μm, the average size of a cell [221]. However, for studies where the collective behaviour of a cell population is of interest, larger electrodes can be used. In impedance-based assays, the microelectrode size directly affects the sensitivity of the measurements. In ECIS, in order to obtain highly sensitive measurements, the impedance of

the working electrode should dominate the overall impedance. Therefore, the impedance of the counter electrode has to be significantly smaller which is usually achieved by making its area much larger than that of the working electrode. A larger surface area can also be obtained through roughening of the counter electrode surface. Moreover, since the impedance of the electrode is connected in series with the solution resistance, decreasing the size of the working electrode, i.e. increasing its impedance, will allow the electrode resistance to dominate the solution resistance [13, 272]. Giaever and Keese have reported that decreasing the electrode area, increased the sensitivity of ECIS measurements [13, 248]. However, decreasing the electrode size will increase the interfacial double layer capacitance [228], therefore introducing some limitations on how small the microelectrodes can be made. In a study by Abdur Rahman et al., a 50 μm electrode diameter was set as a lower limit for microelectrode size, below which high interfacial capacitance and non-uniform current distribution occurred [273].

The sensitivity of the impedance measurements has been shown to decrease due to the capacitance introduced by the passivated electrode interconnections [274]. As the capacitance is inversely proportional to the thickness of the insulating layer, increasing the thickness of the passivation will reduce the capacitive coupling between the electrode interconnections and the solution. This parasitic passivation impedance can also be minimized by decreasing the electrode lead trace area. Price et al. observed that the passivated lead trace area to passivation coating thickness ratio has a critical value of 5.5, under which the impedance contribution of the coating is minimized. ECIS standard 8W1E (8 Wells, 1 Electrode/well) arrays have a passivated area of approximately 14 mm^2 with coating thickness of 2 μm. The passivation area to passivation thickness ratio is therefore much higher (~ 700) than the critical ratio defined by Price et al. This means that for ECIS arrays a coating capacitive component has to be considered at high frequencies.

The electrical performance of microelectrodes is obviously a primary criterion to be considered when designing a MEA chip. Other than the electrode impedance, the electric field distribution, the current density and the parasitic capacitance, issues like noise and electromagnetic interference should also be taken into account [221, 270]. Breckenridge et al. concluded that a minimum distance of 100 μm centre-centre distance should be left between any two electrodes to reduce interference and signal attenuation [275]. The distance between the electrodes should not be too large though if cell-cell communications studies are of interest. Depending on the specific design of the microelectrodes, other factors might have to be considered. For instance, when designing interdigitated microelectrodes, the number, width, height and spacing between the interdigitated fingers have been found to affect the sensitivity and signal to noise ratio of the measurements and therefore have to be optimized [271, 272, 276, 277]. Other considerations like power consumption/dissipation, heat dissipation, type of connections and circuitry used also have a huge effect on the proper functioning of the chip.

Microelectrode arrays can either be individually addressed or considered as an integrated array depending on how the microelectrodes are connected. Although integrated arrays offer an average response for a cell population which is useful for certain cellular assays, cytotoxicity assays for instance, individually addressable MEAs offer advantages such as high spatial resolution as well as the possibility of sensing from multiple sites. They therefore have a great potential in neural networks and cell signalling studies [221]. How the electrodes will be addressed should be considered before designing the MEA system.

In the current study, 6 and 16 microelectrodes/well are designed to allow for a high spatial resolution, monitoring a wider area of the culture well. Being individually-addressed allow for wounding the cell layer at one location while monitoring the response of the surrounding cells.

A miniaturization of the microelectrode size down to 20 μm is attempted to allow for single cell studies.

2.8.2. MEA Materials

As described in the previous section, microelectrode arrays basically constitute of three layers: the substrate, the conducting layer and the insulating passivation layer. Choosing the right material for each of these layers is essential to obtain the required electrode performance and sensitivity [221, 270, 271, 278].

Choosing an appropriate substrate material is the first step in the fabrication of microelectrode arrays. Typical substrates include silicon [274, 279, 280], glass [230, 240, 241, 273, 281-288] as well as polymers [289-291]. Silicon has always been the substrate of choice for the fabrication of semiconductors. Despite it not being transparent and having the disadvantage of introducing a parasitic capacitance when coated with silicon oxide, it is still used for MEA fabrication for biological applications as it allows for the integration of the measurement electronics [221].

Glass is increasingly used as a MEA substrate for cellular assays, due to its transparency, biocompatibility, high insulation and temperature resistance. Polymers are also transparent, highly biocompatible, and generally cheaper than glass, which makes polymer substrates a perfect candidate for disposable electrodes [221].

There are lots of properties that need to be considered before deciding on a suitable electrode material. Durability, biocompatibility, low impedance and of course low cost and availability are all desirable characteristics of the microelectrode material of choice [221, 270, 271, 292-294].

Despite their relatively high cost, gold (Au) [230, 240, 273, 276, 281, 285, 289, 295-302] and platinum (Pt) [286, 287, 303-306] remain the most commonly used electrode materials ever since the introduction of MEAs in the 1970s [307]. Their inertness, low resistivity and ease of fabrication have made them great candidates for different applications [292]. Moreover, the interfacial impedance of gold or platinum can be reduced by increasing the surface roughness, hence increasing the surface area. Platinum black has been used for plating gold and platinum microelectrodes resulting in a lower impedance [221, 270, 308]. However, this technique was shown to be unstable as the platinum black layer does not have a high durability [221]. After the introduction of a method for sputtering titanium nitride (TiN) on platinum [309], TiN has been used for gold and platinum plating providing a lower impedance than that of the naked electrode [310-312].

Electrode materials other than gold and platinum are also being used. First introduced as an electrode material by Gross et al [288, 313], indium-tin-oxide is increasingly used for the fabrication of MEAs due to its transparency, corrosion resistance and high biocompatibility. Other possible electrode materials include: glassy carbon [314], graphene [315], titanium [280], palladium [279], rhodium [316] and iridium [317].

The top layer of the microelectrode structure is the passivation layer. Generally, the main factor that should be considered when choosing the passivating material is the dielectric constant affecting the electrode capacitance. The dielectric strength is also a very important factor as exceeding it causes the insulation between the traces and the solution to break down. Another thing to consider is the thickness of the passivation layer, the thinner the insulation the lower its breakdown voltage [308]. Moreover, a thicker passivation layer will have a lower coating capacitance allowing for a more sensitive measurement.

The most commonly used passivation layers include silicon nitride [301], silicon dioxide [241], as well as polymer compounds including polyimide [287, 306] and photoresist [240, 273, 285, 286, 288]. Silicon nitride (Si_3N_4) is characterized by its high impermeability to ions and is a good choice for uniform insulative coating on a surface. Although silicon dioxide (SiO_2) has good insulating properties, it is not completely impermeable to ions and some ions might be able to pass through it to the electrode layer. Polymers are also used for passivation as they exhibit high biocompatibility and good dielectric features. However, a thick layer is normally required to obtain good insulation [221]. In this study, 1μm of Parylene-C has been used for passivation with either platinum or gold as the electrode material on a glass substrate.

2.8.3. Microelectrode Fabrication

2.8.3.1. Photolithography

Photolithography is the most commonly used process for the fabrication of MEAs [318]. Advances in photolithographic techniques have made it possible to fabricate miniaturized micro- and nano- electrodes as well as multilayered structures [319, 320]. The basic steps of the photolithographic process are shown in Figure 2.15. The first step is to grow an insulating layer (for silicon substrates) on top of the substrate usually by oxidation. An adhesion layer is then deposited by evaporation or sputtering on top of the substrate in order to increase adhesion between the substrate and the electrode materials. Typical adhesion materials include titanium (Ti), chromium (Cr) and tantalum (Ta) [270]. After depositing the metal layer, a layer of positive or negative photoresist is added before being patterned by exposing it to UV light through a photomask. This process makes the photoresist either more (in case of positive photoresist) or less (in case of negative photoresist) soluble to a developing solution. After developing the photoresist, the metal is then etched using wet or dry etching. In wet etching, chemical solutions are used to remove the unprotected material while dry etching uses a physical or a chemical etching process, or a combination of the two as in the case of reactive

ion etching. The photoresist is then stripped off to reveal the required final pattern. After removal of the photoresist, an insulating layer is deposited onto the wafer and the same patterning steps are followed to open up selected areas in the passivation to define the measuring electrodes [318, 320].

An alternative to the etching process is the lift-off method. In this process, a photoresist sacrificial layer is directly deposited on the substrate and patterned, yielding a negative pattern, before the metal layer is deposited on top. After developing, the photoresist together with the metal on top of it is removed, leaving only the metal layer that is directly adhered to the substrate. The main disadvantage of this process is that after removal of the photoresist layer, the metal on the side walls of the photoresist pattern could continue to adhere to the substrate. In the current study, only etching processes were used for microelectrode fabrication [321].

2.8.3.2. Screen-Printing

Screen-printing is a simpler, cheaper process than photolithography. In this technique, the desired electrodes are defined by printing a thixotropic fluid (a special ink with a time-dependent shear thinning property) through a high precision mesh screen or stencil with the required electrode patterns using a squeegee [322]. Ink materials include carbon nanotubes, platinum, silver, organo-gold, dielectrics, gold, carbon, and graphite [270]. The resolution of this technique is however limited and complicated designs are usually hard to print. Nonetheless, screen-printing is increasingly being used to fabricate disposable microelectrode arrays and has been reported as a microfabrication technique for electrochemical [323, 324] and biological applications [325, 326].

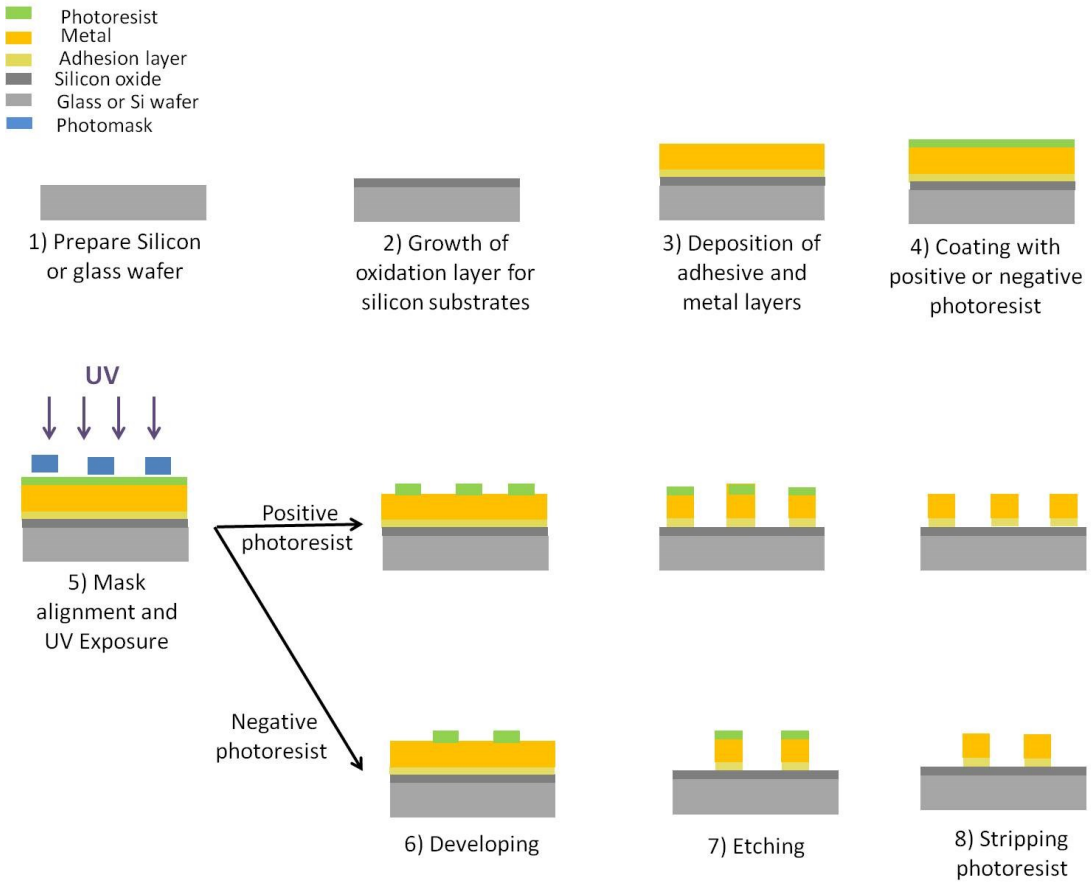

Figure 2.15: Photolithography. A schematic diagram showing the basic steps of the photolithographic etching process.

2.8.3.3. Laser Ablation

Laser ablation is another alternative platform for microelectrode fabrication, micromachining and the production of microelectronic devices. A laser beam is used to directly pattern the electrode material through irradiation, allowing rapid prototyping and low-cost manufacture of complex chips and devices. Special mask projection methods can also be used to produce more complex designs [327].

Rizvi et al. have used an excimer laser to fabricate microelectrodes for dielectrophoresis studies using laser ablation techniques [328]. In another study, they built a multi-level device by ablation of electrode patterns and layered insulators. Using a chrome-on-quartz mask, they were able to produce electrode structures with typical sizes of 10 μm [329]. Laser ablation has

also been combined with other techniques in order to achieve better fabrication capabilities. For example, Cugnet et al. [330] reported the fabrication of a microelectrode array based on femtosecond laser ablation and screen- printing processes. In a different study, Lee et al. have used an inkjet-based ultrashort pulsed laser patterning on a polymer substrate. They were able to achieve damage-free laser ablation through the optimization of the laser processing parameters including the input energy, scanning speed, and number of scans [331].

2.8.4. Surface Modifications

After the fabrication of the required MEA, usually a few surface modifications are done to guide and immobilize the cultured cells/tissues onto the electrodes or to improve the electrical performance of the chip [221, 294]. As mentioned previously in Section 2.8.2., coating the electrode with materials like platinum black or TiN can be used to increase the surface area and lower the electrode impedance [270, 308, 309]. Increasing the surface roughness and coating with specific proteins allow for an improved cell attachment to the electrode surface [221]. The hydrophilicity of the electrode surface is also an important element that needs consideration. As cells do not adhere to a hydrophobic surface, modifications that will increase the surface hydrophilicity are required if the MEAs are to be in direct contact with the biological cells [318]. In the current study, oxygen plasma has been used to make the surface of the MEA chip hydrophilic. All chips have been incubated with culture medium at least 2 hours prior to cell seeding, therefore coating the chip surface with serum proteins.

2.9. Summary

This chapter has described recent advances in disease modelling including the use of stem cells and employing impedance measurements for a real-time, non-invasive quantification of cellular behaviour and model validation. Mechanisms underlying acute liver failure and age-

related macular degeneration have been briefly described, and the therapeutic potential of antioxidants and electrical stimulation has been presented. The theory behind electrical impedance spectroscopy and the ECIS platform used in the current study has also been explained. Finally, microelectrode design considerations and fabrication methods have been discussed.

In this work, two stem cell-based disease models-on-a-chip are proposed for ALF and AMD. Hepatotoxicity assays are conducted to model ALF, while electrical wounding is used to mimic RPE loss in AMD before exploring two therapeutic approaches. The next chapter introduces the materials and methods used for the different studies performed in this work.

Chapter 3

Materials and Methods

3.1. HepaRG-based ECIS model for hepatotoxicity studies

3.1.1. HepaRG cell culture on ECIS microelectrodes

HepaRG cells (HRG116, BioPredic international, Rennes, France) were grown following the supplier's protocols and using specialized media obtained from Biopredic Int. Each medium was made up using William's E Medium with GlutaMAX™ (Sigma), as the basal medium; with appropriate additives (ADD). Briefly, HepaRG cells were seeded (day 0) at $2.5x10^5$ cells/cm^2, initially in Thaw, Seed and General Purpose HepaRG medium (GPS; ADD670) on ECIS microelectrode arrays (Applied Biophysics, USA), and the medium was changed daily. On day 3, the medium was changed to metabolic maintenance medium (MMM; ADD620) and HepaRGs were cultured, with the medium changed every other day, until they terminally differentiated into a co-culture of hepatocytes (the main functional cells of the liver) and cholangiocytes (the epithelial cells of the bile duct). On day 8, cells were washed twice with Hank's balanced salt solution (HBSS; Sigma-Aldrich) before adding Rifampicin (Sigma) in serum-free hepatocyte induction medium (HIM; ADD650) with a ratio of 1:1000 (Rifampicin: HIM). The liver enzyme-inducer, Rifampicin, was used to upregulate the detox CYP450 enzymes, specially CYP3A4, that are involved in drug metabolism and might be inhibited due to the presence of Dimethyl sulfoxide (DMSO) in the culture medium.

On day 9, HepaRGs were subjected to the different drugs and test compounds with different concentrations. Impedance was then monitored with measurements taken at 160s intervals over a 62.5 Hz to 64 kHz frequency (*f*) range, for up to 96 hours post-induction. The ECIS-Zθ built-in model was used to translate impedance measurements into quantitative data on cell-cell junctions (R_b), cell-electrode adhesion (α) as well as the cell membrane capacitance (C_m).

3.1.2. Hepatotoxins

All hepatotoxins and compounds were added to the HepaRG cultures on day 9 after an induction phase as previously described. The model hepatotoxin paracetamol (APAP; A7085, Sigma-Aldrich) was added to the culture medium, MMM, with concentrations of 5mM, 10mM and 20mM using DMSO-vehicle as controls (< 0.1% DMSO final concentration in all experiments). The effect on impedance measurements and modelling parameters was then observed. To test the effects of antioxidants on APAP-induced toxicity in HepaRGs, N-acetyl-L-cysteine (NAC; Sigma-Aldrich) was used. After 24h of incubation with APAP, medium was aspirated and 400 µl of MMM containing 10mM NAC was added to the HepaRG culture. Cells were incubated with NAC for 24h before the medium was aspirated again.

Phorbol-12-myristate-13-acetate (PMA; P8139, Sigma-Aldrich) is known to disrupt the integrity of hepatocellular TJs. Effects of various concentrations (50, 100, 200 ng/ml) of PMA on R_b (TJ barrier resistance) were tested using impedance monitoring for 24 hours on HepaRG cells.

Parallel biochemical, Presto-blue and ATP-depletion, endpoint cell viability assays were also conducted for APAP and PMA. Moreover, the disrupting effect of APAP on HepaRG tight junctions was confirmed using fluorescence immunostaining of tight junction proteins, as well as transmission electron microscopy (TEM) imaging. All HepaRG biochemical assays and

staining were performed by the HepLab group, University of Edinburgh. A brief description of the methods used in such assays is provided in Appendix E.

The effect of other hepatotoxins on HepaRGs was also investigated. Amiodarone (Sigma) was added to the HepaRG culture medium with concentrations of 25, 50, 75 and 100 μM, while Cyclosporine-A (CsA; Sigma) was added using 10, 20, 30 and 40 μM concentrations. To test the effect of NAPQI (*N*-acetyl-*p*-benzoquinone imine; Sigma) on HepaRG tight junctions, 125, 250 and 500 μM concentrations were added to different wells before monitoring real-time effect of the compound on impedance measurements. Table 3.1 summarizes the different compounds used for the HepaRG-based assays and their corresponding concentrations.

Test compound/ drug	**Concentrations**
Paracetamol (APAP)	5 mM, 10 mM, 20 mM
Phorbol-ester (PMA)	50 ng/ml, 100 ng/ml, 200 ng/ml
Amiodarone	25 μM, 50 μM, 75 μM, 100 μM
Cyclosporine-A (CsA)	10 μM, 20 μM, 30 μM, 40 μM
NAPQI	125 μM, 250 μM, 500 μM
NAC	10 mM

Table 3.1: Hepatotoxins and their corresponding doses.

3.1.3. ECIS arrays

Three different ECIS arrays were used for the HepaRG-based assays. All arrays were incubated with GPS medium for 2 hours before seeding with HepaRG. ECIS 8W10E^{+} arrays were mainly used for the APAP and PMA hepatotoxicity assays. This array has 8 wells, each having two sets of 20 circular 250 μm diameter measuring gold electrodes located on interdigitated fingers to provide measurements of cells upon a total of 40 electrodes. Each well has a substrate area

of 0.8 cm^2 and a maximum volume of 600 µL. Due to their interdigitated design, these arrays provide an average for the cell population response, making them a good candidate for toxicity studies.

Another array employing interdigitated fingers is the ECIS 96W20idf (96 wells, 20 interdigitated fingers/well). This array has 96 wells and therefore is ideal for high throughput screening. 96W20idf arrays were used to conduct amiodarone, cyclosporine-A, paracetamol and phorbol-ester hepatotoxicity assays in parallel. Each well has a substrate area of 0.32 cm^2. The electrodes have a 20 interdigitated finger configuration with a total electrode area of 3.92 mm^2.

The third array used in this study is the ECIS 8W1DD (8 wells, 1 electrode/well, different diameters). This array is nearly identical to the ECIS 8W1E (described in Section 3.2.1) standard array with each well having a substrate area of 0.8 cm^2 and one working electrode. The working electrodes come in four different diameters (25, 50, 100, 250 µm) with two wells of each size. The small sized electrodes were used in an attempt to differentiate between hepatocyte and cholangiocyte responses in a sub-population study. Figure 3.1 shows the different ECIS arrays used in the HepaRG-based studies.

3.1.4. Impedance data analysis

Impedance data were analyzed using Matlab. Generally, normalized data has been adopted to provide a more accurate way of comparing impedances of different culture wells. Data were normalized through dividing the impedance (or its corresponding modelling parameters) by its value at the challenge starting point (t=0). Moreover, non-normalized data has also been provided to show the true impedance values.

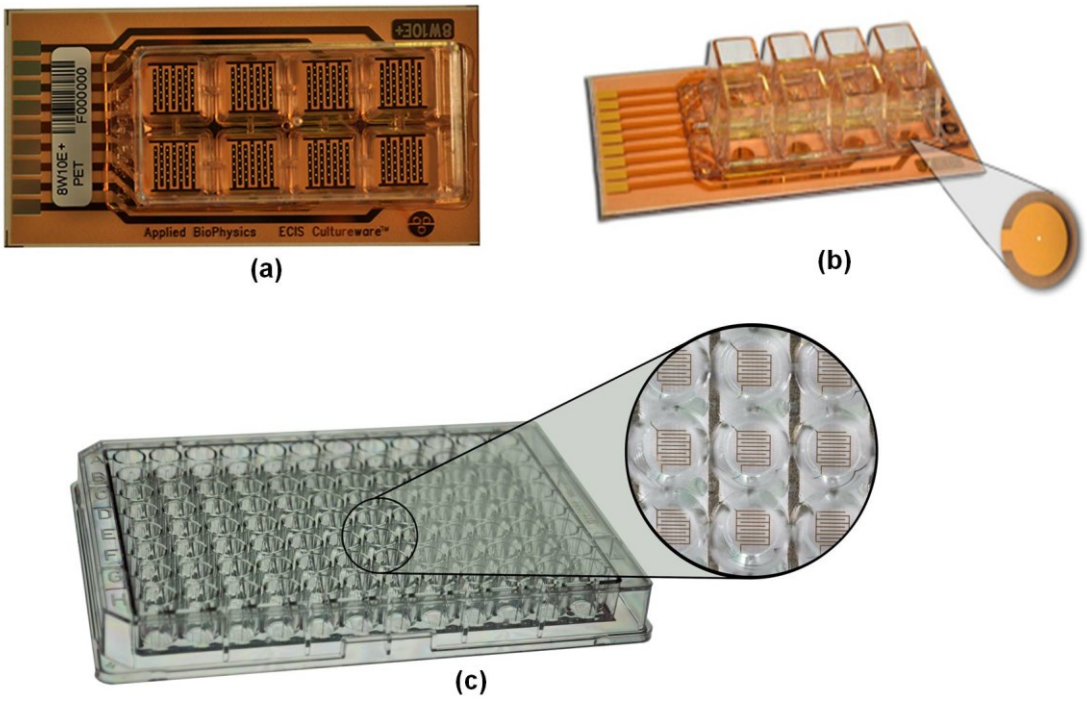

Figure 3.1: ECIS microelectrode arrays. (a) 8W10E^{+} (b) 8W1DD (c) 96W20idf [332]

3.2. Electrically-induced Injuries

3.2.1. Keratinocytes ECIS wound healing assays

Adult Human Epidermal Keratinocytes (HEKa, Invitrogen) were cultured with a density of 2500 cells/cm^2 in Epilife medium. ECIS 8W1E (8 Wells, 1 Electrode/well) arrays were used for the electrical wounding assays. These arrays have 8 wells with one 250 µm diameter sensing gold electrode/well. Each well has a 0.8 cm^2 surface area. Microelectrodes are fabricated on a transparent Lexan polycarbonate substrate onto which 50 nm thick gold electrodes are sputtered and passivated with 2 µm polymer resin. Sensing electrodes have a typical area of 0.05 mm^2 while the counter electrode has an area of 18 mm^2. Arrays were incubated with the culture medium for 2 hours in a humidified incubator with 5% CO_2, 37^{o}C, prior to cell seeding.

Trial and error experiments were initially conducted to optimize the wounding parameters. After three independent experiments, it was decided on using a current of 3 mA at 40 kHz for

30s to achieve controlled wounding of keratinocytes. A formula defining wound severity was proposed in Equation (5.1) in Section 5.1, depending on the wounding pulse amplitude, frequency and duration.

3.2.1.1. HEKa staining

After wounding, the culture medium was removed from all wells and the cells were washed with phosphate buffered saline (PBS). 100 µl of Acridine Orange/ Ethidium Bromide (AO/EB) vital staining solution was added at room temperature for 10 minutes before being removed and washed with PBS. The cells were then fixed in 10% formaline and ECIS culture wells were carefully removed from the substrate. One drop of DAPI (4′,6-diamidino-2-phenylindole) was added onto each electrode for nuclei DNA staining and a cover slip was put onto the electrodes before checking under a fluorescence microscope.

3.2.2. Age-related macular degeneration model-on-a-chip

3.2.2.1. hiPSC-RPE culture on ECIS microelectrode arrays

hiPSC-RPE cell lines were generated from a patient with LORMD and a healthy sibling as described in Appendix E and perfomed in Chandran's Lab. by Shyamanga Borooah. Case and control hiPSC-RPE were then cultured on ECIS Medusa arrays (Applied Biophysics, NY, USA) incorporating a 2-electrode set up: working and counter electrodes. Each array has 8 wells of 0.8 cm^2 surface area with two 250 µm diameter gold working microelectrodes per well. The electrodes have the same areas previously described for 8W1E arrays (0.05 mm^2 for the sensing electrode and an area of 18 mm^2 for the counter electrode). The spacing between the electrodes on a Medusa array is 4.83 mm. The two working electrodes are addressed individually and measurements from one working electrode are recorded at a time. The Medusa array is useful for duplicating readings in the same well or to wound/electroporate one electrode

while leaving the other as a control within the same well. When connected to the array holder only the upper four wells are measured. To use the other four wells, the array is turned around and the contact pads at the other end are connected. Figure 3.2 shows a typical Medusa array. The ECIS electrode array was placed in an array holder inside a humidified incubator at 37°C and 5% CO_2. All wells were incubated for 2 hours with the culture medium before seeding at confluency (100,000 cells/ cm^2). Cells were initially cultured with retinal differentiation medium with 10% fetal calf serum (90% RDM, 10% FCS). On day 2 of culture, the media was changed to RDM with 2% serum and on day 6, RDM with no serum was used until the end of the experiment. Media was changed 3 times per week. Cells were cultured for 25 days to achieve RPE maturation before starting the wound healing assay.

Figure 3.2: ECIS Medusa array. A picture of an ECIS Medusa array. Each well has two 250 µm diameter working electrodes. Only four wells can be connected at a time [332].

3.2.2.2. hiPSC-RPE ECIS wound healing assay

An elevated current pulse (3 mA, 40 kHz, 30 seconds), optimized by trial-and-error experiments, was used to wound the confluent cell monolayer. Trial and error experiments were minimized by using the formulas (5.2- 5.4) to derive theoretical wounding parameters that generated the same current density used for wounding keratinocytes. The wounding pulse was mirrored by a drop in impedance to that of the cell free electrode. The system then switched

back to its normal operation to monitor cell repair. The same wounding parameters were used with all cell lines.

Trypan blue was used to confirm cell death. 15 minutes after wounding, the medium was aspirated and 200 µl of diluted trypan blue was added to the well under investigation. After 15 minutes, trypan blue was removed and the wounded cells were optically observed. Only dead cells were stained blue as their plasma membranes were terminally compromised.

3.2.2.3. Quantitative data analysis

i. Average cell migration

The migration rate of the case and control cell lines after electrical wounding was determined according to Equation (3.1):

$$m = r/t \quad (\mu m/h) \tag{3.1}$$

Where; *m* is the migration rate, *r* is the electrode's radius (125 µm) and *t* is the time in hours required for the impedance to reach its value prior to wounding.

ii. Impedance based adhesion assay

Cells were seeded with a high density (typically 100,000 cells/cm^2) and the changes in their impedances were monitored for 1-2 days. The time it takes the cells to attach to the electrode surface and start spreading till they form a confluent layer is an indicator of the cell adhesion properties [12, 96]. Impedance measurements during the attachment phase were fitted with a straight line and the slope of the case and control curves were determined accordingly. Biochemical adhesion assays were also performed to confirm the obtained results. These were performed by Shyamanga Borooah and described in Appendix E.

iii. Cell-substrate adhesion parameter

The built-in ECIS model analyzes current pathways, arriving at a transfer function (Equation (2.5)) that defines the measured impedance. Experimental data can then be fitted to the model transfer function and the model parameters (R_b, α, C_m) can be extracted [255]. A schematic diagram of the ECIS model showing the different current pathways in between, under and through the cells is shown in Figure 2.13.

ECIS model was used to determine the cell-adhesion parameter (α). α depends on the cell radius (r), the medium resistivity (ρ) and the cell-substrate distance (h) according to Equation (2.6). ECIS model was used to investigate the differences in cell-substrate adhesion between the cell lines under investigation, and the corresponding effects on their migration rates.

iv. Healing Kinetics

ECIS data was exported to Matlab for further analysis. To better understand the healing kinetics, the healing impedance graphs were fitted to a sigmoid curve (also referred to as a sigmoidal dose-response) in which the hill slope and inflection points were calculated using Equation (3.2), therefore providing additional data on the differences between case and control migration. Please note that this sigmoidal equation has also been used to investigate the kinetics underlying APAP hepatotoxicity for the HepaRG-based model.

$$y = a + \frac{b - a}{1 + 10^{(c-x)d}} \tag{3.2}$$

Where; a is the y value at the sigmoid bottom plateau, b is the y value at the sigmoid top plateau, c is the inflection point, which is the x value when the response is half way between a and b, and d is the hill slope (slope factor or hill coefficient) which describes the steepness of the

curve. If it is positive, the curve increases as *x* increases. If it is negative, the curve decreases as *x* increases. The hill slope has no units.

v. Moving Variance

Matlab was used to analyze the increase in monitored impedance fluctuations accompanying cell transition using the moving variance method. First the signal was normalized and detrended using the Matlab 'detrend' function. Removing a trend that could have occurred due to a systematic increase or decrease in the data, reduces the overall variation and helps focus the analysis on the fluctuations under investigation. A sliding window was then used, within which the variance was calculated, to determine the amplitude of the impedance fluctuations. The variance was calculated over a total of 512 points (22.75h) within a 150 point window using a 1 point sliding step, and was plotted against time.

3.2.2.4. Immortalized-RPE wounding

Telomerase- immortalized retinal pigment epithelium (hTERT-RPE1) (ATCC CRL-4000^{TM}) were cultured in ATCC-formulated DMEM:F12 with 10% fetal bovine serum (FBS) and 0.01 mg/ml hygromycin B. Cells were seeded with a density of 40,000 cells/cm^2 and cultured for two days before starting the migration assay. Culturing medium was changed 3 times per week.

Two ECIS modes were used for hTERT-RPE1 migration studies: electrical wounding and electric fence. 8W1E was used for wounding while medusa arrays, with 2 sensing electrodes, were used for electric fencing. All arrays were incubated with complete culture medium for 2 hours before cell seeding with a density of 40,000 cells/ cm^2. A current of 1 mA at 40 kHz was applied for 30s to achieve complete cell death monitored by the drop in impedance to that of the cell-free electrode, and complete cell detachment.

For the electric fence technique, the fence was turned on instantly after adding the cell suspension. The fence excitation was applied to one of the two electrodes in the Medusa array well while the other electrode was left as a control. The ECIS default fence parameters were used (1 mA, 40 kHz, 3 pulses, pulse on for 1000 ms, pulse off for 10msec, 1 cycle, capacitance target: 4nF). The migration rate was calculated according to Equation (3.1) for both wounding and fencing.

Wounding on different-sized electrodes was also investigated using an ECIS 8W1DD array. The formulas (5.2-5.4) were again used to derive theoretical wounding parameters that generated the same current density generated with previous wounding studies.

3.2.2.5. Effect of antioxidants on RPE migration

To test the effect of the antioxidant N-acetyl-L-cysteine (NAC) on wound healing and migration of the hiPSC-derived RPE cells, 10 mM NAC was added to the culture medium either for 2h or 24h before electrical wounding. The effect of NAC on the impedance measurements was then monitored for 24h.

Furthermore, 100 μM hydrogen peroxide (H_2O_2) prepared in retinal differentiation medium with no antioxidants (RDM – Antioxidants) was added to some wells with and without the presence of NAC to investigate the effect of oxidative stress and antioxidants on RPE migration.

3.2.3. Electrically-induced Liver injuries

Human hepatocellular carcinoma HepG2/C3A cells were obtained from the American Type Culture Collection CRL-10741, USA and cultured in Minimum Essential Medium Eagle (MEME Sigma). Cells were cultured on ECIS 8W1E arrays with a density of 11,000 cells/cm^2. Trial and error experiments, based on the previously derived formulas, were used to define a

suitable wounding threshold. Parameters of 3 mA, 40 kHz, 20s were used to achieve complete cell death.

3.3. ECIS Impedance measurements

All impedance measurements in this work were conducted using the commercial Electric Cell-Substrate Impedance Sensing instrument (ECIS ZΘ, Applied Biophysics). Multiple frequency impedance measurements (f = 62.5, 125, 250, 500, 1000, 2000, 4000, 8000, 16000, 32000 and 64000 Hz) were recorded every 160 seconds. The measured complex impedance had a resistive and capacitive component which was determined through in-phase and out-of-phase measurements using a lock-in amplifier. The sensitivity of a monitoring frequency recorded in the impedance, resistance or capacitance measurements can be easily extracted from normalized presentations by plotting the ratio of the respective quantity for a cell-covered electrode to a cell-free electrode as a function of frequency ($Z_{cell\text{-}covered}$ / $Z_{cell\text{-}free}$, $R_{cell\text{-}covered}$ / $R_{cell\text{-}free}$, $C_{cell\text{-}covered}$ / $C_{cell\text{-}free}$). The frequency range of choice should be the one that shows a maximum normalized value. According to Figure 3.3, a frequency close to 4 kHz provided the highest sensitivity in recording resistance measurements, while a high frequency greater than 40 kHz would be appropriate to monitor capacitance measurements. In this work, resistance data is presented at 4 kHz to reflect the establishment of cell-cell junctions and the capacitance at 64 kHz, which translates linearly to cell coverage.

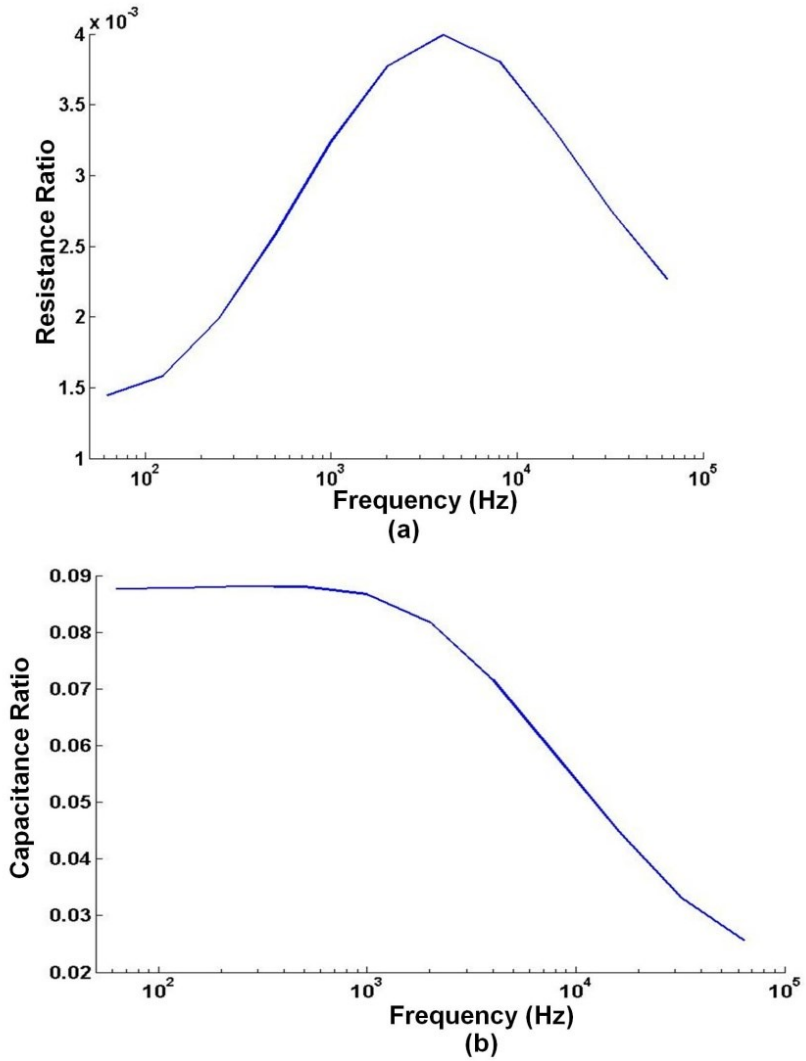

Figure 3.3: Choosing a sensitive frequency range. (a) The ratio between the cell-covered to cell-free resistances. The frequency at which the resistance ratio is maximized is expected to provide the highest sensitivity. (b) The ratio between the cell-covered to cell-free capacitances. The frequency where the capacitance is at its lowest is the most sensitive.

3.4. Statistical Analysis

All data are represented as mean ± standard error. Matlab was used to perform one-way Anova and Tukey-Kramer multicomparison tests to determine whether the groups under investigation were significantly different from each other. Probability levels of $P<0.05$ and $P<0.01$ were used to determine data significance.

3.5. High-density, individually-addressed microelectrodes for ECIS measurements

3.5.1. Biocompatibility studies

20mm x 20mm chips were cut from 3 inch diameter, 0.5 mm thick glass wafers (Borofloat33, Plan Optik). The chips were cleaned by immersing in piranha solution (3:1, H_2SO_4:H_2O_2) for 10 minutes before being rinsed with de-ionized (DI) water and then dried using a nitrogen gun. The chips were then coated with the passivation materials under investigation: 1 μm of Parylene C (deposited using a SCS Labcoter machine), 800 nm of plasma enhanced chemical vapour deposited (PECVD) silicon nitride or 800 nm of PECVD silicon dioxide. The coated slides were placed inside 35mm plastic petri dishes (Fisher) before cell seeding. As a control, cells were cultured directly in a 35 mm petri-dish. All petri-dishes were incubated for 5 days before comparing the biocompatibility of the different materials.

To test biocompatibility of adhesives that could be used to fix the culture chamber onto the glass chips, a commercial adhesive (Dymax, 1161-M) was compared against polydimethylsiloxane (PDMS). The commercial adhesive was applied and cured according to the manufacturer's protocol. PDMS was prepared with a ratio of 10:1 between the Sylgard 184 silicone elastomer and its curing agent. The prepared PDMS was degassed in a vacuum chamber for 20-30 minutes to get rid of any bubbles present in the mixture. After applying PDMS to the edges of the culture chamber and fixing it on top of the glass chip, the chip was placed on a hot plate at 100 ^oC for 20 minutes until the PDMS was cured.

Human fibroblasts (NIH 3T3) were used for the biocompatibility studies. They were cultured in Dulbecco's Modified Eagle Medium (DMEM + 10% serum + 1% penicillin streptomycin) at 3000 cells/ cm^2 inside the chambers being studied. The culture chambers fixed with PDMS and the commercial adhesive were incubated at 37 °C, 5% CO_2 for 5 days.

3.5.2. Hydrophilicity measurements

An FTA 32 goniometer (First Ten Angstroms) was used to determine the hydrophilicity of the Parylene C coated chips. A drop of de-ionized water was placed on the chip surface using a pipette tip and the contact angle was measured. The chip was treated with oxygen plasma and the contact angle was re-measured to test the treatment effect on improving the chip hydrophilicity.

3.5.3. Microfabrication of MEA chip

3 inch diameter, 0.5 mm thick glass wafers (Borofloat33, Plan Optik) were used to fabricate the MEA chips. After wafer cleaning with Piranha solution (H_2SO_4 : H_2O_2, 3:1) followed by DI water rinse and drying, 100nm platinum was deposited on top of a 10nm titanium adhesion layer by electron-beam evaporation (Helios Series cluster tool, Advanced Neotech Systems Inc. (ANS)). The wafer was then spin coated with SPR350 positive photoresist (SVG Track System) and a mask was used to expose the metal (Karl Suss MA8 Contact Aligner). After developing the photoresist (SVG Track System), the metal was etched by ion etching using argon plasma (JLS RIE 80). The photoresist was O2-plasma stripped by placing in a barrel asher for 75 mins, followed by acetone and isopropyl alcohol (IPA) rinse. The wafer was then coated with a 1000 nm insulating layer of Parylene-C (SCS Labcoter). The same steps from photoresist spin coating and UV exposure, to photoresist developing were followed. Parylene was then etched using O_2 plasma (JLS RIE 80) and the resist was stripped as previously described. The wafer was then diced into four 30mm × 30mm chips. The detailed run sheet of the fabrication process is shown in Appendix F. The fabricated chips had 16 square measurement microelectrodes with varying sizes of 20, 50, 100 and 200 μm (See Figure 5.12). A 2 cm diameter culture chamber was then fixed onto the fabricated chips using PDMS.

A printed circuit board (PCB) which allows electrical connection with the ECIS MEA was fabricated in-house according to a previous design [333]. The PCB was made out of four layers of 1.6 mm FR-4 glass textolite (Figure 3.4). Layer four is designed to support the glass chip that is placed inside the opening of layer 3. Layer 4 was also used as a back plate for nylon screws. Layer two was used to create an enough space between the chip and the top layer, where all the electrical connections are made, to allow for the use of spring probes. The four layers of the PCB were screwed together using M3 nylon screws and nuts. The spring probes were then connected to ECIS holder arrays using IDC ribbon cables.

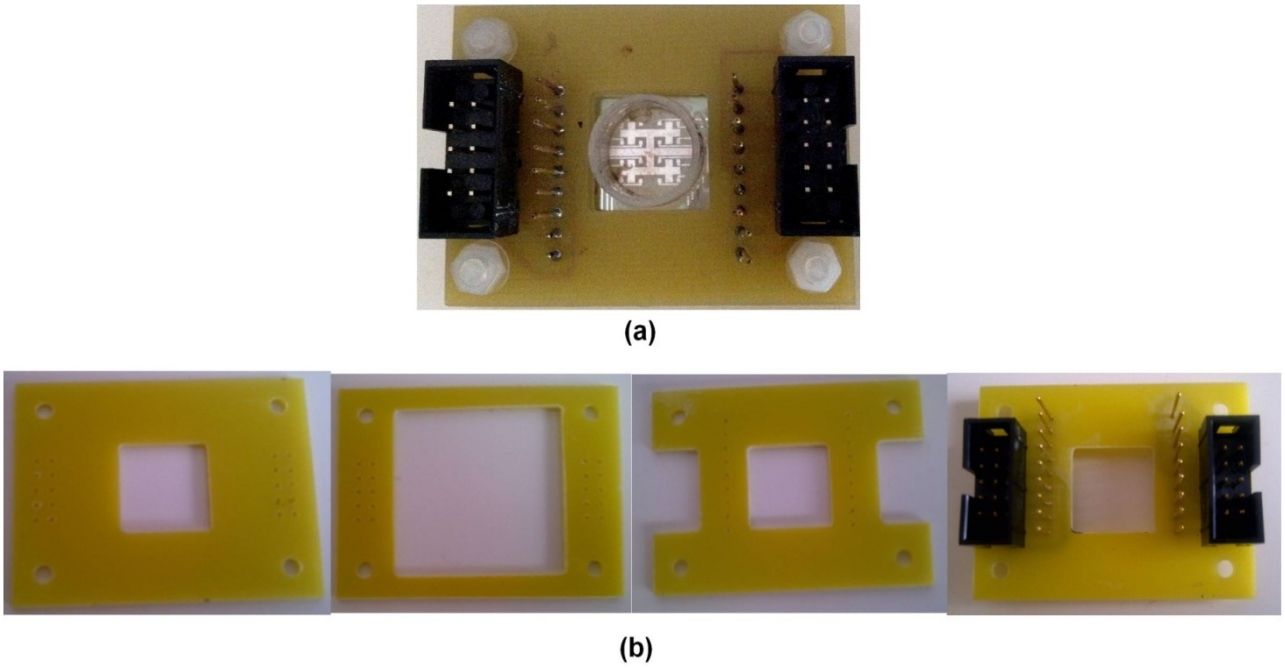

Figure 3.4: PCB for MEA-ECIS connection. (a) A picture of the PCB assembly holding a MEA chip with a culture chamber on top. (b) An exploded view of (a) showing the different layers of the PCB.

3.6. Electrical Stimulation

3.6.1. Initial experiments

A commercial microfluidic channel (Ibidi μ-slide $I^{0.1}$ luer) was used for the initial electrical stimulation experiments. The microfluidic channel was 50 mm long, 5 mm wide and 200 μm

high with two 60 μl medium reservoirs where the salt bridges were inserted. 3mm diameter tygon tubes were filled with 2% agar and were used for the application of electric fields without having the Ag/AgCl electrodes in direct contact with the cell culture. The electrical stimulation set up is shown in Chapter 6, Figure 6.4. The agar salt bridges were prepared by mixing 1g of agar in 50ml of phosphate buffered saline (PBS (2x)). The mixture was then placed on a hot plate and stirred until the powder completely dissolved. The tubes were filled with the mixture using a 1 ml glass pipette. The tubes were left over night for the agar/PBS gel to solidify. Freshly prepared agar tubes were used for every experiment.

An electrophoresis power supply (EPS 600) was used to supply a DC voltage. Two 0.5 mm diameter Ag/AgCl electrodes were connected to the power supply and immersed in 50ml glass beakers filled with PBS. For each of the agar bridges, one end was immersed in one of the beakers of PBS, while the other end was inserted in one of the microchannel reservoirs.

A handheld voltmeter (Precision Gold) was used to measure the potential difference before and after the salt bridges. The electric field (EF) applied to the channel was calculated by dividing the potential difference at the two ends of the channel by the channel's length. Simulations of the electric potential inside the microchannel were performed using COMSOL Multiphysics.

To ensure the presence of an EF inside the channel, 5 μm diameter, negatively charged, polystyrene beads (Sigma Aldrich) suspended in PBS were added to the channel and a DC voltage ranging from 10-30V was applied. The polarity was also reversed midway through the experiment to check the effect on the particles movement.

For the cell-based experiments, various EF strengths (50-300 mV/mm) were applied. An EF of 300 mV/mm was observed to have the largest effect on cell migration and alignment and was therefore used for all electrotaxis experiments.

hTERT-RPE1 cells were seeded into the channel with a low density (1500 cells/channel) and incubated for 4 hours before the application of a DC EF. Because the experiment was performed in an incubator with no CO_2 supply, 100mM of HEPES buffer (Sigma Aldrich) was added to the culture medium. The experiments were performed at 37 ^oC and time lapse videos were recorded using digital inline holographic microscopy.

The manual tracking plugin in ImageJ was used together with the ImageJ chemotaxis tool to manually track cells and define their motion paths under the effect of 0 and 300 mV/mm EFs. The change in cell alignment was defined by measuring the orientation angle, between the cell long axis and the horizontal axis (0^o), before and after EF application.

3.6.2. Impedance-based electrical stimulation

For impedance-based electrical stimulation, an initial trial was conducted using the previous set up but with an ECIS flow array (1F8x1E) instead of the ibidi microchannel. The array had eight 250 μm diameter electrodes inside a flow channel of 50 mm length, 5 mm width and with a total channel volume of 90 μL. ECIS measurements were paused for half an hour intervals during which an external EF was applied to the array.

3.6.3. Radial electrical stimulation

A design for radial impedance-based electrical stimulation is proposed in this work. Inventor Autodesk has been used to design the microelectrode array, the electrical stimulation inserts, and the ECIS microscope stage, while COMSOL Multiphysics has been used for EF simulations. The chip has six 500 μm diameter circular microelectrodes, where one central electrode is surrounded by five outer electrodes. The average spacing between the inner and outer electrodes is 6mm. 1 mm wide metal tracks connect the sensing electrodes to the contact pads having the same dimensions of those on ECIS arrays (2.38 mm x 4.44 mm with a pitch of

3.175 mm centre to centre). Spacing between all tracks is 1mm. In order to have a radial EF that can direct cell migration towards a central wound in the cell layer, an insert was designed to place six 3 mm O.D. tubes in a circular arrangement, 1 cm apart from an inner 0.38 mm I.D. (Zeus) agar tube that is vertically aligned with the inner wounding electrode. A 107x160 mm holder, inspired from the design of the ECIS microscope stage, is designed to connect the chip contact pads to the ECIS pin connector. The chip holder also has a 40x50 window to allow for optical observations. All inserts, culture chamber and chip holder were 3D printed in-house at the mechanical workshop. The culture chamber has 4 x 19 mm groves that allow the insert to be placed at a distance 1mm above the substrate, forming a roof over the electrodes. The chamber also has three 3mm diameter, 2mm long feet to allow later alignment of the chamber and inserts with the electrodes.

Disposable MEAs are suggested for the radial electrical stimulation experiments. Rectangular polystyrene substrates (5x9 cm) were laser cut from a T-75 tissue flask. 100 nm gold, with a 3nm chromium adhesion layer, was sputtered through a mask leaving only the required pattern on the substrate. A second mask will be used for passivation through which 1 μm of Parylene-C is deposited to define the electrode openings. Three holes, that fit the chamber's feet, can then be drilled in the substrate surface allowing the alignment of the chamber and the inserts with the electrodes.

3.7. Summary

This chapter described the materials, methods and cell culturing protocols used in this work. The microelectrode designs and fabrication processes used were also demonstrated. More detail on the biochemical assays employed in this work is provided in Appendix E.

Chapter 4

Drug-induced injuries: Acute liver failure disease model-on-a-chip

This chapter introduces a HepaRG-based ECIS model for drug-induced acute liver failure. The establishment and characterization of the model, which integrates impedance sensing with the progenitor HepaRG cell line, is described. The kinetics of hepatotoxicity induced by several drugs and test compounds are then investigated using bioimpedance measurements and modelling. Finally, the potential of using impedance sensing to monitor differences between sub-populations of the hepatic co-culture is discussed.

4.1. HepaRG-based ECIS model for hepatotoxicity studies: Model overview

In this work, a robust platform for assessing drug hepatotoxicity has been developed for *in vitro* toxicity studies. A human liver model combining the highly-differentiated human hepatic cell line HepaRG with ECIS technology has been established. This liver-on-a-chip model allows for real-time, non-destructive, label-free monitoring and computational modelling of toxicity assessments. The model has been used to assess liver injury induced by the following drugs: paracetamol (APAP), amiodarone and Cyclosporine-A (CsA).

The same protocol was followed for all hepatotoxicity assays. Figure 4.1 shows the protocol and technical workflow of these impedance-based assays. HepaRGs were seeded at confluency and were cultured for 8 days during which they differentiated into a hepatocyte: cholangiocyte

co-culture. After the cell differentiation and maturation stage was complete, the impedance measurements reached a steady state plateau. The toxicity assays were then conducted on day 8 of culture starting with an induction phase as explained in more detail in Section 4.3. Quantitative, real-time impedance measurements reflected changes in cell behaviour and morphology in response to well-known model hepatotoxins. Impedance data were then further analyzed and modelled, deconvolving the impedance Z into its biologically-relevant parameters:

- Tight junctions , barrier resistance parameter (R_b)
- Cell-substrate adhesion parameter (α)
- Cell-membrane capacitance (C_m)

As previously explained in Chapter 2 (Section 2.7.1.1), the range of frequencies at which the measurements are highly sensitive to cellular change, can be extracted from the impedance spectrum. The sensitivity of a chosen frequency can be determined by plotting the ratio of the impedance, resistance or capacitance for a cell-covered electrode to a cell-free electrode as a function of frequency. According to Figure 3.3 in Chapter 3, a frequency close to 4 kHz provided the highest sensitivity in recording resistance measurements, while a high frequency greater than 40 kHz would be appropriate to monitor capacitive measurements. In the current study, a frequency of 4 kHz was chosen to monitor changes in resistance while a frequency of 64 kHz was used for capacitance measurements.

4.2. Establishment and characterization of the HepaRG-model on ECIS microelectrodes

To directly establish the HepaRG-based human liver model on ECIS microelectrode arrays, cells were seeded at high density (250,000 cells/cm^2) on ECIS 8W10E$^+$ (8 wells, 10 interdigitated fingers with a total of 40 electrodes) arrays. Seeding at confluency meant that any

observed changes in impedance were caused by cell differentiation and associated changes in cell morphology, and not by an increase in cell density. Impedance was recorded every 160s to monitor the kinetics of cell differentiation in real-time over 8 days of culture during which cells self-organized into a characteristic hepatocyte:cholongiocyte co-culture (Figure 4.2).

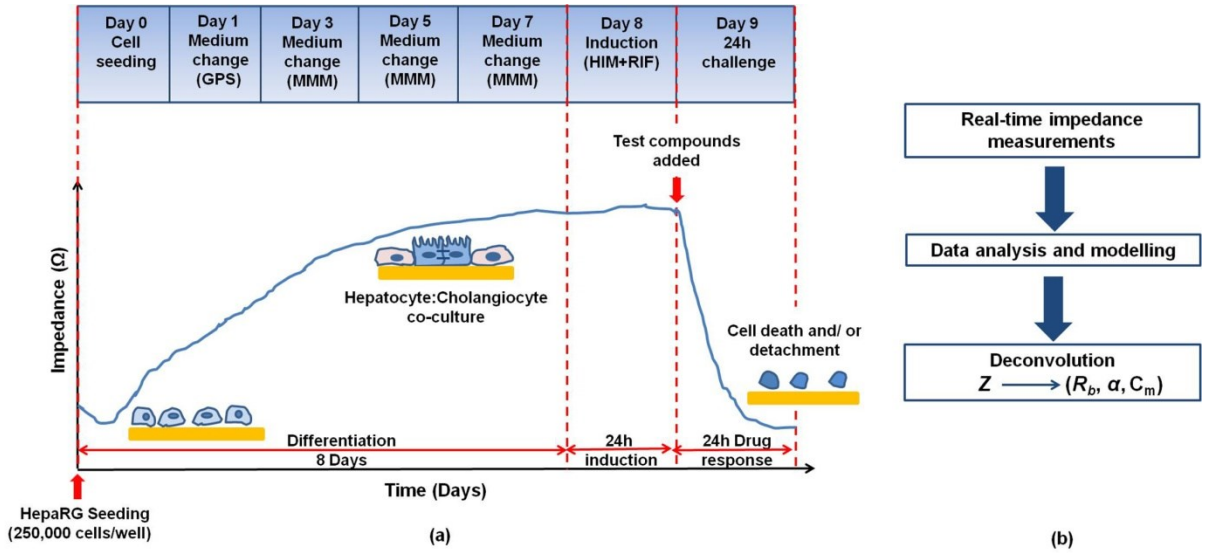

Figure 4.1: Technical workflow for the human HepaRG-based Liver-on-a-chip approach. (a) Protocol timeline: The blue panel shows the experiment protocol while the graph illustrates the change in impedance measurements. HepaRG cells were seeded on day 0 at high density on ECIS microelectrode arrays. The impedance, *Z*, is recorded in real-time throughout cell differentiation (8 days). HepaRG cells self-organize into a terminally-differentiated hepatocyte:cholangiocyte co-culture; mirrored by an increase in impedance indicative of tissue barrier formation. On day 8, toxicity assays were conducted starting with a 24h induction phase followed by a 24h drug response phase at which the effect of the test compound under investigation was recorded at multiple frequencies. Ultimately, impedance of cells exposed to high toxic level reach the value of the cell-free electrode, demonstrating complete cell death and detachment from the microelectrodes. (b) Technical Workflow: A workflow showing the different steps of the hepatotoxicity impedance-based assay. After recording the impedance measurements, data were further analyzed using the built-in ECIS model. The impedance was then deconvolved into its biologically-relevant cell electrical parameters: R_b (cell-cell junctions), α (cell-electrode adhesion) and C_m (cell membrane capacitance).

Figure 4.3(a) shows the protocol timeline of the characterization and establishment phase of the HepaRG-based ECIS model. Cells were cultured in general purpose seeding medium (GPS) for the first two days before switching to metabolic maintenance medium (MMM) on day 3. The culturing medium was then changed every other day until the cells were terminally-differentiated. Figure 4.3(b) depicts the mean resistance (n=21) at 4 kHz (R_{4kHz}) throughout the period of establishment of the human liver model on ECIS microelectrodes. The 8W10E$^+$ 40

electrodes/well provided an average for the co-culture response. Media changes were characterized by a peak in resistance associated with cell response to environmental change (temperature, nutrients, pH). The impedance measured independently across the wells demonstrated the robustness and reproducibility of the HepaRG human liver model on the ECIS chip. For all subsequent studies, real-time impedance was monitored prior to toxicity tests, as a calibration step to evaluate the quality of HepaRG-based model established onto the ECIS microelectrodes. Prior to the hepatotoxin challenge, all human liver models were evaluated against these criteria, decreasing considerably the potential for false toxicity reading due to poor establishment of the model.

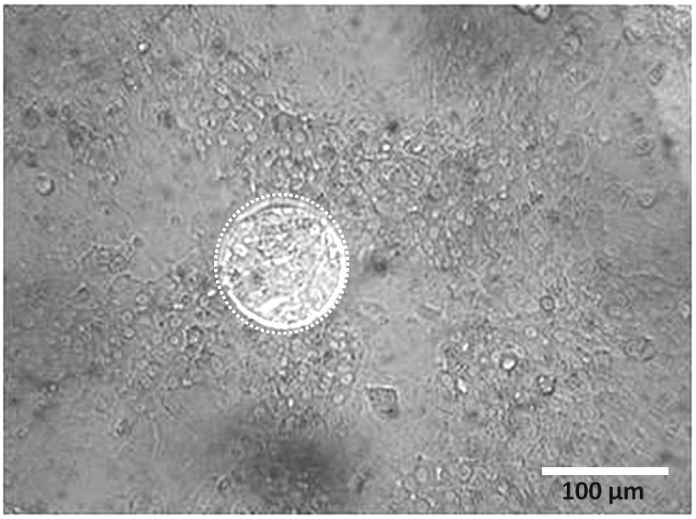

Figure 4.2: HepaRG on ECIS microelectrodes. A phase-contrast image of day 8 HepaRG co-culture on a 100 µm diameter ECIS microelectrode (illustrated by the dotted circle); partitioned into *in vivo*-like hepatic cords and cholangiocyte-like cells.

To further characterize the hepatocyte:cholangiocyte co-culture, the ECIS built-in model was used for an in-depth analysis. It is worth noting that the model is valid only when the cells completely cover the electrodes. Therefore, following completion of the cell attachment phase (12h), the cell-cell junction barrier resistance (R_b), cell-substrate adhesion (α) and the cell membrane capacitance (C_m) were all measured throughout the establishment of the HepaRG-based model. R_b increased until day 6 thus demonstrating gradual and robust barrier formation

through establishment of cell-cell junctions reaching a maximum value of 3.43 ± 0.30 $\Omega.cm^2$. Cell-adhesion (α) was found to increase sharply during the first 25h then more gradually before finally reaching a steady-state plateau at 6.30 ± 0.37 $\Omega^{0.5}$cm on day 6. First, α translated as further cell spreading onto the microelectrodes after the initial attachment phase, whereas the steady increase in α-associated cell-adhesion after the drop is likely associated with establishment of the co-culture. Cell membrane capacitance (C_m), averaged over the two cell populations, was observed to increase in about 25h and to remain at a constant plateau value of 1μF/cm^2 thereafter. The C_m, R_b, and α parameters characterized the establishment and behaviour of HepaRG co-culture for all experiments.

In parallel, staining and biochemical assays were used to characterize morphology and phenotype of HepaRG cell cultures (on day 8) as a baseline assessment of functional competence as a drug-testing model. Figure 4.3(d) shows fluorescent staining panel of nuclear (DAPI; blue), actin filaments F-actin (phalloidin; red) and the drug metabolic enzyme CYP3A4 (green). Figure (4.3(d)) shows that HepaRGs maintained high CYP3A4 activity (green); with punctate F-actin 'bands' surrounding bile canaliculae which is representative of structural hepatic polarity. Real-time PCR demonstrated strong CYP1A2, CYP2E1 and CYP3A4 (metabolic/detox enzymes belonging to the cytochrome P450 family) mRNA gene expression compared with a representative hepatic cell line (HepG2/C3A) as shown in Figure 4.3(e). Thus, the HepaRG cells were shown to maintain intact phenotype and metabolic competence for metabolism of the hepatotoxins used in this study.

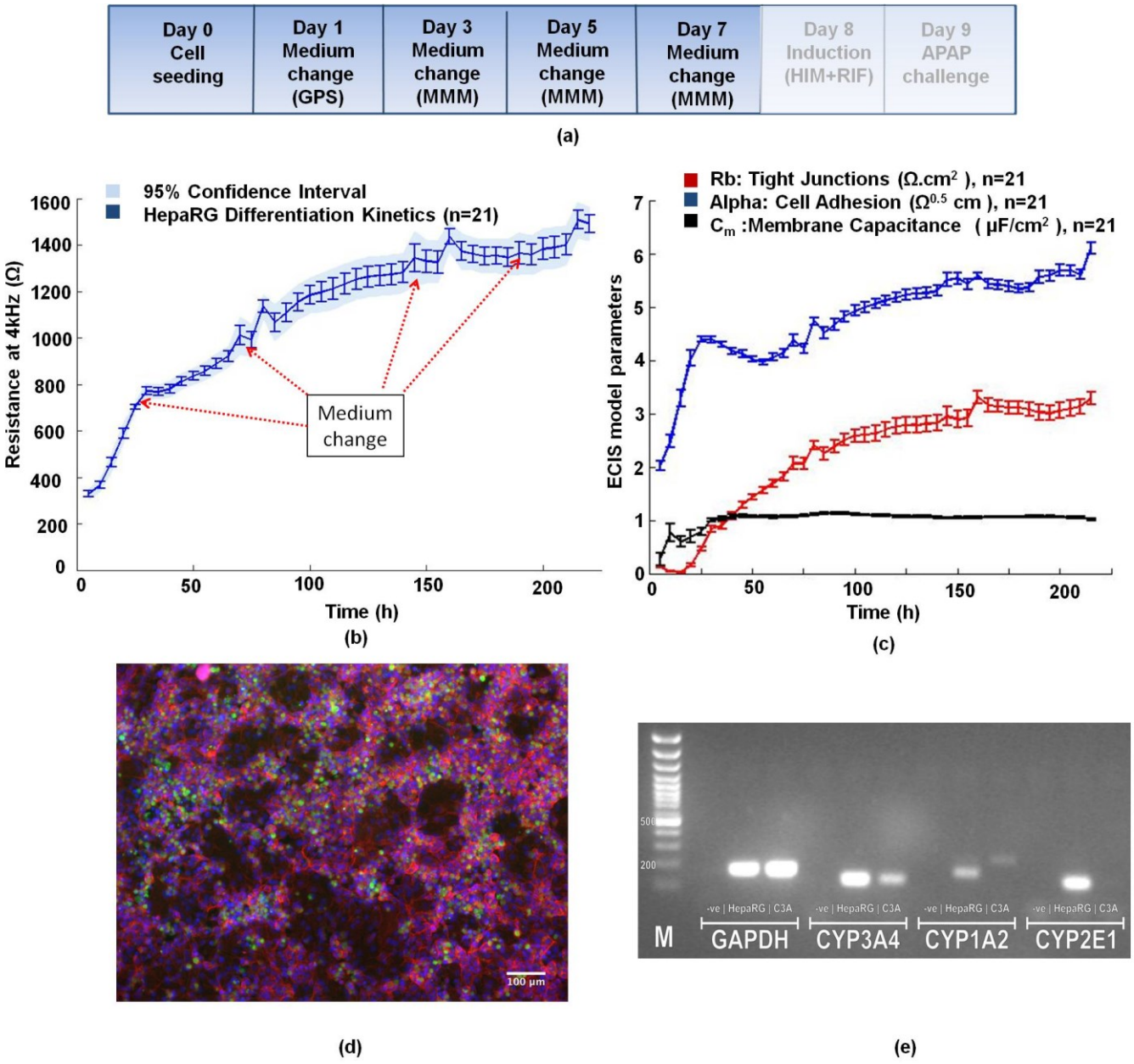

Figure 4.3: Establishment and characterization of human hepatic HepaRG-based model on impedance sensing arrays. (a) Protocol timeline: The blue panel shows the protocol followed for the establishment of the HepaRG-based model on ECIS arrays. (b) Resistance measurements: The resistance at 4 kHz (R_{4kHz}) increased steadily until reaching a plateau on day 6, reflecting the completion of the differentiation phase and epithelial polarization. (c) ECIS model parameters: Graphs show the changes in the barrier function (R_b), cell-substrate adhesion (α) and cell membrane capacitance (C_m) with the establishment of HepaRG cell-cell tight junctions, and cell-electrode adhesion. (d)Immunostaining: Immunofluorescent staining of HepaRG cells on day 8 showed a highly differentiated phenotype: Extensive hepatic CYP3A4 activity (green); punctate staining of F-actin bands indicative of bile-canaliculae structures [red; phalloidin-staining]; with vivo-like hepatic cords and cholangiocyte-like cells. (e) RT-PCR: Metabolic competence for APAP metabolism was shown by high expression of CYP2E1, CYP1A2, and CYP3A4 isoforms, compared with a representative hepatic cell line (HepG2/C3A).

Figure 4.4 shows the corresponding capacitance measurements at 64 kHz during the HepaRG differentiation phase. The capacitive part of the impedance is a reflection of the electrode cell-coverage. As the HepaRGs were cultured at confluency, thus already covering the electrodes at the beginning of the experiment, the measured capacitance showed a relatively small change with the establishment of the HepaRG-based model. Hence resistance has been selected to monitor HepaRG differentiation kinetics.

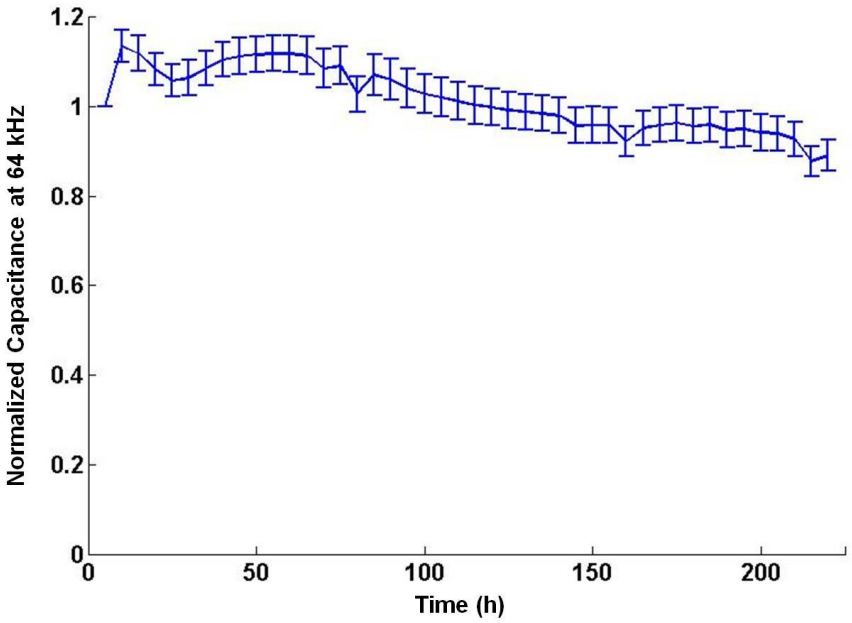

Figure 4.4: Normalized capacitance as a function of time during HepaRG differentiation. The imaginary part of the impedance (capacitance) mirrors cell-electrode coverage. Because HepaRGs were cultured at confluency, the capacitance measurements at 64 kHz showed almost no change and therefore it could not be used to monitor HepaRG differentiation.

4.3. Hepatotoxicity impedance-based assays

4.3.1. Paracetamol (Acetaminophen)

Acetaminophen (APAP) hepatotoxicity remains the leading cause of acute liver failure. Despite the suggested role for tight junctions and cell adhesion in hepatic polarity and maintaining the

functional liver architecture, temporal and quantitative effects of direct APAP toxicity on adhesion structures have not been previously explored and mechanistic insight into APAP-induced TJ disruption in hepatocytes is lacking. Thus, the HepaRG-based ECIS platform was used to investigate dose-dependent effects of APAP on cell-cell TJs, cell-substrate adhesion and the integrity of the cell membrane.

Following the establishment of HepaRG co-culture for 8 days, a 24h CYP3A4-induction with Rifampicin was conducted. CYP3A4, a member of the CYP450 family, metabolizes acetaminophen to the reactive metabolite, NAPQI (N-Acetyl-p-benzoquinone imine). Since CYP450 detox enzymes can be inhibited by solvents such as DMSO, a possible constituent of proprietary culture medium, induction with the liver enzyme-inducer Rifampicin was used. It is worth mentioning that Rifampicin induction had no effect on the cells as reflected by the resistance measurement and its deconvolved modelling parameters as shown in Figure 4.5.

The HepaRG culture was then subjected to a dose-response challenge with the hepatotoxin acetaminophen (0-20 mM). Quantitative impedance measurements were taken every 160s over 24h in an effort to detect earlier, key biological events (cell behavior parameters: R_b, α, C_m) in response to APAP. Following paracetamol addition, a time- and dose-dependent decrease of impedance was observed at all frequencies indicating a global decline in cellular health.

Figure 4.6 (b) shows the corresponding decrease in normalized R_{4kHz} with the measurements dropping to almost that of the cell-free electrode, at the highest dose (20 mM). The corresponding non-normalized data with the no-cell (medium only) control are shown in Figure 4.7. Normalized data was a more accurate way to compare the amount of decrease accompanying APAP introduction to the different culture wells. Data was normalized by dividing the measured impedance (or the deconvolved parameter) by the value at the challenge starting point (t=0) as explained in Section 3.1.4.

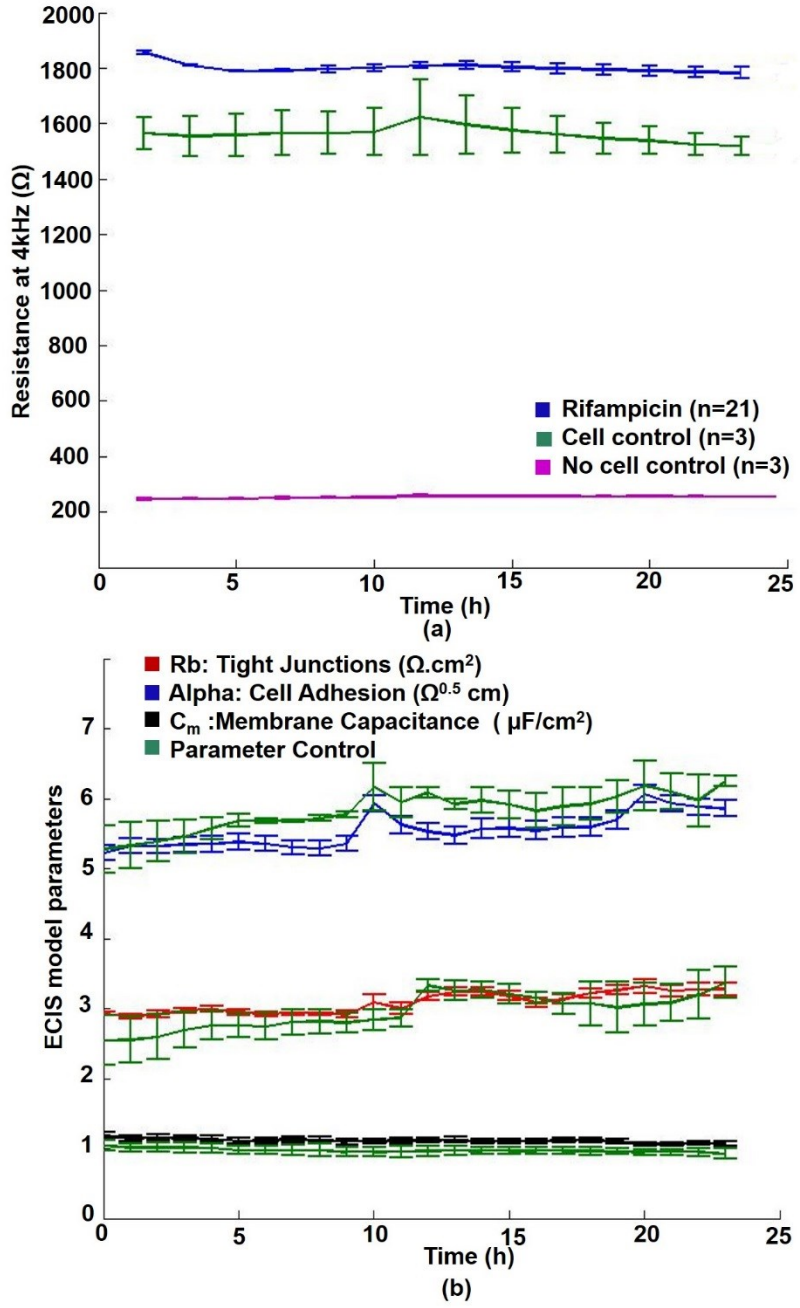

Figure 4.5: Effect of Rifampicin on HepaRGs. All the toxicity assays were preceded by a 24h induction phase of rifampicin. Rifampicin showed no effect on HepaRGs as monitored by ECIS. (a) Effect of Rifampicin on resistance: inducing the cells did not have any effect on cell behaviour or their morphology as reflected by resistance measurements. (b) Induction did not cause any disruption to the cell-cell tight junctions, cell-substrate adhesion or cell membrane integrity as illustrated by the modelled R_b, α and C_m values.

To investigate further the mechanisms of paracetamol toxicity on HepaRGs, the APAP-induced effect on R_b, α, as well as C_m was investigated. It was clear that R_b values decreased in a dose-dependent manner (Figure 4.6 (c)). Similarly, Figure 4.6 (d) demonstrates dose-dependent decrease in the cell-adhesion parameter (α) over the 24h exposure.

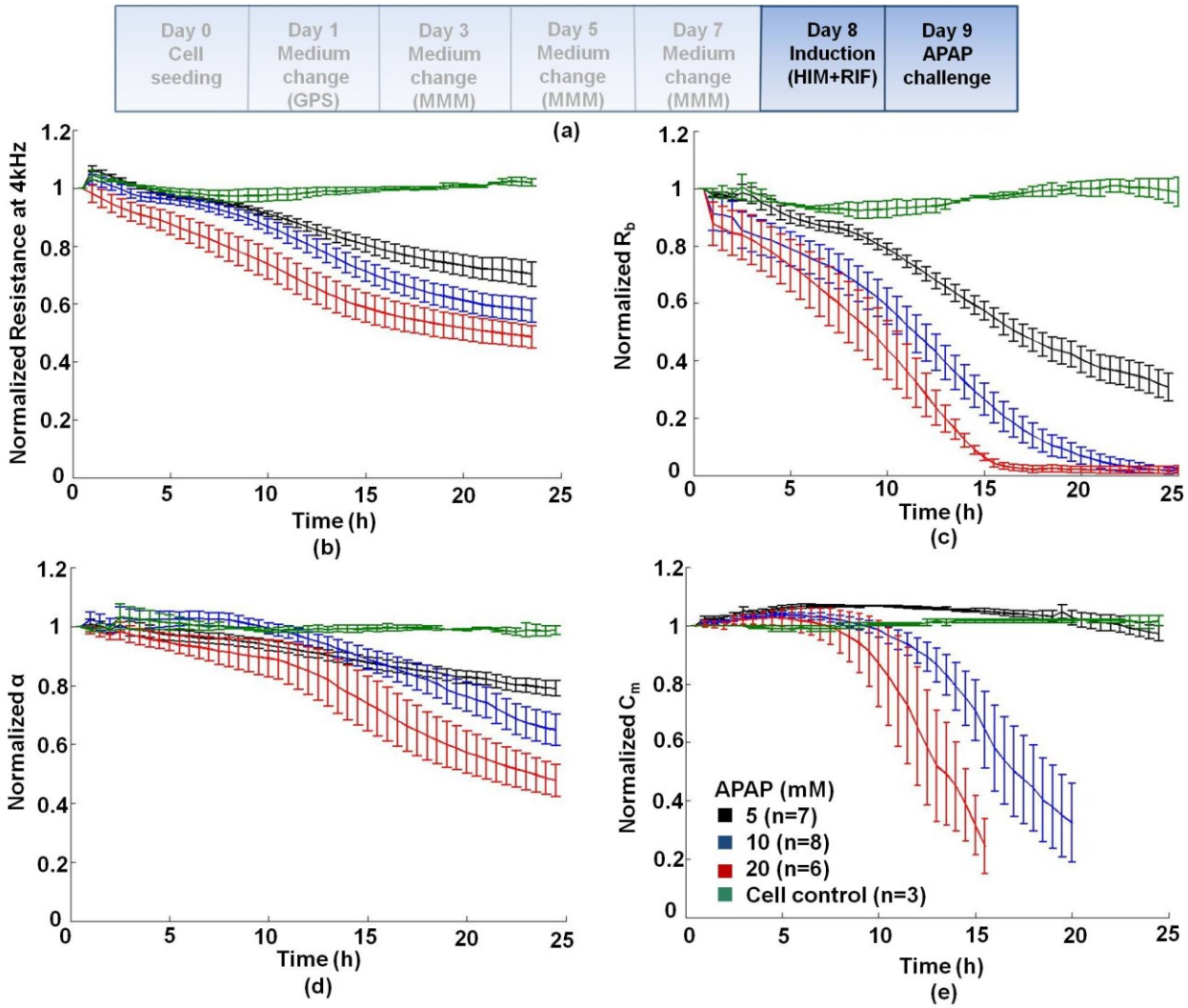

Figure 4.6: Real-time normalized impedance monitoring of HepaRG-based liver-on-chip device following 24h APAP challenge. (a) Protocol timeline: Following 24h Rifampicin induction in confluent HepaRG cells on day 8, cells were treated on day 9 for 24h with APAP (0mM, untreated control; 5mM; 10mM; and 20mM); (b) Post-challenge resistance kinetics: APAP caused a dose-dependent decline in normalized resistance at 4kHz (c) Cell-cell tight junctions: APAP disrupted TJs in a dose- and time-dependent manner; (d) Cell-substrate adhesion disruption suggesting cell detachment from the electrode surface (e) Decrease in C_m values reflecting how cell membrane integrity was compromised at high APAP doses (10-20 mM).

Although no significant differences between APAP doses were evident before 15h, α could clearly quantify and discriminate between APAP-induced effects on cell adhesion in real-time (15-24h) as opposed to standard 24h end point hepatotoxicity assays. In contrast to R_b and α, the cell membrane capacitance, C_m, did not alter in a dose-dependent manner (Figure 4.6(e)).

Cell membrane integrity was compromised only at high paracetamol doses (10 mM, 20 mM), with no effect detected at low doses.

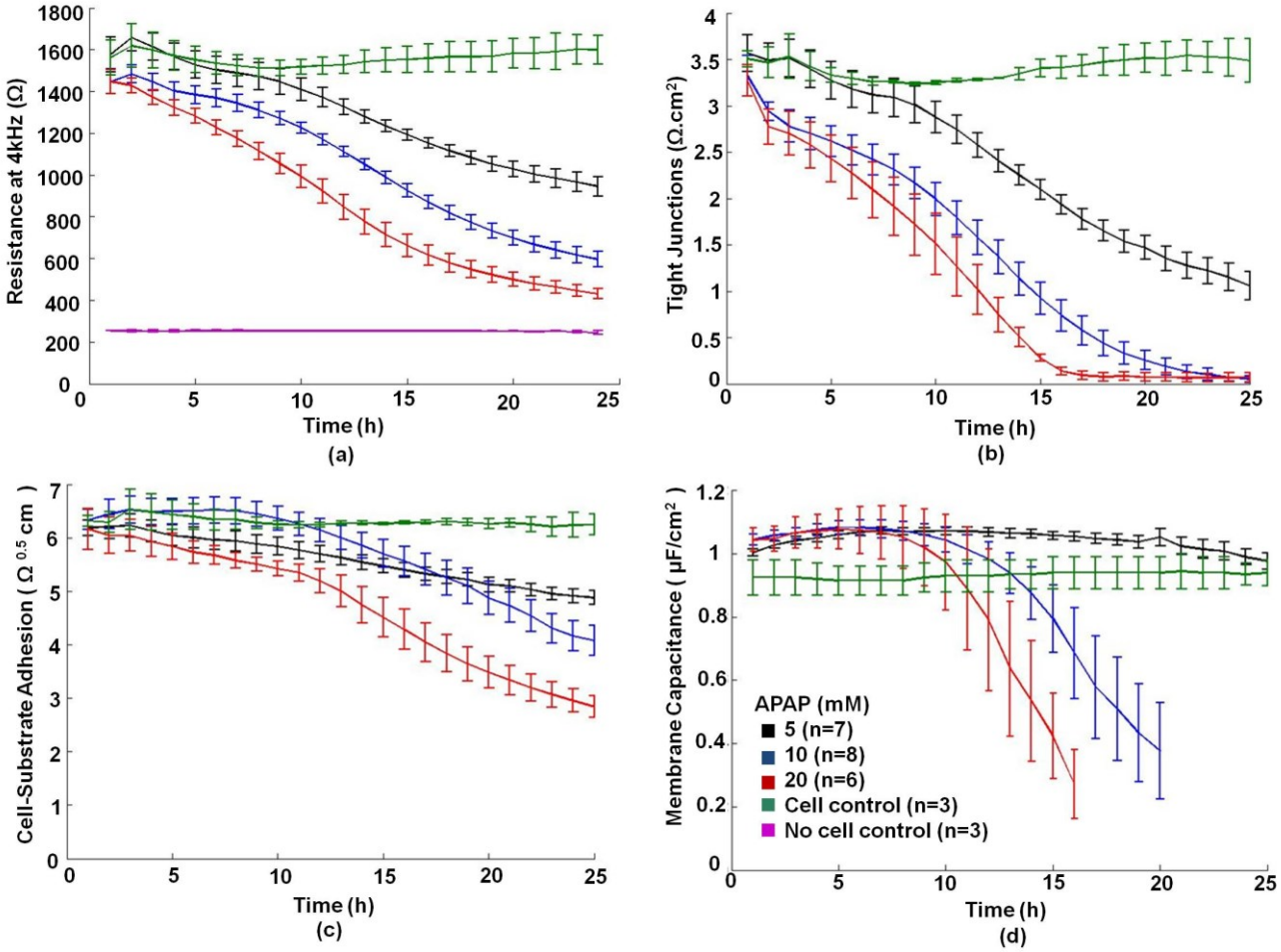

Figure 4.7: Non-normalized APAP dose response. (a) The 24h effect of APAP on the true, non-normalized resistance in real-time showing dose- and time- dependent decrease in measured values. The effect of APAP on tight junctions, cell-substrate adhesion and cell membrane capacitance is illustrated in (b), (c) and (d) respectively.

At higher doses, a drop in C_m after 8 hours could be associated with sudden rupture of the cell plasma membrane, with total cell death quantified at 20h for 10 mM and 15h for 20 mM APAP. The measured resistance as well as the model parameters at 6, 12 and 24h are presented in Table 4.1 and illustrated by the bar graphs in Figure 4.8.

APAP Challenge	Control	6 hrs	12 hrs	24 hrs
Resistance (Ω)				
5 mM	1680.90 ± 126.82	1603.0 ± 73.6	1346.1 ± 34.3*	930.92 ± 95.27**
10 mM	1508.30 ± 74.02	1418.50 ± 49.13	1042.2 ± 36.6**	585.45 ± 72.24**
20 mM	1513.8 ± 101.3	1191.20 ± 52.68**	706.7 ± 60.1**	421.6 ± 20.4**
R_b (Ω.cm^2)				
5 mM	3.585 ± 0.36	3.53 ± 0.25	2.6 ± 0.1**	1.13 ± 0.32**
10 mM	3.25 ± 0.33	2.37 ± 0.28**	1.15 ± 0.26**	0.185 ± 0.080**
20 mM	3.45 ± 0.23	1.78 ± 0.30**	0.20 ± 0.09**	0**
α (Ω$^{0.5}$cm)				
5 mM	6.4 ± 0.2	6.30 ± 0.16	5.880 ± 0.087	2.97 ± 0.29**
10 mM	6.32 ± 0.24	6.75 ± 0.30	5.84 ± 0.08	2.67 ± 0.67**
20 mM	6.27 ± 0.69	5.93 ± 0.10	4.69 ± 0.37	1.49 ± 0.75**
C_m (μF/cm^2)				
5 mM	1.01 ± 0.01	1.060 ± 0.007	1.060 ± 0.016	1.040 ± 0.017
10 mM	1.03 ± 0.04	1.080 ± 0.049	0.9 ± 0.1	0**
20 mM	1.10 ± 0.07	1.06 ± 0.14	0.36 ± 0.22*	0**

Table 4.1: Non-normalized APAP dose response. The effect of APAP on the non-normalized resistance, R_b, α and C_m at different time points of the toxicity assay. From the table, it is clear that the earliest and most significant effect of APAP is on the cell-cell tight junctions even at the low dose of 5mM. * P<0.05; ** P<0.01 (significantly different from control). The greyed areas indicate time points at which the model could be invalid due to cell detachment resulting in a non-confluent cell layer.

The resistance bar graphs show a time dependent APAP dose response. For the highest dose (20mM), the decline is significant even after only 6 hours of the challenge. After 12 hours, the decrease in resistance is significant for the other doses and at the end of the 24h assay, the resistances reach their minimum values close to that of the cell free electrode for the high doses. As mentioned before, the main effect of APAP was on the cell-cell junctions. At 6h, a significant decrease in R_b is measured for the high doses (10-20 mM, more significant for 20mM). At 12h, the decrease in R_b is significant even for the 5mM dose while the cell-cell junctions are almost demolished for the 20mM. The effect of APAP on cell-substrate adhesion does not occur as early as that on cell-cell junctions. No significant decrease in adhesion is monitored at 6h or 12h. At 24h, however, all doses show a significant decrease in cell-substrate adhesion. The effect of APAP on the integrity of the cell membrane is only monitored for the high doses. It is more pronounced at 24h where C_m reaches zero as the membrane integrity is completely compromised with cell death and detachment.

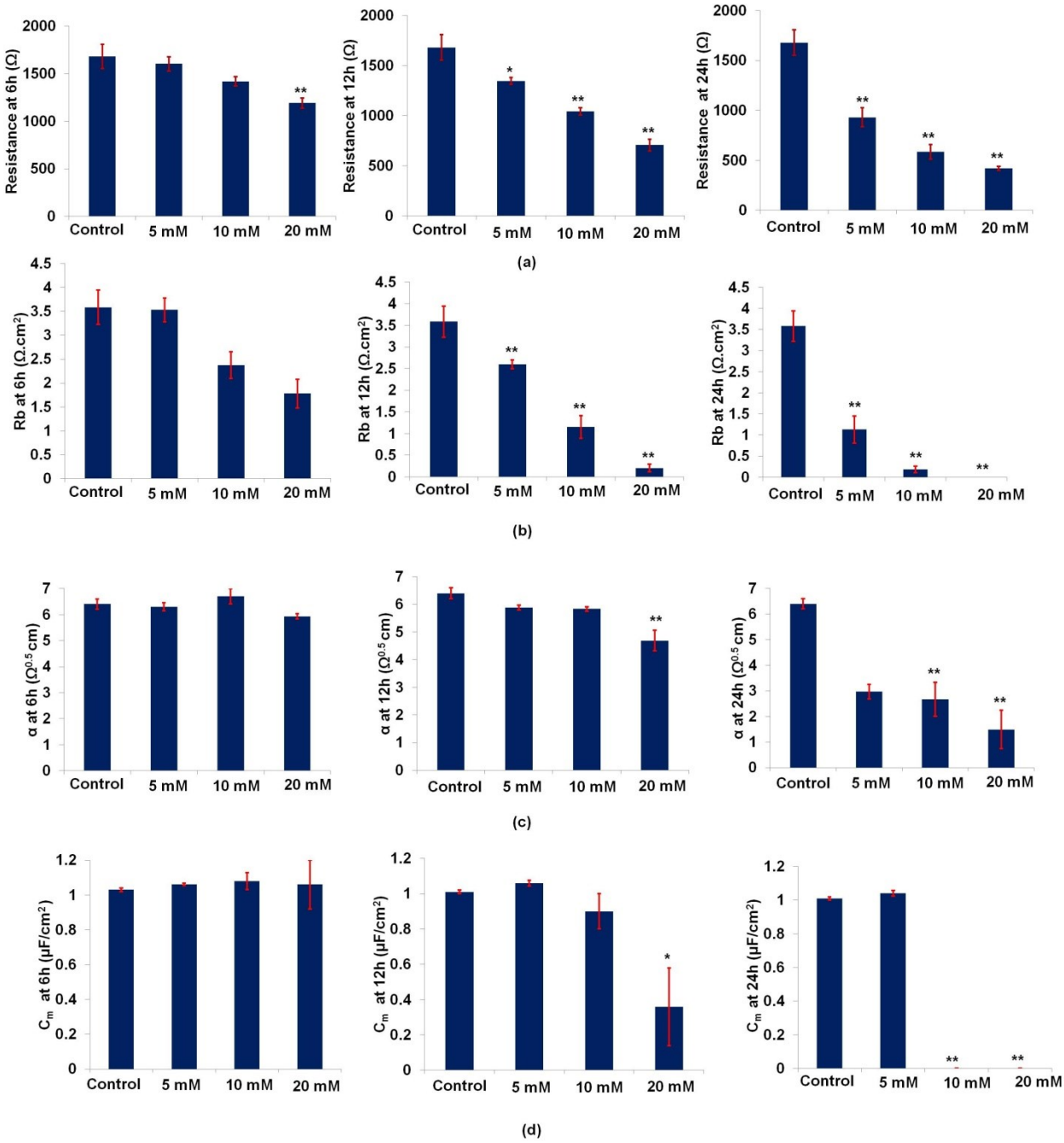

Figure 4.8: Non-normalized APAP dose response bar graphs. The effect of APAP on the non-normalized resistance (a), R_b (b), α (c) and C_m (d) is shown at different time points (6h, 12h and 24h) of the toxicity assay. * P<0.05, ** P<0.01 (significantly different from control).

To summarize, the most prominent effects at all tested APAP doses were on cell barrier resistance. ECIS measurements showed an earlier effect and disruption to R_b, even at a low 'non-toxic' dose of 5 mM. After 10h, parameters of cell adhesion (α) and cell membrane integrity (C_m) decreased at higher doses perhaps indicating a 'tipping point' in real-time where

cells are irreversibly compromised. Since the sensitivity of ECIS measurements to changes in cell-cell junctions and adhesion is more pronounced at low frequencies, resistances at 4 kHz were used to monitor the effect of APAP on HepaRG morphology. The effect of APAP on capacitance measurements at 64 kHz is also shown in Figure 4.9. This translates into electrode cell-coverage and cell attachment/detachment.

In order to gain more insight into the kinetics of APAP toxicity, a sigmoid curve was fitted to the R_{4kHz} measurements (Figure 4.10 (a)). A significant difference ($P<0.01$) between the sigmoidal slope of the 5mM and those of the 10mM and 20mM APAP concentrations was observed. This difference in slopes was related to the dose-dependent decline of the measurements (Figure 4.10 (b)). Moreover, the APAP dose response occurred in a time-dependent manner, with the decrease in resistance measurements passing through two phases: a short phase showing a relatively small decline in resistance following APAP addition, and a longer (main) phase showing a more pronounced APAP toxic effect. A delay in the start of this main phase was noticed and was also significantly ($P<0.01$) dependent on the APAP concentration, varying from 1.0 ± 0.2h for the 20 mM dose and 5 ± 1h for 10 mM to 8.0 ± 1.5h for the 5 mM concentration (Figure 4.10 (c)).

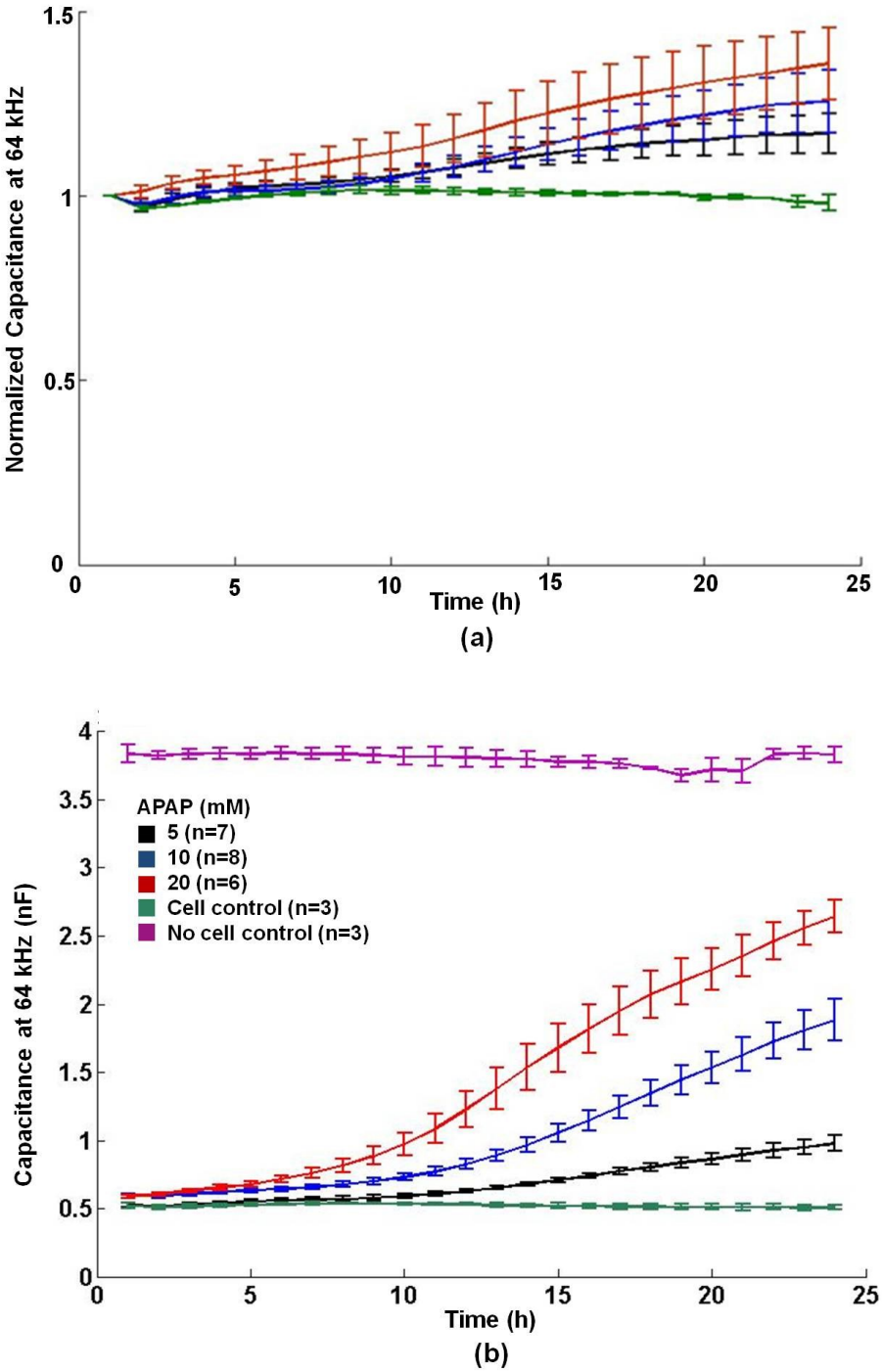

Figure 4.9: APAP capacitance dose-response. (a) Normalized capacitance measurements showing earlier cell detachment at the highest dose following APAP introduction. (b) Non-normalized capacitance.

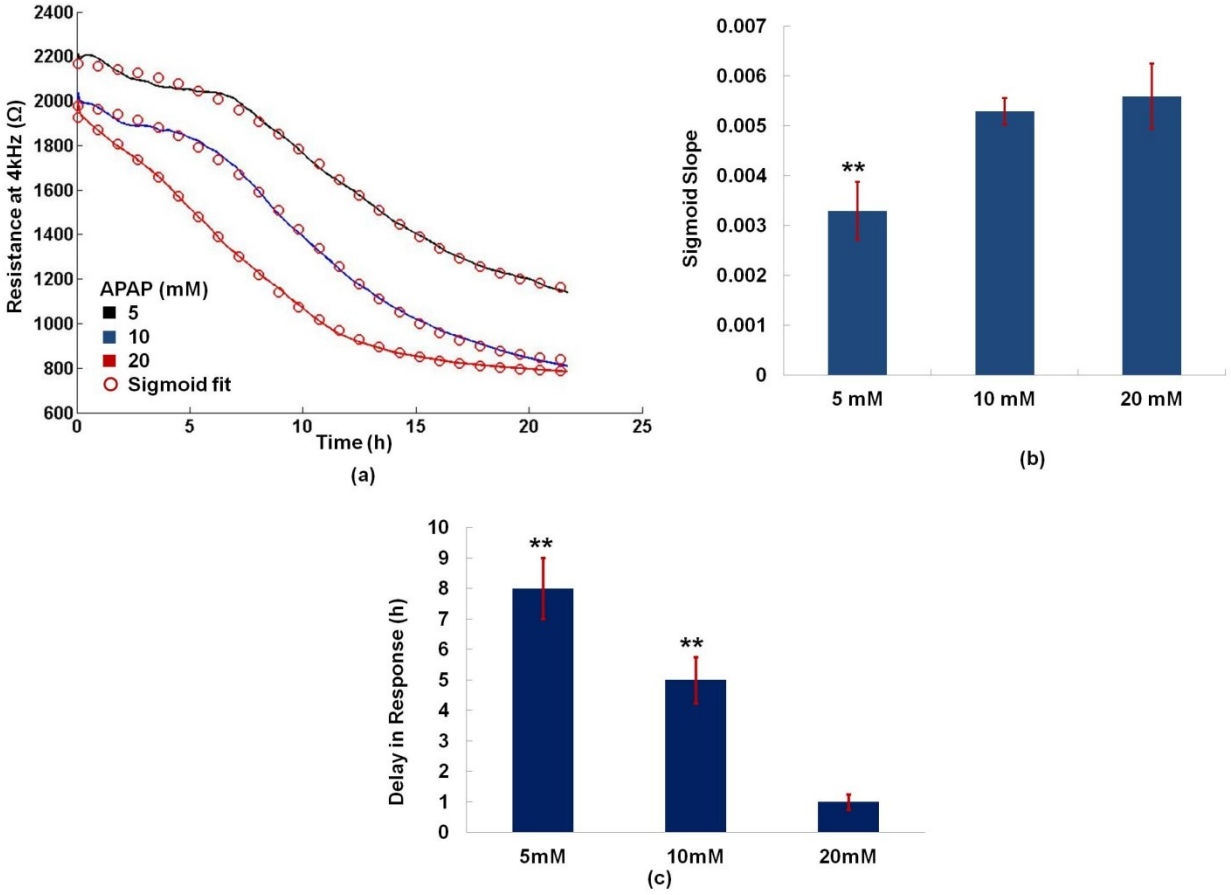

Figure 4.10: Sigmoidal fitting of the non-normalized APAP dose response. (a) Sigmoid curve fitted to non-normalized resistance measurements following the addition of 5 mM, 10 mM and 20 mM APAP (b) Bar graph comparing the sigmoidal slopes of the different APAP doses. The higher doses (10 mM, 20 mM) of APAP showed a significantly higher sigmoidal slope, indicating a faster decline in the measured resistances.(c) Bar graph showing the delay in response for the three APAP concentrations. The APAP effect was accompanied by a delay in the main phase response that varied from around 1h for the 20mM and 5h for the 10mM to almost 8h for the 5mM APAP doses. ** P<0.01.

i. Biochemical hepatotoxicity assays and staining

a. PrestoBlue and ATP-depletion

To assess hepatotoxic response to APAP in HepaRG cells and for comparison with impedance measurements, dose-dependent hepatotoxicity was detected at 24 hours, by multiplexing ATP-depletion endpoint assay with the PrestoBlue cell viability assay (Please note that all hepatotoxicity biochemical assays and staining were performed by the HepLab group at the Royal Infirmary, University of Edinburgh).

Such assays estimate the functional or metabolic state of the cell, typically, mitochondrial reductive activity/ dysfunction as a correlate of oxidative stress in response to a hepatotoxin. Prestoblue and ATP values are expressed relative to the levels found in control cells, arbitrarily set at a value of 100%. Interestingly, the effect of APAP on cell viability and ATP depletion was not as dramatic as monitored with impedance sensing. ATP content decreased to only 50% of control values at 20 mM APAP; with minimal change observed for 5-10 mM. Cell metabolic activity, as measured by Prestoblue (providing also a quantitative measure of viability and cytotoxicity), was more pronounced in sub-toxic (5 mM) and intermediate (10 mM) dose APAP, compared with ATP-depletion assay.

Moreover, unlike quantitative real-time ECIS cytotoxicity monitoring, these biochemical tests can not simultaneously provide information on individual structural components, and lack the sensitivity and specificity required for time-resolved mechanistic studies.

b. HepaRG Intercellular integrity following APAP toxicity

To ascertain whether reduced R_b values were due to physical disruption of TJs, potentially leading to cell death, TEM (transmission electron microscopy) coupled with ZO-1 (Zona Occuldens, TJ- associated protein) immunofluorescent staining was performed after 24h of APAP exposure.

Phase-contrast images showed the progressive loss of the characteristic hepatocyte (H)/ cholangiocyte (Ch) *in vivo*-like hepatic cord phenotype with increasing APAP concentrations as shown in Figure 4.12.

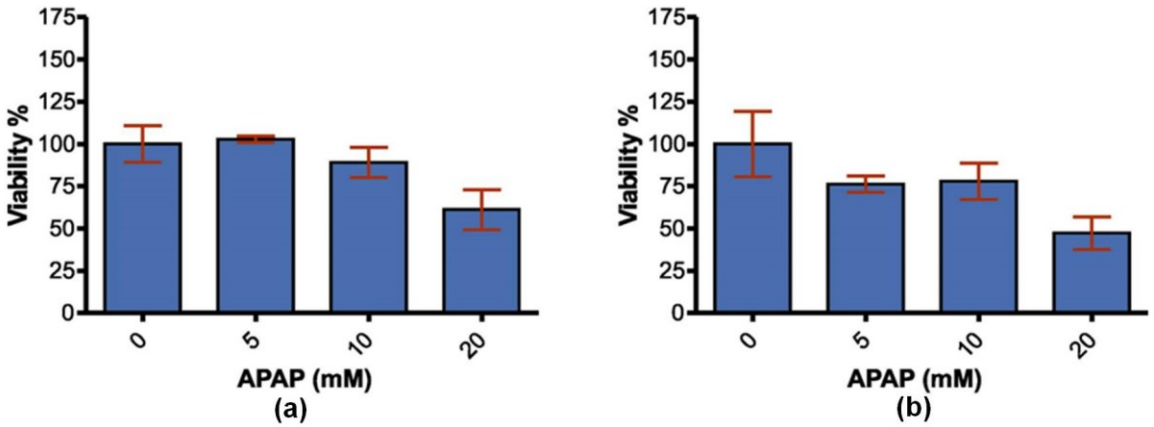

Figure 4.11: Parallel biochemical hepatotoxicity assays following 24h APAP challenge. (a) Classic ATP-depletion endpoint assays. (b) PrestoBlue live-cell viability. Prestoblue and ATP values are expressed relative to the levels found in control cells, arbitrarily set at a value of 100%.

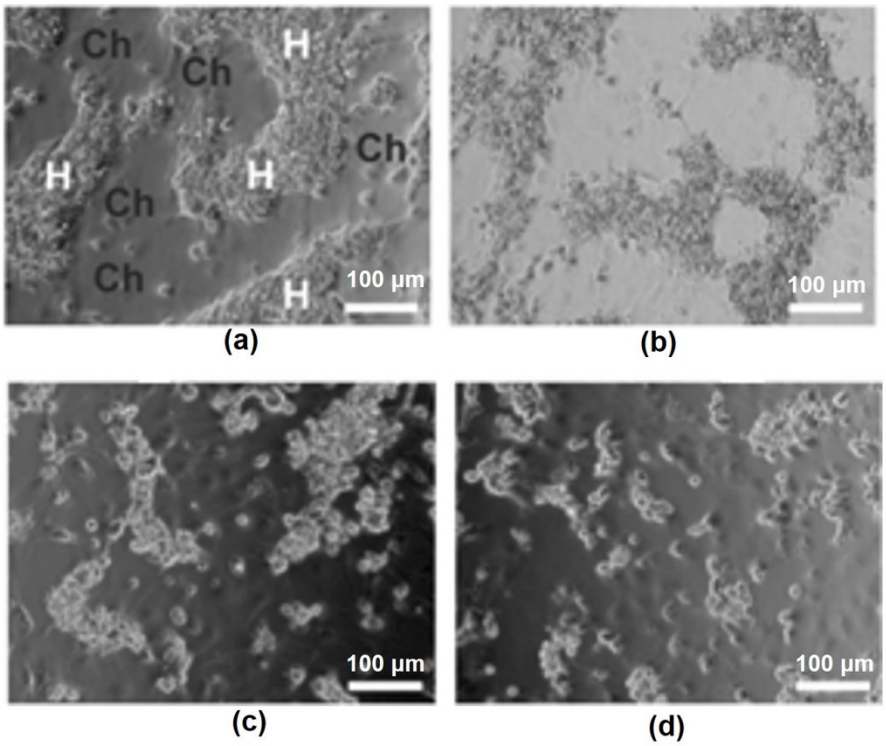

Figure 4.12: HepaRG phase contrast images following 24h APAP challenge. Characteristic hepatocyte (H) / cholangiocyte (Ch) *in vivo*-like hepatic cord phenotype in control cultures (a) is progressively lost with increasing APAP concentrations: (b) 5mM, (c) 10mM (c), (d) 20mM.

Confocal microscopy demonstrated structural disruption of TJ, indicated by a reduced intensity of the green immunofluorescence staining of ZO-1 with increasing APAP dose (Figure 4.13). Down-regulation of ZO-1 proteins may result in decreased cell survival through disruption of TJ integrity and adhesion to extracellular matrix components in HepaRG cells. The 'chicken wire' network of delineated ZO-1, progressively decreased, as the hepatic cord phenotype was compromised.

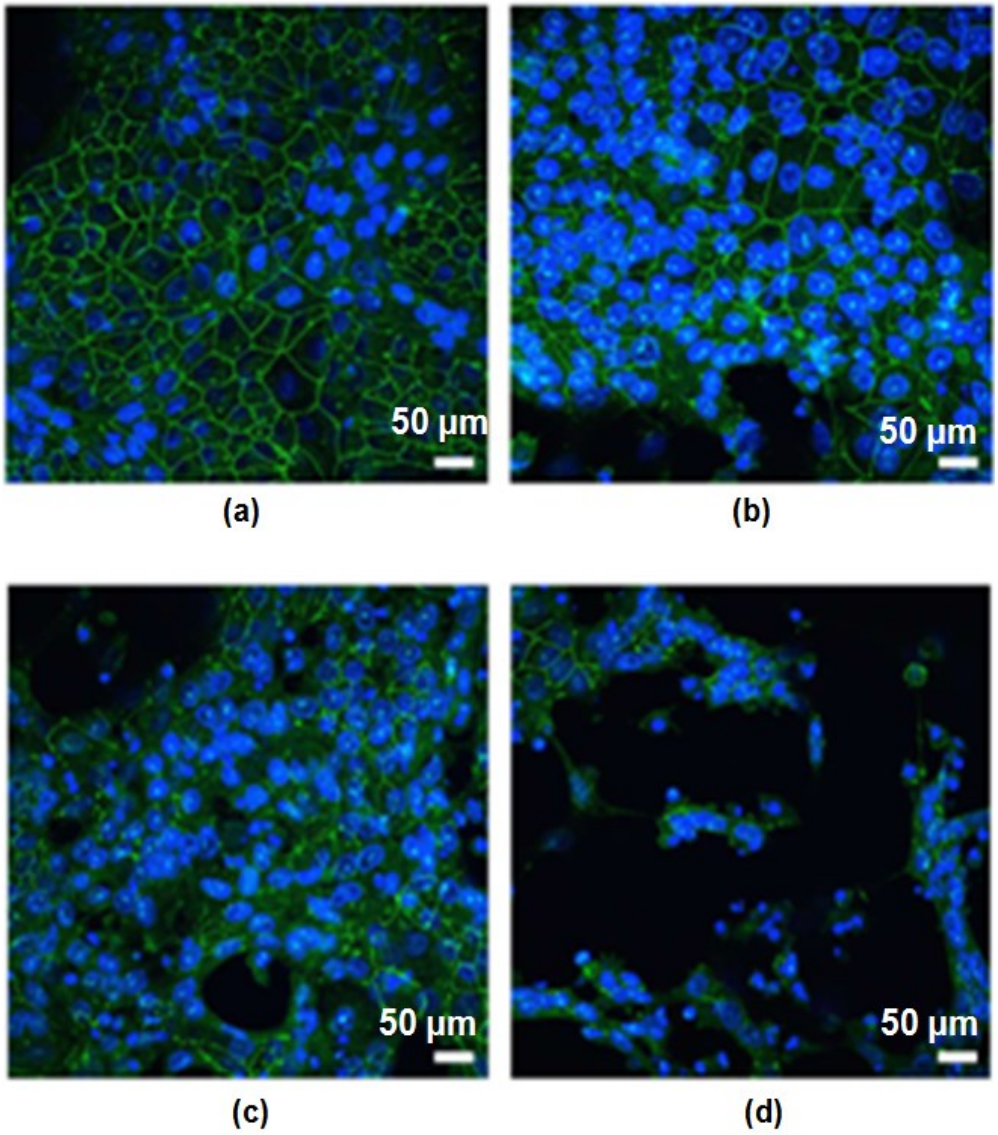

Figure 4.13: ZO-1 immunofluorescence staining of HepaRG following APAP treatment for 24h. Confocal microscopy demonstrated reduced intensity (green immunofluorescence staining) of the hepatic tight junction-associated structural protein ZO-1, with increasing APAP. The 'chicken wire' network of delineated ZO-1, progressively decreased, as the hepatic cord phenotype was compromised. (a) Untreated control (0 mM), (b) 5mM, (c) 10 mM, (d) 20 mM.

TEM imaging confirmed dose-dependent disruption of TJ-barrier function prior to cell death with 10mM, 20mM doses. Examination of TEM ultrastructure at 5mM APAP showed no evidence of TJ structures. However, an 'electron-dense' perimeter was observed around hepatocytes; perhaps indicative of subcellular redistribution of TJ proteins in response to cellular stress Figure 4.14 (b).

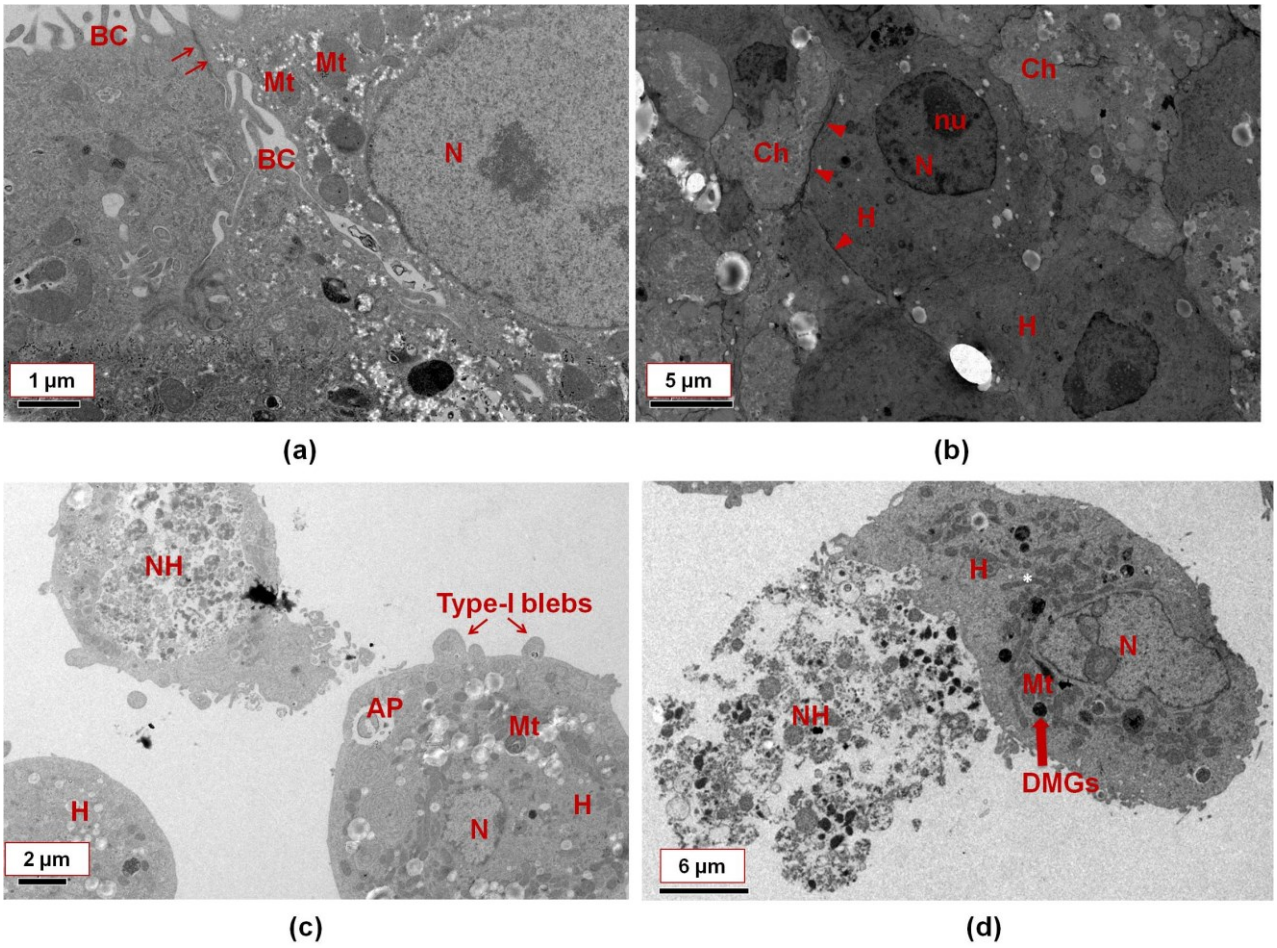

Figure 4.14: TEM ultrastructural imaging of HepaRG following 24h APAP challenge. (a) Typical ultrastructure in untreated controls, showing numerous mitochondria (Mt) with tight junctions (arrows), which seal bile canalicular lumen (BC) formed between two adjacent hepatocytes. (b) At 5 mM APAP, although discrete TJ structures were not visible, an 'electron-dense' perimeter surrounded hepatocytes (red arrowheads), adjacent cholangiocytes (Ch). At 10mM (c) and 20 mM (d) APAP, TJs were not present, with cells commonly exhibiting necrotic (NH) or apoptotic (AP) appearance, with Type-I blebbing. Altered mitochondria shape was evident, although retaining some dense mitochondrial granules (DMGs). The images also show the cells Nucleus (N) and nucleolus (nu).

Figure 4.14(a) shows typical ultrastructure in untreated controls, showing numerous mitochondria (Mt) with tight junctions (red arrows), which seal bile canalicular lumen (BC) formed between two adjacent hepatocytes. Tight junctions were completely demolished for the higher 10 mM and 20 mM APAP doses (Figure 4.14(c) and (d) respectively). Many cells showed a necrotic (NH) or apoptotic (AP) appearance, with Type-I blebbing. Altered mitochondria shape was also evident, although retaining some dense mitochondrial granules (DMGs).

4.3.2. Phorbol ester

Phorbol ester activation of phosphokinase C (PKC) has been shown to disrupt TJ integrity and significantly reduce polarity in human hepatic HepG2 cells [35]. To validate R_b impedance measurements, and test whether APAP-induced disruption of TJs could implicate a PKC-dependent signalling pathway, a dose-response with the PKC-activator, phorbol-12-myristate-13-acetate (PMA) was performed using different concentrations of 50, 100 and 200 ng/ml (Figure 4.15). The only quantified effect of PMA was on R_b, decreasing by around 30% at all doses before increasing again towards their original values (Figure 4.15(c)). Figure 4.16 shows the corresponding non-normalized data of the 24h PMA test. Exact values for the non-normalized resistance, R_b, α and C_m at 6h, 12h and 24h of the PMA challenge are provided in Table 4.2. A significant decrease ($P<0.01$) in the resistance measurements was recorded at 6h for the highest (200 ng/ml) dose. Interestingly, this was the first dose to increase and return back close to its original resistance values. At 12h, all doses showed a significant decrease in resistance ($P<0.01$). After this decline in resistance values, all doses showed an increase in the measurements. The decrease in resistance measurements was attributed to R_b disruption, since both α and C_m showed almost no change at all with the introduction of PMA.

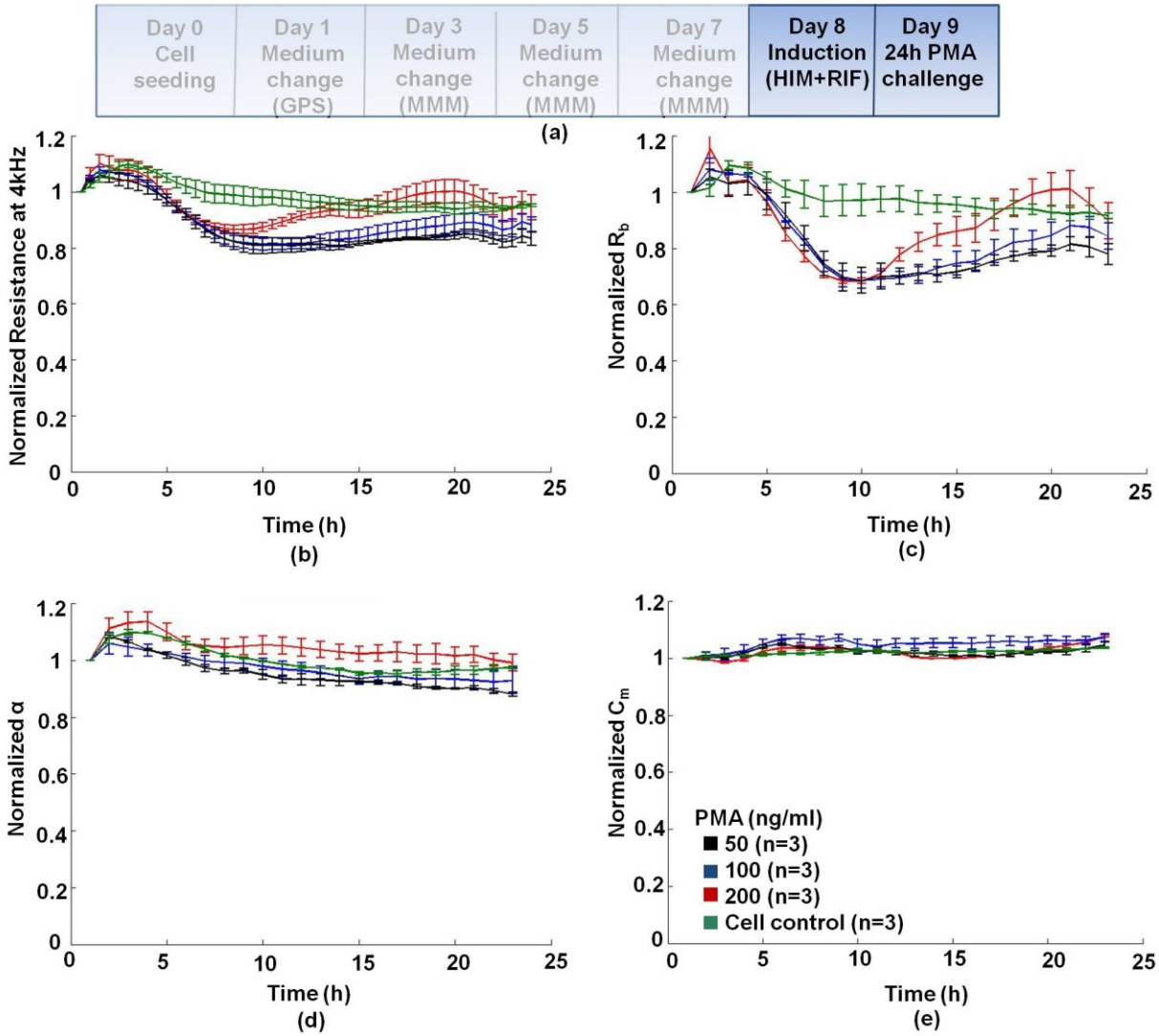

Figure 4.15: HepaRG tight junction disruption following PMA challenge (a) Normalized resistance initially decreased 20% followed by an increase back to pre-challenge resistance values; (b) R_b (cell-cell tight junctions): the only measured effect of the PKC-activator PMA was on R_b, which decreased by 30% at all doses tested, returning close to original values. (c-d) No effects were detected on either cell-electrode adhesion (α), or C_m (cell membrane integrity).

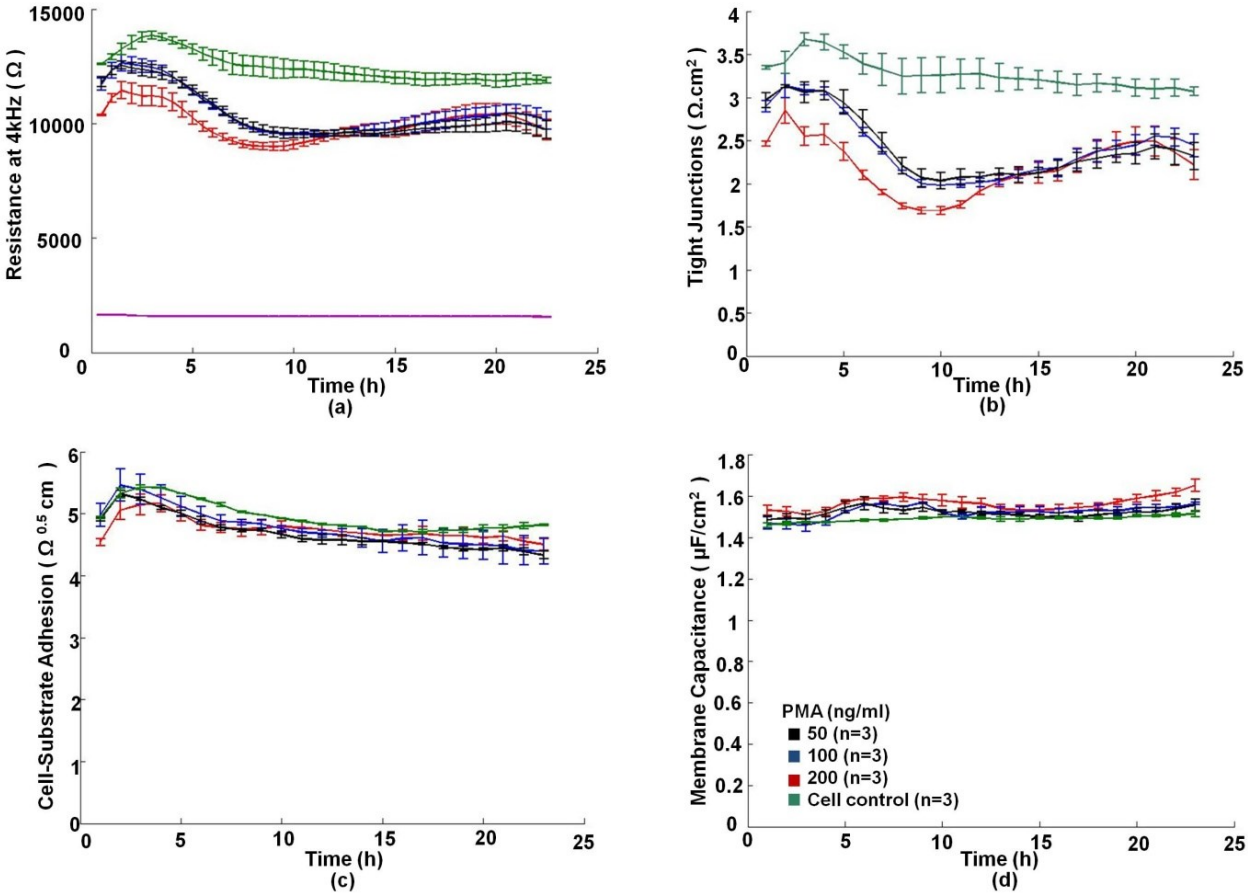

Figure 4.16: Non-normalized PMA dose response. (a) Non-normalized resistance initially showed a decrease following the introduction of phorbol-ester to the cell culture. This was followed by an increase back to the pre-challenge original values; (b) The only significant effect of phorbol-ester was on R_b (cell-cell tight junctions), which like the resistance decreased at all doses tested returning close to original values; (c-d) No effects were detected on either α or C_m.

PMA Challenge	Control	6 hrs	12 hrs	24 hrs
Resistance (Ω)				
50 ng/ml	8415.60 ± 137.35	7779.9 ± 143.9	6943.5 ± 116.6**	7447.1 ± 260.1*
100 ng/ml	8339.2 ± 151.1	7582.4 ± 296.5	6846.20 ± 94.17**	7666.5 ± 218.5
200 ng/ml	7546.90 ± 58.38	6803.7 ± 44.4**	6459.8 ± 146.2**	7509.1 ± 308.9
***R_b* (Ω.cm²)**				
50 ng/ml	2.970 ± 0.078	2.620 ± 0.089	2.09 ± 0.07**	2.43 ± 0.14*
100 ng/ml	2.90 ± 0.07	2.52 ± 0.02*	2.010 ± 0.057**	2.55 ± 0.10*
200 ng/ml	2.46 ± 0.03	2.010 ± 0.007**	1.770 ± 0.063**	2.49 ± 0.17
***α* (Ω^0.5cm)**				
50 ng/ml	4.80 ± 0.02	4.840 ± 0.076	4.610 ± 0.052	4.50 ± 0.05
100 ng/ml	4.93 ± 0.11	4.920 ± 0.075	4.660 ± 0.037	4.56 ± 0.18
200 ng/ml	4.530 ± 0.046	4.790 ± 0.082	4.790 ± 0.073	4.63 ± 0.08
***C_m* (µF/cm²)**				
50 ng/ml	1.480 ± 0.017	1.560 ± 0.032	1.520 ± 0.013	1.52 ± 0.02
100 ng/ml	1.470 ± 0.018	1.560 ± 0.006	1.510 ± 0.014	1.53 ± 0.02
200 ng/ml	1.530 ± 0.024	1.59 ± 0.01	1.550 ± 0.035	1.60 ± 0.02

Table 4.2: Non-normalized phorbol ester dose-response. The only significant effect of PMA was on cell-cell tight junctions (R_b); whilst no significant decrease was measured for either the cell adhesion parameter or cell membrane capacitance. * P<0.05; ** P<0.01: significantly different from control. The greyed areas indicate time points at which the model could be invalid due to cell death/detachment resulting in a non-confluent cell layer.

For R_b measurements however, both the 100 and 200 ng/ml doses showed a significant decrease at 6h; and at 12h all doses expressed a significant decrease in R_b (P<0.01). At 24h, the values of R_b increased for all doses returning close to the original values in the case of the highest dose (200 ng/ml), whereas the other doses (50 ng/ml, 100 ng/ml) still showed a less significant decrease (P<0.05). Figure 4.17 shows bar graphs describing the effect of PMA at 6h, 12h and 24h on HepaRGs.

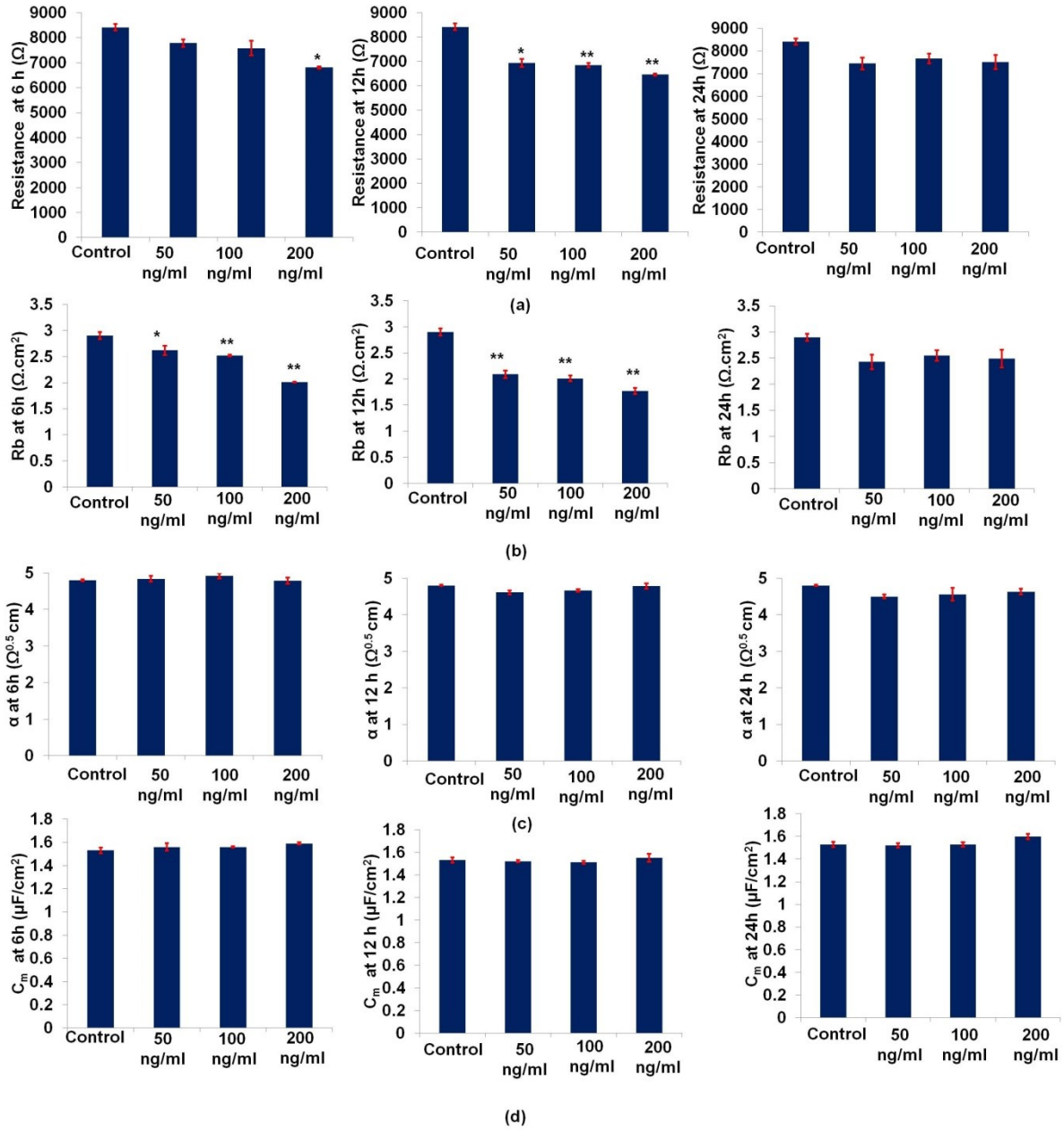

Figure 4.17: Non-normalized PMA dose response. Bar graphs showing the effect of PMA on the non-normalized parameters (a) Resistance , (b) R_b (c) α and (d) C_m at different time points (6, 12, 24h) of the toxicity assay. * P<0.05, ** P<0.01.

Biochemical hepatotoxicity assays were also performed at the end of the PMA challenge (24h). PMA was found to cause moderate increases of both ATP-content (Figure 4.18 (a)), and PrestoBlue live-cell viability (Figure 4.18 (b)). This might be due to hormetic effects (low dose stimulation) of the PKC activator, PMA.

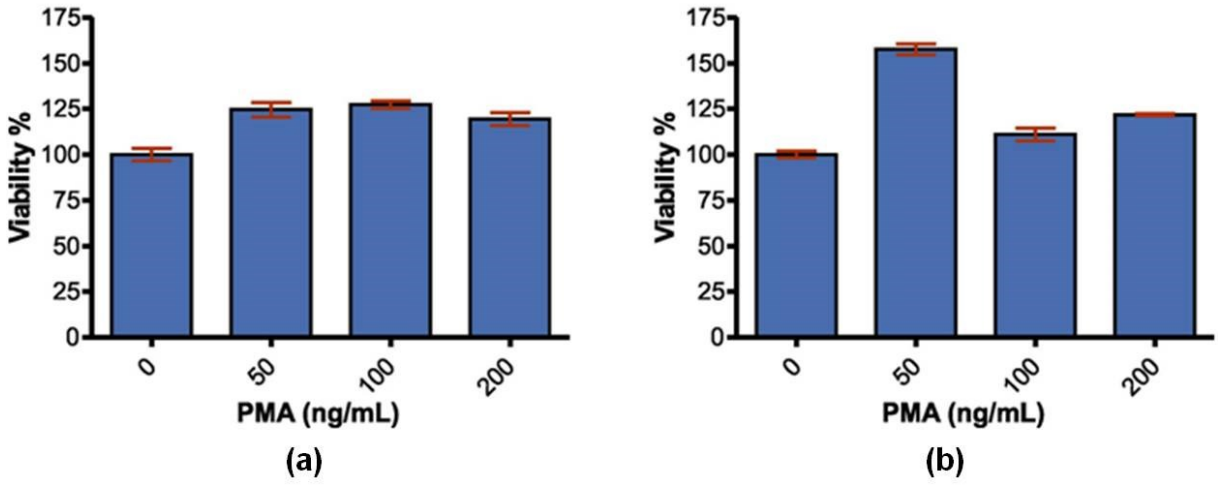

Figure 4.18: Parallel biochemical hepatotoxicity assays following 24h APAP challenge (a) Classic ATP-depletion endpoint assays.(b) PrestoBlue live-cell viability Prestoblue and ATP values are expressed relative to the levels found in control cells, arbitrarily set at a value of 100%.

4.3.3. NAPQI effects on TJs

Excessive production of the metabolite NAPQI is the major cause behind APAP hepatotoxicity [25]. Direct effects of different concentrations of NAPQI on tight junctions were therefore tested using impedance sensing. At a high dose of NAPQI (500 μM), normalized resistance showed an approximate 50% decrease over 20 hours, indicating a decline in cellular health (Figure 4.19 (a)). An abrupt (0-2 hours) and sustained (0-20 hours) disruption of TJs occurred, with a 50% decrease in the impedance parameter (R_b) after 6 hours (Figure 4.19 (b)). α also declined by 20% after 20 hours for the highest dose (Figure 4.19(c)). Minimal effects recorded on both R_b and α (at 125 and 250 μM), may reflect detoxification of NAPQI by intrinsic stores of glutathione (GSH), as high doses of APAP are required to deplete mitochondrial GSH.

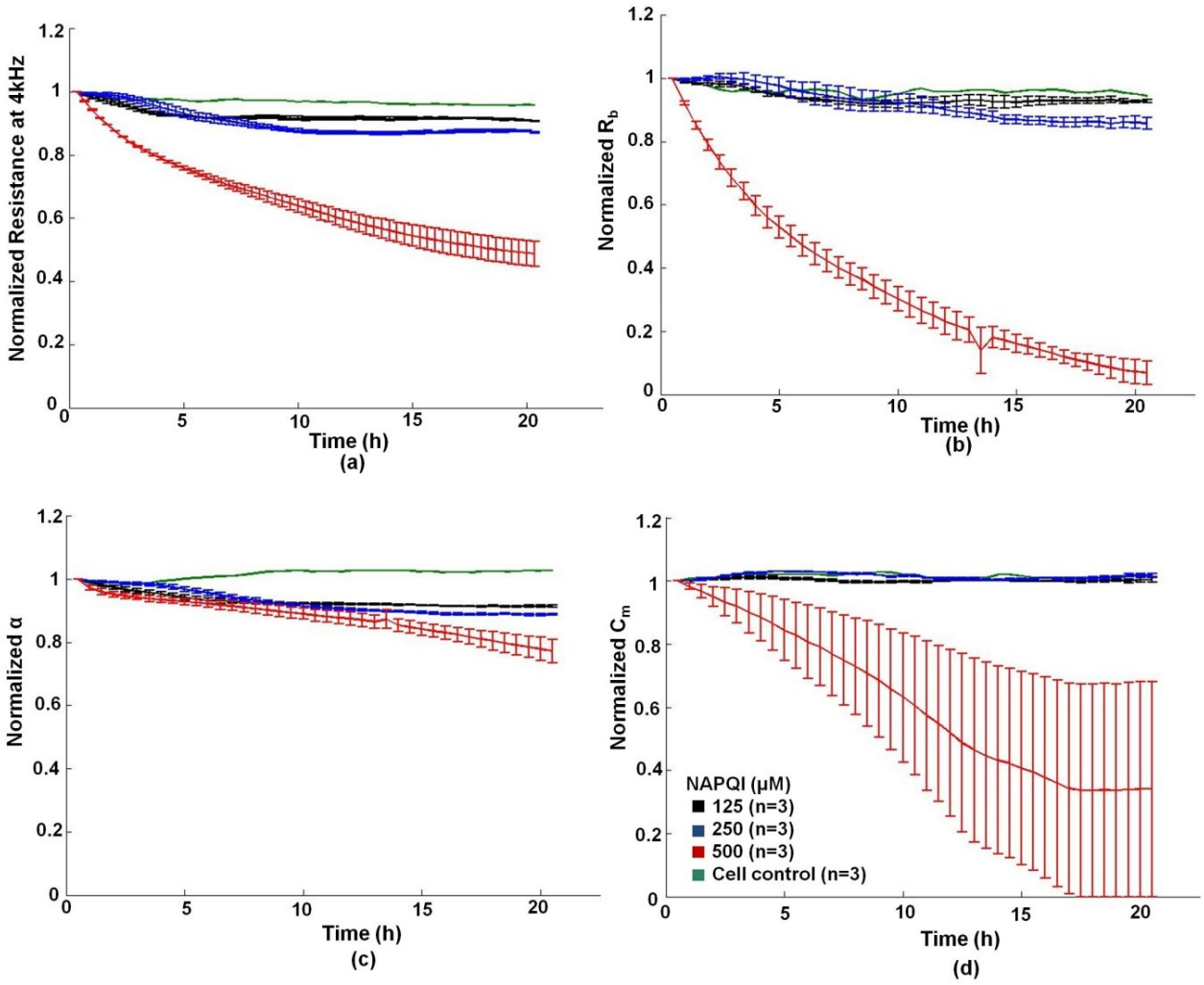

Figure 4.19: Effect of NAPQI on tight junctions. (a) Effect of NAPQI on normalized resistance, cell-cell junctions (b), cell adhesion (c) and cell-membrane integrity (d).

4.3.4. Other hepatotoxins

To demonstrate versatility of the HepaRG-based ECIS model, case studies demonstrating the potential utility of impedance biosensing were performed, incorporating impedance spectroscopic modelling in drug development. Different classes of drugs causing other types of liver injury, were tested on HepaRG cells. Specifically, dose-dependent real-time toxicity profiles of the model hepatotoxins amiodarone and Cyclosporin-A after acute exposure (0-24h).

i. Amiodarone

Following the same protocol used for APAP toxicity assay, amiodarone was added to the HepaRG culture medium with different concentrations (25, 50, 75 and 100 µM) and a 24h dose-response assay was conducted. amiodarone was found to affect the time course impedance in the highest dose of toxin tested (100 µM). Figure 4.20 (a) depicts the drop of 4 kHz resistance associated with the addition of 100 µM of toxin. Consequently a corresponding drop in R_b, α and C_m was observed at this concentration.

Significant effects of the lowest dose of amiodarone was found in the barrier function R_b after 10h of exposure; whereas both the cell adhesion parameter and the cell membrane integrity were unaffected.

ii. Cyclosporine-A

Cholestatic drugs, which induce leaky TJs, can generate toxic mechanisms (similar to APAP) in HepaRG cells, including ROS-mediated disruption of TJs. The immunosuppressive agent cyclosporine-A (CsA) is known to cause cholestasis [34]. CsA was added to HepaRG on Day 9 of culture with 10, 20, 30 and 40 µM concentrations and a 24h impedance-based toxicity assay was performed (Figure 4.21). A dose- dependent decrease in resistance was monitored after adding CsA. The main effect of CsA was on the cell-cell junctions. The decrease was dose dependent with no effect on R_b for the lowest dose (10 µM).

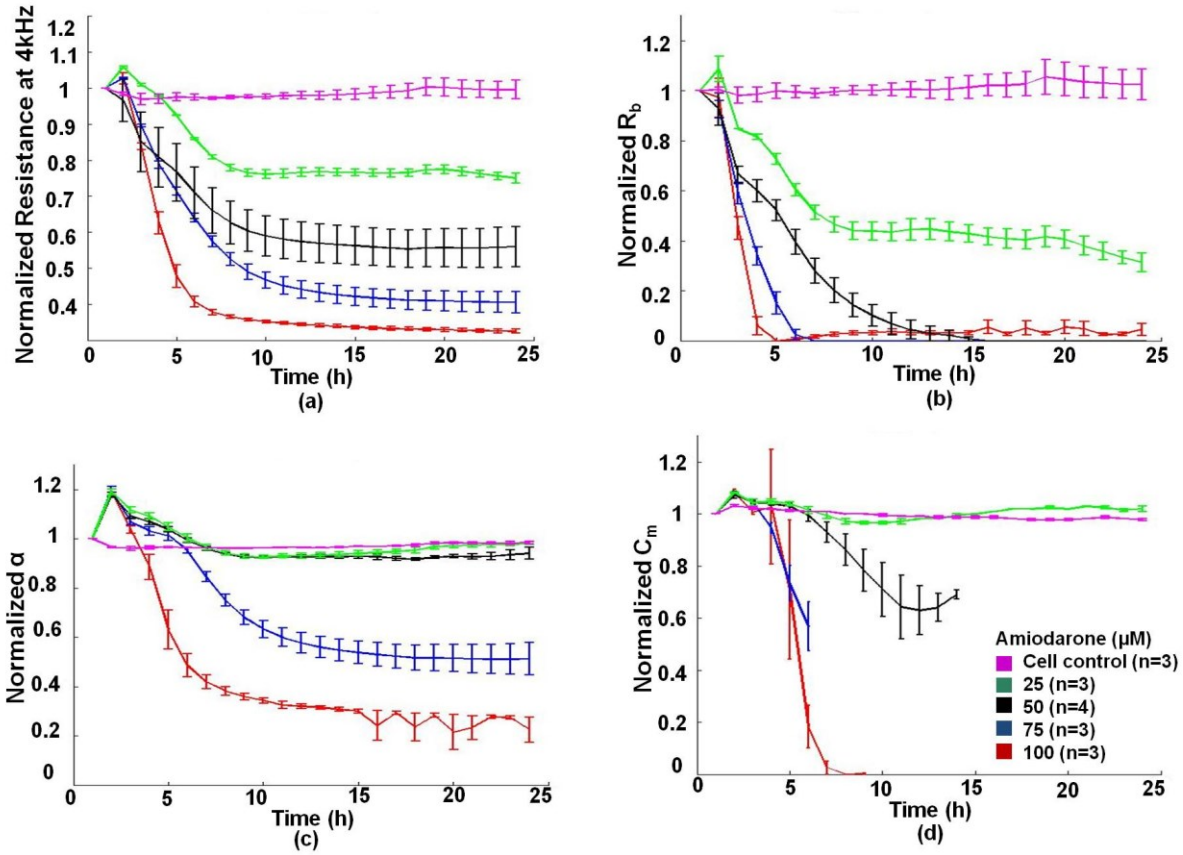

Figure 4.20: Amiodarone challenge. (a) Following amiodarone addition, a drop in resistance was observed in a dose dependent manner. (b) Effect on cell-cell junctions (R_b): amiodarone affects Rb in a dose-dependent manner. (c) Effect on cell-electrode adhesion: α decreases at high doses of amiodarone (75μM, 100μM) suggesting that cells detach from the electrode's surface depending on the dose used. (d) Effect on membrane integrity: the cell membrane is compromised depending on the dose with no effect at all for the low dose (25μM).

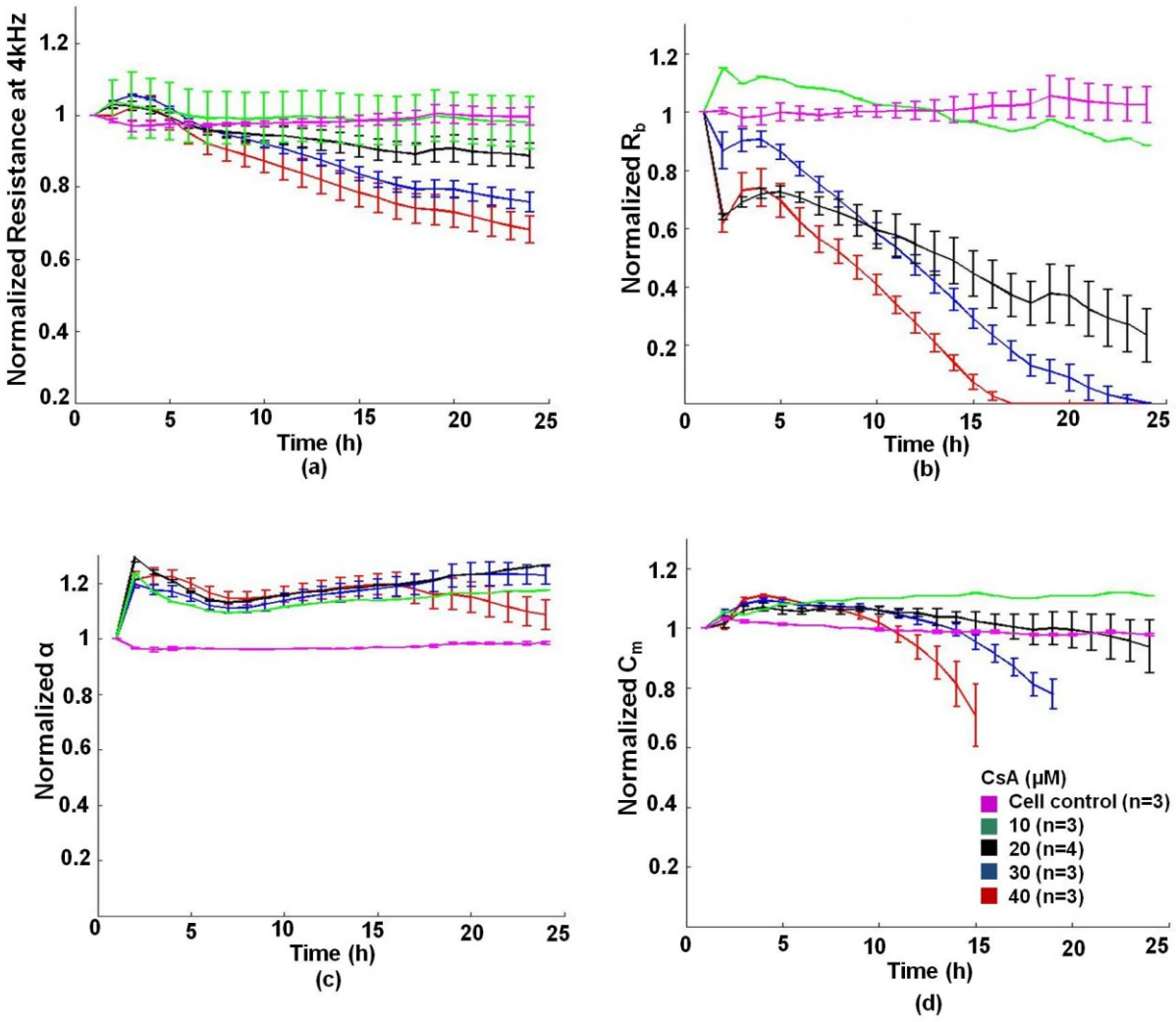

Figure 4.21: Cyclosporine-A challenge (a) A slight decrease in resistance was monitored after adding CsA which occurred in a dose dependent manner. **(b)** Effect on cell-cell junctions (Rb): the main effect of CsA was on the cell-cell junctions. **(c)** Effect on cell-electrode adhesion **(d)** Effect on membrane integrity

4.4. Monitoring sub-populations

As previously described in Section 4.2, HepaRG cells terminally differentiate into a hepatocyte:cholangiocyte co-culture on top of the ECIS 250 μm microelectrodes. In order to monitor responses from each sub-population separately, smaller sized electrodes (25, 50, 100 μm) were used. Clear differences in the measured impedances between the two populations at high frequency were monitored. The sub-populations were optically identified based on their morphology as described by the supplier (Biopredic international, Rennes, France).

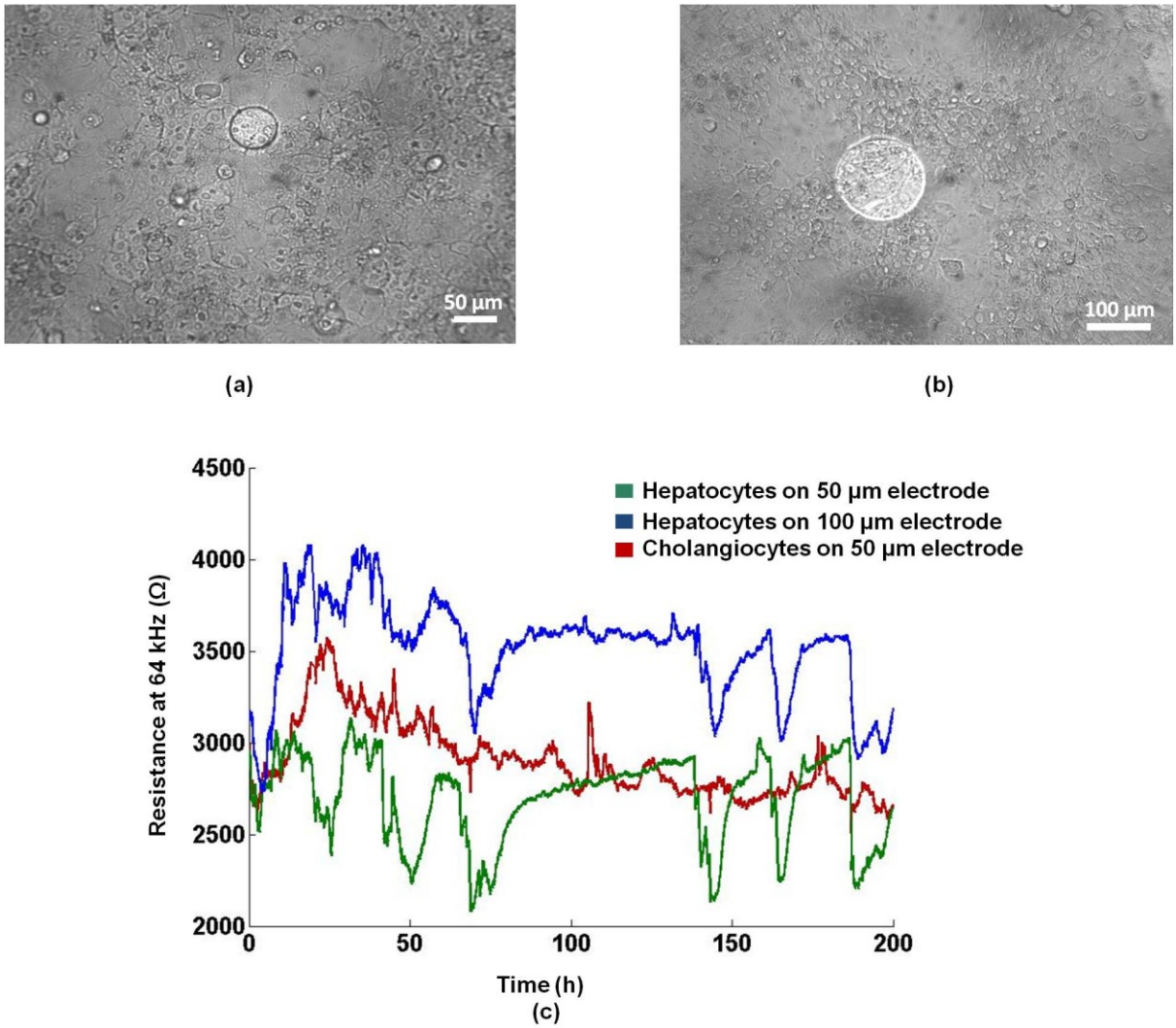

Figure 4.22: HepaRG sub-population ECIS monitoring. (a) Hepatocytes covering a 50 µm diameter microelectrode (b) Hepatocytes covering a 100 µm diameter microelectrode (c) Resistance at 64 kHz on 100 µm diameter electrodes, sampling hepatocytes in one well (blue) and Cholangiocytes in another well (red). Measurements from a 50 µM electrode sampling hepatocytes is also shown in green.

It was noticed that small electrodes sampling hepatocytes displayed 24h cycles of large peaks in impedance measurements (Figure 4.22). However, microelectrodes sampling only cholangiocytes did not show these peaks. Interestingly, the 24h cycles observed for hepatocytes disappeared when cultured with reduced serum (2% FBS). This ruled out environmental or equipment factors as the possible reason behind the observed cycles. An explanation for such measurements is that the small electrodes might be picking up a hepatocyte circadian rhythm behaviour. Larger electrodes (250 µm diameter) average the measurements of a larger group of cells, and that could be why the 24h cycle peaks were only monitored using small electrodes.

Biochemical assays will be needed to confirm if what is measured for hepatocytes is indeed due to a circadian rhythm.

4.5. Summary

This chapter described the first disease model-on-a-chip presented in this thesis. The ALF model employs a liver biochip approach integrating the hepatic progenitor cell line, HepaRG, with the impedance sensing platform, ECIS. After the establishment and characterization of the HepaRG-based ALF model, impedance spectroscopy was used to investigate the effect of the model hepatotoxins; paracetamol, amiodarone and Cyclosporine-A on the hepatic co-culture. Dose- and time- dependent responses to the tested drugs were observed. Moreover, impedance analysis and modelling showed how cell-cell tight junctions and cell-adhesion are compromised due to drug-induced toxic effects; revealing an unknown mechanism of paracetamol hepatotoxicity. The obtained results were confirmed using biochemical assays, immunofluorescence staining of tight junctional ZO-1 proteins as well as ultrastructural TEM imaging.

Smaller electrodes sampling a sub-population of the HepaRG co-culture showed differences in the measured impedance. While the impedance measurements of the hepatocytes sub-population displayed 24h cycles of large peaks, electrodes sampling only cholangiocytes did not share this phenomenon. Starvation of hepatocytes by reducing serum concentration seemed to demolish this response, suggesting that these 24h cycles might represent a circadian rhythm. More assays will be needed however to confirm that.

The ALF model-on-a-chip allowed for a non-invasive, quantitative assessment of the effect of hepatotoxins on tight junctions and tissue structure, providing an invaluable tool for pre-clinical drug studies and revealing previously unknown mechanisms underlying paracetamol toxicity; a temporal, dose-dependent disruption of tight junctions.

Chapter 5

Electrically-induced Injuries: An *in vitro* model-on-a-chip for age-related macular degeneration

In the previous chapter, the potential of impedance sensing in studying drug-induced injuries has been established. Impedance sensing can also be used to study electrically-induced injuries. These types of assays are usually referred to as electrical wound healing assays as they focus on studying cell migration during healing processes and regeneration. In this study, keratinocytes were initially used as a model for electrically-induced injuries to better understand ECIS wounding mode and the quantitative monitoring of cell regeneration and migration. ECIS electrical wounding assays were then used to model degeneration of retinal pigment epithelium associated with age-related macular degeneration (AMD). Moreover, in a preliminary study, electrical wounding was used to investigate the migration abilities of hepatocytes in order to gain more insight into the regenerative abilities of liver cells.

Finally, high density microelectrode arrays with high spatial resolution and different-sized, individually-addressed square microelectrodes were designed and fabricated in-house before being used for ECIS wound healing assays.

5.1. Optimization of ECIS wounding parameters

Wound healing is a naturally occurring response to tissue injury. Following an injury, cellular events take place to reconstitute and restore the tensile strength of injured skin. The ability of keratinocytes to renew and regenerate is well known, making this cell type a suitable candidate for cell migration studies. An adult human epidermal keratinocytes (HEKa) cell line was used for the initial electrical wounding experiments to establish an in-depth understanding of ECIS wound healing assays and optimize the wounding parameters.

ECIS 8W1E (8 wells, 1 electrode/well) arrays were used for the wounding experiments where each of the culture wells was seeded with 2500 cells/cm^2. The wounding process started after the establishment of a confluent cell layer, 4-7 days after seeding. In order to determine the wounding threshold, a trial and error experiment was conducted using previously established wounding parameters as an initial guide [84]. Table 5.1 shows the different wounding parameters used together with their effect on ECIS measurements and wound healing. Impedance data was modelled using the ECIS built-in model and the effect of wounding on the tight junctions, cell-substrate adhesion as well as the cell membrane capacitance was also investigated. It was noticed that current amplitudes < 3 mA did not cause complete cell death, reflected by the very fast cell recovery (~1-2h). Electroporation was suggested to occur under these conditions. Applying a wounding pulse for a long time led to no recovery after wounding, possibly due to thermal effects causing damage to the cells around the wound edges, therefore affecting their functionality and hindering the migration process. Moreover, low frequencies (<10 kHz) were shown to cause electrode damage if applied for a long time. After 3 independent experiments, it was concluded that wounding pulses of 3 mA at 40 kHz for 30s were suitable for studying HEKa migration and an average migration rate of 11.27 ± 0.53 μm/h was determined.

From Table 5.1, a formula predicting the severity of the wound for specific wounding parameters was developed as follows:

$$Wound\ Severity = \frac{Applied\ Current\ (mA) * Pulse\ duration\ (s)}{Frequency\ (kHz)} \quad (5.1)$$

For each cell type, a threshold using the above formula can be determined, below which electroporation is most probable to take place and above which no wound healing is expected. It has to be noted that trial and error experiments still have to be performed first in order to determine such a threshold for a specific cell line. Moreover, slight differences in healing times might occur even when using the same wounding threshold.

Figures 5.1 (a) and (b) show the resistance and capacitance measurements accompanying keratinocytes wound healing. It is worth noting that while the resistance measurements will decrease with cell death, as more current will be able to flow freely through the culture well, the capacitance measurements will on the other hand increase. This is because the capacitance arising due to the cell dielectric properties contributes to the total impedance in a reciprocal manner according to Kirchoff's law, i.e. the capacitance measurements will decrease with cell attachment and increase with cell detachment and/or death. Although the HEKa impedance measurements after wounding dropped close to the level of the cell-free electrode (~2000 Ω), the cells did not completely detach from the electrodes. This behaviour has been reported for other cell types [84].

Trial	Current (mA)	Frequency (kHz)	Time (s)	Effect on R (%)	Effect on C (%)	Effect on R_b (%)	Effect on α (%)	Effect on C_m (%)	Healing time (h)	Wound Severity
1	1	40	0.2	No effect						0.005
2	1	40	1	No effect						0.025
3	0.6	4	1	No effect						0.15
4	0.4	2	1	No effect						0.2
5	0.3	1	1	16.6% decrease	14% increase	51.23% decrease	25% decrease	50% decrease	2	0.3
6	2.5	40	10	50% decrease	30.7% increase	100% decrease	41.6% decrease	14.2% decrease	6	0.625
7	3	40	10	56% decrease	46.4% increase	100% decrease	35% decrease	27.5% decrease	7	0.75
8	3	100	30	55% decrease	43% increase	50% decrease	75% decrease	36.3% decrease	8	0.9
9	3	64	30	71% decrease	60% increase	100% decrease	32.4% decrease	18% decrease	9	1.406
10	3	40	30	70% decrease	28.5% increase	100% decrease	100% decrease	100% decrease	11	2.25
11	3	40	30	70% decrease	39% increase	100% decrease	70% decrease	40% decrease	10	2.25
12	3	40	30	73% decrease	65.5% increase	100% decrease	100% decrease	100% decrease	12	2.25
13	3	64	60	74% decrease	66.6% increase	100% decrease	70% decrease	100% decrease	11	2.8125
14	3	64	60	70% decrease	43.5% increase	100% decrease	60% decrease	100% decrease	10.5	2.8125
15	3	64	60	75% decrease	75% increase	100% decrease	100% decrease	100% decrease	11.2	2.812
16	3	40	60	75% decrease	70% increase	100% decrease	100% decrease	100% decrease	12	4.5
17	3	40	60	61.5% decrease	64.2% increase	100% decrease	100% decrease	100% decrease	11	4.5
18	3	40	125	75.7% decrease	70.5% increase	100% decrease	100% decrease	100% decrease	No recovery	9.375
19	3	40	180	75% decrease	71.4% increase	100% decrease	100% decrease	100% decrease	No recovery	13.5
20	3	40	180	74.2% decrease	34% increase	100% decrease	100% decrease	100% decrease	No recovery	13.5
21	3	40	300	66.6% decrease	65.7% increase	100% decrease	100% decrease	100% decrease	No recovery	22.5
22	3	20	180	71.4% decrease	66.6% increase	100% decrease	100% decrease	100% decrease	No recovery	27
23	3	10	180	Electrode was damaged						27
24	3	40	3 pulses of 125s	75% decrease	60 % increase	100% decrease	100% decrease	100% decrease	No recovery	28.125

Table 5.1: Trial and error wounding parameters. After HEKa reached confluency, different wounding parameters were applied to each of the culture wells. The healing process was monitored through ECIS impedance measurements in real-time for 24h.

In these cases, it is suggested that cells from the wound edges migrate underneath the dead cell layer to close the wound. Furthermore, the possibility of wounding the cell layer using a train of short pulses using the electric fence set up was explored. Fencing was applied for 20 minutes, lysing the cells on top of the electrode. Impedance measurements dropped close to that of a cell-free electrode followed by a 16h recovery. However, the cells still did not detach from the electrodes. In order to confirm cell death, viability staining was performed using Ethidium Bromide (AO/EB). Dead cells on top of the microelectrodes stained red while the healthy cells in the rest of the wells were stained green. DAPI was also used for nuclei staining.

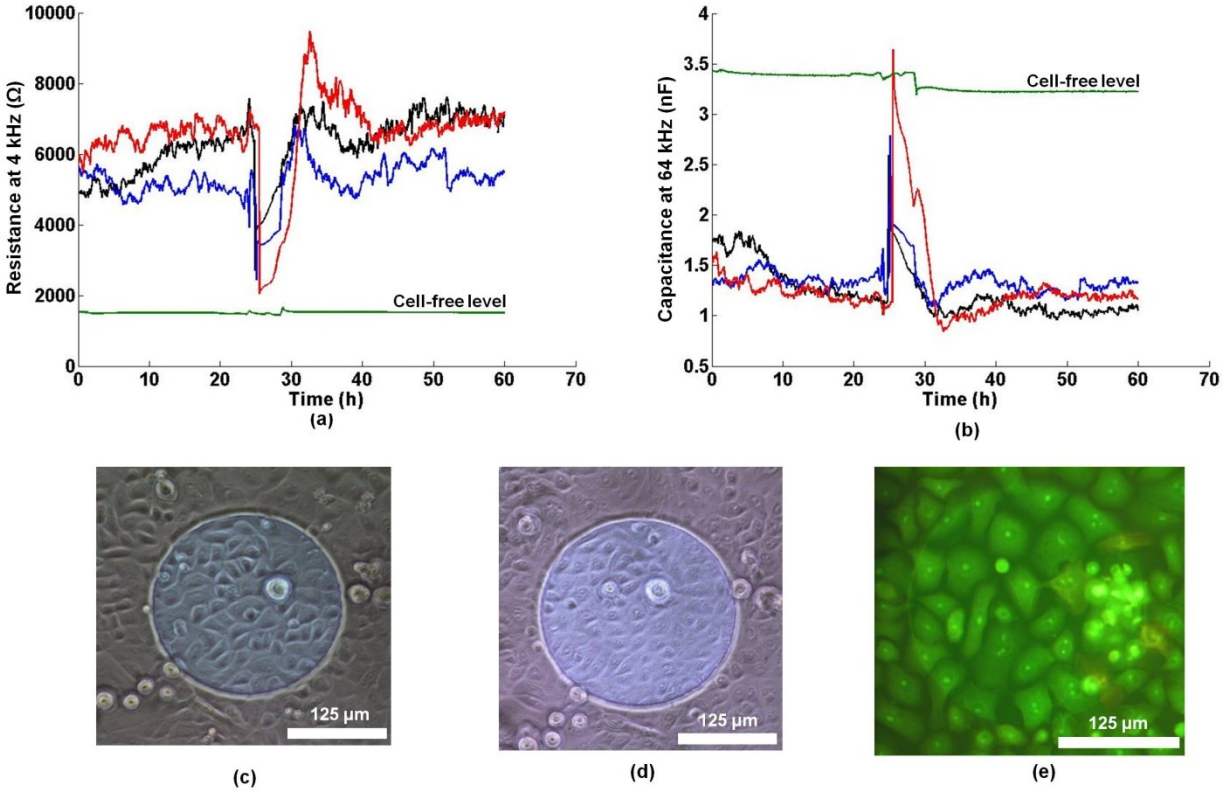

Figure 5.1: Keratinocytes ECIS wounding assay. (a) Resistance measurements during wound healing after wounding using different wounding parameters. (b) Capacitance measurements during HEKa healing after wounding the cells using different wounding parameters. (c) Confluent HEKa on ECIS microelectrodes before wounding. (d) HEKa after wounding with a pulse of 3 mA, 40 kHz for 60s. (e) AO/EB staining showing living cells (green) on top of a microelectrode after wound healing.

5.2. hiPSCs-based ECIS model of macular degeneration

5.2.1. Establishment and Characterization of the AMD model-on-a-chip

The dysfunction of retinal pigment epithelial (RPE) cells, RPE degeneration and the decline in their wound healing abilities are the main implications in age-related macular degeneration (AMD). In this work, ECIS electrical wounding assays have been used to mimic the loss of RPE in AMD. Induced pluripotent cells were successfully derived from a patient with late-onset retinal macular degeneration (LORMD) and one unaffected sibling according to a previously published protocol [334, 335] and as briefly explained in Appendix E. In each case, the cells were differentiated towards RPE cells before being plated on ECIS microelectrode arrays (Figure 5.2 (a)). Final RPE maturation was completed on the microelectrode arrays using a stepped 25-day protocol that progressively moved towards a serum-free medium (Figure 5.2 (b)). The hiPSC-RPE control and case cell lines were plated at confluency onto ECIS Medusa arrays with a density of 100,000 cells/cm^2 on day 0. Retinal differentiation medium (RDM) was used as the culturing medium with the concentration of fetal bovine serum being changed from 10% initially, to 2% for days 2-5, and then to 0% from day 6 onwards. The medium was changed every other day until the maturation of RPE was achieved.

Real-time quantitative monitoring of the spectroscopic complex impedance, with a resistive and capacitive component, was performed throughout the RPE maturation phase by acquiring multi-frequency data points at a 160s interval. Generally, the method of Wegener et al. [12], in which the resistance is measured at medium frequencies while the capacitance measurements are recorded at high frequencies, was followed. The resistance in that case mainly reflects the establishment of cell-cell junctions and cell-substrate adhesion, while the capacitance measurements made at high frequencies corresponds linearly to cell coverage. According to

Figure 3.3 in Chapter 3, the monitoring frequencies chosen for resistance and capacitance measurements, providing highly sensitive measurements, were 4 kHz and 64 kHz respectively.

The 25-day time-course maturation process was found to be highly robust and reproducible for both case (N= 9) and control wells (N= 11) thus offering a criterion by which to reject faulty *in vitro* models. The changes in the resistance measured at 4 kHz that characterized RPE maturation and were associated with initial cell spreading, morphological changes and barrier formation are shown in Figure 5.2 (c). First a steep increase in resistance that peaked at 15 kΩ was observed on day 2 of culture and this was followed by a slow decrease over 5.5 days to a plateau with an average value of 8.5 kΩ. The formation of the confluent cell layer and the hiPSC-RPE differentiation stages were also observed under a microscope. It was noticed that the drop in ECIS measurements following the peak in resistance was mirrored by a change in cell morphology from fibroblastic-like cells towards polygonal cobble-stone mature epithelial cells. After RPE maturation, an automated electrical wound healing assay was performed and subsequent cell migration associated with healing phase was monitored. Before conducting the electrical wounding assay, the establishment and maturation of the RPE layer on top of the microelectrodes was confirmed using biochemical assays. Immunostaining showing the expression of the transmembrane RPE specific protein Bestrophin(red), Ezrin(green) and DAPI(blue) illustrated markers of mature RPE (Figure 5.2 (d)) , while RT-PCR revealed that both case and control hiPSC-RPE lines expressed global epithelial and RPE specific markers, including the phagocytosis marker MERTK, the basal marker BEST1, the apical membrane associated marker Ezrin, the pigmentation marker PEDF(pigment epithelium derived factor), the visual cycle marker RPE65 as well as C1QTNF5 and ACTIN (Figure 5.2 (e)).

5.2.2. Electrical wound healing assays of the hiPSC-RPE layer

As previously described, a mature RPE layer was established after 25 days of culture, which entirely covered the bottom of the culture well including the gold microelectrodes. An RPE injury (analogous to focal RPE loss observed in macular degeneration) was then created as a circular wound with an elevated electrical pulse in the microelectrode area. Then the wound healing process was monitored for both case and control cell lines with ECIS.

Electrical pulse parameters have been optimized through trial and error experiments. A 3 mA current pulse at 40 kHz applied for 30 seconds was found to cause cell death while preserving the microelectrode integrity. Figure 5.3 shows the corresponding drop in R_{4kHz} that followed the electrical wound. R_{4kHz} reached a value of 2600Ω corresponding to a cell-free electrode. This indicated cell death. Light microscopy confirmed that some cells detached from the microelectrode while the few remaining were stained positively with trypan blue indicating irreversible electroporation and death.

Wound healing was then monitored until the RPE layer fully recovered (5 days), and was characterized by two distinct phases (Figure 5.3 (a)). First, the cells from the wound edges migrated underneath the layer of dead cells in a radial pattern to close the wound. They repopulated the microelectrode with a characteristic steep increase in resistance followed by a peak that indicated the end of cell migration. Then a maturation phase was observed where the resistance slowly decreased to a plateau in a similar way to that described for early RPE maturation. Light microscopy indicated that once cell migration was complete, elongated cells switched back to a cobblestone morphology indicating RPE maturation at the end of this phase.

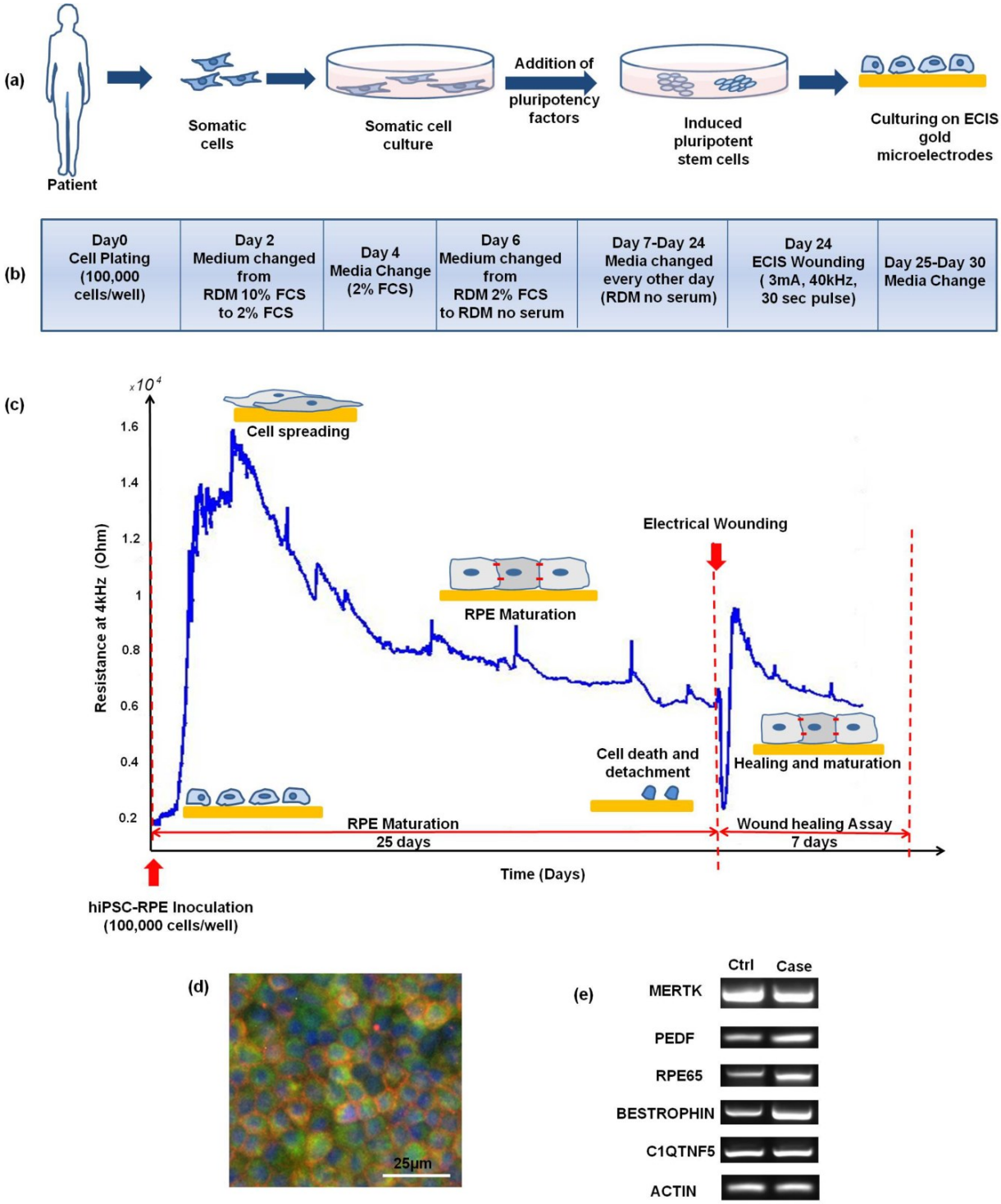

Figure 5.2: Development and characterization of the hiPSC-RPE model on ECIS microelectrodes. (a) Patient's fibroblasts were expanded and reprogrammed to a pluripotent state before being differentiated to RPE. Cells were plated (day 0) on ECIS microarrays. Cells were then allowed to mature for an additional 3 weeks period according to the timeline protocol shown in (b). From day 1 the spectroscopic complex impedance was monitored in real-time throughout RPE maturation and is displayed in (c) as the resistance at 4kHz. It showed an increase with cell spreading and maturation followed by a decrease reflecting changes in cell morphology and size. After 25 days an automated electrical wound healing assay was performed and subsequent cell migration associated with healing phase was monitored. (d) Immunostaining showing the expression of the transmembrane RPE specific protein Bestrophin (red), Ezrin (green) and DAPI (blue) illustrated markers of mature RPE. (e) RT-PCR revealed that both case and control hiPSC-RPE lines expressed global epithelial and RPE specific markers [55].

The mean and standard error of the migration rate for all case and control cell lines is shown in Figure 5.3 (d). It shows that wounding was a reproducible process, producing a defined and concise wound every time. When calculating the migration rate as the time to repopulate a 250 µm electrode, it was found that the control cell line had a significantly ($P< 0.01$) higher migration rate (10.69 ± 0.21 µm/h) than the case cell line (8.60 ± 0.46 µm/h).

The corresponding capacitance measurements at 64 kHz are shown in Figure 5.4. The capacitance increased with cell wounding, close to the value of the cell-free electrode, before decreasing again with the healing process to reach the pre-wounding values. The capacitance measurements of the control cell lines showed a faster decrease reaching a plateau before the case cell line. This was attributed to the control cell line having a higher migration rate than the case cell line.

In order to gain more insight into the healing kinetics, R_{4kHz} was fitted to a sigmoid during the migration phase as exemplified for one case and one control cell line in Figure 5.3 (c). No significant difference ($P= 0.057$) was found between the hill slope of the control (0.54 ± 0.07) and that of the case cell lines (0.41 ± 0.04) (Figure 5.3 (e)). However, there was a significant difference between the case and control at the sigmoid inflection point. Figure 5.3 (f) shows that the inflection point had a significantly ($P= 0.0009$) higher value for the case cell line (8.94 ± 0.29 h) than that of the control cell line (7.06 ± 0.27 h). These results suggest that the lower migration rate of the case cell line might be attributed to a delay in initiating migration. Once the cells rearranged themselves radially and started to move, they migrated with a speed similar to that of the control cell line.

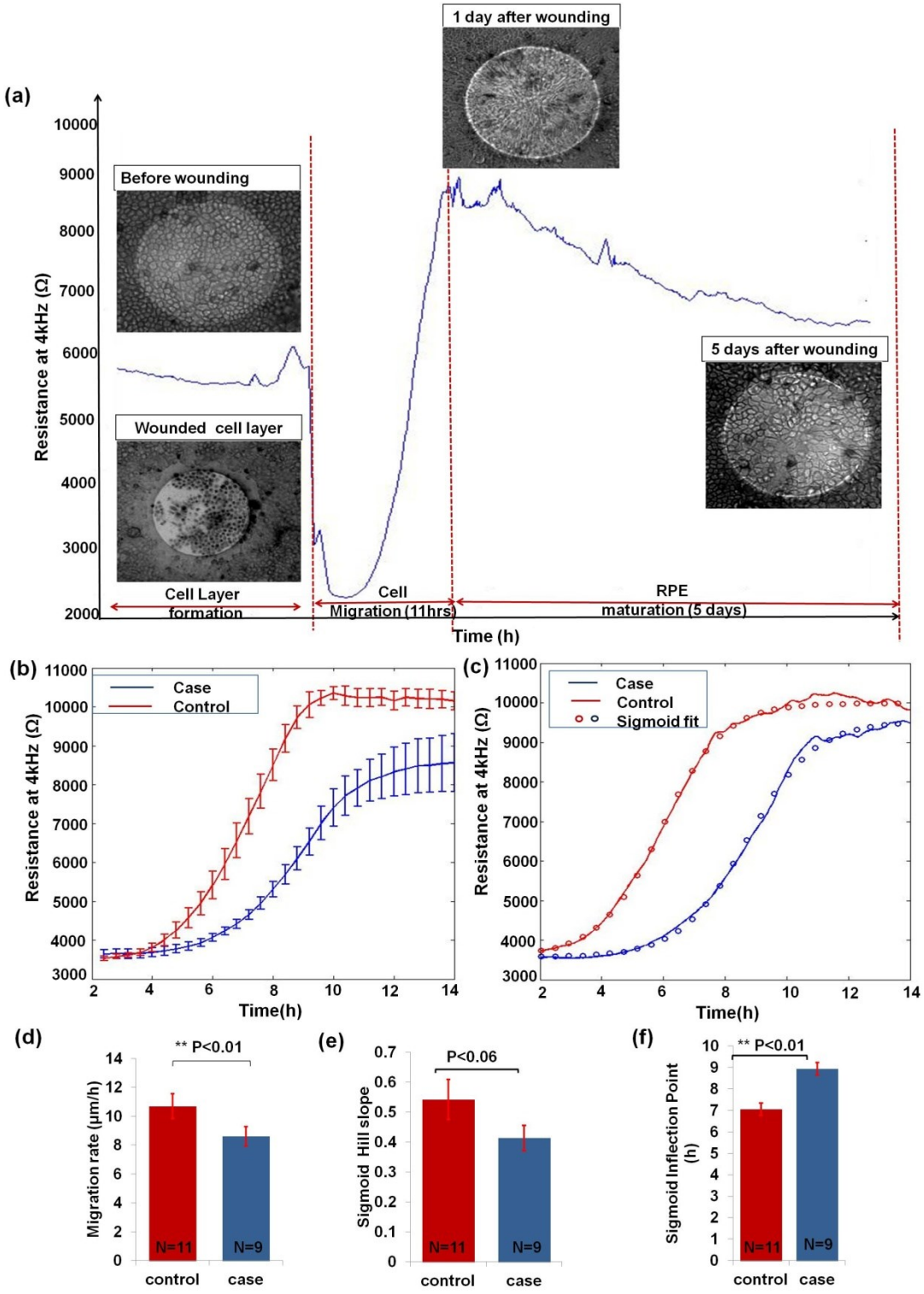

Figure 5.3: hiPSC-derived RPE ECIS Wound Healing Assay. (a) Wounding hiPSC-RPE: The resistance kinetics for one case study after wounding and during healing were monitored. Trypan blue was used to stain dead cells that did not detach from the electrodes. (b) Control vs. Case migration: wounding was a reproducible process, producing a defined wound every time. The control cell line (N= 11) migrated faster than the case cell line (N= 9) to achieve wound healing. (c) Sigmoid fitting: the case and control healing curves were fitted to a sigmoid curve. The parameters of the fitting curve were further analyzed. (d) Migration rate bar graph: the control migration rate was 10.69 ± 0.21µm/h while that of the case cell line was 8.60 ± 0.46 µm/h. The two rates were significantly different (P= 0.0046). (e) Sigmoid hill slope bar graphs: the difference between the control and case hill slopes were not found significantly different. (f) Sigmoid inflection bar graphs: inflection points were found significantly different [55].

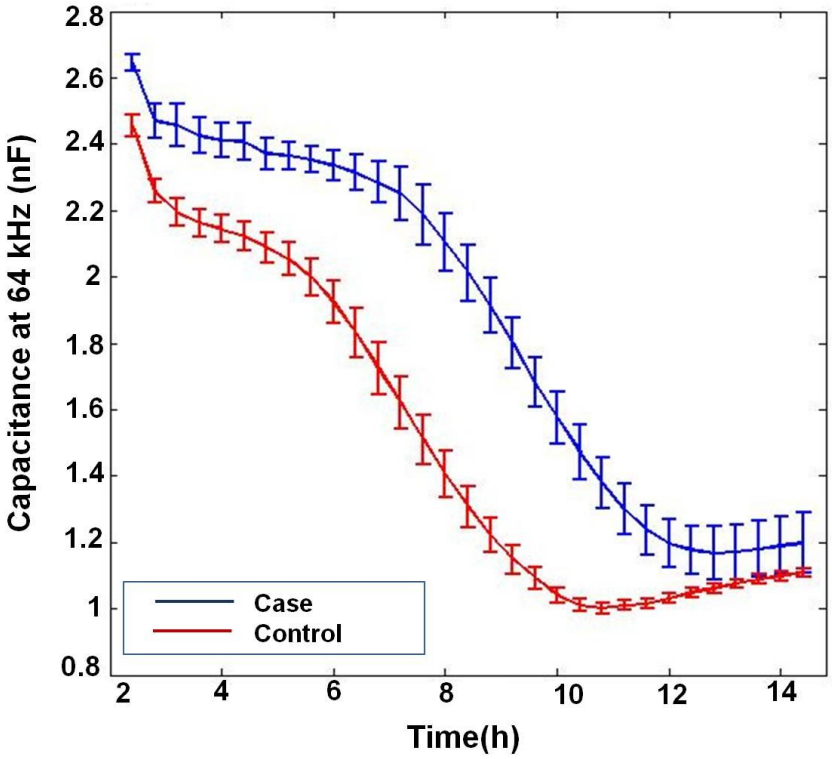

Figure 5.4: Capacitance measurements of hiPSC-RPE migration. The capacitance measurements of the control cell lines showed a faster decrease reaching a plateau before the case cell line. This was attributed to the control cell line having a higher migration rate than the case cell line.

5.2.3. Observed similarities between healing and maturation processes

During the wound healing process, a transitional stage was observed in which cells showed a change in morphology which was similar to the changes accompanying the early RPE maturation (Figure 5.5 (a)), although on a much shorter time scale. Cells around the wound edge went through a transition from cuboidal to elongated cells before returning to their original polygonal morphology after repopulating the electrodes (Figure 5.5 (b)). This was accompanied by a decrease in resistance when the epithelial stage was reached. Increased fluctuations were also observed for these transitional phases. A moving variance analysis of the ECIS measurements was applied after wounding following the work of Schneider et al. [336] (Figure 5.5 (c)). The analysis clearly shows the transition from high cellular activity (high variance

phase) to a more quiescent state (low variance). No significant differences were found between the case and control cells with an average half-time transition of 11.5h. These data suggest that the ability of the case cells to return to the original RPE morphology after completing migration was not affected by the LORMD mutation. Cell morphology and impedance data strongly suggested that cells were able to close the wound through integrin-mediated "mesenchymal" migration [337].

5.2.4. Cell-substrate adhesion properties

One of the advantages of the tissue-on-a-chip approach is the ability to exploit the quantitative impedance data collected throughout RPE maturation and wound healing.

The first monitored difference between the control and case cell lines was at the ECIS attachment and spreading phase during the first 24 hours after culture. R_{4kHz} measurements showed that the case cell line attached to the electrodes and spread to form a confluent layer more readily than the control cell line (Figure 5.6 (a)). The corresponding capacitance (C_{64kHz}) measurements during the same period are shown in Figure 5.7.

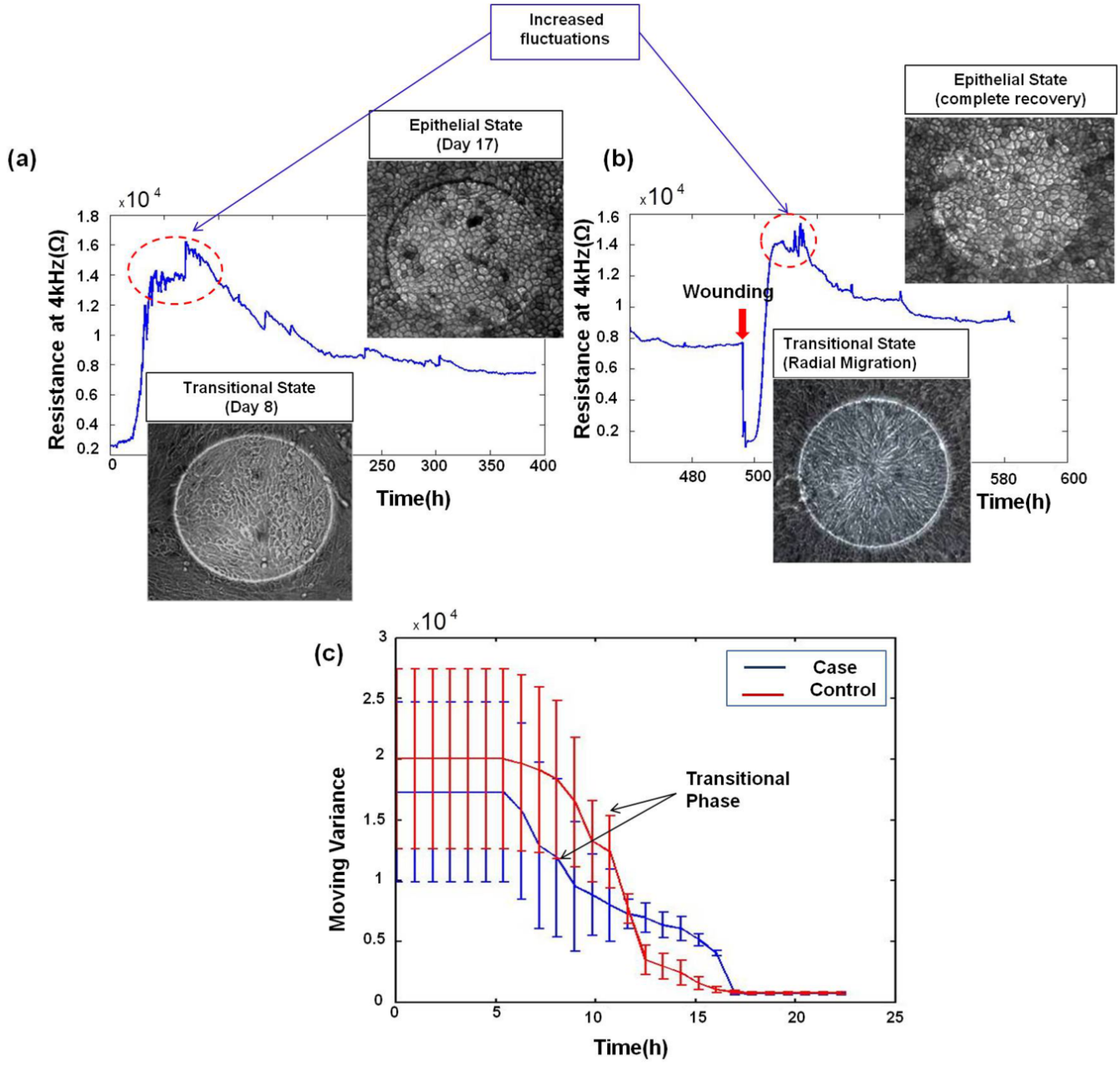

Figure 5.5: Similarities between early RPE maturation and healing processes. (a) Differentiation and morphology changes: case and control cell lines changed their morphology from a fibroblastic-like to a cuboidal shape during the differentiation and maturation stage. This was accompanied by an increase in measurement fluctuations. (b) Wounding and morphology changes: unwounded cells changed morphology from cuboidal to elongated to migrate and repopulate the electrodes. The reverse process then occurred after closing the wound. (c) Moving Variance showed a clear transition phase associated with a transition from an elongated to a cuboidal morphology [55].

As the case and control cell lines were seeded at confluency on the microelectrode arrays, the first 24h of measurements were considered to constitute an impedance-based adhesion assay revealing data on the cell-substrate adhesion. Generally in these types of assays, the microelectrodes are entirely covered with a tight layer of cells that upon attachment to the electrode surface causes a significant increase in the measured resistance. The difference in the measurements between different cell lines can therefore be attributed to cell attachment and adhesion to the substrate [12].

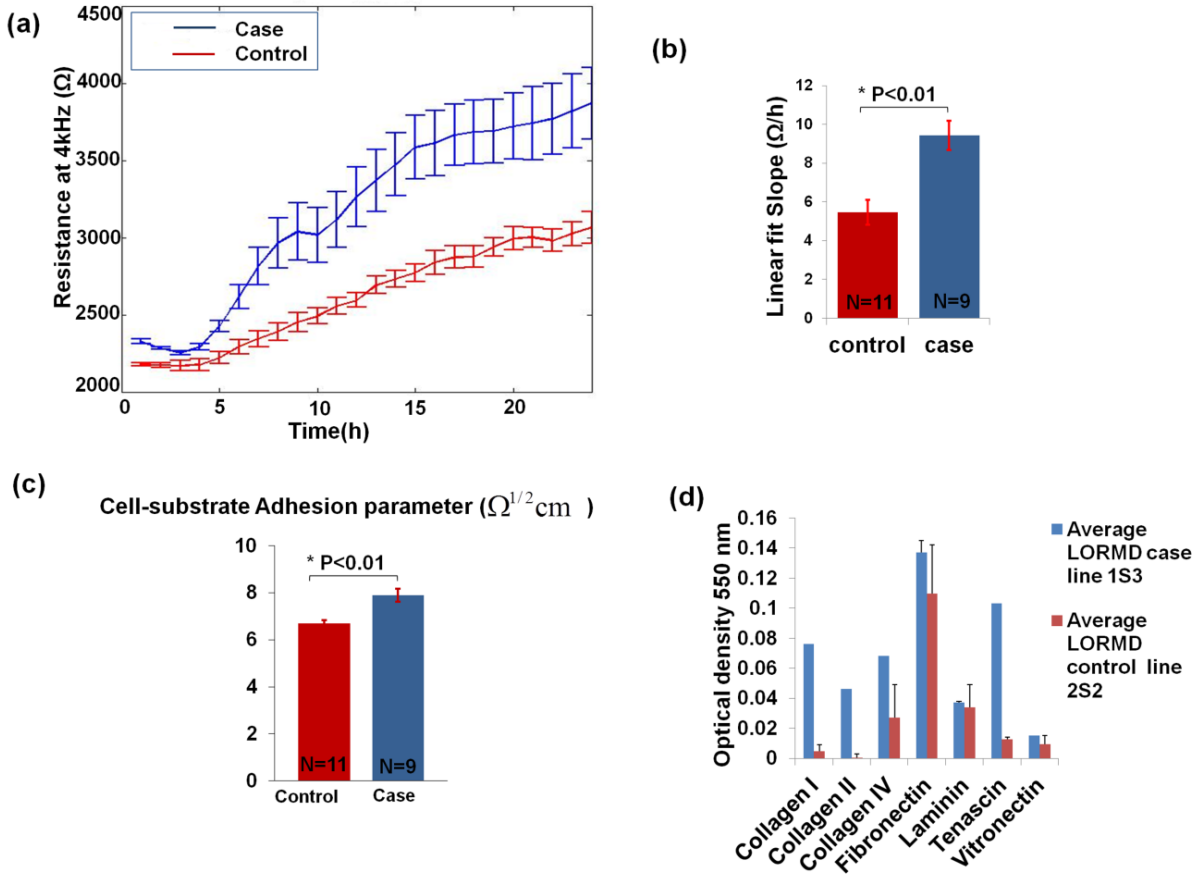

Figure 5.6: Case vs. Control Cell-Substrate Adhesion. (a) hiPSC-RPE ECIS adhesion assay: comparing the resistances of the case and control cell lines during the first 24 hours of culture, showed how the case cell line attached more quickly to the electrodes and were able to reach a plateau faster than the control cell line. (b) Attachment slope: the slopes of the attachment curves for both case and control cell lines were calculated through a linear fit. The slope was significantly higher for the case cell line ($P<0.01$) which was consistent with the case cells arriving at a plateau before the control cells. (c) Cell-substrate adhesion parameter (α): α was determined at t=160h (day 6) for both case and control cell lines. α of the case cell line was significantly higher than that of the control cell line ($P= 0.002$), indicating that the case cell line obtained a higher cell-substrate adhesion. (d) Adhesion biochemical assay: the case cell line showed stronger adhesion to various ECM proteins than the control cell line [55].

For further analysis, the slope of each of the attachment curves was fitted to a linear model and they were found to be significantly different ($P<0.01$) with a value of 5.45 ± 0.64 Ω/h for the control and 9.43 ± 0.76 Ω/h for the case cell line (Figure 5.6 (b)). After this attachment phase however, the case and control cell lines followed similar kinetics throughout the differentiation and maturation phases (Figure 5.8).

To further investigate the potential role of cell adhesion, the ECIS model was used to determine the cell-substrate adhesion parameter (α) after 7 days of culture (t= 160h) (Figure 5.6 (c)). Again the case cell line showed significantly ($P<0.01$) higher adhesion ($7.80 \pm 0.28\Omega^{0.5}$cm) than the control cell line ($6.50 \pm 0.15\Omega^{0.5}$cm).

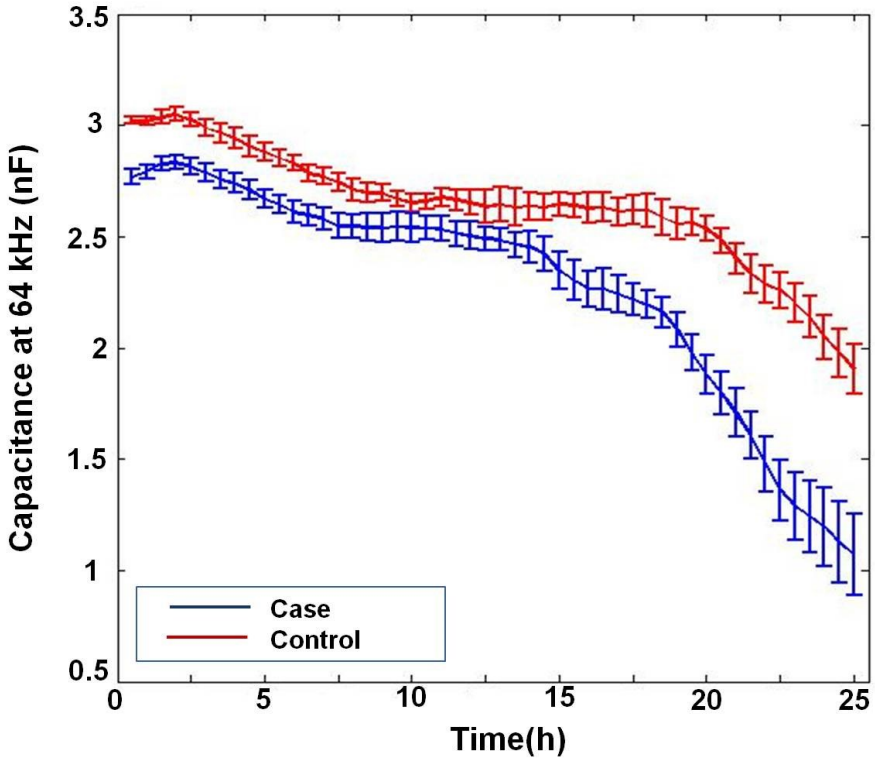

Figure 5.7: Attachment and Spreading Capacitance. During the attachment phase, the capacitance of the case cell line decreased faster than that of the control cell line suggesting that they expressed a stronger adhesion to the electrode surface.

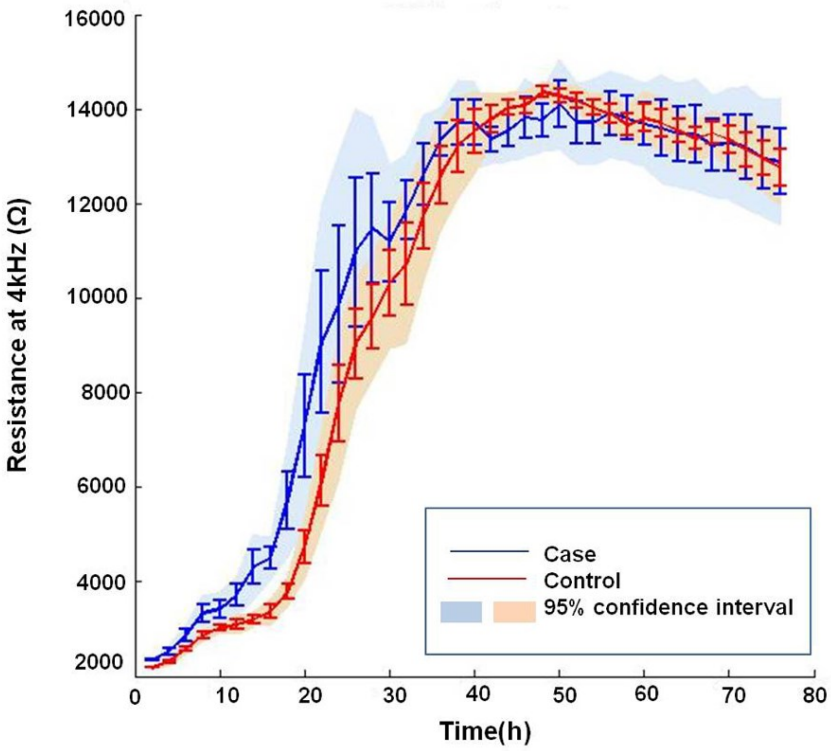

Figure 5.8: Differentiation and maturation kinetics. During the attachment phase (first 24h), the case cell line adhered to the microelectrodes faster than the control cell line expressing a higher resistance and reaching a plateau first. After this phase, both the case and control cell lines followed a similar trend during differentiation and maturation.

These findings were confirmed by a biochemical adhesion assay (Figure 5.6 (d)) that showed a clear difference between the adhesion properties of the case and control cell lines. The case line showed a significantly higher adhesion to ECM proteins (including collagen IV and tenascin) than the control cell line. It is worth mentioning that for the case and control cell lines cultured on ECIS arrays, the microelectrodes were coated with a mixture of proteins present in serum prior to culture.

Finally, to explore further the link between cell adhesion and cell migration, electrical wounding of an additional RPE cell line was conducted. The immortalized cell line hTERT-RPE1 was chosen for this study as it is regularly used for *in vitro* RPE migration assays despite its reported limitations in reflecting *in vivo* behaviour [338]. After hTERT-RPE1 reached

confluency, an ECIS wound healing assay was conducted and the healing rate and adhesion properties were compared to that of the hiPSC-RPE. The wounding parameters for hTERT-RPE1 were 3 mA, 40 kHz, 30s. In contrast to the hiPSC-RPE, the wounded cells completely detached leaving a clear electrode, which already suggested that the cells adhered less to the electrodes (Figure 5.9). Comparing the cell-substrate ECIS parameters of the different cell lines showed that hTERT-RPE1 were the least adherent to the electrode surface followed by the control hiPSC-RPE and then by the case cell line having the highest α. This was in turn reflected in the migration rates with the immortalized hTERT-RPE1 having the highest migration rate of 14.79± 0.39 μm/h followed by the control cell line (10.69 ± 0.21 μm/h) and then by the case line (8.60 ± 0.46 μm/h) having the slowest migration rate of the three cell lines. These data strongly suggest that the difference observed in cell migration rate between the case and the control cell lines may be attributed to a difference in cell adhesion properties.

ECIS electric fence was also used to determine hTERT-RPE1 migration rate (Figure 5.10). The electric fence was switched on before seeding ECIS arrays to prevent the cells from attaching to the electrode surface while they grew everywhere else in the culture well. When the fence was turned off, the cells started to migrate to cover the electrodes. The migration rate calculated using this method was found to be 12.43 ± 1.10 μm/h. The slower migration rate than the one calculated using the regular ECIS wound healing assay might be due to the absence of the adhesion ECM proteins.

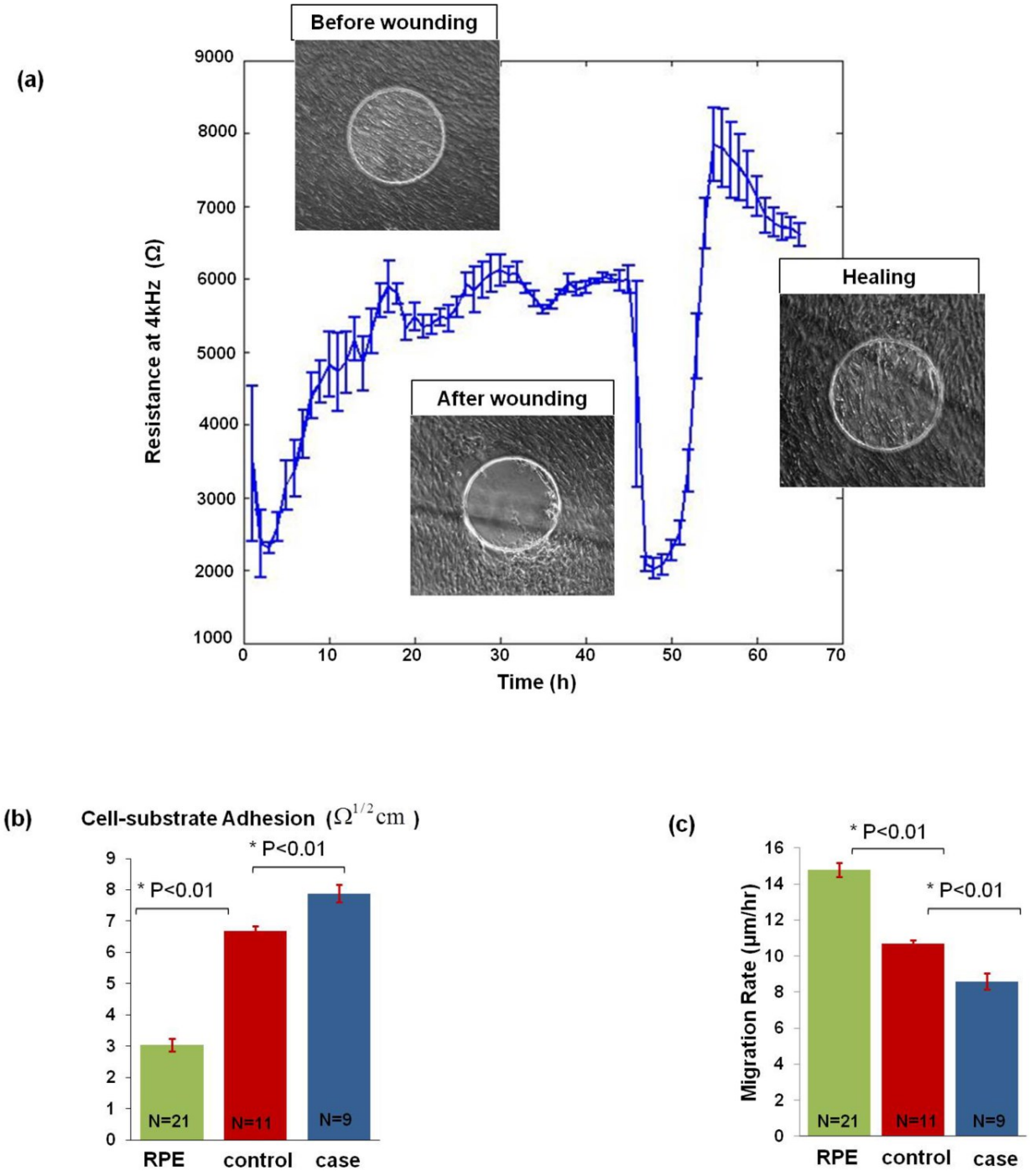

Figure 5.9: Effect of cell-substrate adhesion on the migration of immortalized and hiPSC-derived RPE. (a) Wounding hTERT-RPE1: Graph showing changes in resistance measurements during hTERT-RPE1 attachment and wounding assays. Wounded cells completely detached from the electrode surface upon wounding leaving clear electrodes. Wound healing was achieved as cells migrated to repopulate the electrode. (b) Cell-substrate adhesion bar graph: hTERT-RPE1 had the lowest adhesion parameter (α), followed by the control cell line and the case line with the highest α. (c) Migration rate bar graphs: hTERT-RPE1 had the highest migration rate. It was followed by the control hiPSC-RPE cell line and then by the case cell line [55].

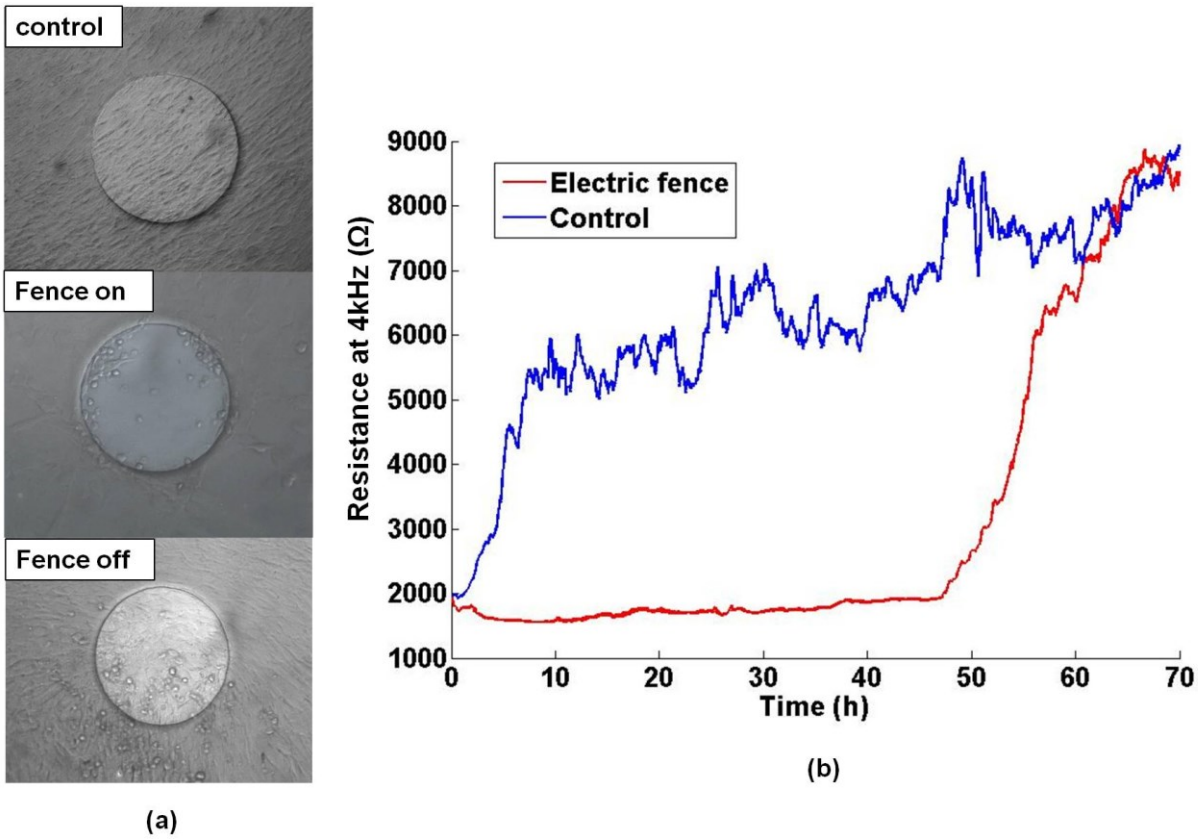

Figure 5.10: hTERT-RPE1 Electric Fence. (a) RPE cells on an ECIS microelectrode with the electric fence on (cell-free electrode) and after turning off the fence (cell-covered electrode). (b) ECIS Impedance measurements for a control well (blue) and a well where the electric fence was applied (red).

5.3. A preliminary study: Electrically-induced liver injuries

In an initial study, ECIS wounding assays were conducted in order to determine the migration abilities of HepaRG cell line. Unfortunately, the hepatocyte:cholangiocyte co-culture was not able to migrate after electrical wounding, showing no signs of recovery. The hepatocyte cell line (C3A) was used in an attempt to study cell migration and regeneration after liver injury. Different wounding parameters were used in trial and error experiments. It was noticed that the healing abilities of the C3A cells were limited to partial injuries. Small wounding thresholds (current amplitudes < 3 mA and short pulse durations ≤ 5s) caused a drop in impedance but not to that of the cell- free electrode indicating that complete cell death was not established. In these situations, C3As showed a fast recovery (1-5 hours) depending on the extent of the injury

which was reflected by the amount of decrease in the impedance measurements; the larger the drop in impedance, the longer it took the cells to recover (Figure 5.11). A wounding threshold of 3 mA, 20s, 40 kHz caused a drop in impedance to that of the cell-free electrode suggesting complete cell death. Recovery in this situation was a long process, and it took the cells almost 4 days to repopulate the electrodes, with a very low migration rate of 1.3 ± 0.2 μm/h. The limited abilities of C3As in wound healing has recently been reported by Navarro [29], where C3A monocultures were observed not to heal after scratch wounding.

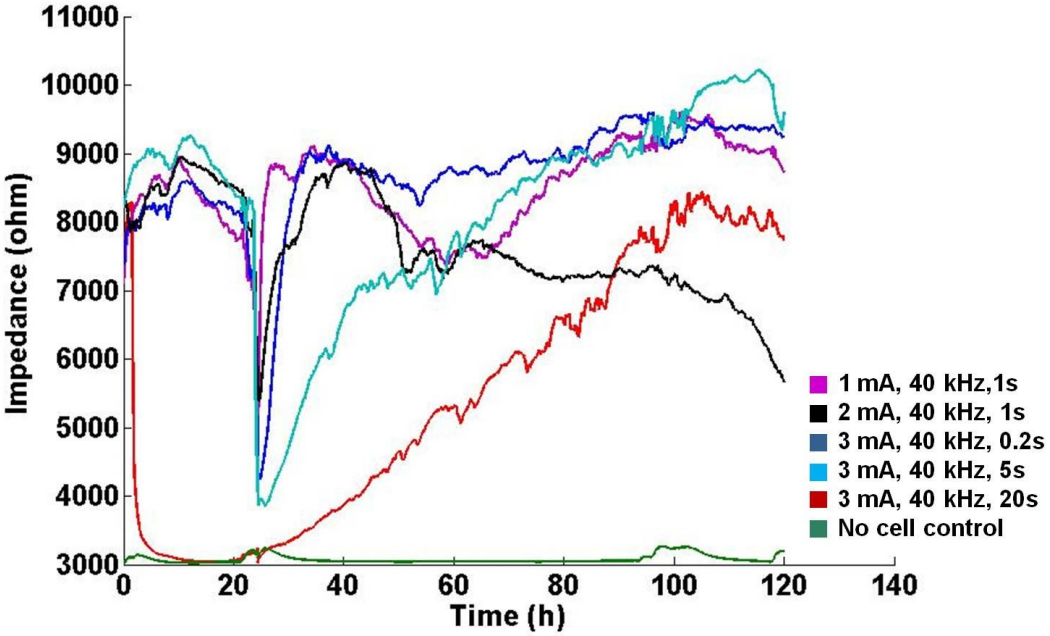

Figure 5.11: Effect of wound severity on C3A wounding. The graph shows the increase in C3As healing time with increasing wound severity. Complete cell death was mirrored by a decrease in impedance to that of the cell-free level. The impedance measurements after wounding illustrate the slow healing ability of this cell line.

5.4. High density, different-sized square microelectrode arrays for ECIS measurements

A microelectrode array with 16 different-sized square electrodes was designed and fabricated in-house. Having multiple individually-addressed electrodes inside the same culture chamber

allows for monitoring a wider cell population, while having small electrodes would allow for single cell migration studies. The chip was used to investigate real time ECIS measurements and to perform electrical wound healing assays.

The MEA design was adopted from a previous design [333]. The chip had 16 working platinum electrodes inside the culture well with 4 different sizes (20 µm, 50 µm, 100 µm, 200 µm) as shown in Figure 5.12. A PCB was designed to connect the microelectrodes to ECIS array holders using ribbon cables. Wells of 2 cm diameter, cut from 5 ml syringes were glued onto the chip to provide a reservoir for cell culture media. Biocompatibility studies were conducted in order to confirm the suitability of the materials used for passivating the chip as well as for attaching the culture well.

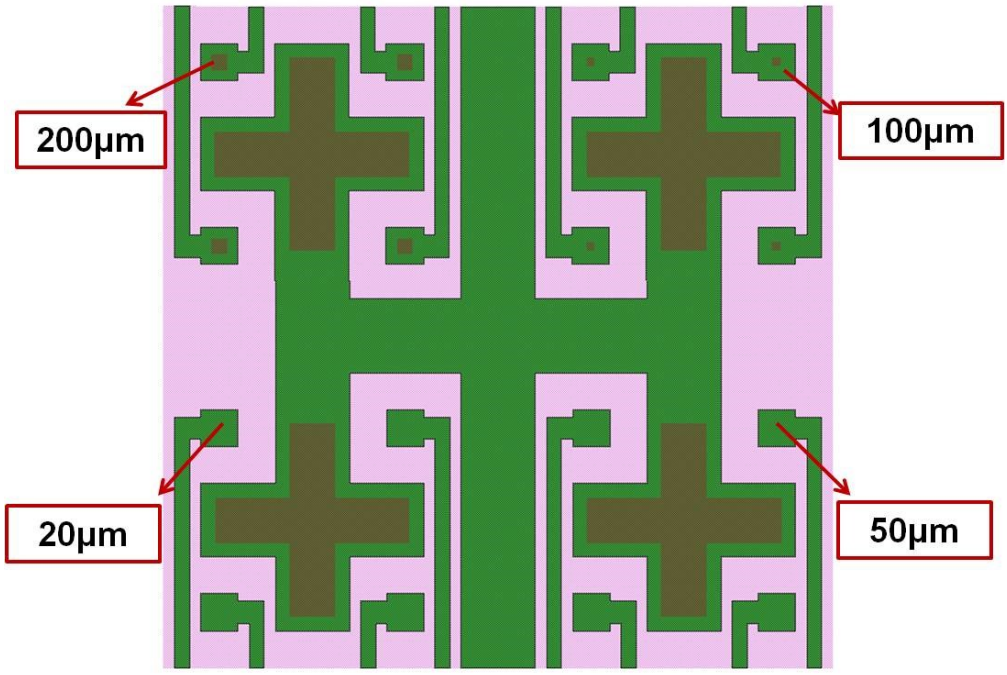

Figure 5.12: Square Microelectrode Array Layout.

5.4.1. Biocompatibility studies

In order to decide on a material for the MEA passivation, the biocompatibility of different insulating materials was investigated. Glass cover slips were coated with silicon dioxide, silicon nitride and Parylene-C and their effect on the attachment and proliferation of fibroblasts (NIH-3T3) was monitored and compared to a control group of cells cultured in a petri-dish. Cells cultured on Parylene-C showed very similar attachment and proliferation to that of the control. In the case of silicon dioxide on the other hand, cells did not proliferate at all even after 4 days of culture (Figure 5.13). It was therefore decided to use Parylene-C as an insulating material for the MEA chip.

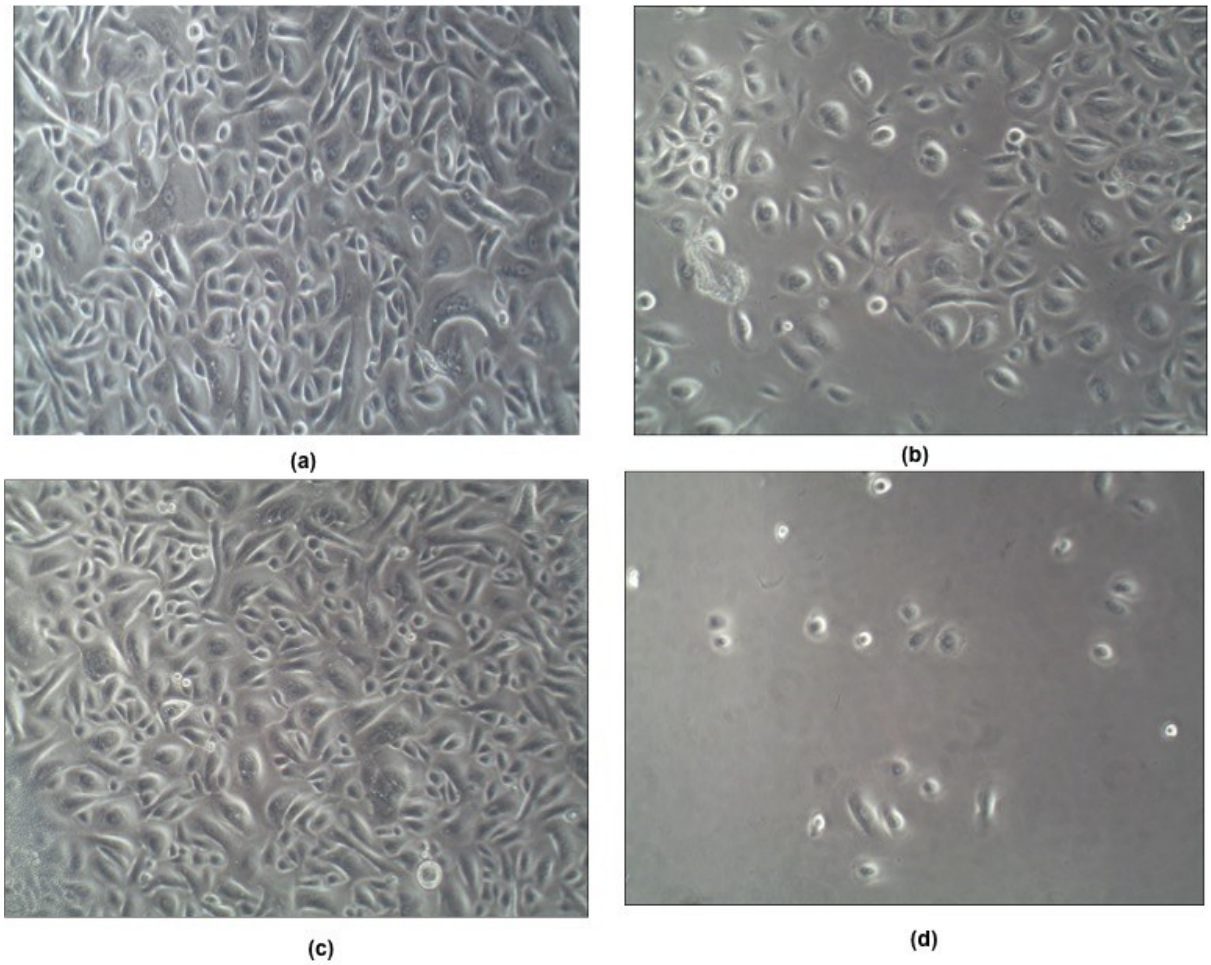

Figure 5.13: Biocompatibility of insulating materials. (a) Control group: fibroblasts cultured in a petri-dish. (b) Silicon nitride: cells showed less spreading than monitored in control. (c) Parylene-C: cell spreading and attahment was comparable to that of the control group. (d) Silicon dioxide: cells did not proliferate.

In order to fix the culture chamber on top of the chip, a biocompatible commercial adhesive (Dymax) was used. However, cells cultured in the adhesive-fixed chamber were all dead after one day of culture. Signs of the adhesive leaking inside the chamber were also noticed (Figure 5.14 (b)). PDMS is highly biocompatible and it has been widely used in biological applications. It was decided on using PDMS to fix the chamber onto the chip (Figure 5.14 (a)).

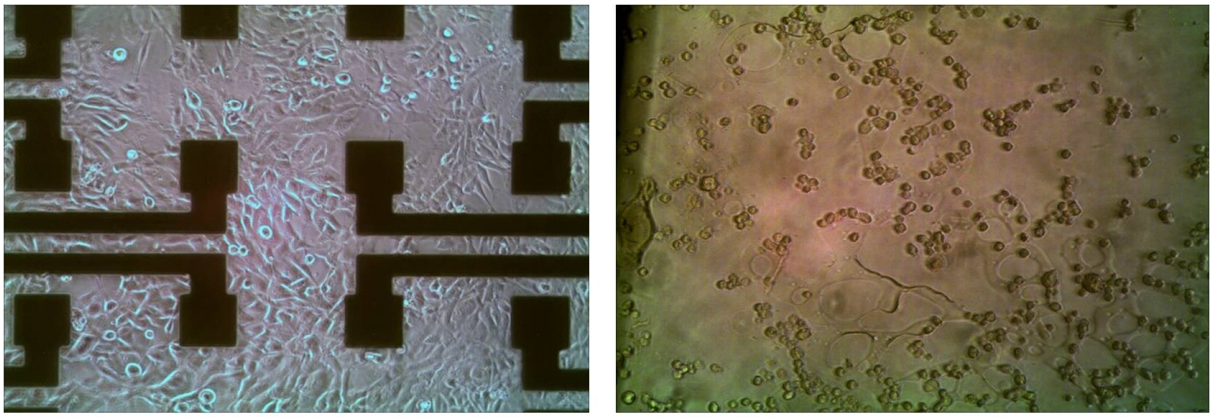

Figure 5.14: Adhesive biocompatibility test. (a) PDMS showed high biocompatibility. (b) Commercial adhesive leaked into the chamber causing cell death.

5.4.2. MEA Surface Modifications

Hydrophilicity is an important factor that is required in order for the cells to attach to a surface and proliferate. After coating the MEA chip with Parlyene-C, the surface hydrophilicity was measured. The contact angle of a drop of water on top of the chip was measured using a goniometer and was found to be 90^{o} indicating that the surface was hydrophobic. Treatment with oxygen plasma has been reported to increase surface hydrophilicity [339]. The parlyene passivated chip was treated with oxygen plasma before re-measuring the contact angle. This time the surface was found to be highly hydrophilic with a contact angle much less than 10^{o} and therefore could not be measured. The surface was considered ready for cell culture.

Another factor that could improve cell attachment and proliferation on the chip is protein coating. The effect of ECM proteins on cell migration and proliferation has been widely studied [231]. Usually, laminin or fibronectin coating is used before cell seeding. In all of the studies presented in this thesis, the electrode arrays were coated with serum proteins by incubating the arrays with culture medium for 2 hours prior to cell culture.

5.4.3. ECIS measurements

After incubating the MEA with culture medium for 2 hours, hTERT-RPE1 were seeded with a density of 40,000 cells/cm^2. The chip was then connected to ECIS using the fabricated PCB as shown in Figure 5.15.

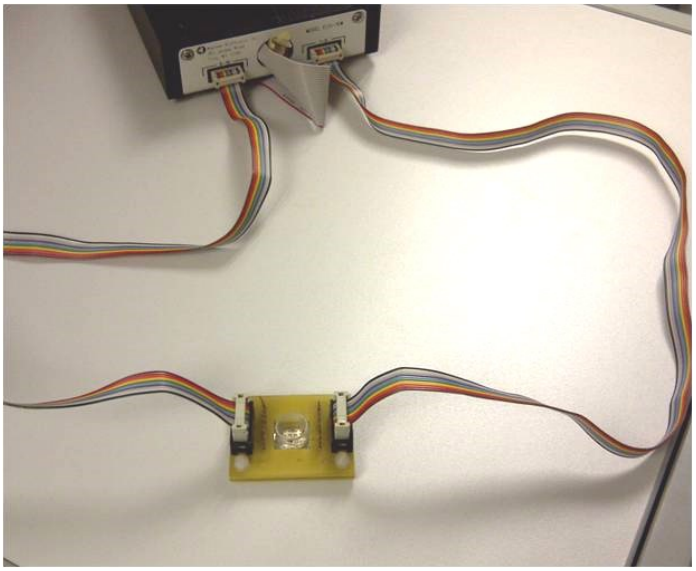

Figure 5.15: MEA –ECIS Interface

Impedance measurements reflected cell growth and proliferation on the different sized microelectrodes with impedance values increasing with decreasing the electrode size (Figure 5.16).

Wounding experiments were performed using ECIS electrical wounding mode using the previously determined wounding threshold for hTERT-RPE1 cell line (1 mA, 40 kHz, 30s).

However, these wounding parameters were determined for 250 µm electrodes and different wounding parameters for smaller electrodes still needed to be determined. Due to the limited number of fabricated MEA chips, ECIS 8W1DD arrays with different sized electrodes were used for these trial and error experiments. The 8W1DD arrays have electrodes of 25, 50, 100 and 250 µm diameter. The impedance measurements showed similar values to those recorded for the MEA chip as shown in Figure 5.17.

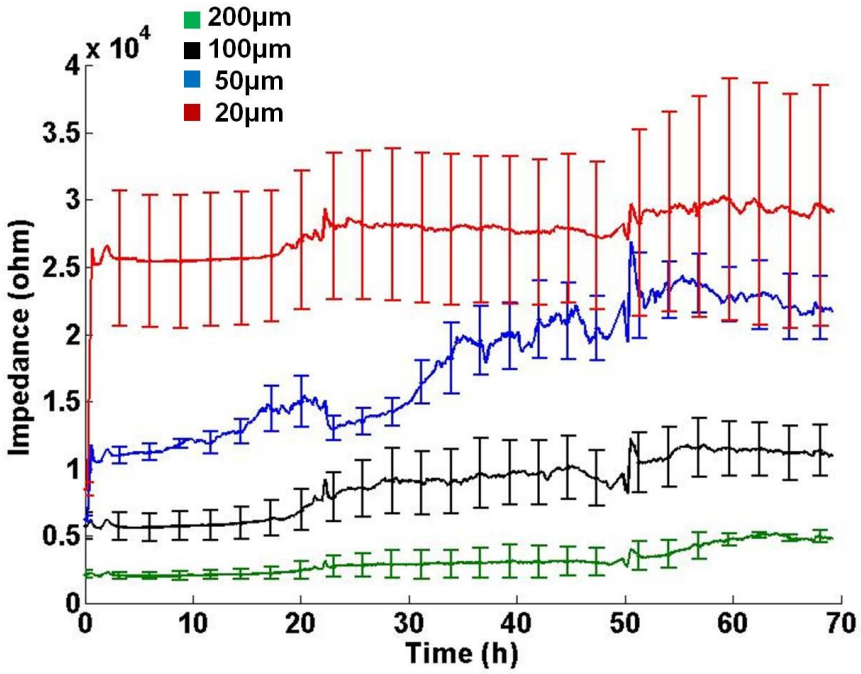

Figure 5.16: hTERT-RPE1 ECIS measurements of the square MEAs. The graphs show the impedance measurements recorded by ECIS for the different-sized square microelectrodes covered by a confluent layer of hTERT-RPE1. The measured impedances decreased with increasing the electrode size.

To arrive at wounding thresholds using a minimum number of trials, it was decided to define wounding parameters that will result in the same current density produced at the 250 µm electrodes with the previously determined wounding pulse.

In ECIS wounding mode, an AC signal is applied through a 1 kΩ resistor connected in series to the oscillator. Since the impedance of the counter electrode can be neglected due to its much larger size in comparison to the working electrode, the relation between the applied wounding

voltage and that measured at the working electrode could be extracted from the simplified ECIS circuit shown in Figure 5.18, according to Equation (5.2).

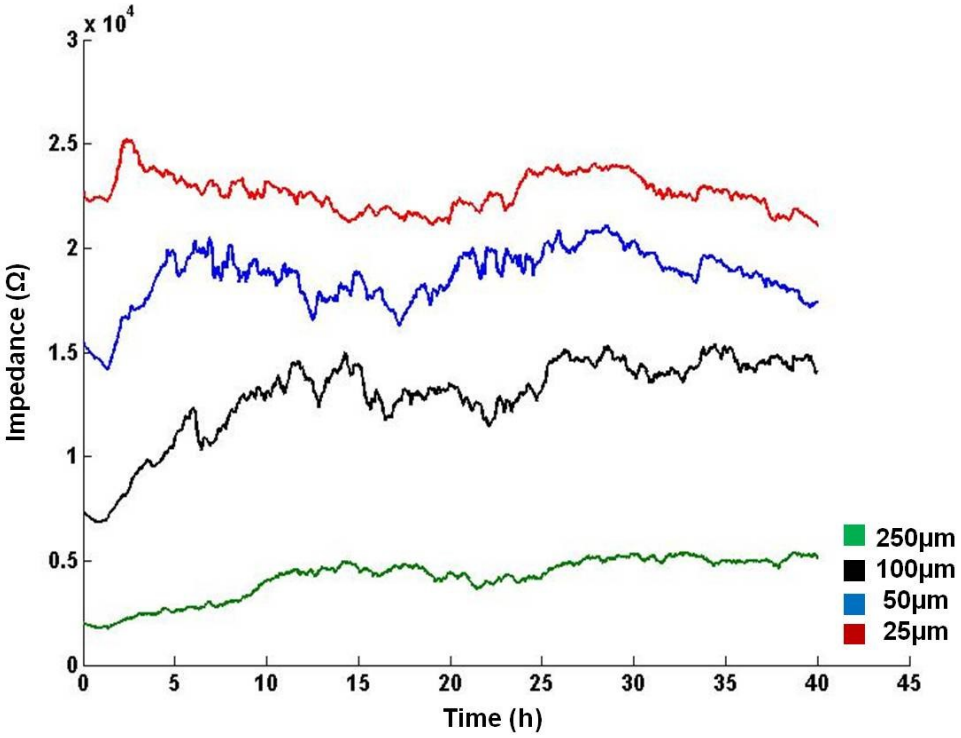

Figure 5.17: 8W1DD impedance measurements. The graphs show how the impedance measurements of hTERT-RPE1 increase with decreasing electrode size.

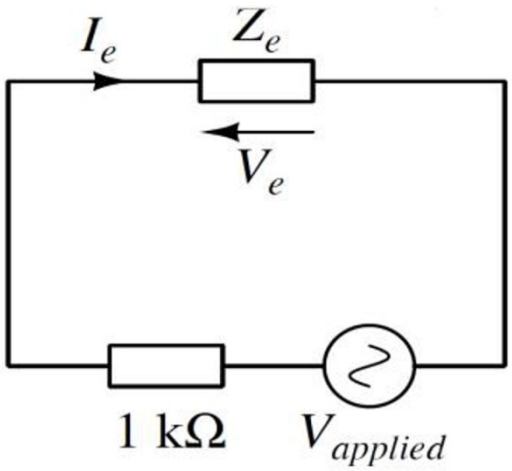

Figure 5.18: ECIS wounding circuit. A schematic diagram showing a simplified ECIS circuit for the wounding mode. A 1kΩ resistor is connected in series to the AC source and the wounding pulse is applied to the working electrode.

$$V_e = V_{applied} * \frac{Z_e}{Z_e + 1000} \text{ (V)} \quad (5.2)$$

After calculating the voltage (V_e) at the 250 µm electrode for an applied wounding pulse of 1V, 40 kHz, 30s, the current density at the electrode was calculated according to:

$$J_e = \frac{V_e}{Z_e * electrode\ area} \text{ (A/m}^2\text{)} \quad (5.3)$$

The amount of charge corresponding to the wounding current at the electrode (I_e) was determined using the equation:

$$Q_e = \frac{I_e}{t} \text{ (C)} \quad (5.4)$$

Once the values of V_e, J_e and Q_e for the 250 µm electrodes were calculated, wounding parameters for the different sized electrodes were determined resulting in the same current density. The theoretically determined wounding parameters did not cause cell wounding in some cases and the actual applied signal had to be slightly higher. This could have resulted due to the simplicity of the model used to determine the wounding parameters. Factors like the solution resistance as well as the amount of ECM produced by the cells should be considered when determining the wounding parameters. Nonetheless, the parameters determined using the above equations provided very close values to the actual final parameters. This saved lots of trials as well as avoided any damage to the electrodes during the trial and error wounding experiments. Table 5.2 shows the different hTERT-RPE1 wounding parameters determined for the different electrodes.

Electrode Size	Wounding Parameters
250 µm	1 mA, 40 kHz, 30s
100 µm	Calculated: 400 µA, 40 kHz, 5s Actual: 600 µA, 40 kHz, 5s
50 µm	Calculated: 100 µA, 40 kHz, 1.2s Actual: 600 µA, 40 kHz, 2s
25 µm	Calculated: 40 µA, 40 kHz, 300 ms Actual: 200 µA, 40 kHz, 1s

Table 5.2: Wounding parameters for different electrode diameters.

Based on the wounding parameters defined for the 8W1DD arrays, RPE cells cultured on the MEA chip were wounded. A defined wound was achieved for the 200 µm, 100 µm, 50 µm square electrodes but not for the 20 µm ones. Figure 5.19 (a) shows wounded RPE cells on top of a 50µm square electrode. The migration process was monitored through the impedance measurements and the migration rate was determined as 12.07 ± 0.1 µm/h (Figure 5.19 (b)). Note that the average migration distance (d) was calculated as:

$$d = \frac{X + X\sqrt{2}}{2} \tag{5.5}$$

Where; X is the length of one side of the square electrode and $X\sqrt{2}$ is the length of its diagonal.

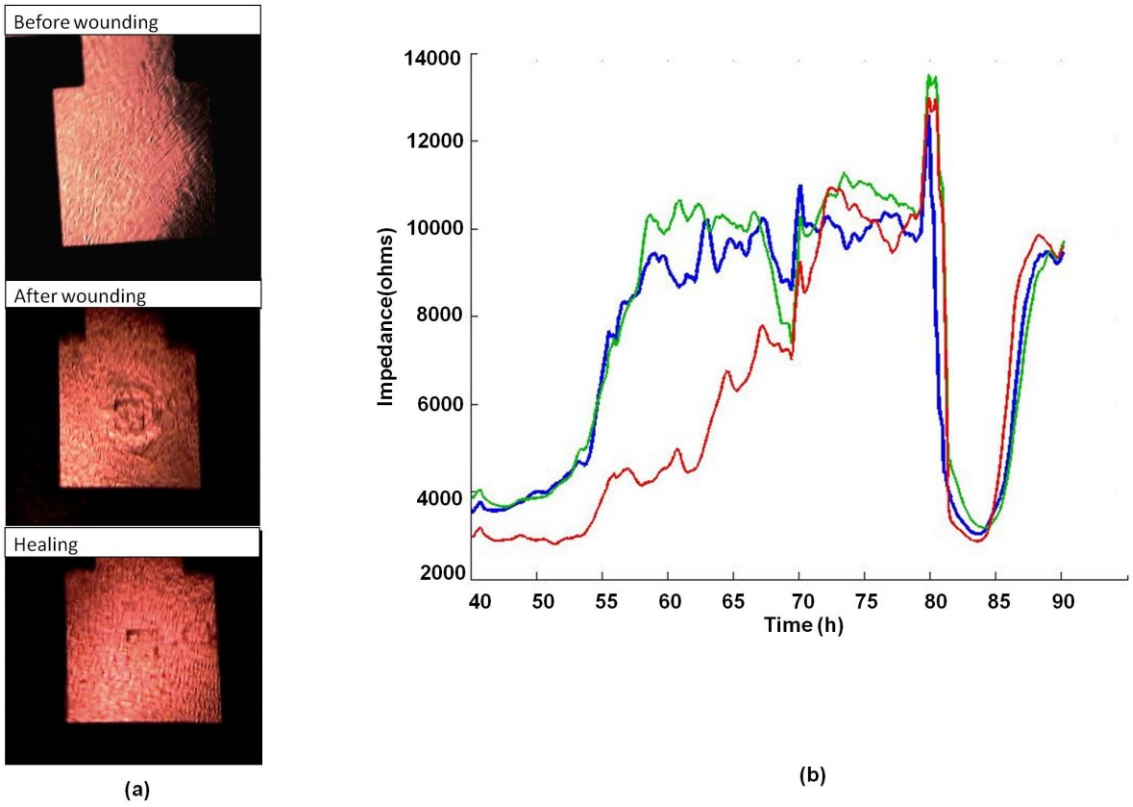

Figure 5.19: Wounding on the MEA chip. (a) Wounding RPE on a 50µm square electrode. (b) Impedance measurements of three 200µm electrodes during ECIS wound healing assays. Please note that the poor quality of the phase contrast images is due to the non-transparency of the platinum electrodes.

5.5. Summary

In the current study, the need for a patient-specific, physiologically relevant *in vitro* model of wound healing and regeneration has been addressed through developing a tissue-on-a-chip approach. Electrically-induced injuries were used to study cell loss and low cell migration abililties in degenerative diseases. . First, keratinocytes were employed as a model to further investigate ECIS electrical wounding mode and find a formula that could help arrive at a wounding threshold. ECIS wounding was then used to mimic RPE loss in age-related-macular degeneration. The hiPSC-RPE-based model was first established on ECIS microelectrodes before cell migration and regenerativeabilities of a control and case cell lines were compared. RPE cells reprogrammed from a patient with LORMD were found to migrate slower than the

control cell line derived from a healthy sibling. ECIS modelling and biochemical assays showed that this is possibly related to the stronger cell-substrate adhesion expressed by the case cell line. Further experiments with an immortalized RPE cell line, confirmed the relationship between higher adhesion and low migration rates.

In a preliminary study, cell migration assays were conducted on the HepaRG cell line to examine its migration ability. HepaRGs did not migrate at all indicating their very low regenerative abilities, which could be a reason behind why this cell line are recommended to be cultured at confluency.

Finally, high density microelectrode arrays with high spatial resolution and different-sized, individually-addressed microelectrodes were designed and fabricated. ECIS RPE wound healing assays were performed on the different-sized square microelectrodes and a migration rate comparable to that obtained with ECIS circular electrodes was determined.

Chapter 6

Towards a new therapy: Stimulation of wound healing

The tissue-on-a-chip disease models proposed in this work offer powerful, high throughput platforms for translational studies and the evaluation of potential therapies. This chapter provides an investigation of two therapeutic approaches where drug-stimulated and electrically-stimulated wound healing are investigated. First, the effect of the antioxidant NAC on cell recovery in ALF and AMD is explored followed by evaluating the potential of electrical stimulation as a new therapy for AMD. Finally, a design that integrates radial electrical stimulation with impedance sensing, allowing for the quantification of cellular behaviour within the EF is proposed.

6.1. Drug-stimulated wound healing

Since oxidative stress is associated with both age-related macular degeneration as well as paracetamol toxicity, the effect of the anti-oxidant N-acetyl-L-Cysteine (NAC) on HepaRG and RPE cell recovery was investigated.

6.1.1. Antioxidants and HepaRG

Following an APAP ECIS toxicity assay, 10mM NAC was added to HepaRGs for 24h and its effect on cell recovery was monitored (Figure 6.1). Following the dose-response decrease in impedance after APAP addition, a slight increase in the measurements was monitored after

NAC introduction. More experiments are needed however to make sure that this effect was indeed due to NAC and not just due to the addition of fresh medium.

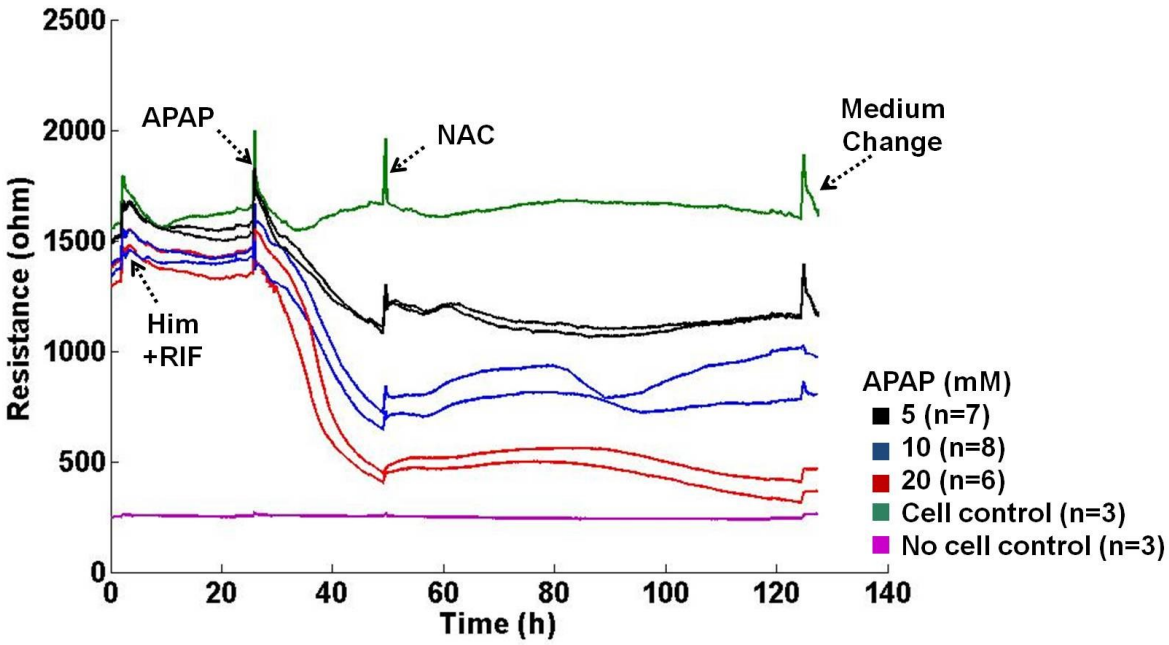

Figure 6.1: The effect of NAC on paracetamol toxicity. After the 24h induction and 24h APAP assay, 10 mM NAC caused a small increase in the measured resistance. However, this effect might be due to the addition of fresh medium pointing towards the need for more experiments.

6.1.2. Antioxidants and RPE

The effect of NAC on the migration of the case and control hiPSC-RPE cell lines was investigated. 10 mM NAC was added to the culture medium and cells were either incubated for 2h or for 24h with NAC before wounding. NAC had no effect on the migration of the case cell line. However, a decrease in the control cell migration was observed after incubating the cells with NAC for 2h (Figure 6.2).

To understand more the effect of oxidative stress on RPE migration, 100 µM hydrogen peroxide (H_2O_2) was introduced to the culture medium for 3 hours before conducting the wounding experiment. Before stressing the cells using H_2O_2, RDM was substituted by an antioxidant-free culture medium (RDM – antioxidants) and cells were incubated for 24h before the oxidative

stress experiment. For some wells, 10 mM NAC was added for 2h before adding H_2O_2. For the rest of the wells, H_2O_2 was added directly to the medium without the addition of NAC first. Interestingly, the oxidative stress has caused a slight increase in the control cell line migration rate (Figure 6.3). Increase in migration rate with oxidative stress has been reported before [340]. NAC treatment before the addition of H_2O_2 caused the migration rate to decrease. For the case cell line, oxidative stress did not affect the migration rate while NAC treatment caused a slight increase in migration. This might be due to the fact that for the case cell line, the cells are already stressed due to AMD. More experiments with different NAC and H_2O_2 concentrations and varying incubation times are required before arriving at any conclusions.

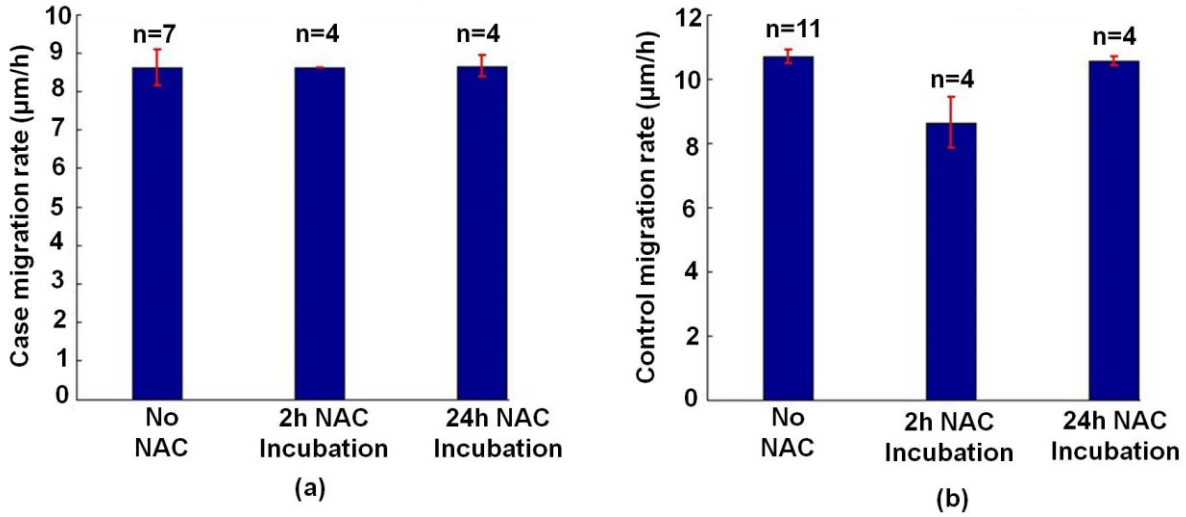

Figure 6.2: The effect of NAC on RPE migration. (a) NAC had no effect on the case migration rate. (b) 2h incubation with NAC caused a decrease in the control cell migration.

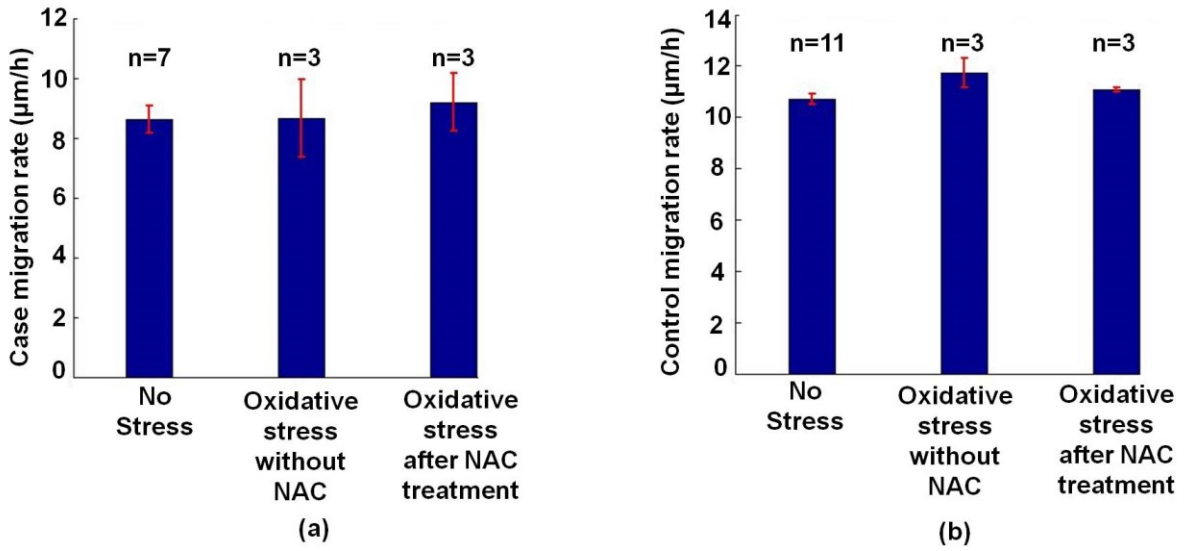

Figure 6.3: Oxidative stress and RPE migration. (a) No effect on case migration was monitored with oxidative stress. However, NAC treatment caused a slight increase in migration rates. (b) An increase in the control migration rate was noticed with oxidative stress. This increase dropped with NAC treatment.

6.2. Electrically-stimulated wound healing

6.2.1. Linear Electrical stimulation

The role of electrotaxis in directing cell migration has been widely investigated. In this work, preliminary studies were conducted to investigate the potential of electrical stimulation in enhancing RPE wound healing. The immortalized RPE (hTERT-RPE1) cell line was used for the initial electrical stimulation experiments. A microfluidic channel was used instead of the traditional electrotaxis chamber shown in Figure 6.4 (a). Cells were seeded on the commercial 'Ibidi' microfluidic channels (Figure 6.4 (b)) and an external EF was applied between the ends of the channel 4 hours after seeding. A DC voltage was applied using an electrophoresis power supply and 2% agar salt bridges were used to connect the Ag/AgCl electrodes to the microfluidic channel. A handheld voltmeter was used to measure the potential difference before and after the salt bridges. The experimental set up is shown in Figure 6.4 (c).

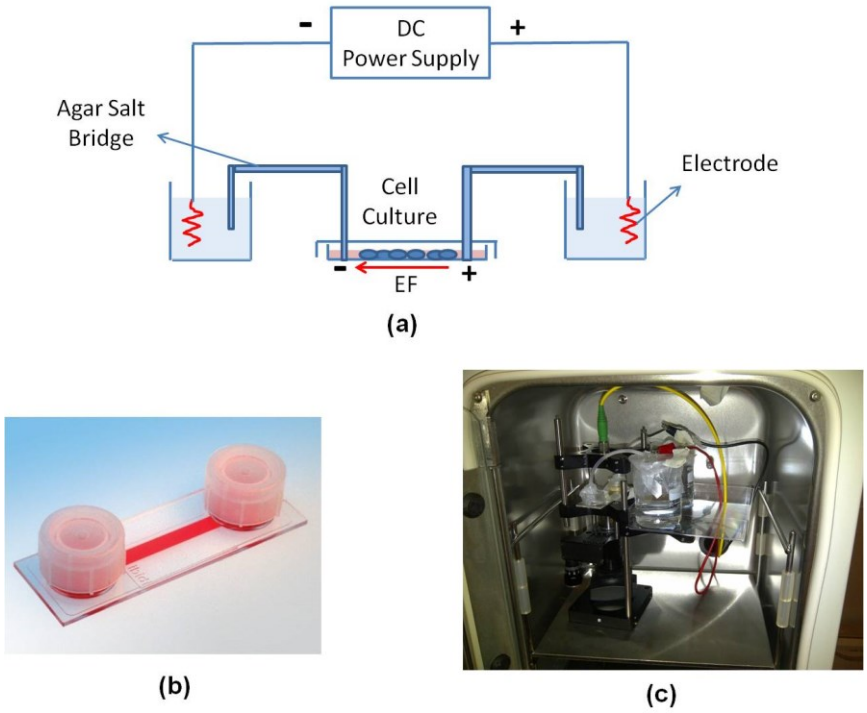

Figure 6.4: Electrical Stimulation set up. (a) Traditional electrotaxis chamber. (b) Microfluidic channel used for initial electrical stimulation experiments. (c) Experimental set up.

To ensure the presence of an EF inside the channel with the external application of a DC potential, charged polystyrene beads were added to the culture medium. The negatively charged particles moved towards the cathodic end of the microfluidic channel even when the polarity was reversed. The potential inside the channel was simulated using COMSOL Multiphysics and is shown in Figure 6.5.

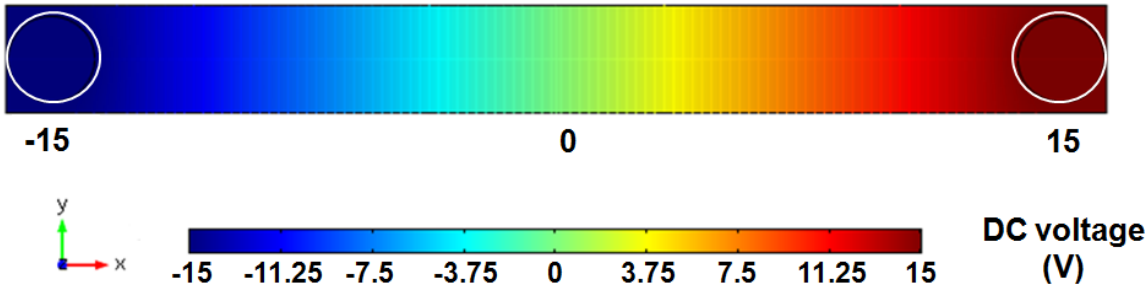

Figure 6.5: COMSOL voltage simulation inside the microfluidic channel. Simulation showing the change in the DC potential inside the channel during the electrical stimulation experiments. The two white circles represent the ports of the channel into which the agar bridges are inserted for EF application.

Electrical stimulation was performed inside an incubator (with no CO_2 supply), at a controlled temperature of 37 °C. 100 mM HEPES buffer was added to the culture medium to compensate for the absence of the CO_2 supply. Time-lapse microscopy of cell migration under the effect of 50-300 mV/mm EFs was recorded using a digital inline holographic microscope. A 300 mV/mm EF was applied for 5 hours and was found to direct cell migration in a direction roughly perpendicular to the EF, in comparison to the random migration monitored under no EF conditions. The hTERT-RPE1 cells also aligned their long axes with an orientation angle (Θ) of 155.90° ± 1.12° that was significantly different from the orientation angle under no EF conditions ($P < 0.01$). Cell elongation was also observed. Cell migration was tracked using the ImageJ manual tracking plugin. Figure 6.7 shows the direction of cell migration under no EF conditions against an applied EF of 300 mV/mm.

6.2.2. Impedance monitoring of Electrically-stimulated healing

Combining electrical stimulation and impedance sensing would allow for quantitative monitoring of electrically-stimulated healing in real time. In such a set up, the on-chip electrical wounding technique is used to create a defined injury before quantitatively monitoring the healing process under the effect of external electrical stimulation. As a first attempt to use impedance measurements to monitor cell migration under the effect of an external EF, ECIS flow arrays were used. The arrays have 8 working electrodes of 250 μm diameter inside a microfluidic channel. The electrical stimulation set up was the same as for the initial electrotaxis experiments and is shown in Figure 6.8. In order to avoid interference between ECIS electrical signals and the external EF, the EF was applied for half an hour intervals during which ECIS measurements were paused.

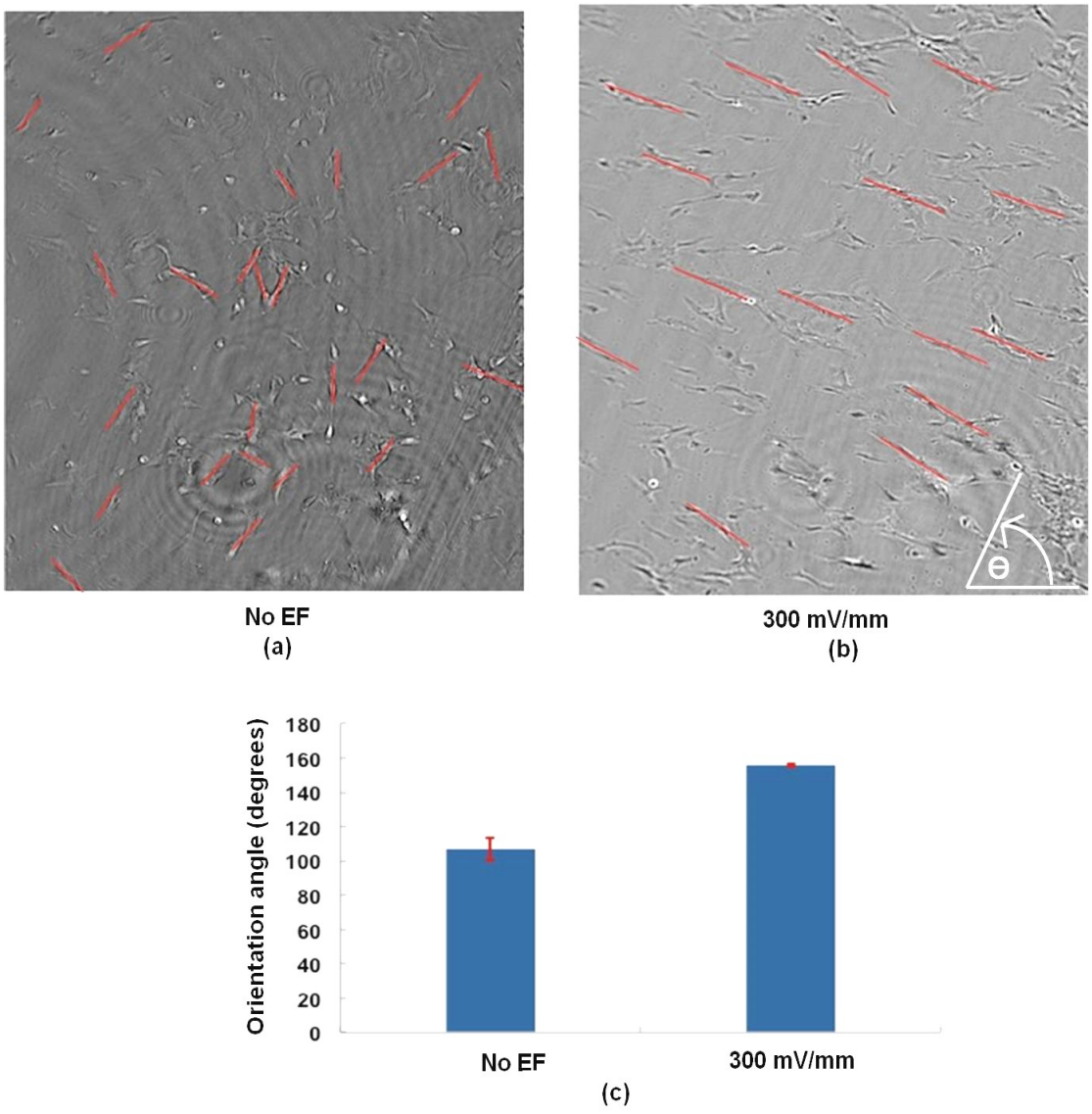

Figure 6.6: Effect of electrical stimulation on cell alignment. (a) Random cell alignment under no EF conditions. (b) Cell alignment in the presence of a 300 mV/mm. The orientation angle Θ is measured from the 0º horizontal axis in the direction of cell motion (c) Bar graphs showing the effect of an external EF on the alignment (orientation angle). The difference in the orientation angle was significantly different ($P < 0.01$) between no EF and 300 mV/mm conditions.

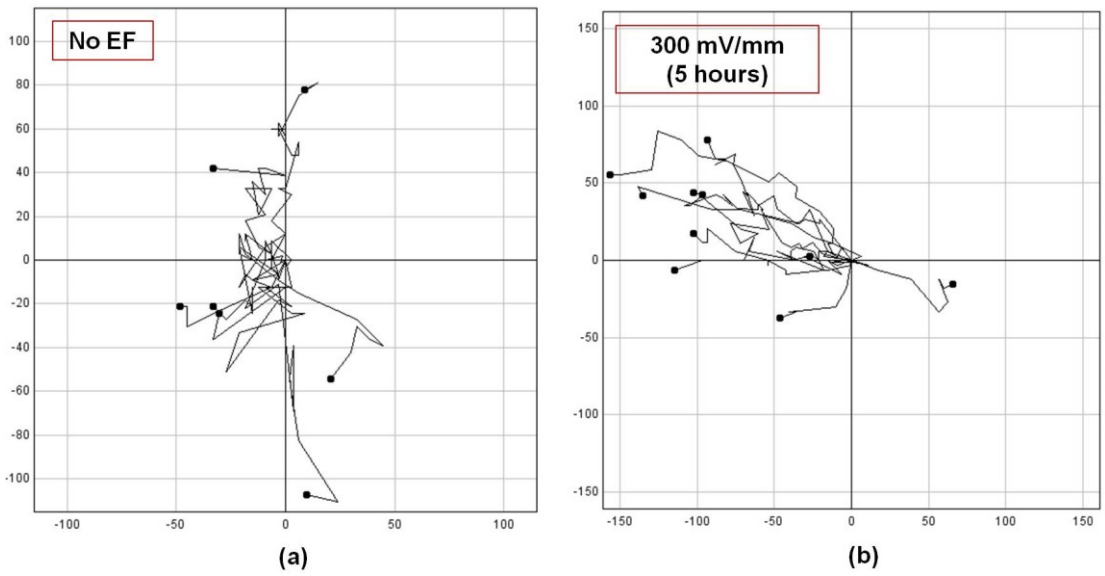

Figure 6.7: Tracking RPE cell migration. (a) Random cell migration under no EF conditions. (b) An EF of 300 mV/mm directed RPE cell migration in a direction perpendicular to the applied EF.

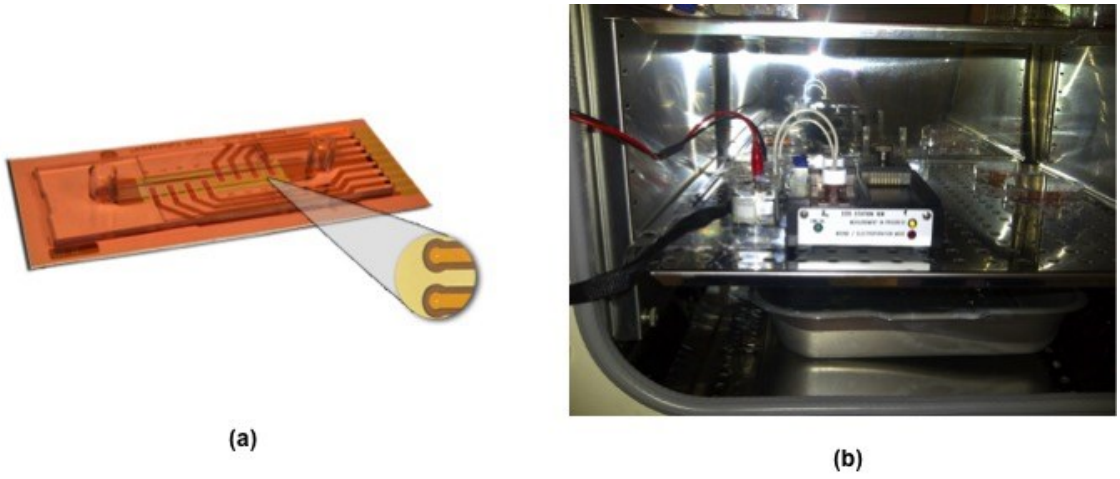

Figure 6.8: ECIS-based electrical stimulation set up. (a) ECIS flow arrays. (b) Experiment set up.

hTERT-RPE1 cells were cultured until confluency before wounding the cell layer using wounding parameters of 1mA, 40 kHz, 30s. When applying an external EF, the counter electrode was damaged as the gold layer lifted off. The counter electrode (CE) on those arrays ran through the length of the channel, which according to the EF simulations (Figure 6.5) meant that the two ends of the CE were at different potentials, hence the damage due to the

electrochemical corrosion. The design of the ECIS flow arrays was therefore unsuitable for the electrical stimulation set up presented in this study. It was decided that a new design is needed to allow for the use of ECIS and electrical stimulation.

6.2.3. A proposed design for impedance-based radial electrical stimulation

Electrical stimulation experiments are usually applied linearly in one direction to investigate the effect of EFs on cell migration and wound healing. A stimulating system where an external EF is applied radially, could speed up the wound healing process by directing the cells towards a wounded area, to close it from several directions in parallel.

A design for a MEA chip that can monitor cell radial migration is proposed as part of an impedance-based electrically stimulating system. The MEA has five 500 μm diameter surrounding a central 500 μm electrode onto which an ECIS wounding pulse can be applied. A counter electrode shaped like a horse-shoe surrounds the 6 working electrodes (Figure 6.9).

In order to have a radial EF that can direct cell migration towards the central wound, an insert with 6 outer holes, for holding the 2% agar bridges, is inserted inside the culture chamber, forming a roof 1 mm above the cell culture, reducing Joule heating and minimizing the medium evaporation. The stimulation insert also has a central opening that holds an agar tube above the central working electrode onto which an injury is electrically induced. The culture chamber also has three feet to allow for later alignment of the chamber and insert with the inner electrode. The outer agar bridges all have the same polarity, opposite to that of the single inner agar bridge. The central tube is chosen to be smaller than the working electrode (500 μm) in order to direct cell migration towards the centre of the wound. Figures 6.10 and 6.11 show the designs of the culture chamber and the insert respectively. Another design for an insert that allows for optical observations is also shown (Figure 6.11 (b)).

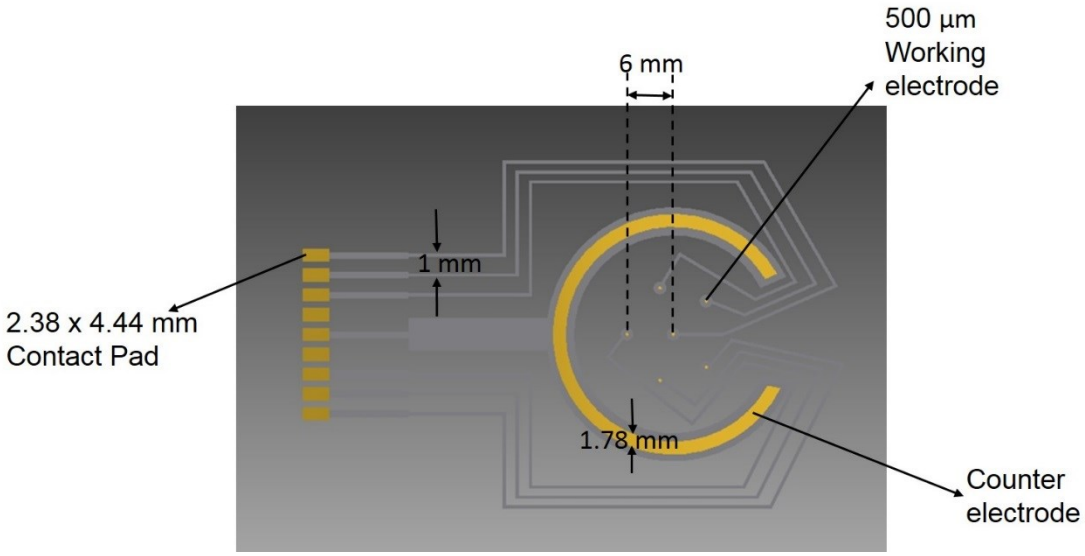

Figure 6.9: Proposed design for the radial MEA. The electrode openings are shown in gold.

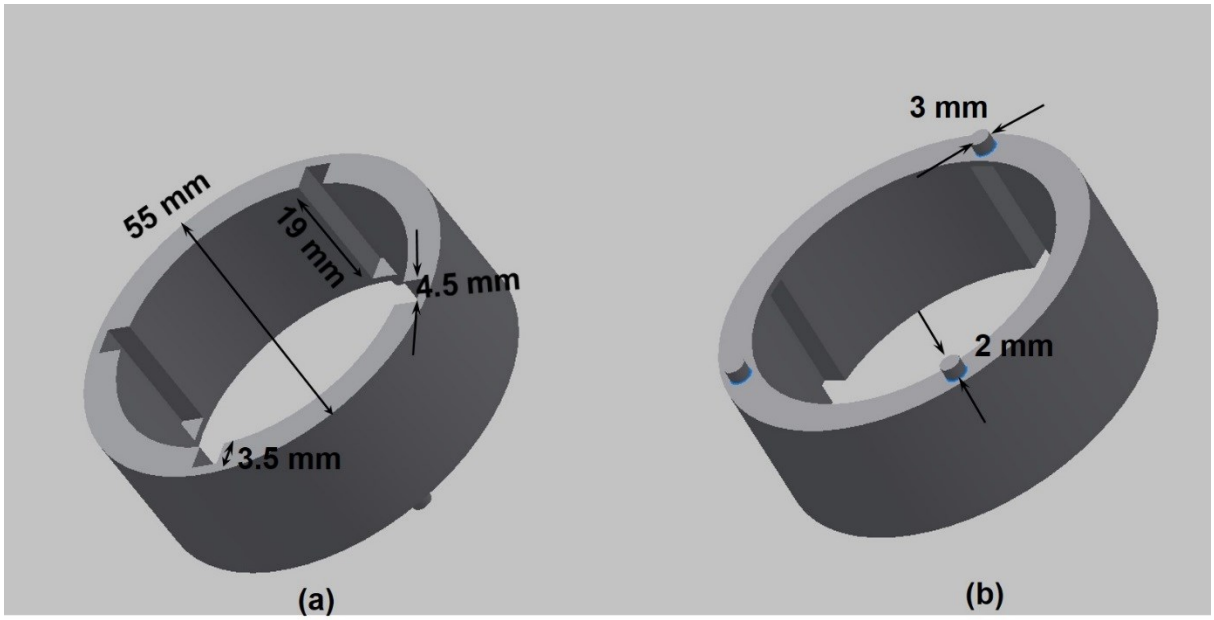

Figure 6.10: Proposed design for the culture chamber. (a) Top view: The chamber has groves that allow for positioning the stimulation insert 1mm above the electrodes. (b) Bottom view: The chamber also has three feet that allow for later alignment of the chamber and insert with the central wounding electrode.

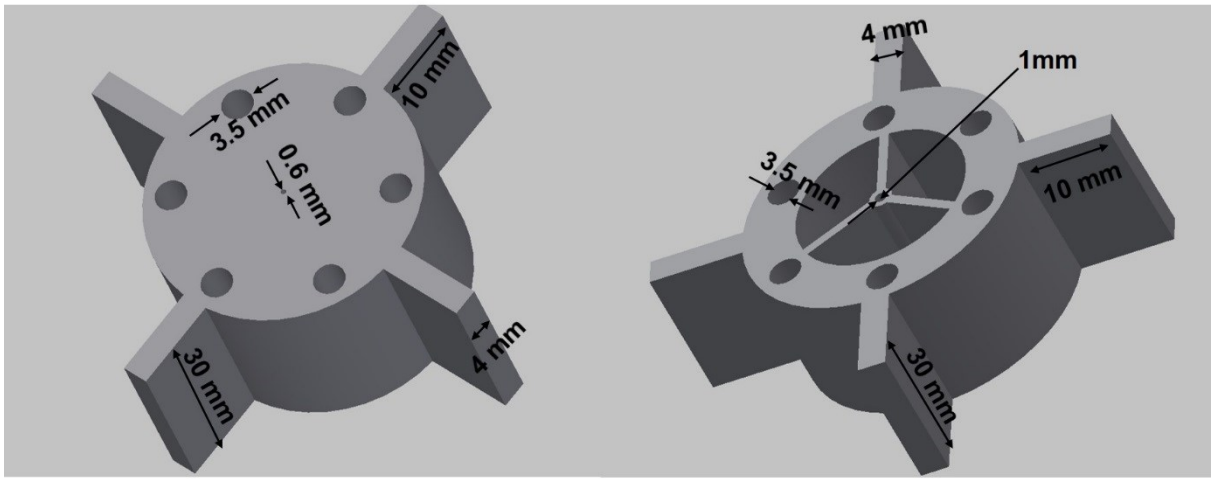

Figure 6.11: Proposed design for the stimulation inserts. (a) The insert can hold 6 outer tubes surrounding a much smaller inner tube. The insert also has rectangular arms that fit into the groves of the culture chamber. (b) An insert design with three windows that allow for optical observations.

The potential gradient resulting from such an arrangement is simulated using COMSOL Multiphysics and is shown in Figure 6.12. The insert is designed so that all of the electrodes remain at a constant potential in order to avoid corrosion of the gold layer and the electrode damage that was previously reported when using ECIS flow arrays. A chip holder that allows for optical observations and connects the MEA chip with ECIS is also designed as shown in Figure 6.13.

Because the MEA surface conditions affect cell migration, disposable MEAs, fabricated by screen printing or laser ablation, are suggested for the electrical stimulation system. This will ensure the same surface conditions, not mediated by cell attachment proteins, for all experiments. A very simple technique for microelectrode fabrication has been investigated. Rectangular polystyrene substrates were laser cut from a T-75 tissue flask. The microelectrodes were prepared by sputtering gold through a mask, leaving only the required patterns on the polystyrene substrate. Based on the previous biocompatibility studies, Parlyene-C will be used

for passivation and can be deposited using a second mask to define the electrode openings. To test the feasibility of the set up and the alignment of the various parts of the system, all inserts, culture chamber and chip holder has been 3D printed in-house. Figure 6.14 shows how the radial MEA can be connected to ECIS using the 3D-printed chip holder.

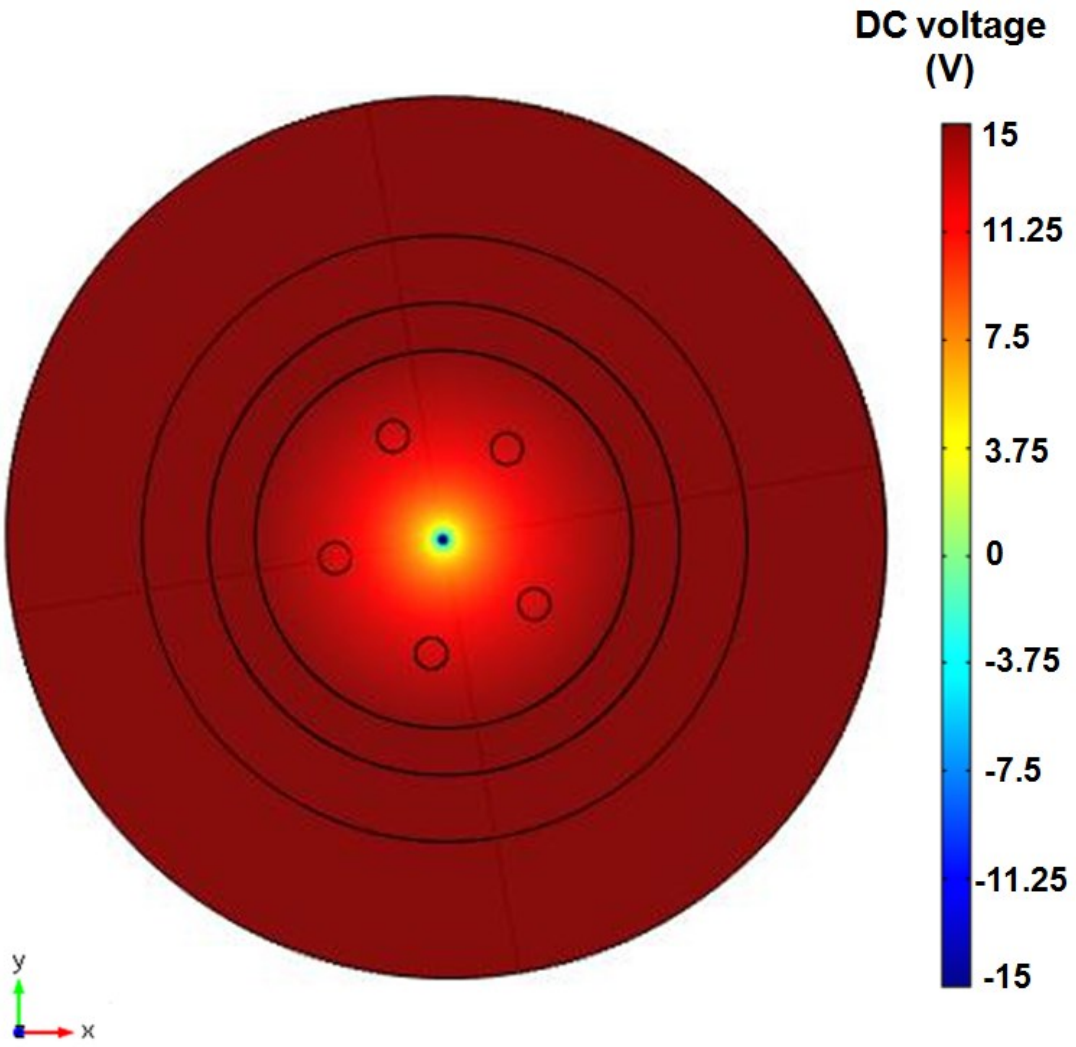

Figure 6.12: COMSOL voltage simulation of the radial set up. The black circles show the location of the working and counter electrodes with respect to the DC potential. The outer circle represents the inner edge of the insert.

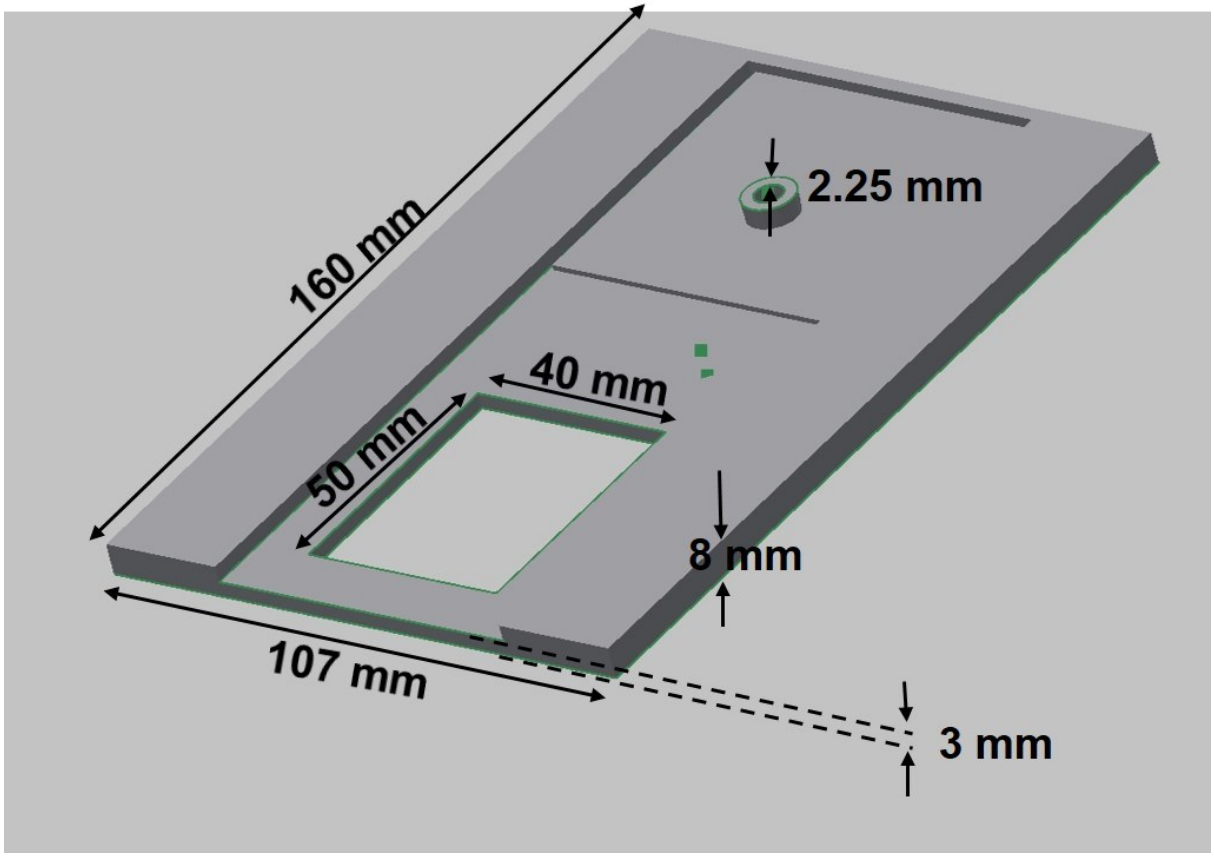

Figure 6.13: Proposed design for the radial MEA holder. The chip holder has a window that allows for optical observations. The chip also has a threaded hole that allows for connection with ECIS array holder.

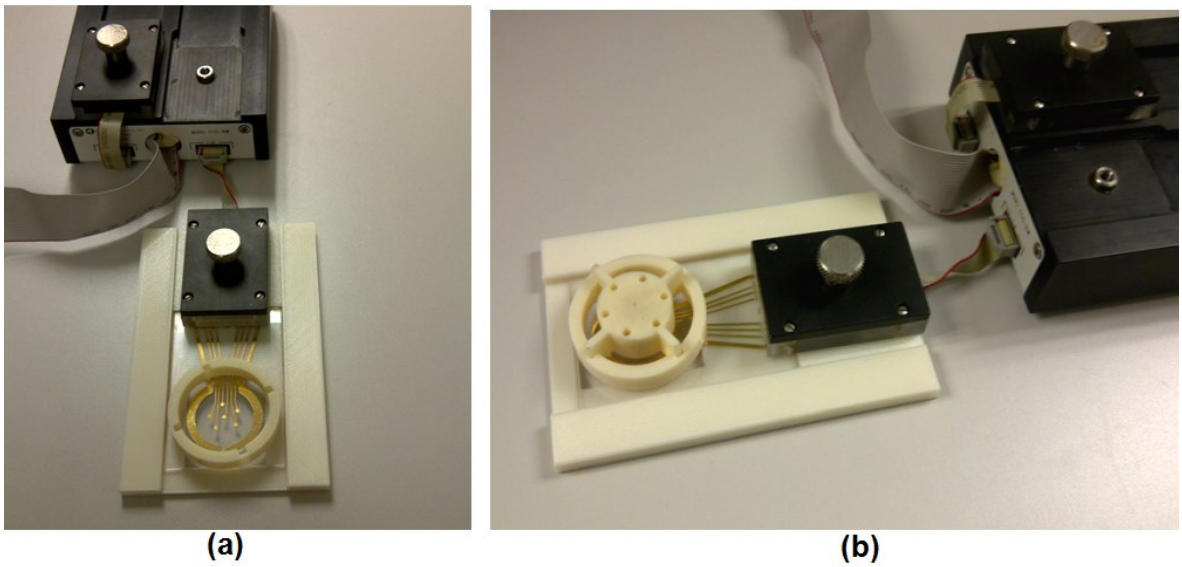

Figure 6.14: Radial MEA-ECIS interface. (a) A picture showing how the MEA holder connects a prototype chip to the ECIS holder array. (b) A picture showing the position of the 3D-printed insert with respect to the culture chamber and the microelectrodes.

An initial experiment using polystyrene particles was performed in a petri-dish where five agar bridges were arranged radially, encircling an inner agar bridge with opposite polarity. Holes were drilled in the petri-dish cover to keep the agar bridges in place during the experiment. Initially, the negatively charged particles moved towards the positive inner tube as required. However, a few issues were monitored. First, to obtain an EF that caused the particles to move, high voltages (70-100 V) needed to be applied. This is due to the EF distribution, being dispersed into the whole area of the petri-dish instead of being confined to a small area, as in the case of a microfluidic channel or an electrotaxis chamber. Secondly, because of the thermal effects of applying such high voltages, the agar bridges melted during a period of 30 mins of EF application. Moreover, the medium evaporated fairly quickly, possibly due to heating effects. All these issues need to be addressed before applying radial electrical stimulation to cultured cells and are discussed in the next chapter.

6.3. Summary

This chapter examined the potential of two approaches as new therapies for stimulating cell recovery and healing in drug-induced acute liver failure and age-related macular degeneration. First, the therapeutic potential of the antioxidant NAC on paracetamol toxicity and on RPE healing capabilities was investigated. While 10 mM NAC caused a slight increase in impedance measurements following paracetamol addition, a similar increase was recorded when adding fresh culture medium. More experiments will therefore be needed to examine the effect of different NAC concentrations. For hiPSC-RPE cultures, NAC had no effect on the migration of the case cell line. However, a decrease in the control cell migration was found after incubating the cells with NAC for 2h. Oxidative stress induced with H_2O_2 had no effect on the case cell line migration, whereas the control cell line exhibited an increased migration rate with stress.

The potential of using electrical stimulation to enhance RPE migration in degenerative diseases was then examined. Externally applied EFs directed RPE cell migration perpendicular to the field. Furthermore, the cells were elongated and changed their alignment with the EF application.

Impedance sensing could offer a real-time, quantitative method of monitoring electrically-stimulated cell migration. In an unsuccessful trial, ECIS flow arrays were used with an externally applied EF to monitor the directed RPE migration. However, the design of the ECIS electrodes led to the damage of the chip when subjected to the DC EF.

A design combining between impedance sensing and an electrically stimulating system is proposed. This system will apply an EF in a radial direction, aiming at stimulating cell migration and directing cells to close a wound from different directions at once, hence speeding up the healing process.

The obtained results together with some limitations and considerations of the proposed disease models-on-a-chip are discussed in the next chapter.

Chapter 7

Discussion

7.1. Stem cell-based disease models: insights into disease mechanisms

7.1.1. Drug-induced liver failure: APAP disruption of tight junctions

Tight Junction (TJ) barrier dysfunction and chemical disruption of adhesion sites are the main features in the pathogenesis of various diseases including hepatitis, inflammatory bowel disease and cancer [341]. Pro-apoptotic signals are also accompanied by diminished intercellular and cell-substrate interactions. Therefore, development of non-invasive technologies, which can assess tight junctions and tissue structure quantitatively, will provide an invaluable tool for pre-clinical drug discovery. In this work, a human HepaRG-based liver biochip, combining human HepaRG cells with impedance spectroscopy, is introduced as a new enabling tool for drug hepatotoxicity screening. Impedance measurements have been used to examine the effect of the model hepatotoxins: paracetamol (APAP), amiodarone and cyclosporine-A (CsA) on the hepatocyte:cholangiocyte co-culture. The measurements showed a dose- and time-dependent decrease in response to the added drugs. Subsequent ECIS modelling of the total impedance signal has revealed previously unknown, temporal effects of APAP toxicity; specifically, the dose-dependent disruption of hepatic tight junctions and cell-matrix adhesion, as reflected by the extracted barrier resistance R_b, and the adhesion parameter α respectively.

Follow-up studies provided a more mechanistic insight into APAP toxicity. Activation of the protein kinase C (PKC) signalling pathway has been shown to affect epithelial barriers [342]. A preliminary study using the HepaRG-based ECIS chip, has demonstrated that the (PKC) activator, phorbol ester (PMA) caused an induced-disruption of TJs similar to APAP. This suggests that APAP toxicity, likely via oxidative stress, may involve a PKC-dependent signalling pathway.

TJ destabilization, evident even at sub-toxic APAP concentration (5 mM), was confirmed via down-regulation of the TJ-specific protein ZO-1 and through TEM ultrastructural imaging; which in turn, showed signs of cellular apoptosis and necrosis, at intermediate doses (10mM). Using confocal immunofluorescent staining, it was shown that APAP-induced diminution in expression of the TJ-associated protein ZO-1, indicative of injury to the epithelial tight junction complex, correlates with a fall in impedance measurements (at 24h).

7.1.2. Age related macular degeneration: a role for cell-adhesion

In this study, a tissue-on-a chip approach was developed to investigate RPE layer damage and repair, in order to mimic retinal macular degeneration. Differences in wound healing between case and control RPE cell lines, associated with an inherited macular degeneration were reproducibly and quantitatively identified. The obtained results demonstrated that the healing rate was reduced in the case cell line and that differences in healing resulted from a reduced migration rate in the case RPE line when compared to the control.

Although the central role of cell adhesion in cell migration is established, the relation between migration rate and adhesion level is more subtle. Generally a cell line will have an optimum cell migration rate at intermediate levels of adhesion to allow both efficient cell-substrate attachment, and release [343]. In the present study, the lower migration rate of the case cell line was found to be associated with a stronger cell-substrate adhesion than that of the control

cell line. Moreover, the cells undergoing migration adopted a radial pattern of wound healing around the site of damage suggesting a single cell "mesenchymal" migration as opposed to collective "Amoeboid" migration [337]. "Mesenchymal" migration is integrin dependent and therefore directly linked to cell adhesion properties.

Adhesion and migration parameters were measured separately and therefore represent independent, quantitative parameters that will help to achieve a better understanding of the complex relationship between adhesion and migration. In the future, this could be used to identify potential therapeutic agents that promote cell migration and healing by modulating cell adhesion (lower or higher).

The case cell line (late onset retinal macular degeneration) results from a mutation in the gene encoding the protein C1QTNF5 [49]. Previous studies have indicated that mutant C1QTNF5 may affect cellular adhesion. Studies performed by Shu et al. [344] found that HEK-EBNA cells stably expressing C1QTNF5 had reduced adhesion to laminin coated plates when compared with cells transfected with wild type protein. However, no differences were found when comparing fibronectin coated plates. These differences might have resulted from a number of causes including inherent adhesion differences in the cell lines [345]. ECIS Medusa microarrays in this study were coated only with FCS and not with laminin, which may result in a different cell-substrate adhesion profile. Further studies will need to be performed using other substrates for comparison.

There have been previous studies on the effect of different agents on the adhesion and migration of RPE [95, 347]. Chan et al. have investigated the role of antioxidants on RPE adhesion and migration using ECIS wound healing assays. They studied the inhibitory effect of (-)-Epigallocatechin gallate (EGCG) [95], resveratrol [220] and lycopene [94] on platelet-derived growth factor (PDGF-BB) induced ARPE19 cell migration and adhesion to fibronectin. They

reported that while all the three antioxidants have inhibited PDGF-BB induced RPE migration, only (-)-EGCG had an effect on adhesion to fibronectin. Reservatrol and lycopene inhibited migration signalling pathways with no effect on adhesion. *In vivo,* optical coherence tomography studies in AMD suggested that aberrant adhesion/migration of intraretinal RPE might underlie progression to more advanced disease [347].

The role of oxidative stress in age-related macular degeneration has been implicated [134, 135, 137]. However, the role of oxidative stress on RPE migration and adhesion is still not clear. Jiang and He [340], have reported that an increase in ROS production enhanced RPE migration under the influence of the oxidative stress agent, tertiary-butyl hydroperoxide (TBH), in small concentrations (up to 30 μM/L). Higher concentrations of TBH on the other hand completely inhibited RPE migration. The focal adhesion kinase (FAK) and vinculin expression in RPE cells decreased and their distribution were changed after the treatment of higher concentrations of TBH.

In another study [348], long term cultured RPE cells (> 5 weeks) were found to develop resistance to negative effects of oxidative stress. ARPE-19 cells cultured for 5 weeks were less sensitive to chronic oxidative stress induced by hydrogen peroxide than those cultured for 1 week. Long-term cultured RPE cells are expected to secrete more ECM proteins and be more adhered to a substrate than more recently cultured cells. This again suggests a relation between cell adhesion and effect of oxidative stress.

When hiPSC-derived RPE cells were subjected to a low concentration (10 μM) of hydrogen peroxide (H_2O_2), it was noticed that RPE migration rate increased for the control but not the case cell line. The different effect of oxidative stress on both cell lines may be attributed to differences in their cell adhesion properties as demonstrated in the results. More studies are

needed where the effect of higher H_2O_2 concentrations on control and case cell migration is investigated in more depth.

7.2. Electric Cell-Substrate Impedance Sensing: Considerations and Limitations

Due to its high sensitivity and non-invasive, quantitative nature, ECIS has emerged as a well-established platform for cellular-based assays. Although the measurement itself is fairly simple, arriving at the right interpretation of the impedance measurements requires a thorough understanding of various factors. It also has to be noted that despite its great capabilities, ECIS has some limitations that need to be considered before designing an experiment.

7.2.1. ECIS sensitivity

Real-time impedance measurements are a reflection of cell growth and maturation, mirroring with high sensitivity the establishment of barrier functions as well as the formation of a confluent cell layer that is ready for manipulation. ECIS measurements are sensitive enough to record cell micromotion reflected by small fluctuations in the measurements, a property that was first reported by Giaever and Keese [13]. Micromotion has been linked to cell metabolism and is observed on ECIS circular electrodes for all cell lines. It can be quantified and used to detect small changes in cell behaviour [349].

Increased fluctuations monitored by ECIS were also reported by Schneider et al. [336] and were attributed to the ruffling of cell membranes during EMT (epithelial-to-mesenchymal-transition) process. The ECIS-based age macular degeneration model presented in Chapter 5, Section 5.2.3 of this thesis have shown similar fluctuations that were monitored during maturation and after wounding of the hiPSC-RPE. A shift in fluctuations, associated with a

change in cell morphology from cuboidal to elongated shape suggesting an EMT/MET transition, was observed.

The high sensitivity of ECIS comes with a downside though, with the impedance not always reflecting a change in cell physiology. Changes in environmental parameters (pH, temperature) will instantly affect the impedance measurements and therefore need to be considered when analyzing the data. A change in medium properties will affect cell behaviour, in response to nutrients for instance, which will be reflected in the measured impedances. In this work, changing the culture media caused a temporary increase in impedance measurements.

7.2.2. ECIS and cell confluency

Establishing a confluent cell layer on ECIS microelectrodes is essential for meaningful modelling [12, 13]. As the model is based on the analysis of current pathways in between the cell-cell junctions, through the cell-electrode gap as well as through the cell membrane, only a confluent cell layer will ensure the validity of the modelling parameters (R_b, α, C_m). This requirement limits the use of the mathematical model. In toxicity assays for instance, the model is only valid during the early hours (< 15h) of the assay when most of the cells are still alive and attached to the electrodes. It is worth mentioning that another model limitation was found when culturing the hiPSC-RPE cells for more than 25 days where poor fitting was observed. This might have been due to the secretion of a large amount of ECM proteins, adding an extra impedance that was not substituted for in ECIS mathematical model.

Confluency is also a necessity for wound healing assays. A confluent cell layer has to be formed before applying a wounding pulse in order to define an accurate migration rate. It will also prevent damage of the electrode when applying an elevated current pulse.

7.2.3. Measurement frequency

ECIS measurements can either be made while scanning through multiple frequencies (MFT mode) or recorded at a specific single frequency (SFT mode). While MFT is required for ECIS modelling, SFT allows for a much higher temporal resolution [350]. However, it does not allow for deconvolution of the impedance into its biologically relevant parameters.

In this study, the impedance was measured systematically at 11 frequencies. For the sake of clarity, the results were presented at two relatively low and high frequencies (4 kHz and 64 kHz) that maintained sensitive meausrements. Because at low frequencies the current flowing between the ECIS microelectrodes can only pass in between or under the cells, low frequencies are normally used to study the tightness of cell-cell junctions as well as the cell-substrate adhesion. At high frequencies on the other hand, the current can capacitively couple through the cell membrane and the measurements are therefore a reflection of electrode cell coverage. Recording ECIS measurements at a frequency of 4 kHz has been reported to accurately reflect changes in cell motility and morphology with high sensitivity. Even slight alterations in cell-cell junctions and cell-substrate adhesion have been detected at this frequency [248, 256]. The measurements at 4 kHz are a reflection of all alterations in sub- and intercellular spaces including tight junctions. At higher monitoring frequencies, intercellular and subcellular resistive components do not contribute to ECIS measurements as much as they do at a lower frequency of 4 kHz. In the higher frequency range (typically $\geq$ 40 kHz), capacitive contributions arising from the cell membranes are detected with high sensitivity as a significant fraction of the current can couple through the membranes. Cell membrane capacitances add to the electrode capacitance in a reciprocal manner following Kirchhoff's laws, resulting in decreasing measured capacitance values with increasing coverage of cells. The measured

capacitance above a certain threshold frequency depends linearly on the fraction of electrode covered with cells [12].

Plots of the resistance and capacitance vs. frequency can be used to determine the appropriate range of frequencies for a certain study. In this work, the highest sensitivity, represented as the largest difference between cell covered electrodes and cell-free measurements, was observed at around 4 kHz for resistance and 64 kHz for capacitance. Hence, the choice of these two frequencies for data representation.

Using the correct frequency is crucial for an efficient wounding assay. Electrical wounding is typically performed at high frequencies, as the current can penetrate the cell membrane leading to irreversible electroporation when applied for a time longer than a specific threshold [84]. However, it has to be noted that long application of a wounding pulse can cause cell death due to heating rather than membrane rupture. Cells may even stick to the electrodes hindering the migration of healthy cells from the wound edges.

7.2.4. Choosing a suitable electrode array design

Selecting a microelectrode array that is suitable for the application in hand is an element worth considering [350]. Arrays with one sensing electrode are usually used to study barrier function and cell migration. The fluctuations in impedance measurements obtained using this type of array will allow for monitoring micromotion, and make it an ideal candidate for wound healing studies. Based on that, 8W1E arrays and Medusa arrays having one or two sensing electrodes per well, were used for wound healing assays in the current studies. On the other hand, arrays with multiple electrodes per well or interdigitated electrodes average the impedance over a larger electrode area, including more cells in the measurements and resulting in reduced fluctuations due to micromotion. For the toxicity assays presented in this work, interdigitated electrodes averaging the response of the cell culture were the electrodes of choice.

It is important to note that even for the ECIS 250 μm diameter electrodes, impedance measurements are still averaged for cells on top of the sensing electrode, which does not allow for studies of single cells.

Small electrodes for single cell studies have been widely employed for extracellular recordings and neural network studies. Decreasing the electrode size to a single cell resolution however, increases the electrode characteristic impedance and noise. Choosing an electrode size again depends on the application. While small electrodes in the range of 10-30 μm might provide more insights on single cell electrical properties and morphology, other properties like barrier functions and cell-cell signalling cannot be studied. However, small electrodes could allow monitoring of unknown behaviours that might have been averaged out by the 250 μm diameter electrodes. When using ECIS 8W1DD arrays to monitor maturation of HepaRG, the smaller electrodes (25-50 μm) were able to resolve peaks in the impedance measurements that followed a specific cycle and were not identified with the 250 μm electrodes. It was suggested that these measurements were a reflection of a circadian rhythm, although a thorough investigation is needed before confirming that. Moreover, electrodes sampling only hepatocytes provided measurements that were significantly different than those of electrodes sampling cholangiocytes. This suggests that small electrodes, that can accommodate a sub-population of cells, will be ideal for co-culture studies. However, it is still difficult to get exactly one or two cells of the same sub-population on one electrode, and cell immobilization techniques might be required in these cases.

ECIS modelling with small electrodes on the 8W1DD arrays, as well as on the MEA chip fabricated in- house, failed. This might have been due to the presence of only 1-2 cells on top of the sensing electrode, not allowing for a full analysis of the current pathways. Electrical wounding on the small electrodes was not an easy process either, and the wounding process

was not controlled. This could have been due to the miniaturized dimensions of the electrode, meaning that cells surrounding the electrode were also killed due to heating, leading to an uncontrolled wound.

Another option when deciding on an array to use for impedance sensing is to use custom chips specifically designed for the study under investigation. While ECIS multi-electrode arrays have multiple electrodes covering a wide area of the culture well, these electrodes are not individually addressed and the final impedance measurements represent an average. Having electrodes that can be addressed individually allows for a more detailed study. In wound healing assays for example, having more than one electrode could reveal information on how cells distant from the wound react to an injury created on another electrode in the same well. In this work, microelectrode arrays with different-sized, individually-addressed square microelectrodes with high spatial resolution were fabricated and used for RPE ECIS wound healing assays. The different-sized electrodes (20 μm, 50 μm, 100 μm, 200 μm) were used to monitor RPE spreading and attachment before wounding assays were conducted. A migration rate comparable to that obtained with ECIS 250 μm circular electrodes was obtained.

7.2.5. Defining wounding thresholds

Defining the right wounding parameters is essential for an efficient wound healing assay. If the wounding pulse is too short, insufficient wounding or electroporation can occur, whereas if the wounding is too long or performed at a low frequency the electrode could be damaged [84]. However, determining a wounding threshold is not an easy task with many factors needing to be considered. Trial and error experiments are normally used to define wounding parameters for a specific cell type. Unfortunately, this method is time consuming and not cost efficient. Arriving at a formula that will relate wounding parameters together and can be used to determine the wounding threshold would be very useful. The extent of the wound is dependent

on the wounding pulse amplitude, frequency and duration as proposed in Equation (5.1). In reality, it is not that simple however as a wounding threshold is also dependent on the cell electrical properties, cell-substrate adhesion, protein coatings present as well as on the conductivity of the culture medium, all of which are reflected by the impedance measurements. Therefore, the impedance of the cell layer to be wounded has to be taken into consideration.

Trial and error experiments were initially performed in this work to define suitable parameters for the keratinocytes wounding model. To wound other cell lines however, theoretical wounding parameters, resulting in the same current density obtained with the previously determined threshold, were derived using Equations (5.2 - 5.4). The same process was used to define suitable wounding parameters for different sized electrodes. Although these theoretically-derived wounding parameters did not cause total cell death in some cases, they were very close to the value of the final wounding pulse. This method therefore dramatically minimized the process of defining the appropriate wounding threshold.

As an alternative to the regular electrical wounding assay, an electric fence method can be used where elevated current pulses are applied onto the sensing electrodes preventing cells from attaching to the electrode. When the fence is lifted off, cells start to migrate inwards to populate the electrodes. An advantage of the electric fence technique is the absence of debris resulting from dead cells around the electrodes that might hinder cell migration. However, for a physiologically relevant wound healing study, a confluent cell layer has to be established and wounded before investigating the healing process. Fencing on the other hand represents a very good tool to study the influence of different protein coatings on cell migration as the electrode surface is not altered by cell attachment or removal.

7.3. Electrical stimulation: Effects on cell alignment and migration

The therapeutic potential of electrical stimulation has been pointed out in the treatment of various diseases including chronic wounds, cancer and spinal cord injuries with varying reported successes. The potential of using electrical stimulation for AMD treatment has been examined in this work. An externally applied EF (50-300mV/mm) caused RPE cells to migrate in a direction perpendicular to that of the EF. RPE directed migration due to an applied EF has been previously reported by various research groups, with different migrating directions being observed. Different cell types have been known to exhibit varying migration capabilities, with different electrotactic response between different cell lines and even between cells originating from the same tissue. Cells derived from the same tissue have been found to migrate in opposite directions or even fail to migrate directionally at all [185, 186]. The effect of electrical stimulation on cell migration is therefore cell-type specific and experiments will have to be conducted for each cell line on an individual basis.

The applied EF has also caused the cells to realign their long axes almost perpendicular to the field. This behavior has been reported before by Gamboa et al. as well as other groups [182]. As cell alignment is known to play a major role in tissue regeneration, applying an external electric field could be used as a therapeutic approach for degenerative diseases [351].

In healthy retina, RPE loss is compensated for by an increase in RPE cell size and migration to close the wound. In the current study, it was observed that applying an external EF was accompanied by RPE cell elongation. The three changes in RPE behavior and physiology: alignment, elongation and directed cell migration, occurring due to the application of an external EF, demonstrate a huge potential for the use of electrical stimulation in AMD treatment.

In a clinical study by Karba et al [199], applying an EF radially, with a positive electrode placed on the wound surrounded by four negative electrodes, was reported to significantly enhance healing of pressure ulcers in patients with spinal cord injuries. On the other hand, applying the EF linearly with the electrodes placed at opposite sides across the wound caused minor improvements. In the current study, both case and control hiPSC-RPE cells were shown to migrate radially after wounding. These results inspired the design of a new stimulating system that is proposed in this work. This system will apply an EF in a radial direction, aiming at stimulating cell migration and directing cells to close a wound from different directions at once, hence speeding up the healing process. Moreover, electrical stimulation will be combined with impedance sensing to provide a method of quantifying the effects of the EF on the cultured cells in real-time. In a previous unsuccessful trial presented in this work, ECIS flow arrays were used in an attempt to monitor RPE migration directed by an external EF. However, due to the design of the ECIS electrodes, with the counter electrode having a different potential at its two ends, the chip was damaged when subjected to the DC EF due to electrochemical corrosion. This issue is addressed in the proposed system with all of the electrodes designed to remain at a constant potential in order to avoid lifting of the gold layer and electrode damage. However, preliminary experiment using charged polystyrene beads in a petri-dish has uncovered other issues underlying the radial stimulation set up. As the EF was dispersed in the petri-dish, very high potentials had to be applied to arrive at the required EF strength. Due to thermal effects accompanying these high voltages, the agar bridges melted during a period of 20-30 minutes. Medium evaporation was also observed.

The design proposed in this work already addresses the issue of medium evaporation, as the electrical stimulation insert is positioned 1mm above the substrate forming a roof and keeping Joule heating at a minimum. This means however that the second design of the insert with windows to allow for optical observations might not be suitable for such studies.

In order to obtain higher EF strengths while applying lower DC potentials, the distance between the inner agar bridge and the outer bridges could be made smaller. Agar bridges with higher conductivity could also be prepared, using for instance 10x PBS instead of the 2x PBS used in this study. More trials will be needed to arrive at an optimized design that can be used for radial electrical stimulation of cell cultures.

7.4. Summary

This chapter discusses the results obtained in this work. Mechanisms underlying the modelled diseases were described; specifically the APAP-induced tight junction disruption as well as the role of cell adhesion in macular degeneration. Some considerations and limitations surrounding ECIS measurements and electrical wounding were also presented. Finally, the therapeutic potential of electrical stimulation in degenerative retinal diseases was discussed.

Chapter 8

Conclusions and Perspectives

This chapter provides a summary of the work presented in this thesis with an outlook on areas for future developments, followed by some concluding remarks.

8.1. Summary

In this thesis, the need for a physiologically relevant *in vitro* disease model that can be investigated quantitatively and reproducibly has been addressed through developing a tissue-on-a-chip approach. The disease models combining stem cell technology and electric cell-substrate impedance sensing, provided a high-throughput platform that can investigate disease mechanisms in real-time. The first model-on-a-chip was developed for drug-induced acute liver failure studies. The progenitor cell line, HepaRG, was cultured on ECIS microelectrodes and allowed to terminally differentiate into a hepatocyte:cholangiocyte co-culture. Hepatotoxicity assays were then conducted using the model hepatotoxins: Paracetamol, Amiodarone and Cyclosporine-A. This hybrid technology uncovered an unknown outcome of paracetamol toxicity; temporal, dose-dependent disruption of intercellular (tight) junctions and cell–substrate adhesions, detectable even at sub-toxic APAP dose. These tight junction disruptions were confirmed using TEM imaging and fluorescence immunostaining of the tight junction protein (ZO-1). Further validating assays were conducted using phorbol-ester that is known to disrupt tight junctions, and NAPQI, a product of APAP metabolism.

The second model-on-a-chip developed in this work is for age-related macular degeneration. An hiPSCs-derived model of the RPE layer was developed directly on ECIS gold microelectrode arrays and its robustness, reproducibility and suitability was quantitatively addressed by real-time impedance sensing before initiating an integrated electrical wound healing assay. This method mimicked RPE cell loss accompanying macular degeneration and was used to detect variations in migration rate between a cell line derived from a patient with late-onset retinal macular degeneration versus a control cell line derived from an unaffected sibling. The migration rate of the case cell line was significantly lower than that of the healthy control. ECIS modelling and biochemical assays showed that this might be related to the stronger cell-substrate adhesion expressed by the case cell line. Further experiments with an immortalized RPE cell line, confirmed the relationship between higher adhesion and low migration rates.

To better understand ECIS electrical wounding, keratinocytes were initially used for wounding assays. A wounding threshold for the HEKa cell line was determined and a formula relating the applied wounding parameters to wound severity was proposed. Furthermore, cell migration assays were conducted on the HepaRG cell line showing that this cell line does not migrate after wounding.

Microelectrode arrays with high spatial resolution and different-sized, individually- addressed microelectrodes for ECIS measurements were designed and fabricated in-house. The fabricated square microelectrodes were used to electrically wound RPE using ECIS and a migration rate comparable to that obtained with ECIS circular electrodes was determined.

Two therapeutic approaches have been examined in this work: antioxidants and electrical stimulation. The effect of the antioxidant NAC on paracetamol toxicity as well as on speeding up RPE migration was investigated. 10 mM NAC following the paracetamol challenge, showed

some signs of cell recovery with a slight increase in impedance measurements observed after incubating with the antioxidant for 24h. However, a similar increase in impedance was recorded when adding fresh culture medium. For NAC-stimulated hiPSC-RPE cultures, no effect on the migration of the case cell line was monitored. On the other hand, the control cell migration was found to decrease after incubating the cells with NAC for 2h. The effect of NAC on oxidatively-stressed hiPSC-RPE cells was also examined. However, no conclusive results were achieved. More experiments will be needed to fully understand the role of oxidative stress in RPE migration and to test the effect of different NAC concentrations on the recovery of HepaRG and RPE.

The potential of using electrical stimulation to enhance RPE migration in degenerative diseases has been demonstrated. Externally applied EFs have been shown to direct cell migration almost perpendicular to the EF. The cells have also been observed to elongate and to change their alignment due to EF application.

Combining impedance sensing and electrical stimulation will allow for a quantitative method that can monitor electrically-stimulated cell migration in real-time. In an unsuccessful trial, ECIS impedance measurements were combined with electrical stimulation to monitor the directed RPE migration. However, the design of the ECIS electrodes led to the chip damage when subjected to the DC EF. Finally, a design that could allow electrical stimulation to be applied radially and quantitatively monitor changes in cellular behaviour within the EF has been proposed.

8.2. Perspectives

8.2.1. Disease models-on-a-chip: Quantifying disease kinetics

The liver disease-model developed in this work has revealed unknown TJ-disruption in paracetamol-induced acute liver failure; whereas the age-related macular degeneration model pointed out towards a role for adhesion in RPE degeneration. The effect of other drugs and hepatotoxins on liver cells can be examined. In AMD, deriving diseased cell lines from several patients is required for a more thorough understanding of the genetic disorder.

Combining stem cells with microelectrode technologies and impedance sensing, various diseases can be modelled. Stem cell-based disease models-on-a-chip can be developed to provide high throughput platforms for the quantification, characterization and evaluation of different aspects of the modelled diseases. These models can therefore be employed to develop novel drugs and therapies for incurable diseases, as well as gain more insights on kinetics and underlying mechanisms of curable ones.

8.2.2. Therapeutic approaches and translational medicine

Using the disease models-on-a-chip, different therapies and approaches can be examined and evaluated. Preliminary studies have explored the role of the antioxidant NAC in cell recovery. More studies examining the effects of other antioxidants with different concentrations and various incubation times on cell migration and recovery are needed. The effect of TJ-stabilizing agents in ALF, as well as that of adhesion modulating agents in AMD could help arrive at treatments for the two diseases.

Electrical stimulation has been used in various clinical trials to treat different diseases, with varying successes, and has been reported to have a great therapeutic potential. A new design

has been proposed in this work to allow for radial electrical stimulation instead of applying the EF linearly in one direction. More experiments are required to optimize such design for cellular assays. Moreover the effect of electrical stimulation on different cell lines post to drug- and electrically-induced injuries should be examined in order to evaluate the potential role of radial electrical stimulation in therapy.

8.2.3. Perspectives in MEA designs

In this work, arrays with 6 and 16 microelectrodes/well were designed. MEAs with higher electrode densities and smaller electrode spacings are required for a higher monitoring resolution. Such arrays can provide more detail on the response of a cell population. In wound healing assays for instance, the difference in response/migration of cells around the wound edge as opposed to those further away from the wound can be investigated. Furthermore, small electrodes can be employed for these high density arrays to allow for single cell studies and sub-population monitoring. They could also reveal unknown kinetics that could have been averaged out by larger electrodes.

8.3. Conclusions

Stem cell-based disease models-on-a-chip are cutting-edge tools in disease modelling that have emerged as new paradigms in drug development and personalized medicine.

The AMD disease model-on-a-chip developed in this work is a powerful platform for translational studies. Combining hiPSCs technology with impedance sensing, it is amenable to a high throughput with considerable potential to investigate novel therapies by enabling real-time, quantitative and reproducible patient-specific RPE cell repair studies. The proposed liver-on-a-chip approach enables non-invasive assessment of discrete structural elements, which maintain tissue polarity; providing a novel tool for pre-clinical drug discovery, disease

modelling, and therapeutic strategies. The ALF model-on-a-chip allowed for the discovery of a previously unknown effect of paracetamol on the liver; disruption of cell-cell tight junctions and cell adhesion. Finally, electrical stimulation has been shown to control and direct cell migration and alignment, and has therefore a great therapeutic potential in degenerative diseases.

References

1. Thomson, J.A., et al., *Embryonic stem cell lines derived from human blastocysts.* Science, 1998. **282**: p. 1145-1147.
2. Borooah , S., et al., *Using human induced pluripotent stem cells to treat retinal disease.* Progress in Retinal and Eye Research, 2013. **37**: p. 163-181.
3. Hall, S.S., *Diseases in a dish.* Scientific American, 2011. **304(3)**: p. 40-45.
4. Wichterle, H., et al., *Directed Differentiation of Embryonic Stem Cells into Motor Neurons.* Cell, 2002. **110**(3): p. 385-397.
5. Rodriguez, L.L. and I.C. Schneiderw, *Directed cell migration in multi-cue environments.* Integrative Biology, 2013. **5**: p. 1306.
6. Takahashi, K. and S. Yamanaka, *Induction of Pluripotent Stem Cells from Mouse Embryonic and Adult Fibroblast Cultures by Defined Factors.* Cell, 2006. **126**: p. 663-676.
7. Tiscornia, G., E. Vivas, and J. Izpisúa Belmonte, *Diseases in a dish: modeling human genetic disorders using induced pluripotent cells.* Nature Medicine, 2011. **17**(12): p. 1570-1576.
8. Inoue, H. and S. Yamanaka, *The use of induced pluripotent stem cells in drug development.* Clinical pharmacology & Therapeutics, 2011. **89**(5): p. 655-661.
9. Sterneckert, J.L., P. Reinhardt, and H.R. Schöler, *Investigating human disease using stem cell models.* Nature Reviews, 2014. **15**: p. 625-639.
10. Park, H.E., et al., *Real-Time Monitoring of Neural Differentiation of Human Mesenchymal Stem Cells by Electric Cell-Substrate Impedance Sensing.* Journal of Biomedicine and Biotechnology,2011. **2011**: p. 1-8.
11. Hildebrandt, C., et al., *Detection of the osteogenic differentiation of mesenchymal stem cells in 2D and 3D cultures by electrochemical impedance spectroscopy.* J Biotechnol, 2010. **148**: p. 83-90.
12. Wegener, J., C.R. Keese, and I. Giaever, *Electric Cell-Substrate Impedance Sensing (ECIS) as a Noninvasive Means to Monitor the Kinetics of Cell Spreading to Artificial Surfaces.* Experimental Cell Research, 2000. **259**: p. 158-166.
13. Giaever, I. and C.R. Keese, *Micromotion of mammalian cells measured electrically.* PNAS, 1991. **88**: p. 7896-7900.
14. Jun, H., et al., *Effect of cell senescence on the impedance measurement of adipose tissue-derived stem cells.* Enzyme Microb Technol, 2013. **53**: p. 302-306.
15. Lee, R., et al., *Real-time monitoring of adipocyte differentiation using a capacitance sensor array.* Lab chip, 2013. **13**: p. 3410-3416.
16. Zhou, J., et al., *Assessment of cadmium-induced hepatotoxicity and protective effects of zinc against it using an improved cell-based biosensor.* Sensors and Actuators A, 2013. **199**: p. 156-164.
17. Yeon, J.H. and J.-K. Park, *Cytotoxicity test based on electrochemical impedance measurement of HepG2 cultured in microfabricated cell chip.* Analytical Biochemistry, 2005. **341**: p. 308-315.
18. Meissner, R., et al., *Distinguishing drug-induced minor morphological changes from major cellular damage via label-free impedimetric toxicity screening.* Lab Chip, 2011. **11**: p. 2352-2361.

19. Johnson, P.T., et al., *Synaptic Pathology, altered gene expression, and degeneration in photoreceptors impacted by drusen.* Invest Ophthalmol Vis Sci, 2005. **46**(12): p. 4788-4795.
20. *Macular degeneration*. Accessed: 1 August 2015; Available from: http://www.nhs.uk/conditions/macular-degeneration/Pages/Introduction.aspx.
21. Cherry, A.B. and Q.D. George, *Reprogrammed cells for disease modelling and regenerative medicine.* Annu Rev Med, 2013. **64**: p. 277-290.
22. Colman, A. and O. Dreesen, *Pluripotent Stem Cells and Disease Modeling.* Cell Stem Cell, 2009. **5**: p. 244-247.
23. Grskovic, M., et al., *Induced pluripotent stem cells - opportunities for disease modelling and drug discovery.* Nature Reviews, 2011. **10**: p. 915-929.
24. Williams, R., *Classification and clinical syndromes of acute liver failure* in *Acute Liver Failure*. 1996, Cambridge University Press. p. 1-9.
25. Fontana, R.J., *Acute Liver Failure including Acetaminophen Overdose.* Med clin North Am., 2008. **92**(4): p. 761-794.
26. Hinson, J.A., D.W. Roberts, and L.P. James, *Mechanisms of acetaminophen-induced liver necrosis.* Handbook of experimental pharmacology, 2010: p. 369-405.
27. Jaeschke, H., M.R. McGill, and A. Ramachandran, *Oxidant stress, mitochondria and cell death mechanisms in drug-induced liver injury: lessons from acetaminophen hepatotoxicity.* Metab Rev, 2012. **44**: p. 88-106.
28. Ishibashi, H., et al., *Liver architecture, cell function, and disease.* Semin Immunopathol, 2009. **31**: p. 399-409.
29. Navarro, M., *Improved predicitve models for pre-clinical drug toxicity studies*. 2014, The University of Edinburgh.
30. Decaens, C., et al., *Which in vitro models could be best used to study hepatocyte polarity?* Biology of the cell/ under the auspices of the European Cell Biology Organization, 2008. **100**: p. 387-398.
31. Andersson, T.B., K.P. Kanebratt, and J.G. Kenna, *The HepaRG cell line: a unique in vitro tool for understanding drug metabolism and toxicology in human.* Expert Opin Drug Metab Toxicol, 2012. **8**: p. 909-920.
32. Le Vee, M., et al., *Polarized expression of drug transporters in differentiated human hepatoma HepaRG cells.* Toxicology in vitro, 2013. **27**: p. 1979-1986.
33. Antherieu, S., et al., *Oxidative stress plays a major role in chlorpromazine-induced cholestasis in human HepaRG cells.* Hepatology, 2013. **57**: p. 1518-1529.
34. Sharanek, A., et al., *Different dose-dependent mechanisms are involved in early cyclosporine a-induced cholestatic effects in hepaRG cells.* Toxicological Sciences, 2014. **141**: p. 244-253.
35. Mee, C.J., et al., *Polarisation Restricts Hepatitis C Virus Entry into HepG2 Hepatoma Cells.* Journal of Virology, 2009. **83**(12): p. 6211-6221.
36. LeCluyse, E.L., et al., *Organotypic liver culture models: meeting current challenges in toxicity testing.* Critical reviews in toxicology, 2012. **42**: p. 501-548.
37. Takebe, T., et al., *Vascularised and functional human liver from an iPSC-derived organ bud transplant.* Nature, 2013. **499**: p. 481-484.
38. Gomez-Lechon, M.J., et al., *Competency of different cell models to predict human hepatotoxic drugs.* Expert Opinion on Drug Metabolism & Toxicology, 2014. **10**(11): p. 1553-1568.
39. Antherieu, S., et al., *Optimisation of the HepaRG cell model for drug metabolism and toxicity studies.* Toxicology in Vitro, 2012. **26**: p. 1278-1285.
40. McGill, M.R., et al., *HepaRG Cells: A Human Model to Study Mechanisms of Acetaminophen Hepatotoxicity.* HEPATOLOGY, 2011. **53**(3): p. 974-982.

41. Swift, B., N.D. Pfeifer, and K.L.R. Brouwer, *Sandwich-Cultured Hepatocytes: An In Vitro Model to Evaluate Hepatobiliary Transporter-Based Drug Interactions and Hepatotoxicity.* Drug Metab Rev, 2010. **42**(3): p. 446-471.
42. Bressler, N.M., S.B. Bressler, and S.L. Fine, *Age-related macular degeneration.* Survey of Ophthalmology, 1988. **32**(6): p. 375-413.
43. Strauss, O., *The Retinal Pigment Epithelium in Visual Function.* Physiol Rev, 2005. **85**: p. 845-881.
44. Kolb, H., *Simple Anatomy of the Retina*, in *The organization of the retina and visual system*, H. Kolb, E. Fernandez, and R. Nelson, Editors. 1995, Univeristy of Utah Health Sciences Center: Salt Lake City.
45. *Eye Anatomy Detail*. Accessed: 1 July 2015; Available from: http://www.medicinenet.com/imagecollection/eye_anatomy_detail_picture/picture.html
46. Cai H. and Del Priore L.V., *Bruch membrane aging alters the gene expression profile of human retinal pigment epithelium.* Curr Eye Res., 2006. **31**(2): p. 181-189.
47. Thurman, J.M., et al., *Oxidative stress renders retinal pigment epithelial cells susceptible to complement mediated injury.* J Biol Chem., 2009. **284** (25): p. 16939-16947.
48. Panda-Jonas S., Jonas J.B., and J.-Z. M., *Retinal pigment epithelial cell count, distribution, and correlations in normal human eyes.* Am J Ophthalmol., 1996. **121**(2): p. 181-189.
49. Hayward, C., et al., *Mutation in a short-chain collagen gene, CTRP5, results in extracellular deposit formation in late-onset retinal degeneration: a genetic model for age-related macular degeneration.* Hum Mol Genet, 2003. **12**(20): p. 2657-2667.
50. Tu, X. and K. Palczewski, *Crystal structure of the globular domain of C1QTNF5: Implications for late-onset retinal macular degeneration.* J Struct Biol, 2012. **180**(3): p. 439-446.
51. Mandal, M., et al., *CTRP5 is a membrane-associated and secretory protein in the RPE and ciliary body and the S163R mutation of CTRP5 impairs its secretion.* Invest Ophthalmol Vis Sci, 2006. **47**(12): p. 5505-5513.
52. Borooah, S., et al., *Late-onset retinal macular degeneration: clinical insights into an inherited retinal degeneration.* Postgrad Med J, 2009. **85**: p. 495-500.
53. Meyer J.S., et al., *Modeling early retinal development with human embryonic and induced pluripotent stem cells.* PNAS, 2009. **106**: p. 16698-16703.
54. Takahashi K., et al., *Induction of pluripotent stem cells from adult human fibroblasts by defined factors.* Cell 2007. **131**: p. 861-872.
55. Gamal, W., et al., *Real-time quantitative monitoring of hiPSC-based model of macular degeneration on Electric Cell-Substrate Impedance Sensing microelectrodes.* Biosensors and Bioelectronics, 2015. **71**: p. 445-455.
56. Ciambrone, G.J., et al., *Cellular Dielectric Spectroscopy: A Powerful New Approach to Label-Free Cellular Analysis.* Journal of Biomolecular Screening, 2004. **9**(6): p. 467-480.
57. Atienzar, F.A., et al., *Predictivity of dog co-culture model, primary human hepatocytes and HepG2 cells for the detection of hepatotoxic drugs in humans.* Toxicology and Applied Pharmacology, 2014. **275**: p. 44-61.
58. Materne, E., A.G. Tonevitsky, and U. Marx, *Chip-based liver equivalents for toxicity testing - organotypicalness versus cost-efficient high throughput.* Lab on a Chip, 2013. **13**: p. 3481-3495.
59. Kustermann, S., et al., *A label-free, impedance-based real time assay to identify drug-induced toxicities and differentiate cytostatic from cytotoxic effects.* Toxicology in Vitro, 2013. **27**: p. 1589-1595.

60. Plumb, J.A., *Cell Sensitivity Assay: The MTT Assay*, in *Cancer Cell Culture: Methods and Protocols*, S.P. Langdon, Editor. Humana Press Inc.: Totowa, New Jersey.
61. Ishiyama, M., et al., *A Combined Assay of Cell Viability and in vitro Cytotoxicity with a Highly Water-Soluble Tetrazolium Salt, Neural Red and Crystal Violet.* Biol. Pharm. Bull., 1996. **19**(11): p. 1518-1520.
62. Mandel, L.J., R.B. Doctor, and R. Bacallao, *ATP depletion: a novel method to study junctional properties in epithelial tissues. II. Internalization of Na+, K+-ATPase and E-cadherin.* Journal of Cell Science, 1994. **107**: p. 3315-3324.
63. Meissner, R., B. Eker, and P. Renaud, *Continuous and label-free toxicity screening of human hepatocytes on chip reveals frequency-dependent impedance profiles*, in *MicroTAS 2011*. 2011. p. 1487-1489.
64. Abassi, Y.A., et al., *Kinetic Cell-Based Morphological Screening: Prediction of Mechanism of Compound Action and Off-Target Effects.* Chemistry & Biology, 2009. **16**: p. 712-723.
65. Asphahani, F. and M. Zhang, *Cellular impedance biosensors for drug screening and toxin detection.* Analyst, 2007. **132**: p. 835-841.
66. Opp, D., et al., *Use of electric cell-substrate impedance sensing to assess in vitro cytotoxicity.* Biosensors and Bioelectronics, 2009. **24**: p. 2625-2629.
67. Atienzar, F.A., et al., *The Use of Real-Time Cell Analyser Technology in Drug Discovery: Defining Optimal Cell Culture Conditions and Assay Reproducibility with Different Adherent Cellular Models.* J Biomol Screen, 2011. **16**: p. 575-587.
68. Xiao, C. and J.H.T. Luong, *Assessment of cytotoxicity by emerging impedance spectroscopy.* Toxicology and Applied Pharmacology, 2005. **206**: p. 102-112.
69. Xiao, C., et al., *Assessment of Cytotoxicity Using Electric Cell-Substrate Impedance Sensing: Concentration and Time Response Function Approach.* Analaytical Chemistry, 2002. **74**: p. 5748-5753.
70. Pradhan, R., et al., *Frequency dependent impedimetric cytotoxic evaluation of anticancer drug on breast cancer cell.* Biosensors and Bioelectronics, 2014. **55**: p. 44-50.
71. Ehret, R., et al. *Cell-based in vitro systems for continuous monitoring of bioenergetics and cell impedance*. *SENSOR +TEST* Proceedings,2011. **C8**: p. 512-515.
72. Friedl, P. and D. Gilmour, *Collective cell migration in morphogenesis, regeneration and cancer.* Nature Reviews. Molecular Cell Biology, 2009. **10**: p. 445-457.
73. Riahi, R., et al., *Advances in Wound-Healing Assays for Probing Collective Cell Migration.* Journal of Laboratory Automation, 2012. **17**(1): p. 59-65.
74. Li, M., J.D. Firth, and E.E. Putnins, *An in vitro analysis of mechanical wounding-induced ligand-independent KGFR activation.* Journal of Dermatological Science, 2009. **53**: p. 182-191.
75. M. Fronzaa, et al., *Determination of the wound healing effect of Calendula extracts using the scratch assay with 3T3 fibroblasts.* Journal of Ethnopharmacology, 2009. **126**: p. 463-467.
76. Lee, J., et al., *Stamp Wound Assay for Studying Coupled Cell Migration and Cell Debris Clearance.* Langmuir, 2010. **26**(22): p. 16672-16676.
77. Poujade, M., et al., *Collective migration of an epithelial monolayer in response to a model wound.* PNAS, 2007. **104**(41): p. 15988-15993.
78. Doran, M.R., et al., *A cell migration device that maintains a defined surface with no cellular damage during wound edge generation.* Lab Chip, 2009. **9**: p. 2364-2369.
79. Varani, J., W. Orr, and P.A. Ward, *A Comparison of the Migration Patterns of Normal and Malignant Cells in Two Assay Systems.* Am J Pathol, 1978. **90**: p. 159-172.
80. Legrand, C., et al., *Airway Epithelial Cell Migration Dynamics: MMP-9 Role in Cell-Extracellular Matrix Remodeling.* The Journal of Cell Biology, 1999. **146**(2): p. 517-529.

81. Rolli, C.G., et al., *Switchable adhesive substrates: Revealing geometry dependence in collective cell behavior.* Biomaterials, 2012. **33**: p. 2409-2418.
82. Zordan, M.D., et al., *A High Throughput, Interactive Imaging, Bright-Field Wound Healing Assay.* Cytometry Part A, 2011. **79A**: p. 227-232.
83. Zhang, M., et al., *A simple microfluidic strategy for cell migration assay in an in vitro wound-healing model.* Wound Rep Reg, 2013. **21**: p. 897-903.
84. Keese, C.R., et al., *Electrical Wound-Healing Assay for cells in vitro.* PNAS, 2004. **101**(6): p. 1554-1559.
85. Noiri, E., et al., *Permissive Role of Nitric Oxide in Endothelin-induced Migration of Endothelial Cells.* J. Biol. Chem., 1997. **272**(3): p. 1747-1752.
86. Noiri, E., et al., *Podokinesis in endothelial cell migration: role of nitric oxide.* Am. J. Physiol, 1998. **274**: p. C236- C244.
87. Jiang, W.G., et al., *Influence of interleukin-8 (IL-8) and IL-8 receptors on the migration of human keratinocytes, the role of PLC-γ and potential clinical implications.* Experimental and Therapeutic Medicine, 2012. **3**: p. 231-236.
88. Shi, Y., et al., *CARP, a Cardiac Ankyrin Repeat Protein, Is Up-Regulated during Wound Healing and Induces Angiogenesis in Experimental Granulation Tissue.* American Journal of Pathology, 2005. **166**(1): p. 303-312.
89. Waters, C.M., et al. *Cell migration activated by platelet-derived growth factor receptor is blocked by an inverse agonist of the sphingosine 1-phosphate receptor-1*. The FASEB Journal express article, 2005. **20**(3): p.509-511.
90. Lorenowicz, M.J., et al., *PKA and Epac1 regulate endothelial integrity and migration through parallel and independent pathways.* European Journal of Cell Biology, 2008. **87**: p. 779-792.
91. Charrier, L., et al., *ADAM-15 inhibits wound healing in human intestinal epithelial cell monolayers.* Am J Physiol Gastrointest Liver Physiol, 2005. **288**: p. G346-G353.
92. Kucharzik, T., et al., *Activation of epithelial CD98 glycoprotein perpetuates colonic inflammation.* Laboratory Investigation, 2005. **85**: p. 932-941.
93. Jiang, W.G., et al., *Expression of WAVEs, the WASP (Wiskott–Aldrich syndrome protein) family of verprolin homologous proteins in human wound tissues and the biological influence on human keratinocytes.* Wound Repair and Regeneration, 2010. **18**: p. 594-604.
94. Chan, C.M., et al., *Lycopene inhibits PDGF-BB-induced retinal pigment epithelial cell migration by suppression of PI3K/Akt and MAPK pathways.* Biochemical and Biophysical Research Communications, 2009. **388**: p. 172-176.
95. Chan, C.M., et al., *Effects of (-)-epigallocatechin gallate on RPE cell migration and adhesion.* Molecular Vision, 2010. **16**: p. 586-595.
96. Heijink, I.H., et al., *Characterisation of cell adhesion in airway epithelial cell types using electric cell–substrate impedance sensing.* Eur Respir J, 2010. **35**: p. 894-903.
97. Schiller, K.R., P.J. Maniak, and S.M. O'Grady, *Cystic fibrosis transmembrane conductance regulator is involved in airway epithelial wound repair.* Am J Physiol Cell Physiol, 2010. **299**: p. C912-C921.
98. Lundien, M.C., et al., *Induction of MCP-1 Expression in Airway Epithelial Cells: Role of CCR2 Receptor in Airway Epithelial Injury.* Journal of Clinical Immunology, 2002. **22**(3): p. 144-152.
99. Gorshkova, I., et al., *Protein Kinase C- Regulates Sphingosine 1-Phosphate-mediated Migration of Human Lung Endothelial Cells through Activation of Phospholipase D2, Protein Kinase C- , and Rac1.* J. Biol. Chem., 2008. **283**(17): p. 11794-11806.
100. Heijink, I.H., et al., *Cigarette smoke impairs airway epithelial barrier function and cell–cell contact recovery.* Eur Respir J, 2012. **39**: p. 419-428.

101. Sanders, A.J., et al., *Activated leukocyte cell adhesion molecule impacts on clinical wound healing and inhibits HaCaT migration.* International Wound Journal, 2011. **8**(5): p. 500-507.
102. Estrada, R., et al., *Up-regulating Sphingosine 1-Phosphate Receptor-2 Signaling Impairs Chemotactic, Wound-healing, and Morphogenetic Responses in Senescent Endothelial Cells.* J. Biol. Chem., 2008. **283**: p. 30363-30375.
103. Helfer, B., et al., *Caspase-8 Promotes Cell Motility and Calpain Activity under Nonapoptotic Conditions.* Cancer Research, 2006. **66**(8): p. 4273-4278.
104. Astrid Escudero-Esparza , A., W.G. Jiang, and T.A. Martin, *Claudin-5 participates in the regulation of endothelial cell motility.* Mol Cell Biochem, 2012. **362**: p. 71-85.
105. Jiang, W.G., et al., *Eplin-alpha expression in human breast cancer, the impact on cellular migration and clinical outcome.* Molecular Cancer, 2008. **7**: p. 71-81.
106. Kwon, M., et al., *Functional Characterization of Filamin A Interacting Protein 1–Like, a Novel Candidate for Antivascular Cancer Therapy.* Cancer Research, 2008. **68**: p. 7332-7341.
107. Horinaga, M., et al., *Novel Enhanced Lung-Colonizing Variant of Murine MBT-2 Bladder Cancer Cells.* UROLOGY, 2005. **66**: p. 676-681.
108. Jinfeng Chen, J., et al., *Placenta Growth Factor, PLGF, Influences the Motility of Lung Cancer Cells, the Role of Rho Associated Kinase, Rock1.* Journal of Cellular Biochemistry, 2008. **105**: p. 313-320.
109. Wu, N.L., et al., *Zeaxanthin inhibits PDGF-BB-induced migration in human dermal fibroblasts.* Experimental Dermatology, 2010. **19**: p. e173-e181.
110. Saxena, N.K., et al., *Concomitant Activation of the JAK/STAT, PI3K/AKT, and ERK Signaling Is Involved in Leptin-Mediated Promotion of Invasion and Migration of Hepatocellular Carcinoma Cells.* Cancer Research, 2007. **67**: p. 2497-2507.
111. Ablin, R.J., et al., *Prostate transglutaminase (TGase-4) antagonizes the anti-tumour action of MDA-7/IL-24 in prostate cancer.* Journal of Translational Medicine, 2011. **9**: p. 49.
112. Lee, C.C., et al., *Overexpression of sprouty 2 inhibits HGF/SF-mediated cell growth, invasion, migration, and cytokinesis.* Oncogene, 2004. **23**: p. 5193-5202.
113. Hsu, C., et al., *Effects of negative pressures on epithelial tight junctions and migration in wound healing.* Am J Physiol Cell Physiol, 2010. **299**: p. 528-534.
114. Young, E.F. and L.B. Smilenov, *Impedance-Based Surveillance of Transient Permeability Changes in Coronary Endothelial Monolayers after Exposure to Ionizing Radiation.* Radiation Research, 2011. **176**(4): p. 415-424.
115. Norling, L.V., et al., *Cutting Edge: Humanized Nano-Proresolving Medicines Mimic Inflammation-Resolution and Enhance Wound Healing.* J Immunol, 2011. **186**: p. 5543-5547.
116. Wu, T.H., et al., *Reducing scar formation by regulation of IL-1 and MMP-9 expression by using sustained release of prednisolone-loaded PDLL microspheres in a murine wound model.* J Biomed Mater Res Part A, 2013. **101A**: p. 1165-1172.
117. Toh, Y., K. Blagovic, and J. Voldman, *Advancing stem cell research with microtechnologies: opportunities and challenges.* Integr Biol (Camb), 2010. **2**: p. 305-325.
118. Cagnin, S., et al., *Overview of Micro- and Nano-Technology Tools for Stem Cell Applications: Micropatterned and Microelectronic Devices.* Sensors, 2012. **12**: p. 15947-15982.
119. Ricotti, L. and A. Menciassi, *Engineering Stem Cells For Future Medicine.* IEEE Transactions on Biomedical Engineering, 2013. **60**(3): p. 727-734.

120. Cho, S. and H. Thielecke, *Electrical characterization of human mesenchymal stem cell growth on microelectrode.* Microelectronic Engineering, 2008. **85**: p. 1272-1274.
121. Fan, J.Y., et al., *Morphological Changes of the 3T3-L1 Fibroblast Plasma Membrane Upon Differentiation to the Adipocyte Form.* J Cell Sci, 1983. **61**: p. 219-230.
122. Angstmann, M., et al., *Monitoring human mesenchymal stromal cell differentiation by electrochemical impedance sensing.* Cytotherapy, 2011. **13**: p. 1074-1089.
123. Kramer, A.H., et al., *Real-time monitoring of 3T3-L1 preadipocyte differentiation using a commercially available electric cell-substrate impedance sensor system.* Biochem Biophys Res Commun, 2014. **443**: p. 1245-1250.
124. Bagnaninchi, P.O. and N. Drummond, *Real-time Label-free Monitoring of Adipose-derived Stem Cell Differentiation with Electric Cell-substrate Impedance Sensing.* PNAS, 2011. **108**(16): p. 6462-6467.
125. Dalton, B.A., et al., *Role of the heparin binding domain of fibronectin in attachment and spreading of human bone-derived cells.* J Cell Sci, 1995. **108**: p. 2083-2092.
126. Park, I., et al., *The correlation between human adipose-derived stem cells differentiation and cell adhesion mechanism.* Biomaterials, 2009. **30**: p. 6835-6843.
127. Maercker, C., et al., *Development of Live Cell Chips to Monitor Cell Differentiation Processes.* Engineering in Life Sciences, 2008. **8**(1): p. 33-39.
128. Woodbury, D., et al., *Adult Rat and Human Bone Marrow Stromal Cells Differentiate Into Neurons.* J Neurosci Res, 2000. **61**: p. 364-370.
129. Korin, N. and S. Levenberg, *Engineering Human Embryonic Stem Cell Differentiation.* PNAS, 2007. **24**: p. 243-262.
130. Corradetti, B., et al., *Paracrine signalling events in embryonic stem cell renewal mediated by affinity targeted nanoparticles.* Biomaterials, 2012: p. 1-10.
131. Lobo, V., et al., *Free radicals, antioxidants and functional foods: Impact on human health.* Pharmacognosy Reviews, 2010. **4**(8): p. 118-126.
132. Soneja, A., M. Drews, and T. Malinski, *Role of nitric oxide, nitroxidative and oxidative stress in wound healing.* Pharmacological Reports, 2005. **57**: p. 108-119.
133. Masutani, H., *Oxidative stress and redox imbalance in acetaminophen toxicity.* The Pharmacogenomics Journal, 2001. **1**: p. 165-166.
134. Jarrett, S.G. and M.E. Boulton, *Consequences of oxidative stress in age-related macular degeneration.* Molecular Aspects of Medicine, 2012. **33**: p. 399-417.
135. Cai, J., et al., *Oxidative Damage and Protection of the RPE.* Progress in Retinal and Eye Research, 2000. **19**(2): p. 205-221.
136. Schimel, A.M., et al., *N-Acetylcysteine Amide (NACA) Prevents Retinal Degeneration by Up-Regulating Reduced Glutathione Production and Reversing Lipid Peroxidation.* Am J Pathol, 2011. **178**: p. 2032-2043.
137. Beatty, S., et al., *The Role of Oxidative Stress in the Pathogenesis of Age-Related Macular Degeneration.* Surv Ophthalmol, 2000. **45**(2): p. 115-134.
138. Liu, Y., et al., *Citreoviridin induces ROS-dependent autophagic cell death in human liver HepG2 cells.* Toxicon, 2015. **95**: p. 30-37.
139. Downs, I., et al., *The ROS Scavenger, NAC, regulates Hepatic Va14iNKT Cells Signaling during Fas mAb-Dependent Fulminant Liver Failure.* PLoS ONE, 2012. **7**(6): p. e38051.
140. Tsai, G.Y., et al., *Effect of N-acetylcysteine on the early expression of inflammatory markers in the retina and plasma of diabetic rats.* Clinical and Experimental Ophthalmology, 2009. **37**: p. 223-231.
141. McCaig, C.D., B. Song, and A.M. Rajnicek, *Electrical Dimensions in Cell Science.* Journal of Cell Science, 2009. **122**: p. 4267-4276.
142. Gedded, L.A. and H.E. Hoff, *The discovery of bioelectricity and current electricity. The Galvani-Volta controversy.* IEEE Spectrum, 1971. **8**: p. 38-46.

143. Hoff, H.E., *Galvani and the pre-Galvanian electrophysiologists.* Ann Sci, 1936. **1**: p. 157-172.
144. Piccolino, M., *Luigi Galvani and animal electricity: two centuries after the foundation of electrophysiology.* Brain Res Bull, 1997. **46**: p. 381-407.
145. McCaig, C.D., et al., *Controlling Cell Behaviour Electrically: Current Views and Future Potentail.* Physiol Rev, 2005. **85**: p. 943-978.
146. Levin, M., *Large-scale Biophysics: Ion Flows and Regeneration.* Trends in Cell Biology, 2007. **17**(6): p. 261-270.
147. Zhao, M., *Electrical fields in wound healing—An overriding signal that directs cell migration.* Seminars in Cell & Developmental Biology, 2009. **20**: p. 674-682.
148. Cortese, B., et al., *Influence of electrotaxis on cell behaviour.* Integrative Biology, 2014. **6**(9): p. 817-830.
149. Van Haastert, P.J. and P.N. Devreotes, *Chemotaxis: signalling the way forward.* Nature Reviews, 2004. **5**: p. 626-634.
150. Iglesias, P.A. and P.N. Devreotes, *Navigating through models of chemotaxis.* Curr Opi Cell Biol, 2008. **20**: p. 35-40.
151. Janetopoulos, C. and R.A. Firtel, *Directional sensing during chemotaxis.* FEBS Lett, 2008. **582**: p. 2075-2085.
152. Wu, D., X. Ma, and F. Lin, *DC Electric Fields Direct Breast Cancer Cell Migration, Induce EGFR Polarisation, and Increase the Intracellular Level of Calcium Ions.* Cell Biochem Biophys, 2013. **67**: p. 1115-1125.
153. Mukerjee, E.V., et al., *Microneedle array for measuring wound generated electric fields.* IEEE Eng Med Biol Soc, 2006. **1**: p. 4326-4328.
154. Nuccitelli, R., et al., *Imaging the electric field associated with mouse and human skin wounds.* Wound Repair Regen, 2008. **16**: p. 432-441.
155. Tai, G., et al., *Electrotaxis and wound healing: experimental methods to study electric fields as a directional signal for cell migration.* Methods Mol Biol., 2009. **571**: p. 77-97.
156. Li, J. and F. Lin, *Microfluidic devices for studying chemotaxis and electrotaxis.* Trends in Cell Biology, 2011. **21**(8): p. 489-497.
157. Lin, F., et al., *Lymphocyte Electrotaxis In Vitro and In Vivo.* J Immunol, 2008. **181**: p. 2465-2471.
158. Kao, Y.-C., et al., *Modulating chemotaxis of lung cancer cells by using electric fields in a microfluidic device.* Biomicrofluidics, 2014. **8**: p. 024107.
159. Rezai, P., et al., *Electrotaxis of Caenorhabditis elegans in a microfluidic environment.* Lab Chip, 2010. **10**: p. 220-226.
160. Huang, C.-W., et al., *Electrotaxis of lung cancer cells in a multiple electric field chip.* Biosensors and Bioelectronics, 2009. **24**: p. 3510-3516.
161. Wadhawan, N., et al., *Growth and positioning of adipose-derived stem cells in microfluidic devices.* Lab Chip, 2012. **12**: p. 4829-4834.
162. Tsai, H., et al., *Electrotaxis of oral squamous cell carcinoma cells in a multiple electric field chip with uniform flow field.* Biomicrofluidics, 2012. **6**: p. 034116.
163. Altizer, A.M., et al., *Endogenous electric current is associated with normal development of the vertebrate limb.* Dev. Dyn., 2001. **221**: p. 391-401.
164. Pullar, C.E., et al., *4 integrin and epidermal growth factor co-ordinately regulate electric field-mediated directional migration via Rac 1.* Mol. Biol. Cell, 2006. **17**: p. 4925-4935.
165. Rajnicek, A.M., K.R. Robinson, and C.D. McCaig, *The direction of neurite growth in a weak dc electric field depends on the substratum contributions of substrate adhesively and surface charge.* Dev Biol, 1998. **203**: p. 412-423.
166. Cork, R.J., et al., *The growth of PC12 neuritis is biased toward the anode.* J Neurobiol, 1994. **25**: p. 1609-1616.

167. Borgens, R.B., E. Roederer, and M.J. Cohen, *Enhanced spinal cord regeneration in lamprey by applied electric fields.* Science, 1981. **213**: p. 611-617.
168. Borgens, R.B., *Electrically-mediated regeneration and guidance of adult mammalian spinal axons into polymeric channels.* Neuroscience, 1999. **91**: p. 251-264.
169. Ambrose, E.J., A.M. James, and J.H.B. Lowick, *Differences between the electrical charge carried by normal and homologous tumour cells.* Nature, 1956. **177**: p. 576-577.
170. Djamgoz, M.B.A., et al., *Directional movement of rat prostate cancer cells in direct current electric field: involvement of voltage gated Na channel activity.* J Cell Sci, 2001. **114**: p. 2697-2705.
171. Mycielska, M.E. and M.B.A. Djamgoz, *Cellular mechanisms of direct current electric field effects: galvanotaxis and metastatic disease.* J Cell Sci, 2004. **117**: p. 1631-1639.
172. Zhao, M., et al., *Electrical stimulation directly induces pre-angiogenic responses in vascular endothelial cells by signalling through VEGF receptors.* J Cell Sci, 2003. **117**: p. 397-405.
173. Zhao, M., et al., *Electrical signals control wound healing through phophatidylinositol-3-OH kinase-gamma and PTEN.* Nature, 2006. **442**: p. 457-460.
174. Reid, B., et al., *Wound healing in rat cornea: the role of electric currents.* FASEB J, 2005. **19**: p. 379-386.
175. Reid, B., R. Nuccitelli, and M. Zhao, *Non-invasive measurement of bioelectric currents with a vibrating probe.* Nat Protoc, 2007. **2**: p. 661-669.
176. Song, B., et al., *Electrical cues regulate the orientation and frequency of cell division and the rate of wound healing in vivo.* PNAS, 2002. **99**(21): p. 13577-13582.
177. Messerli, M.A. and D.M. Graham, *Extracellular Electrical Fields Direct Wound Healing and Regeneration.* The Biological Bulletin, 2011. **221**(1): p. 79-92.
178. Song, B., et al., *Nerve regeneration and wound healing are stimulated and directed by an endogenous electrical field in vivo.* J Cell Sci, 2004. **117**: p. 4681-4690.
179. Li, J., et al., *Activated T lymphocytes migrate toward the cathode of DC electric fields in microfluidic devices.* Lab Chip, 2011. **11**: p. 1298-1304.
180. Li, J., et al., *Microfluidic device for studying cell migration in single or co-existing chemical gradients and electric fields.* Biomicrofluidics, 2012. **6**: p. 024121.
181. Eaglstein, W.H. and V. Falanga, *Chronic Wounds.* Surg Clin North Am, 1997. **77**: p. 689-700.
182. Gamboa, O.L., et al., *Electrical estimulation of retinal pigment epithelial cells.* Experimental Eye Research, 2010. **91**: p. 195-204.
183. Sulik, G.L., et al., *Effects of steady electric fields on human retinal pigment epithelial cell orientation and migration in culture.* Acta Ophthalmologica, 1992. **70**: p. 115-122.
184. Han, J., et al., *Electric Fields Contribute to Directed Migration of Human Retinal Pigment Epithelial Cells via Interaction between F-actin and B1 Integrin.* Current Eye Research, 2009. **34**: p. 438-446.
185. Ferrier, J., et al., *Osteoclasts and osteoblasts migrate in opposite directions in response to a constant electrical field.* J Cell Physiol, 1986. **129**: p. 283-288.
186. Grahn, J.C., et al., *Melanocytes do not migrate directionally in physiological DC electric fields.* Wound Rep Reg, 2003. **11**: p. 64-70.
187. Brunt, K.R., R.D. Weisel, and R.K. Li, *Stem cells and regenerative medicine- future perspectives.* Can J Physiol Pharmacol, 2012. **90**(3): p. 327-335.
188. Meng, X., et al., *PI3K mediated electrotaxis of embryonic and adult neural progenitor cells in the presence of growth factors.* Experimental Neurology, 2011. **227**: p. 210-217.
189. Jahanshahi, A., et al., *In Vitro and In Vivo Neuronal Electrotaxis: A Potential Mechanism for Restoration?* Mol Neurobiol, 2014. **49**: p. 1005-1016.

190. Feng, L., et al., *Guided migration of neural stem cells derived from human embryonic stem cells by an electric field.* Stem Cells, 2012. **30**(2): p. 349-355.
191. Babona-Pilipos, R., M.R. Popovic, and C.M. Morshead, *A Galvanotaxis Assay for Analysis of Neural Precursor Cell Migration Kinetics in an Externally Applied Direct Current Electric Field.* J. Vis. Exp., 2012. **68**: p. e4193.
192. Kirson, E.D., et al., *Disruption of Cancer Cell Replication by Alternating Electric Fields.* Cancer Research, 2004. **64**: p. 3288-3295.
193. Kirson, E.D., et al., *Alternating electric fields arrest cell proliferation in animal tutor models and human brain tumors.* PNAS, 2007. **104**: p. 10152-10157.
194. Nuccitelli, R., et al., *Nanosecond pulsed electric fields cause melanomas to selfdestruct.* Biochem Biophy Res commun, 2006. **343**(2): p. 351-360.
195. Nuccitelli, R., et al., *A new pulsed electric field therapy for melanoma disrupts the tutor's blood supply and causes remission without recurrence.* Int. J. Cancer, 2009. **125**: p. 438-445.
196. Balakatounis, K.C. and A.G. Angoules, *Low-intensity Electrical Stimulation in Wound Healing: Review of the Efficacy of Externally Applied Currents Resembling the Current of Injury.* Open Access Journal of Plastic Surgery, 2008. **8**: p. 283-291.
197. Shapiro, S., et al., *Oscillating field stimulation for complete spinal cord injury in humans: a phase 1 trial.* J. Neurosurg. Spine, 2005. **2**: p. 3-10.
198. Demir, H., H. Balay, and M. Kirnap, *A Comparitive Study of the Effects of Electrical Stimulation and Laser Treatment on Experimental Wound Healing in Rats.* Journal of Rehabiliation Research & Development, 2004. **41**(2): p. 147-154.
199. Karba, R., et al., *DC Electrical Stimulation for Chronic Wound Healing Enhancement. Part1. Clinical Study and Determination of Electrical Field Distribution in the Numerical Wound Model.* Bioelectrochemistry and Bioenergetics, 1997. **43**: p. 265-270.
200. Naeini, A.T., et al., *Experimental Cutaneous Wound Healing in Rabbits: Using Continuous Microamperage Low-voltage Electrical Stimulation.* Comp clin Pathol, 2008. **17**: p. 203-210.
201. Mehmandoust, F.G., et al., *Anodal and Cathodal Pulsed Electrical Stimulation on Skin Wound Healing in Guinea Pigs.* Journal of Rehabiliation Research & Development, 2007. **44**(4): p. 611-618.
202. Bayat, M., et al., *Experimental Wound Healing using Microamperage Electrical Stimulation in Rabbits.* Journal of Rehabiliation Research & Development, 2006. **43**(2): p. 219-226.
203. Ojingwa, J.C. and R.R. Isseroff, *Electrical Stimulation of Wound Healing.* The Journal of Investigative Dermatology, 2002. **36**(4): p. 1-12.
204. Asami, K., *Characterisation of biological cells by dielectric spectroscopy.* Journal of Non-Crystalline Solids, 2002. **305**: p. 268-277.
205. Schwan, H.P., *Electrical Properties of Tissue and Cell Suspensions.* Advances in Biological and Medical Physics, 1957. **5**: p. 147-209.
206. Martinsen, O.G., S. Grimnes, and H.P. Schwan, *Interface phenomena and dielectric properties of biological tissues.* Encyclopaedia of Surface and Colloid Science, 2002. **20**: p. 2643-2653.
207. Heileman, K., J. Daoud, and M. Tabrizian, *Dielectric spectroscopy as a viable biosensing tool for cell and tissue characterization and analysis.* Biosensors and Bioelectronics, 2013. **49**: p. 348-359.
208. Asami, K. and A. Irimajiri, *Dielectrospectroscopic monitoring of early embryogenesis in single frog embryos.* Phys. Med. Biol., 2000. **45**(11): p. 3285.
209. Asami, K., *Characterization of heterogeneous systems by dielectric spectroscopy.* Progress in Polymer Science, 2002. **27**(8): p. 1617-1659.

210. Ron, A., et al., *Theoretical examination of aggregation effect on the dielectric characteristics of spherical cellular suspension.* Biophysical Chemistry, 2009. **140**: p. 39-50.
211. Ron, A., et al., *The effect of irregularity on the dielectric dispersion characteristics of spherical cellular suspension.* Colloids and Surfaces B: Biointerfaces, 2009. **74**(1): p. 127-135.
212. Gheorghiu, E., C. Balut, and M. Gheorghiu, *Dielectric behaviour of gap junction connected cells: a microscopic approach.* Phys. Med. Biol., 2002. **47**(2): p. 341.
213. Grimnes, S. and O.G. Martinsen, *Bioimpedance & Bioelectricity Basics*. Second Edition ed. 2008: Academic Press.
214. Foster, K.R. and H.P. Schwan, *Dielectric properties of tissues and biological materials: a critical review.* Critical Reviews in Biomedical Engineering, 1989. **17**(1): p. 25-104.
215. Pethig, R., *Dielectric Properties of Biological Materials: Biophysical and Medical Applications.* IEEE Transactions on Electrical Insulation, 1984. **19**(5): p. 453-474.
216. K'OwinoI.O and O.A. Sadik, *Impedance Spectroscopy: A Powerful Tool for Rapid Biomolecular Screening and Cell Culture Monitoring.* Electroanalysis, 2005. **17**(23): p. 2101-2113.
217. Ende, D. and K.M. Mangold, *Impedance Spectroscopy.* Chem. Unserer Zeit, 1993. **27**: p. 134-140.
218. Pänke, O., et al., *Impedance Spectroscopy and biosensing.* Adv biochem Eng Biotechnol, 2008. **109**: p. 195-237.
219. Guan, J., Y. Miao, and Q. Zhang, *Impedimetric Biosensors.* Journal of bioscience and bioengineering, 2004. **97**(4): p. 219-226.
220. Chan, C.M., et al., *Inhibitory effects of resveratrol on PDGF-BB-induced retinal pigment epithelial cell migration via PDGFRb,PI3K/Akt and MAPK pathways.* PLoS ONE, 2013. **8**(2): p. e56819.
221. Wang, P. and Q. Liu, *Cell - Based Biosensors: Principles and Applications*. 2010, Norwood: Artech House.
222. Park, S.M. and J.S. Yoo, *Electrochemical Impedance Spectroscopy for Better Electrochemical Measurements.* Analytical Chemistry, 2003. **75**(21): p. 455-461.
223. Macdonald, J.R., *Impedance Spectroscopy.* Ann. Biomed Eng, 1992. **20**: p. 289-305.
224. Lasia, A., *Electrochemical Impedance Spectroscopy and Its Applications*, in *Modern Aspects of Electrochemistry*, B.E. Conway, J. Bockris, and R.E. White, Editors. 1999, Kluwer Academic/Plenum Publishers: New York. p. 143-248.
225. McAdams, E.T., et al., *The linear and nonlinear electrical properties of the electrode-electrolyte interface.* Biosensors and Bioelectronics, 1995. **10**: p. 67-74.
226. Jorcin, J., et al., *CPE analysis by local electrochemical impedance spectroscopy.* Electrochimica Acta, 2006. **51**: p. 1473-1479.
227. Randles, J.E.B., *Kinetics of rapid electrode reactions.* Discussions of the Faraday Society, 1947. **1**: p. 11-19.
228. Franks, W., et al., *Impedance characterisation and modeling of electrodes for biomedical applications.* IEEE Transactions on Biomedical Engineering, 2005. **52**(7): p. 1295-1302.
229. Giaever, I. and C.R. Keese, *Monitoring Fibroblast Behaviour in Tissue Culture with an Applied Electric Field.* PNAS, 1984. **81**(12): p. 3761-3764.
230. AbdurRahman, A.R., et al., *Cell Culture monitoring by impedance mapping using a multielectrode impedance spectroscopy system (CellMap).* Physiological Measurement, 2008. **29**: p. 227-239.
231. Zhang, Y., et al., *Real-time monitoring of extracellular matrix-mediated PC12 cell attachment and proliferation using an electronic biosensing device.* Biotechnology Letters, 2012. **34**(2): p. 397-404.

232. Lo, C.-M., C.R. Keese, and I. Giaever, *Impedance Analysis of MDCK Cells Measured by Electric Cell - Substrate Impedance Sensing.* Biophysical Journal, 1995. **69**: p. 2800-2807.
233. Lovelady, D.C., et al., *Detecting effects of low levels of cytochalasin B in 3T3 fibroblast cultures by analysis of electrical noise obtained from cellular micromotion.* Biosensors and Bioelectronics, 2009. **24**: p. 2250-2254.
234. Atienzar, F.A., et al., *Evaluation of impedance-based label-free technology as a tool for pharmacology and toxicology investigations.* Biosensors, 2013. **3**: p. 132-156.
235. Liu , C.L., et al., *Electric Cell-Substrate Impedance Sensing as a Screening Tool for Wound Healing Agents*, in *Electric Cell-Substrate Impedance Sensing and Cancer Metastasis*, W.G. Jiang, Editor. 2012, Springer. p. 203-216.
236. Han, J., et al., *Zyxin is involved in thrombin signaling via interaction with PAR-1 receptor.* FASEB, 2009. **23**: p. 4193-4206.
237. Yu, N., et al., *Real-Time Monitoring of Morphological Changes in Living Cells by Electronic Cell Sensor Arrays: An Approach To Study G Protein-Coupled Receptors.* Analytical Chemistry, 2006. **78**: p. 35-43.
238. Keese, C.R., et al., *Real-Time Impedance Assay to Follow the Invasive Activities of Metastatic Cells in Culture.* BioTechniques, 2002. **33**: p. 842-850.
239. Wegener, J. and J. Seebach, *Experimental tools to monitor the dynamics of endothelial barrier function: a survey of in vitro approaches.* Cell and tissue research, 2014. **355**: p. 485-514.
240. AbdurRahman, A., C. Lo, and S. Bhansali, *A micro-electrode array biosensor for impedance spectroscopy of human umbilical vein endothelial cells.* Sensors and Actuators B, 2006. **118**: p. 115-120.
241. Wang, L., et al., *An automatic and quantitative on-chip cell migration assay using self-assembled monolayers combined with real-time cellular impedance sensing.* Lab on a Chip, 2008. **8**: p. 872–878.
242. Ehret, R., et al., *Monitoring of cellular behaviour by impedance measurements on interdigitated electrode structures.* Biosensors and Bioelectronics, 1997. **12**(1): p. 29-41.
243. Ertl, P. and R. Heer, *Interdigitated impedance sensors for analysis of biological cells in microfluidic biochips.* Elektrotechnik und Informationstechnik, 2009. **126**(1-2): p. 47-50.
244. Gottschamel, J., et al., *Development of a disposable microfluidic biochip for multiparameter cell population measurements.* Analytical Chemistry, 2009. **81**(20): p. 8503-8512.
245. Berggren, C., B. Bjarnason, and G. Johansson, *Capacitive Biosensors.* Electroanalysis, 2001. **13**(3): p. 173-180.
246. Santos, A., J.J. Davis, and P.R. Bueno, *Fundamentals and Applications of Impedimetric and Redox Capacitive Biosensors.* J Anal Bioanal Tech, 2014. **S7:016**.
247. Giaever, I. and C.R. Keese, *Electric Cell-Substrate Impedance Sensing. Concept to Commercialization,* in *Electric Cell-Substrate Impedance Sensing and Cancer Metastasis*, W.G. Jiang, Editor. 2012, Springer: New York. p. 1-20.
248. Keese, C. and I. Giaever, *A biosensor that monitors cell morphology with electrical fields.* IEEE Eng. Med. Bio., 1994. **13**: p. 402-408.
249. Wegener, J., C.R. Keese, and I. Giaever, *Recovery of Adherent Cells after In Situ Electroporation Monitored Electrically.* BioTechniques, 2002. **33**: p. 348-357.
250. Hongyu, L., D.N. Sheppard, and M.J. Hug, *Transepithelial electrical measurements with the Ussing chamber.* Journal of Cystic Fibrosis, 2004. **3**: p. 123-126.
251. Krug, S.M., M. Fromm, and D. Günzel, *Two-Path Impedance Spectroscopy for Measuring Paracellular and Transcellular Epithelial Resistance.* Biophysical Journal, 2009. **97**: p. 2202-2211.

252. Gitter, A.H., et al., *Ussing chamber for high-frequency transmural impedance analysis of epithelial tissues.* J. Biochem. Biophys. Methods, 1997. **35**: p. 81-88.
253. Stolwijk, J.A., *Electric Manipulation and Impedance Analysis of Adherent Cells on Gold-Film Electrodes*. 2011, Regensburg University.
254. Mucha, A.S., *CMOS integrated impedance sensor arrays for cell adhesion measurement*. 2012, Technische Universitat München.
255. Wegener, J., A. Hakvoort, and H.J. Galla, *Barrier function of porcine choroid plexus epithelial cells is modulated by cAMP-dependent pathways in vitro.* Brain Res, 2000. **853**: p. 115-124.
256. Lo, C.M., C.R. Keese, and I. Giaever. *Monitoring motion of confluent cells in tissue culture*. Exp Cell Res, 1993. **204**: p.102-109.
257. *ACEA Biosciences*. Accessed: 10 January 2015; Available from: www.aceabio.com.
258. Tibaldi, L., et al., *New blocking antibodies impede adhesion, migration and survival of ovarian cancer cells, highlighting MFGE8 as a potential therapeutic target of human ovarian carcinoma.* PLoS One, 2013. **8**(8): p. e72708.
259. Eisenberg, M.C., et al., *Mechanistic modeling of the effects of myoferlin on tumor cell invasion.* PNAS, 2011. **108**(50): p. 20078-20083.
260. Sansing, H., N. Renner, and A.G. MacLean, *An inverted blood-brain barrier model that permits interactions between glia and inflammatory stimuli.* Journal of neuroscience methods, 2012. **207**(1): p. 91-96.
261. Jonsson, M.K.B., Q.D. Wang, and B. Becker, *Impedance-based detection of beating rhythm and pro arrhythmic effects of compounds on stem cell-derived cardiomyocytes.* Assay and drug development technologies, 2011. **9**(6): p. 589-599.
262. Marinova, Z., S. Waltiza, and E. Grunblatt, *5-HT2A serotonin receptor agonist DOI alleviates cytotoxicity in neuroblastoma cells: Role of the ERK pathway.* Progress in neuro-psychopharmacology & biological psychiatry, 2013. **44C**: p. 64-72.
263. Moniri, R., et al., *Dynamic assessment of cell viability, proliferation and migration using real time cell analyser system (RTCA).* Cytotechnology, 2015. **67**(2): p. 379-386.
264. Solly, K., et al., *Application of real-time cell electronic sensing (RT-CES) technology to cell-based assays.* Assay and Drug Development Technologies, 2004. **2**(4): p. 363-372.
265. Asphahani, F., et al., *Real-time characterization of cytotoxicity using single-cell impedance monitoring.* Analyst, 2012. **137**: p. 3011-3019.
266. McGuiness, R.P. and E. Verdonk, *Electrical impedance technology applied to cell-based assays*, in *Label-free biosensors: techniques and applications*. 2009, Cambridge University Press. p. 251-277.
267. Peters, M.F., et al., *Evaluation of cellular dielectric spectroscopy, a whole-cell, Label-free technology for drug discovery on Gi-Coupled GPCRs.* Journal of Biomolecular Screening, 2007. **12**(3): p. 312-319.
268. Kubisch, R., et al., *Characterization of eukaryotic cells as the sensitive layer of cell based cytotoxicity sensors.* Procedia Chemistry, 2009. **1**(1): p. 730-733.
269. Thedinga, E., et al., *Online monitoring of cell metabolism for studying pharmacodynamic effects.* Toxicology and Applied Pharmacology, 2007. **220**: p. 33-44.
270. Huang, X., A.M. O'Mahony, and R.G. Compton, *Microelectrode Arrays for Electrochemistry: Approaches to Fabrication.* Small Journal, 2009. **5**(7): p. 776-788.
271. Xiao-Fei, Y., W. Mao-Hua, and A. Dong, *Progress of Interdigitated Array Microelectrodes Based Impedance Immunosensor.* Chinese Journal of Analytical Chemistry, 2011. **39**(10): p. 1601-1610.
272. Wang, L., et al., *Analysis of the Sensitivity and Frequency Characteristics of Coplanar Electrical Cell-Substrate Impedance Sensors.* Biosensors and Bioelectronics, 2008. **24**: p. 14-21.

273. AbdurRahman, A., D.T. Price, and S. Bhansali, *Effect of Electrode Geometry on the Impedance Evaluation of Tissue and Cell Culture.* Sensors and Actuators B, 2007. **127**: p. 89-96.
274. Narayanan, S., et al., *Analysis of the Passivation Layer by Testing and Modeling a Cell Impedance Micro-Sensor.* Sensors and Actuators A, 2010. **159**: p. 241-247.
275. Breckenridge, L.J., et al., *Advantages of Using Microfabricated Extracellular Electrodes for In Vitro Neuronal Recording.* Journal of Neuroscience Research, 1995. **42**: p. 266-276.
276. Min, J. and A.J. Baeumner, *Characterization and Optimization of Interdigitated Ultramicroelectrode Arrays as Electrochemical Biosensor Transducers.* Electroanalysis, 2004. **16**(9): p. 724-729.
277. Varshneya, M. and Y. Li, *Interdigitated array microelectrodes based impedance biosensors for detection of bacterial cells.* Biosensors and Bioelectronics, 2009. **24**: p. 2951–2960.
278. Judy, J.W., *Microelectrode Technologies for Neuroengineered Systems*, in *25th Annual International Conference of the IEEE Engineering in Medicine and Biology Society*. 2003: Mexico.
279. Van Gerwen, P.V., et al., *Nanoscaled interdigitated electrode arrays for biochemical sensors.* Sensors and Actuators B, 1998. **49**: p. 73-80.
280. Laureyn, W., et al., *Nanoscaled interdigitated titanium electrodes for impedimetric biosensing.* Sensors and Actuators B, 2000. **68**: p. 360-370.
281. Valera, E., et al., *Impedimetric immunosensor for atrazine detection using interdigitated microelectrodes.* Sensors and Actuators B, 2007. **125**: p. 526-537.
282. Silva, L.B., et al., *Characterization of optoelectronic platform using an amorphous/nanocrystalline silicon biosensor for the specific identification of nucleic acid sequences based on gold nanoparticle probes.* Sensors and Actuators B, 2008. **132**: p. 508-511.
283. Tang, L., et al., *Self-assembled CNTs/CdS/dehydrogenase hybrid-based amperometric biosensor triggered by photovoltaic effect.* Biosensors and Bioelectronics, 2008. **24**: p. 319-323.
284. Mohr, A., et al., *Performance of a thin film microelectrode array for monitoring electrogenic cells in vitro.* Sensors and Actuators B, 1996. **34**: p. 265-269.
285. Baaken, G., et al., *Planar microelectrode-cavity array for high-resolution and parallel electrical recording of membrane ionic currents.* Lab Chip, 2008. **8**: p. 938–944.
286. Colella, L., et al., *Microelectrode-based dielectric spectroscopy of glucose effect on erythrocytes.* Bioelectrochemistry, 2012. **85**: p. 14-20.
287. Linderholm, P., et al., *Two-dimensional impedance imaging of cell migration and epithelial stratification.* Lab Chip, 2006. **6**: p. 1155–1162.
288. Gross, G.W., et al., *Stimulation of monolayer networks in culture through thin-film indium-tin oxide recording electrodes.* Journal of Neuroscience Methods, 1993. **50**: p. 131-143.
289. Zou, Z., et al., *Functionalized nano interdigitated electrodes arrays on polymer with integrated microfluidics for direct bio-affinity sensing using impedimetric measurement.* Sensors and Actuators A, 2007. **136**: p. 518-526.
290. Valera, E., D. Muñiz, and A. Rodríguez, *Fabrication of flexible interdigitated μ-electrodes (FIDμEs) for the development of a conductimetric immunosensor for atrazine detection based on antibodies labelled with gold nanoparticles.* Microelectronic Engineering, 2010. **87**: p. 167-173.
291. Ohori, T., et al., *Partly disposable three-way microvalve for a medical micro total analysis system (μTAS).* Sensors and Actuators A, 1998. **64**(1): p. 57-63.

292. Kelly, R.S., *Analytical Electrochemistry: The Basic Concepts*. Analytical Sciences Digital Library. 2009.
293. Potter, S.M., *Distributed processing in cultured neuronal networks*, in *Progress in Brain Research*, M.A.L. Nicolelis, Editor. 2001, Elsevier Science B.V. p. 49-62.
294. Fejtl, M., et al., *On Micro-electrode Array Revival: Its Development, Sophistication of Recording, and Stimulation*, in *Advances in Network Electrophysiology Using Multi-electrode Arrays*. 2006, Springer. p. 24-37.
295. Nagale, M.P. and I. Fritsch, *Individually Addressable, Submicrometer Band Electrode Arrays. 1. Fabrication from Multilayered Materials.* Analytical Chemistry, 1998. **70**: p. 2902-2907.
296. Aguiar, F.A., et al., *Conical recessed gold microelectrode arrays produced during photolithographic methods: Characterisation and causes.* Electrochemistry Communications, 2007. **9**: p. 879-885.
297. Ordeig, O., et al., *On-Chip Electric Field Driven Electrochemical Detection Using a Poly(dimethylsiloxane) Microchannel with Gold Microband Electrodes.* Analytical Chemistry, 2008. **80**: p. 3622–3632.
298. Helali, S., et al., *A disposable immunomagnetic electrochemical sensor based on functionalised magnetic beads on gold surface for the detection of atrazine.* Electrochimica Acta, 2006. **51**: p. 5182-5186.
299. Saum, A.G., R.H. Cumming, and F.J. Rowell, *Use of substrate coated electrodes and AC impedance spectroscopy for the detection of enzyme activity.* Biosensors and Bioelectronics, 1998. **13**: p. 511-518.
300. Houa, Y., et al., *Immobilization of rhodopsin on a self-assembled multilayer and its specific detection by electrochemical impedance spectroscopy.* Biosensors and Bioelectronics, 2006. **21**: p. 1393-1402.
301. Mohr, A., et al., *Performance of a thin film microelectrode array for monitoring electrogenic cells in vitro.* Sensors and Actuators B, 1996. **34**: p. 265-269.
302. Wang, L., et al., *An automatic and quantitative on-chip cell migration assay using self-assembled monolayers combined with real-time cellular impedance sensing.* Lab on a Chip, 2008 **8**: p. 872–878.
303. Ojima, H., et al., *Electrochemical Detection of Protons Produced in an Electrode Reaction Using Interdigitated Microarray Electrodes.* Electroanalysis, 2003. **15**(21): p. 1677-1681.
304. Wittkampf, M., et al., *Characterization of microelectrode arrays by means of electrochemical and surface analysis methods.* Sensors and Actuators B, 1997. **40**: p. 79-84.
305. Liu, Y., E. Koep, and M. Liu, *A Highly Sensitive and Fast-Responding SnO2 Sensor Fabricated by Combustion Chemical Vapor Deposition.* Chem. Mater., 2005. **17**(15): p. 3997-4000.
306. Green, R.A., et al., *Substrate dependent stability of conducting polymer coatings on medical electrodes.* Biomaterials, 2012. **33**: p. 5875-5886.
307. Pickard, R.S., *A Review of Printed Circuit Microelectrodes and Their Production.* Journal of Neuroscience Methods, 1979. **1**: p. 301-318.
308. Geddes, L.A. and R. Roeder, *Criteria for the Selection of Materials for Implanted Electrodes.* Annals of Biomedical Engineering, 2003. **31**: p. 879-890.
309. Schaldach, M., et al., *Pacemaker electrodes made of titanium nitride.* Biomed. Technik, 1989. **34**: p. 185-190.
310. Haemmerle, H., et al., *Extracellular recording in neuronal networks with substrate integrated micro electrode arrays.* Biosensors and Bioelectronics, 1994. **9**: p. 691-696.

311. Nisch, W., et al., *A thin film microelectrode array for monitoring extracellular neuronal activity in vitro.* Biosensors and Bioelectronics, 1994. **9**: p. 737-741.
312. Egert, U., et al., *A novel organotypic long-term culture of the rat hippocampus on substrate integrated multi electrode arrays.* Brain Res. Ptotoc, 1998. **2**: p. 229-242.
313. Gross, G.W. and B.k. Rhoades, *The use of neuronal networks on multielectrode arrays as biosensors.* Biosensors & Bioelectronics, 1995. **10**: p. 553-567.
314. Magee, L.J. and J. Osteryoung, *Fabrication and Characterization of Glassy Carbon Linear Array Electrodes.* Analytical chemistry, 1989. **61**(18): p. 2124-2126.
315. O'Hare, D., J.V. Macpherson, and A. Willows, *On the microelectrode behaviour of graphite–epoxy composite electrodes.* Electrochemistry Communications, 2002. **4**: p. 245-250.
316. Kuban, P., J.M. Berg, and P.K. Dasgupta, *Durable Microfabricated High-Speed Humidity Sensors.* Analytical Chemistry, 2004. **76**: p. 2561-2567.
317. Nolan, M.A. and S.P. Kounaves, *Microfabricated Array of Iridium Microdisks as a Substrate for Direct Determination of Cu2+ or Hg2+ Using Square-Wave Anodic Stripping Voltammetry.* Analytical Chemistry, 1999. **71**: p. 3567-3573.
318. Li, N., A. Tourovskaia, and A. Folch, *Biology on a chip: Microfabrication for studying the behaviour of cultured cells.* Crit Rev Biomed Eng, 2003. **31**: p. 423-488.
319. Jackson, M.J., *Principles of Micro- and Nanofabrication*, in *Micro- and Nanomanufacturing*. 2007, Springer US. p. 1-54.
320. Zaouk, R., B.Y. Park, and M.J. Madou, *Introduction to microfabrication techniques.* Methods Mol Biol., 2006. **321**: p. 5-15.
321. Madou, M.J., *Lithography*, in *Fundamentals of Microfabrication: The Science of Miniaturization*. 2002, CRC Press.
322. Metters, J.P., R.O. Kadara, and C.E. Banks, *New directions in screen printed electroanalytical sensors: an overview of recent developments.* Analyst, 2011. **136**: p. 1067-1076.
323. Craston, D.H., et al., *Microband electrodes fabricated by screen printing processes: Applications in electroanalysis.* Talanta, 1991. **38**(1): p. 17-26.
324. Lee, P.T., D. Lowinsohn, and R.G. Compton, *The use of screen-printed electrodes in a proof of concept electrochemical estimation of homocysteine and glutathione in the presence of cysteine using catechol.* Sensors, 2014. **14**: p. 10395-10411.
325. Wang, S., et al., *Application of disposable screen-printed electrode as an epirubicin sensor and relation among whole blood and tissue concentrations of epirubicin.* Int. J. Electrochem. Sci., 2012. **7**: p. 1543-1555.
326. Brischwein, M., et al., *Measurements on cultured cells using screen printed sensors.* ICEBI, 2007. **17**: p. 94-97.
327. Cui, Z., *Laser Ablation.* Encyclopedia of Microfluidics and Nanofluidics, 2014: p. 1-6.
328. Rizvi, N.H., et al., *Direct manufacture of miniature bioparticle electromanipulator devices using excimer laser mask projection techniques.* Int, J. Japan Soc. of Prec. Eng., 1999. **33**(2): p. 100-104.
329. Gower, M.C., et al., *Manufacture of Miniature Bioparticle Electromanipulators by Excimer Laser Ablation.* Proceedings of SPIE, 1998(1): p. 152-160.
330. Cugnet, C., et al., *A novel microelectrode array combining screen-printing and femtosecond laser ablation technologies: Development, characterisation and application to cadmium detection.* Sensors and Actuators B: Chemical, 2009. **143**(1): p. 158-163.
331. Lee, S.H., et al., *Direct fabrication of micro electrodes on a polymer substrate using selective ultrashort pulsed laser ablation of inkjet-printed Ag lines.* Physic Status Solidi (a), 2012. **209**(11): p. 2142-2146.

332. Applied Biophysics. Accessed: 1 July 2015; Available from: http://www.biophysics.com/cultureware.php.
333. Tabasnikov, A., *Microelectrode arrays for Electrical Cell-Substrate Impedace Sensing (ECIS)*. 2011, The University of Edinburgh.
334. Yusa K., et al., *Targeted gene correction of α1-antitrypsin deficiency in induced pluripotent stem cells.* Nature, 2011. **478**(7369): p. 391-394.
335. Bilican B., et al., *Mutant induced pluripotent stem cell lines recapitulate aspects of TDP-43 proteinopathies and reveal cell-specific vulnerability.* PNAS, 2012. **109**(15): p. 5803-5808.
336. David Schneider, D., M. Tarantola, and A. Janshoff, *Dynamics of TGF-β induced epithelial-to-mesenchymal transition monitored by Electric Cell-Substrate Impedance Sensing.* Biochimica et Biophysica Acta, 2011. **1813**: p. 2099-2107.
337. Huttenlocher, A. and A.R. Horwitz, *Integrins in cell migration.* Cold Spring Harb Perspect Biol 2011. **3:a005074**.
338. Alge C.S., et al., *Differential protein profiling of primary versus immortalized human RPE cells identifies expression patterns associated with cytoskeletal remodelling and cell survival.* J Proteome Res., 2006. **5**(4): p. 862-878.
339. Tan, S.H., et al., *Oxygen plasma treatment for reducing hydrophobicity of a sealed polydimethylsiloxane microchannel.* Biomicrofluidics, 2010. **4**(3): p. 032204.
340. Jiang, Y. and S.K. He, *The effect of oxidative stress on retinal pigment epithelial cell migration.* Zhonghua Yan Ke Za Zhi, 2005. **41**(2): p. 100-105.
341. Rao, R.K. and G. Samak, *Bile duct epithelial tight junctions and barrier function.* Tissue Barriers, 2013. **1**(4): p. e25718.
342. Han, D., et al., *Regulation of drug-induced liver injury by signal transduction pathways: critical role of mitochondria.* Trends Pharmacol Sci, 2013. **34**(4): p. 243-53.
343. Gupton, S.L. and C.M. Waterman-Storer, *Spatiotemporal feedback between actomyosin and focal-adhesion systems optimizes rapid cell migration.* Cell, 2006. **125**: p. 1361-1374.
344. Shu X., et al., *Disease mechanisms in late-onset retinal macular degeneration associated with mutation in C1QTNF5.* Hum Mol Genet, 2006. **15**(10).
345. Kuschel, C., et al., *Cell adhesion profiling using extracellular matrix protein microarrays.* Biotechniques, 2006. **40**(4): p. 523-531.
346. Tsapara, A., et al., *The RhoA Activator GEF-H1/Lfc Is a Transforming Growth Factor -Target Gene and Effector That Regulates -Smooth Muscle Actin Expression and Cell Migration.* Molecular Biology of the Cell, 2010. **21**: p. 860-870.
347. Ho, J., et al., *Documentation of intraretinal pigment epithelium migration via high-speed ultrahigh-resolution optical coherence tomography.* Ophthalmology, 118, 2011(4): p. 687-693.
348. Bailey, T.A., et al., *Oxidative stress affects the junctional integrity of retinal pigment epithelial cells.* Invest Ophthalmol Vis Sci, 2004. **45**(2): p. 675-684.
349. Lo, C.-M., C.R. Keese, and I. Giaever, *Monitoring Motion of Confluent Cells in Tissue Culture.* Experimental Cell Research, 1993. **204**(1): p. 102-109.
350. Szulcek, R., H.J. Bogaard, and G.P. Amerongen, *Electric Cell-substrate Impedance Sensing for the Quantification of Endothelial Proliferation, Barrier Function, and Motility.* J Vis Exp, 2014. **85**: p. 51300.
351. Li, Y., et al., *Engineering cell alignment in vitro.* Biotechnology Advances, 2014. **32**: p. 347-365.
352. Nelson, L.J., et al., *Profiling the Impact of Medium Formulation on Morphology and Functionality of Primary Hepatocytes in vitro.* Scientific Reports, 2013. **3**: p. 2735.

Appendix A

Liver Architecture

The liver is the largest organ in the human body. The main function of the liver is metabolism and drug detoxification. The liver also synthesises essential proteins to maintain vital functions in the body. Hepatocytes comprise almost 78% of the liver cells. They are 10–20 μM in size and are characterized by having apical and basolateral poles which are directly related to their hepatic functionality. This is the result of their strategic location in sheets which allows them to perform different liver functions from drug metabolism to communication between parenchymal and non-parenchymal cells. Another function of hepatocytes is bile secretion into the bile canaliculi, which are formed between the tight junctions of hepatocytes and cholangiocytes (the epithelial cells of the bile duct). Other liver cell types include Kupffer cells, hepatic stellate cells (HSC) and the liver sinusoidal endothelial cells (LSEC). A summary of their functions is provided in Table A.1 [29].

The structural and functional unit of the liver is the hepatic lobule (Figure A.1 (a)). It consists of hexagonal arrangement of hepatocyte plates, extending to form liver cell plates. Each plate is typically one cell thick by 15–25 hepatocytes in length. Blood flows between each two cell plates, from the portal tract to the terminal hepatic venule, forming a “sinusoid” [28].

Liver Cells	% of liver	Function
Hepatocytes	78%	Detoxification Protein synthesis Biliary secretion
Liver sinusoidal endothelial cells (LSEC)	2.8%	Endocytosis Vascularization Migration signalling Blood Clearance
Kupffer cells (Sternzellen)	2.1%	Phagocytosis Endocytosis Immune response
Hepatic stellate cells (HSC) Also known as Ito cells or fat-storing cells.	1.4%	Immune response Storage of Vitamin A and retinol ECM synthesis

Table A.1: Liver cell functions.

It has to be mentioned that for the liver to function properly, hepatic polarity has to be maintained. This is defined by the functional compartmentation of hepatocytes where cells located in different positions between the portal tract and the hepatic venule express different genes and attain distinct functional capabilities [28].

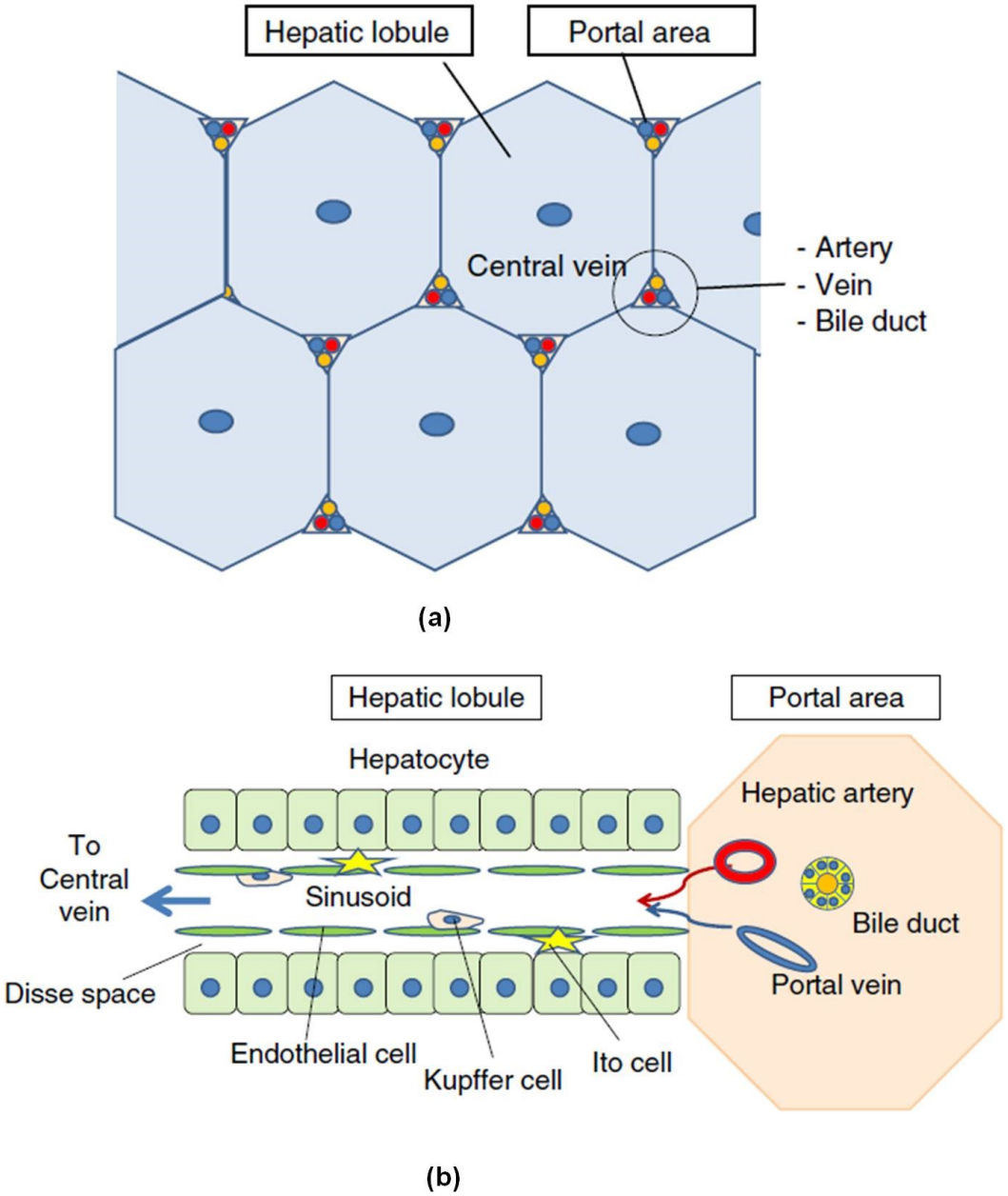

Figure A.1: Liver architecture. (a) Hepatic lobule (b) Hepatic sinusoidal cells [28]

Appendix B

Retinal Structure

The retina is a thin layer of tissue that lines the back of the eye (Figure B.1 (a)). The retina converts light into neural signals and transfers these signals to the brain via the optic nerve. The retinal structure is shown in Figure B.1 (b).

The main light processing function is performed through a layer of light-sensing cells known as the photoreceptors. There are two main types of photoreceptors: rods and cones. Rods are responsible for black and white vision and function mainly in dim light (at night for instance), while cones function in daytime and allow for coloured vision.

The layer that is of most interest in age-related macular degeneration studies is the retinal pigment epithelium (RPE). RPE is located below the photoreceptors and is separated by Bruch's membrane from the blood vessels of the choroid layer. RPE maintains several important functions from absorbing light energy to the transportation of ions, water and metabolites from the subretinal space to the blood. RPE also supplies the photoreceptors with nutrients that it transports from the blood. Another important role of RPE is in phagocytosis (or digestion) of damaged photoreceptor outer segments. Therefore, in diseases like age-related macular degeneration where RPE loss is a main feature, the light sensing cells (photoreceptors) are most affected, eventually leading to blindness [43, 44].

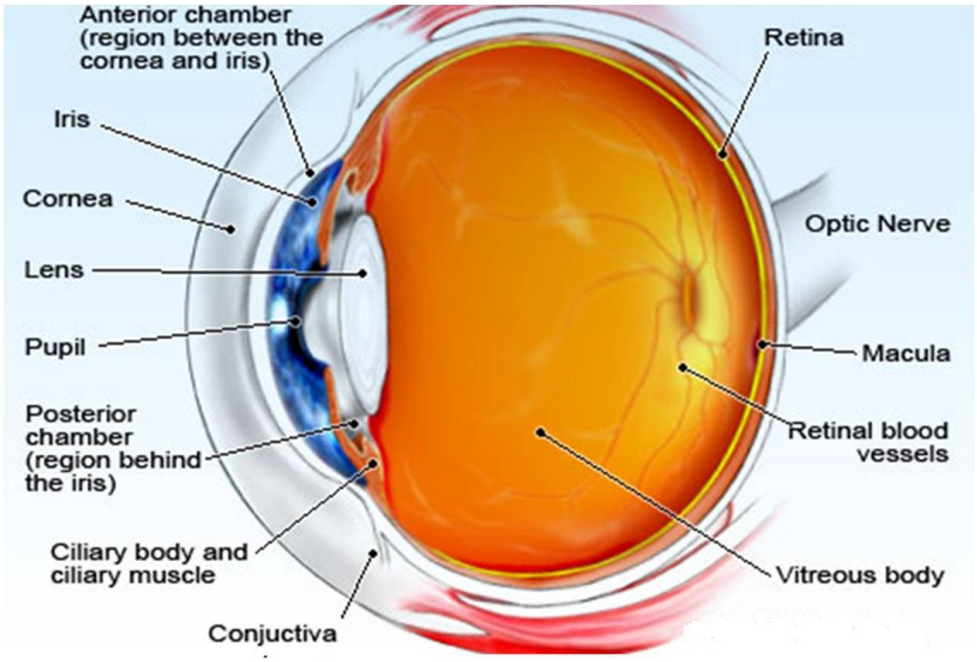

(a)

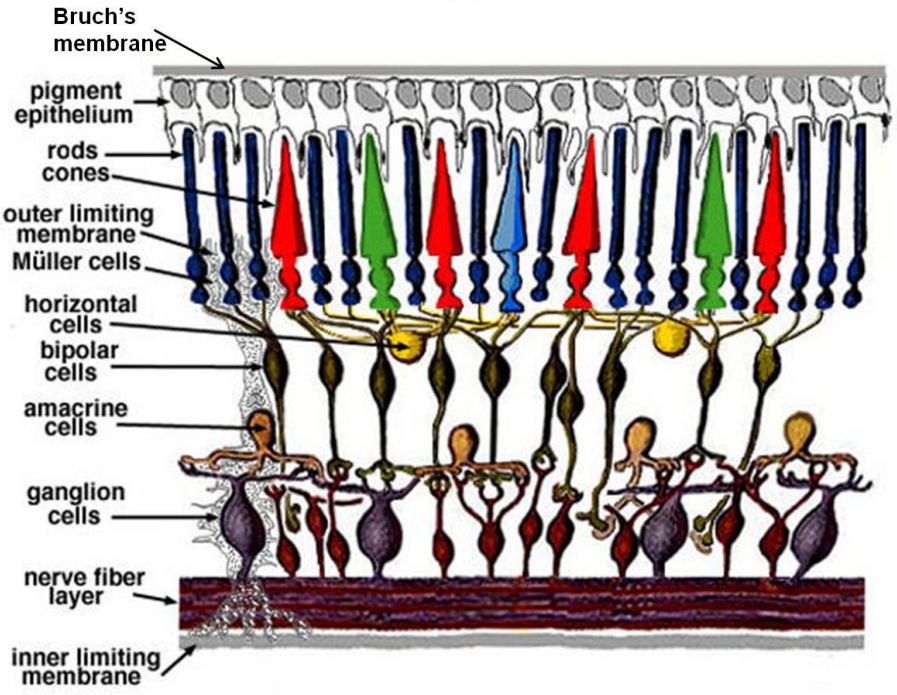

(b)

Figure B.1: (a) Eye Anatomy (b) Retinal structure [44, 45]

Appendix C

Nyquist and Bode plots for simple RC circuits

Equivalent circuits use individual components connected in series and/or in parallel to represent the overall impedance of a system. Figure C.1 shows simple RC circuits with their equivalent Nyquist and Bode plots. For a purely resistive circuit, the Nyquist plot is a fixed point on the x-axis (real part of the impedance), while a capacitive circuit will be plotted as a vertical line that coincides with the y-axis (imaginary part of the impedance). Therefore, for a series RC circuit (Figure C.1(a)), the overall impedance, which is the sum of the individual elements (equation (C.1)), is frequency dependent and its Nyquist plot is presented as shown in Figure C.1(c).

$$Z(\omega) = R + \frac{1}{j\omega C} \qquad (C.1)$$

The behaviour of a parallel RC circuit is more complicated. According to equation (C.2), at high frequencies, the impedance is dominated by the capacitance while at low frequencies the circuit shows a purely resistive behaviour. The Nyquist plot for a parallel RC circuit is a semi-circle and is shown together with its corresponding Bode plot in Figures C.1(d) and (f) [224].

$$Z(\omega) = \frac{R}{1 + j\omega RC} \qquad (C.2)$$

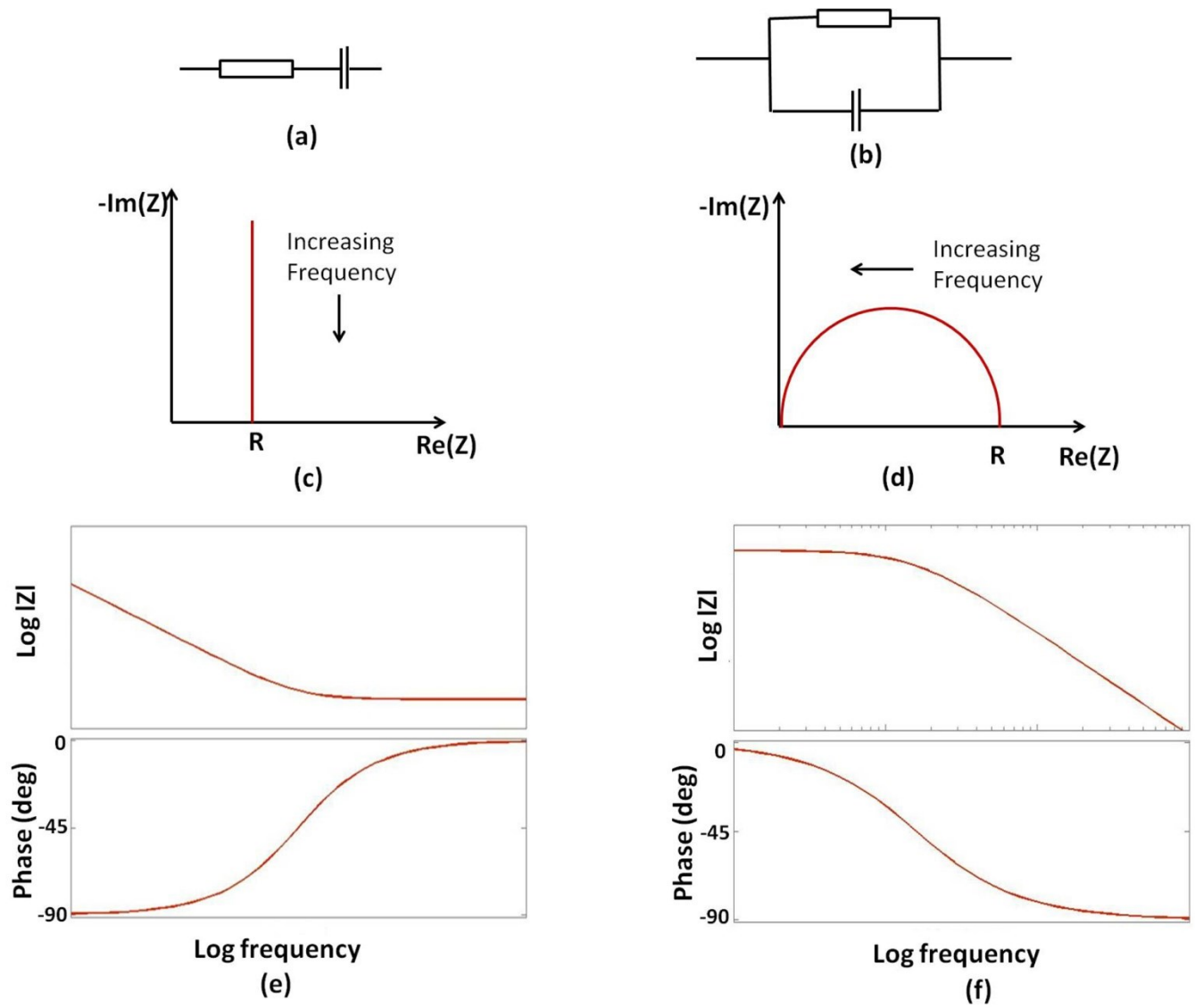

Figure C.1: Nyquist and Bode plots for simple RC circuits [218].

Appendix D

ECIS Model

In the model of Giaever and Keese [13], cells were assumed as circular disks with a radius r_c, hovering at a height h above the working (sensing) electrode in a medium with resistivity ρ. The specific impedance (the impedance for a unit area) for the cell-free electrode is defined as $Z_e(f)$ and represents the impedance at the electrode-electrolyte interface. The specific impedance for the cell is defined as $Z_m(f)$ and is mainly the capacitance of the upper and lower membranes in series, according to the equation:

$$Z_m = \frac{1}{j\omega C_{cl}} \qquad (D.1)$$

where, C_{cl} is the capacitance of the apical and the basal cell membrane capacitance in series, and C_m=2C_{cl} (μF/ cm^2). In all their calculations, C_m was set as 1 μF/ cm^2.

It was assumed that the current flew radially in the space between the electrode and the hovering cells, and that the current density under the cells did not change in the z-direction.

The electrode potential was defined as V_e and the electrolyte above the cell monolayer was assumed to have a constant potential of V_m.

The current flowing from the electrode can take one of two paths; either through the cell, passing through the cell membranes with an impedance Z_m, or through the cell-cell intercellular spaces having a resistance R_b. In Figure D.1, the current $I_e(r)$ is the current

flowing from the electrode within an area defined by the radius r, while $I_m(r)$ is the current passing from the cell into the bulk electrolyte within the same area. $I_r(r)$ is the current flowing in a radial direction within the area below the cells and is assumed to flow in an imaginary cylinder of a radius r and height h, so that for $0 \leq r < r_c$, $I_r(r) = I_e(r) - I_m(r)$.

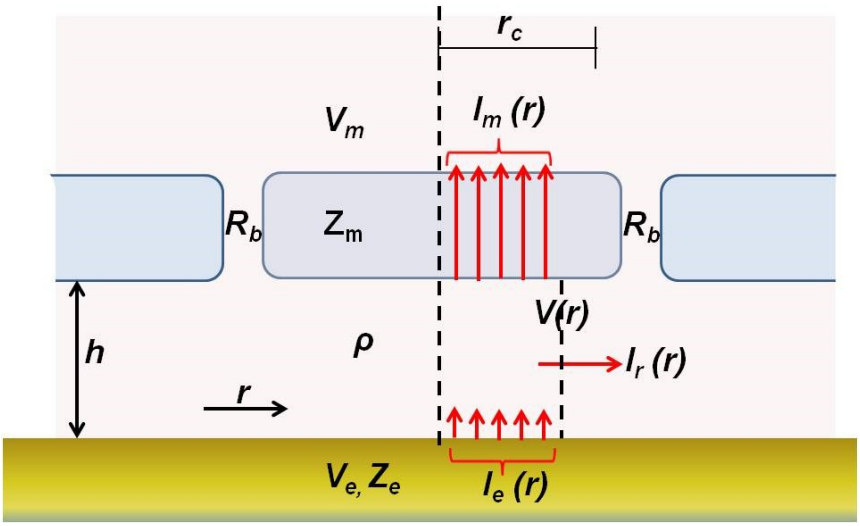

Figure D.1: Different current pathways in ECIS model [254].

Giaever and Keese derived four equations to define the different current pathways:

$$-\frac{dV(r)}{dr} = \frac{I(r)\rho}{2\pi r h} \qquad (D.2)$$

$$\frac{dI_r(r)}{dr} = \frac{dI_e(r)}{dr} - \frac{dI_m(r)}{dr} \qquad (D.3)$$

$$\frac{dI_e(r)}{dr} = \frac{2\pi r}{Z_e}\,(V_e(r) - V(r)) \qquad (D.4)$$

$$\frac{dI_m(r)}{dr} = \frac{2\pi r}{Z_m}\,(V(r) - V_m(r)) \qquad (D.5)$$

These four equations were combined to yield, by differentiation of Equation (D.2), substitution of Equation (D.3) followed by substitution with equations (D.4) and (D.5), the following second order differential equation:

$$\frac{d^2V(r)}{dr^2} + \frac{1}{r}\frac{dV(r)}{dr} - \gamma^2 V(r) + \beta = 0 \qquad (D.6)$$

$$Where; \qquad \gamma^2 = \frac{\rho}{h}\left(\frac{1}{Z_e} + \frac{1}{Z_m}\right) \qquad (D.7)$$

$$and; \qquad \beta = \frac{\rho}{h}\left(\frac{V_e}{Z_e} + \frac{V_m}{Z_m}\right) \qquad (D.8)$$

The approximate solution of this differential equation is:

$$V(r) = CI_o(\gamma r) + \frac{\beta}{\gamma^2} \qquad (D.9)$$

Where; I_o is the modified Bessel function of the first kind of zero order and C is a constant that can be found using suitable boundary conditions, although its value was not stated in the published model.

The total impedance of the cell-covered electrode can finally be determined from:

$$Z_{total} = \left[\frac{1}{Z_e}\left(\frac{Z_e}{Z_e + Z_m} + \frac{\frac{Z_m}{Z_e + Z_m}}{\frac{j\gamma r_c}{2}\frac{I_o(\gamma r_c)}{I_1(\gamma r_c)} + 2R_b\left(\frac{1}{Z_e} + \frac{1}{Z_m}\right)}\right)\right]^{-1} \qquad (D.10)$$

Where, I_0 and I_1 are modified Bessel functions of the first kind of the order zero and one.

If Z_e is measured and Z_m is given a suitable value, two unknowns remain: the intercellular resistance (R_b), and the term $r_c\sqrt{\frac{\rho}{h}}$ (referred to as the cell-substrate adhesion parameter α) that can be determined from the expression:

$$\gamma r_c = r_c\sqrt{\frac{\rho}{h}(\frac{1}{Z_e}+\frac{1}{Z_m})} = \alpha\sqrt{\frac{1}{Z_e}+\frac{1}{Z_m}} \qquad (D.11)$$

The values of R_b and α can be extracted by fitting the measured impedance spectrum to the model.

Appendix E

Biochemical Methods

1. Generation of hiPSC-RPE lines

HiPSC lines were derived from one patient with late-onset retinal macular degeneration (LORMD) and one unaffected sibling, using previously established methods [334, 335]. Briefly, fibroblasts were expanded from 3mm punch biopsies in medium containing 10% fetal bovine serum (FBS), 89% DMEM and 1% penicillin/streptomycin. Once confluent, cells were passaged to MEF feeder layers and reprogrammed using a Sendai reprogramming kit (Invitrogen). After four weeks, morphologically identifiable cells were selected and grown on MEF feeder layers in hiPSC medium containing DMEM/F12 (1:1), 20% KOSR, 1% MEM non-essential amino acids, 100 ng/ml bFGF, 1 mM L-glutamine and 0.1 mM β-mercaptoethanol. Long term culture was maintained feeder free in E8 (Life technologies) medium.

RPE differentiation was established using a variation of a previously published protocol [53]. Briefly, hiPSC colonies were lifted from MEF feeder layers with dispase (0.5 mg/ml) and collagenase (1 mg/ml) and grown as embryonic bodies (EB) for 4 days in EB medium containing DMEM/F12 (1:1), 20% KOSR, 1% MEM non-essential amino acids, 1 mM L-glutamine and 0.1 mM β-ME. At Day 5, EB medium was switched to neural induction medium (NIM) containing DMEM/F12 (1:1), 1% N2 supplement, MEM non-essential amino

acids and 2 µg/ml heparin. At Day 7, suspended EB aggregates were plated to allow them to reattach to the culture plate, where they were grown for an additional 10 days in NIM. At Day 16, NIM medium was replaced with retinal differentiation medium (RDM) containing DMEM/F12 (3:1), 2% B27 supplement (without retinoic acid), MEM non-essential amino acids and penicillin/streptomycin. The cells were maintained as adherent cultures in RDM until the appearance of pigmented RPE cells. Large patches of pigmented RPE cells were micro-dissected and then grown on laminin coated plates initially in 10% FBS/ RDM 90% for two days, followed by 2% FBS/ 98% RDM till confluent before switching to RDM. RPE validation was performed using RT-PCR and immunostaining.

2. Quantitative Real-time PCR (RT PCR) for hiPSC-RPE

Total RNA was extracted using the RNAeasy Mini Plus Kit (Qiagen) and treated with DNase1 to remove any genomic DNA contamination. cDNA was synthesized using a cDNASynthesis Kit (Thermo Scientific), and PCR (34 cycles) was performed using gene-specific primers. PCR products were analyzed on 2% agarose gels. Quantitative RT PCR experiments (40 cycles) were carried out using SYBR® Green Supermix (Bio-Rad) and a Bio-Rad C1000 thermal cycler, and results were analyzed using Bio-Rad CFX software and Microsoft Excel.

3. hiPSC-RPE biochemical Adhesion Assay

Single cell suspensions of hiPSC-RPE were prepared by enzymatic dissociation with 0.1% trypsin-EDTA for 10 minutes. Cells were resuspended in assay buffer with a concentration of 1.0 x 10^6 cells/ml. 100 µL of the cell suspension was added to each well of an extra-cellular matrix adhesion kit (Millipore) before incubation for 1-2h at 37°C in a CO_2 incubator. After incubation, the media was discarded and the wells were washed 3 times with 200 µL assay buffer. 100 µL of cell stain solution was added to each well and they were incubated for 5

minutes at room temperature. Stain was removed and the wells were washed 5 times with de-ionized water before air drying. 100 µL of extraction buffer was added to each well and the wells were incubated with shaking in an orbital shaker for 5 minutes. The absorbance of the wells was measured at a wavelength of 545 nm on a microplate reader.

4. Prestoblue cell viability and ATP-depletion endpoint hepatotoxicity assays

Following the 24 hour treatment with APAP or Phorbol-ester, 10% (v/v) PrestoBlue® (A-13262; Life Technologies) was added to the cell culture medium and incubated for 30 minutes, before the fluorescence signal was measured on a GloMax-Multi+ Microplate Multimode Reader (Promega), and data processed, according to the manufacturer's instructions. After performing the non-toxic PrestoBlue assay, the remaining cells were lysed to determine total cellular ATP levels using the CellTiter-Glo® Luminescent Cell Viability Assay (G7570; Promega), as per vendor's instructions. Bioluminescent signals were detected using the above plate Reader. ATP levels were normalized to controls.

5. Immunocytochemistry

For ZO-1 staining, HepaRG cells were grown on coverslips in a 12 well plate and treated with APAP (0mM, 5mM, 10mM, 20mM). The cells were washed with PBS and then fixed by 10 minutes treatment with methanol. Fixed cells were washed in PBS containing 0.1% Tween 20 - PBS-T (Sigma-Aldrich). The cells were then blocked for 1 hour in 10% normal goat serum/ 0.1% PBS-T (Life Technologies). The cells were then washed twice before being treated with primary antibodies overnight at 4°C. ZO-1 antibody (Santa Cruz; 1:50) was made up in 1% normal goat serum in 0.1% PBS-T. Following primary incubations, the cells were washed twice in PBS-T and then incubated with Alexafluor secondary antibody (Life Technologies) for 1

hour at room temperature. The secondary antibody was made up in PBS. Coverslips were washed twice in PBS-T and twice in PBS then mounted using Fluoroshield with DAPI (Sigma-Aldrich) onto slides. Cells were imaged using a Zeiss LSM700 Confocal Microscope and Zen software.

6. Morphological and ultrastructural assessment

To examine ultrastructural features of APAP toxicity using transmission electron microscopy (TEM), cells were cultured in 6-well plate format and treated for 24 hours (0 mM, 5 mM, 10 mM, 20 mM), then processed following a previous protocol [352].

Appendix F

Microfabrication Runsheet

No	Step	Machine	Parameter/Recipe	Notes
1	**Wafer Cleaning**			
	- Piranha Solution	3:1 (H2SO4:H2O2)	10mins	Add Peroxide to Acid
	- DI dump rinse	Wet Bench	Standard	Ensure removal from surface
	- Wafer Drying	Marangoni Dryer	Standard	
2	**Deposit Metal**			
	- Deposit Titanium	ANS E-Beam Evap	10nm	
	- Deposit Platinum	ANS E-Beam Evap	100nm	
3	**Photolith Metal**			
	- HMDS Box Prime	Wet Bench	10mins	
	- Coat Photoresist	SVG Track (1)	Recipe 9:3:1	Manual
	- Expose: METAL (DF)	KS Contact Aligner	9.0sec	Prox/Spacer
	- Develop Photoresist	SVG Track (2)	Recipe 9:1:1	Manual
	- Hardbake	Gallenkamp Oven	60min	set 140degC (actual: 110degC)
4	**Etch Metal**			
	- Etch Platinum	JLS RIE 80	Prog 8 - 17mins	200W (Ar - 25sccm)
	- Wet Etch Platinum/Titanium	Wet Bench	60sec	HCl:H2O:HNO3 (3:2:1) @45 degC

5	**Resist Strip**			
	- Plasma strip	Barrel Ash	75mins	
	- ACT rinse (1)	Water Bath	15mins	50 degC
	- ACT rinse (2)	Water Bath	15mins	50 degC
	- IPA rinse	Wet Deck	10mins	DI rinse and N2 dry
6	**Coat Passivation**			
	- Parylene C	Labcoter	1000nm	
7	**Photolith Contact**			
	- HMDS Box Prime	Wet Bench	10mins	
	- Coat Photoresist	SVG Track (1)	Recipe 9:2:1	Manual
	- Expose: METAL (DF)	KS Contact Aligner	9.0sec	Prox/Spacer
	- Develop Photoresist	SVG Track (2)	Recipe 9:1:1	Manual
	- Hardbake	Gallenkamp Oven	60min	set 140degC (actual: 110degC)
8	**Etch Contact**			
	- Etch Parylene	JLS RIE 80		
8	**Resist Strip**			
	- Plasma strip	Barrel Ash	75mins	
	- ACT rinse (1)	Water Bath	15mins	50 degC
	- ACT rinse (2)	Water Bath	15mins	50 degC
	- IPA rinse	Wet Deck	10mins	DI rinse and N2 dry
9	**Completion**			
	- HMDS Box Prime	Wet Bench	10mins	
	- Coat Photoresist	SVG Track (1)	Recipe 9:1:1	Manual
	- Dice wafers	Disco Saw	prog 362	
	- Deliver	Package		COMPLETED

Appendix G

Biosensors and Bioelectronics 71 (2015) 445–455

Contents lists available at ScienceDirect

Biosensors and Bioelectronics

journal homepage: www.elsevier.com/locate/bios

Real-time quantitative monitoring of hiPSC-based model of macular degeneration on Electric Cell-substrate Impedance Sensing microelectrodes

W. Gamal [b,1], S. Borooah [a,d,e,f,g,1], S. Smith [b], I. Underwood [c], V. Srsen [b], S. Chandran [a,d,e,f,g], P.O. Bagnaninchi [a,*,2], B. Dhillon [d,g,h,2]

[a] MRC Centre for Regenerative Medicine, The University of Edinburgh, EH16 4UU, United Kingdom
[b] Institute for Bioengineering, School of Engineering, The University of Edinburgh, EH9 3DW, United Kingdom
[c] Institute for Integrated Micro and Nano Systems, School of Engineering, The University of Edinburgh, EH9 3JF, United Kingdom
[d] Centre for Clinical Brain Sciences, The University of Edinburgh, EH16 4SB, United Kingdom
[e] Euan MacDonald Centre for MND Research, The University of Edinburgh, EH16 4SB, United Kingdom
[f] Centre for Neuroregeneration, The University of Edinburgh, EH16 4SB, United Kingdom
[g] The Anne Rowling Regenerative Neurology Clinic, The University of Edinburgh, EH16 4SB, United Kingdom
[h] School of Clinical Sciences, The University of Edinburgh, EH16 4SB, United Kingdom

ARTICLE INFO

Article history:
Received 26 February 2015
Received in revised form
15 April 2015
Accepted 23 April 2015
Available online 25 April 2015

Keywords:
Tissue-on-a-chip
Impedance sensing
Wound healing
Human induced pluripotent stem cells
Macular degeneration
Disease model

ABSTRACT

Age-related macular degeneration (AMD) is the leading cause of blindness in the developed world. Humanized disease models are required to develop new therapies for currently incurable forms of AMD.

In this work, a tissue-on-a-chip approach was developed through combining human induced pluripotent stem cells, Electric Cell–substrate Impedance Sensing (ECIS) and reproducible electrical wounding assays to model and quantitatively study AMD. Retinal Pigment Epithelium (RPE) cells generated from a patient with an inherited macular degeneration and from an unaffected sibling were used to test the model platform on which a reproducible electrical wounding assay was conducted to model RPE damage. First, a robust and reproducible real-time quantitative monitoring over a 25-day period demonstrated the establishment and maturation of RPE layers on the microelectrode arrays. A spatially controlled RPE layer damage that mimicked cell loss in AMD disease was then initiated. Post recovery, significant differences ($P < 0.01$) in migration rates were found between case (8.6 ± 0.46 μm/h) and control cell lines (10.69 ± 0.21 μm/h). Quantitative data analysis suggested this was achieved due to lower cell–substrate adhesion in the control cell line. The ECIS cell–substrate adhesion parameter (α) was found to be $7.8 \pm 0.28\ \Omega^{1/2}$ cm for the case cell line and $6.5 \pm 0.15\ \Omega^{1/2}$ cm for the control. These findings were confirmed using cell adhesion biochemical assays. The developed disease model-on-a-chip is a powerful platform for translational studies with considerable potential to investigate novel therapies by enabling real-time, quantitative and reproducible patient-specific RPE cell repair studies.

1. Introduction

Age-related Macular Degeneration (AMD) is the most common cause of blindness in the developed world (Johnson et al., 2005). The disease usually affects patients in their seventh and eighth decades resulting in the loss of functionally important central vision. There are two main forms of the disease; wet AMD, in which sub-retinal vascular leakage predominates and dry AMD in which deposit formation and cell degeneration are the primary disease processes. Although treatments have recently been developed for wet AMD there is currently no effective treatment for dry AMD. The Retinal Pigment Epithelium (RPE) is a pigmented, polygonal monolayer of cells found directly below the photoreceptor layer in the retina. The primary role of the RPE is in photoreceptor homeostasis. RPE dysfunction, degeneration and reduced repair are implicated in the AMD disease process (Cai and Del Priore, 2006; Thurman et al., 2009). In normal ageing, RPE cell loss is compensated for by increasing cell size and migration of neighboring RPE (Panda-Jonas and Jonas, 1996). In AMD however,

* Corresponding author.
E-mail address: Pierre.Bagnaninchi@ed.ac.uk (P.O. Bagnaninchi).
[1] Co-first authors.
[2] Co-senior authors.

http://dx.doi.org/10.1016/j.bios.2015.04.079
0956-5663/

healing is hampered leading to problems such as incomplete RPE coverage and the consequent death of overlying photoreceptors. Late onset retinal macular degeneration (LORMD) is a rare, autosomal dominant form of macular degeneration (Hayward et al., 2003). LORMD shares key clinical and pathological features with AMD including dark adaptation delay, drusenoid retinal changes prior to sub-retinal deposit, RPE cell loss and neuro-retinal atrophy and has thus been proposed as a good model for AMD (Borooah et al., 2009). In vitro RPE models are required to investigate the underlying mechanisms associated with AMD. However, it is difficult to obtain and culture primary functional human retinal cells, hence the predominance of immortalized cell lines in AMD research (Borooah et al., 2013). In most cases though, the behavior of these immortalized lines poorly reflects what actually happens in vivo (Alge et al., 2006; Klimanskaya et al., 2004. Human induced Pluripotent Stem Cells (hiPSCs) technology offers a novel approach for disease modeling, with the potential to impact translational retinal research and therapy. Recent developments enable the generation of RPE cells derived from patients (hiPSC-RPE) thus allowing in vitro study of human retinal disease that has greater clinical and physiological relevance (Meyer et al., 2009; Takahashi et al., 2007). In this study, RPE was derived from both a patient with an LORMD and from an unaffected sibling (Borooah et al., 2009).

In addition to the limitations of in vitro RPE models, a number of issues associated with the study of wound healing in biology have hampered the development of relevant AMD models. Mechanical wounding methods including scratching (Li et al., 2009; Fronzaa et al., 2009) and stamping are the most commonly used wound healing assays (Lee et al., 2010). Scratching assays however does not produce a highly repeatable wound; a disadvantage that can be overcome by stamping. These methods can also disrupt the ECM layer as well as form debris that might affect the migration process. Gap closure assays can be used to produce cell free regions where cell migration can be monitored after removing a solid (Poujade et al., 2007), liquid (Doran et al., 2009) or gel barrier (Varani et al., 1978). Cells grow around the physical barrier and migrate upon removal. Other wounding techniques include chemical (Legrand et al., 1999) and optical methods (Zordan et al., 2011). However, most of the above methods require extensive manipulation of the cell layer during both wounding as well as repair processes. Moreover, problems of quantification and reproducibility occur due to the difficulty of controlling the wounded areas.

In order to overcome both cell source and current wounding assays limitations, a tissue-on-a-chip approach was investigated by developing and characterising a human induced pluripotent stem cells model of RPE layer on Electric Cell–substrate Impedance Sensing microelectrode arrays. Electric Cell–substrate Impedance Sensing (ECIS) is a technology pioneered by Giaever and Keese in which a small non-invasive AC current (1 μA) is applied using gold microelectrodes (Giaever and Keese, 1984; Giaever and Keese, 1991). Changes in the time-course complex impedance associated with cellular events are monitored by means of in-phase and out-of-phase measurements using a lock-in-amplifier (Giaever and Keese, 1991). ECIS has found many applications from cell attachment and spreading (Wegener et al., 2000; Lo et al., 1995), signal transduction (Han et al., 2009), cytotoxicity (Opp et al., 2009; Lovelady et al., 2009) to metastasis (Keese et al., 2002) and more recently regenerative medicine (Bagnaninchi and Drummond, 2011). ECIS migration assays also allow the combination of electrical wounding and impedance spectroscopy to quantitatively and reproducibly measure cell migration rates and changes in cell morphology accompanying wound healing (Wegener et al., 2000).

In this paper, the need for a physiologically relevant in vitro model of RPE layer repair that can be investigated quantitatively and reproducibly has been addressed through developing a tissue-on-a-chip approach. First the hiPSC-RPE model was established and characterised on ECIS microelectrode arrays. Then an electrical wound healing assay was used to mimic RPE cell damage in both control and diseased hiPSC-RPE cell lines to study differences in repair. Finally the disease model-on-a-chip was used to answer a series of questions concerning the role of RPE adhesion in repair pointing towards potential therapeutic strategies.

2. Materials and methods

2.1. Generation of hiPSC-RPE lines

Derivation of hiPSC lines from one patient with late-onset retinal macular degeneration (LORMD) and one unaffected sibling was achieved using previously established methods (Bilican et al., 2012; Yusa et al., 2011). RPE differentiation was then established using a variation of a previously published protocol (Meyer et al., 2009). For more details on the protocols used, see Supplementary data. The cells were maintained as adherent cultures in retinal differentiation medium (RDM) until the appearance of pigmented RPE cells. Large patches of pigmented RPE cells were micro-dissected and then grown on laminin coated plates initially in 10% FBS/RDM 90% for two days, followed by 2% FBS/98% RDM till confluent before switching to RDM. RPE validation was performed using RT-PCR and immunostaining.

2.2. Quantitative real-time PCR (RT PCR)

Total RNA was extracted using the RNAeasy Mini Plus Kit (Qiagen) and treated with DNase1 to remove any genomic DNA contamination. Synthesization of cDNA was performed using a cDNASynthesis Kit (Thermo Scientific), and PCR (34 cycles) was performed using gene-specific primers. PCR products were analyzed on 2% agarose gels. Quantitative RT PCR experiments (40 cycles) were carried out using SYBR® Green Supermix (Bio-Rad) and a Bio-Rad C1000 thermal cycler, and results were analyzed using Bio-Rad CFX software and Microsoft Excel.

2.3. Tissue culture on microelectrode arrays

Case and Control hiPSC-RPE were cultured on ECIS medusa arrays (Applied Biophysics, NY, USA) incorporating a 2-electrode set up: working and counter electrodes. Each array has 8 wells of 0.8 cm^2 surface area with two 250 μm diameter gold working microelectrodes per well. Microelectrodes are fabricated on a transparent Lexan polycarbonate substrate onto which 50 nm thick gold electrodes are sputtered and passivated with 2 μm polymer resin. Sensing electrodes have a typical area of 0.05 mm^2 while the counter electrode has an area of 18 mm^2. The spacing between the electrodes on a medusa array is 4.83 mm. Because the area of the counter electrode is much larger than that of the working electrode, its impedance contribution can be neglected. The two working electrodes are addressed individually and measurements from one working electrode are recorded at a time. The ECIS electrode array was placed in an array holder inside a humidified incubator at 37 °C and 5% CO_2. All wells were incubated for 2 h with the culture medium before seeding at confluency (100,000 cells/well). Cells were initially cultured with retinal differentiation medium with 10% fetal calf serum. On day 2 of culture, the media was changed into RDM 2% serum and on day 6, RDM with no serum was used until the end of the experiment. Media was changed 3 times per week. Cells were cultured for 25 days to achieve RPE maturation before starting the wound healing assay.

Immortalized RPE cell lines with hTERT (hTERT-RPE1, ATCC)

a

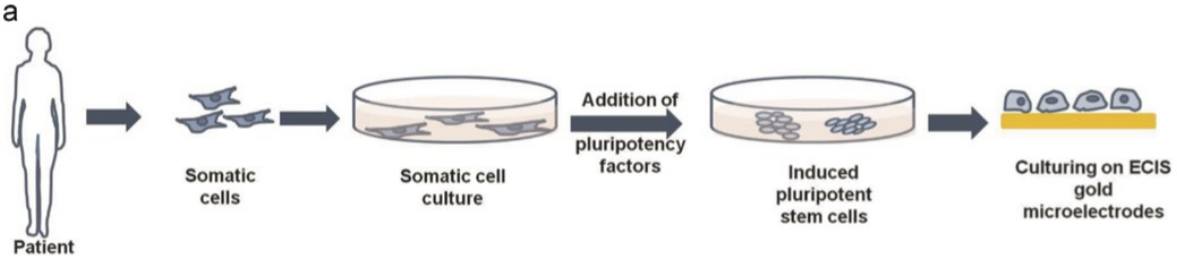

b

Day0 Cell Plating (100,000 cells/well)	Day 2 Medium changed from RDM 10% FCS to 2% FCS	Day 4 Media Change (2% FCS)	Day 6 Medium changed from RDM 2% FCS to RDM no serum	Day 7-Day 24 Media changed every other day (RDM no serum)	Day 24 ECIS Wounding (3mA, 40kHz, 30 sec pulse)	Day 25-Day 30 Media Change

c

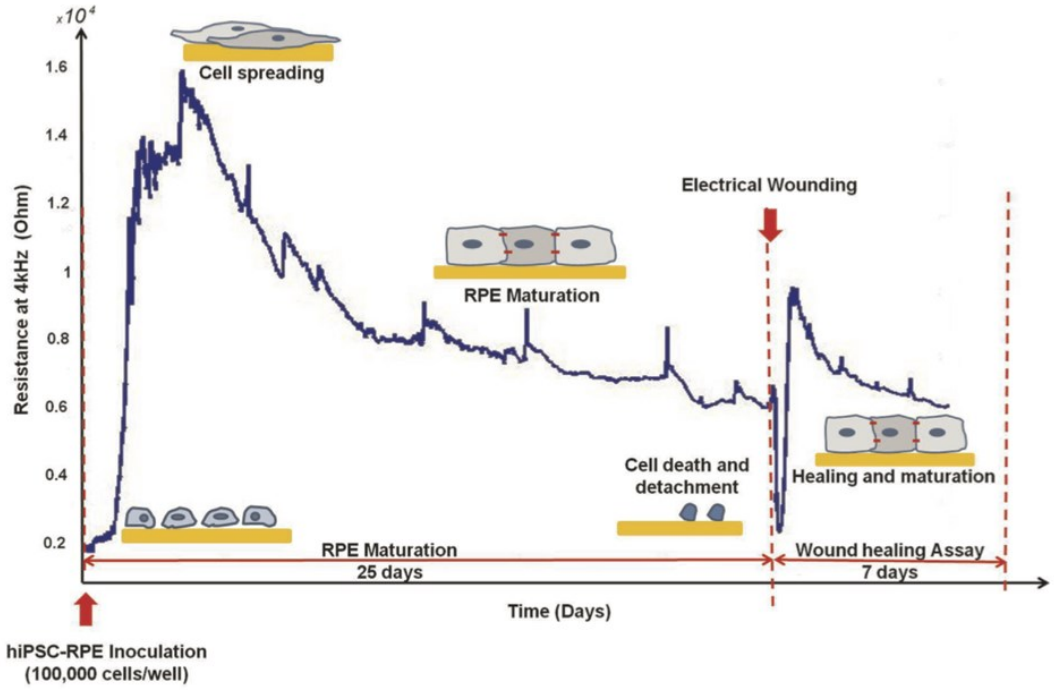

d

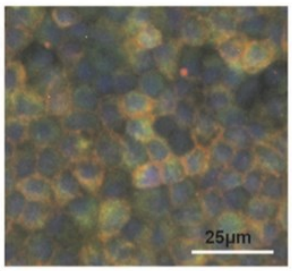

e

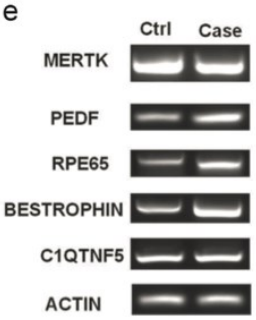

Fig. 1. Development and characterization of the hiPSC-RPE model on ECIS microelectrodes. (a) Patient's fibroblasts were expanded and reprogrammed with Yamanaka factors Klf4, Oct3/4, Sox2, c-Myc to a pluripotent state before being differentiated to RPE. Cells were plated (Day 0) on ECIS microarrays before being allowed to mature for an additional 3 weeks period. (b) Timeline protocol: Cells were cultured with a density of 100,000 cells/cm^2. Culturing medium was switched from RDM 10% FCS to RDM 2% FCS on Day 2 of culture, and then to RDM no serum on Day 6. Medium was changed every other day for 25 days until RPE maturation was obtained. (c) The complex impedance was monitored in real-time throughout RPE maturation and is displayed as the resistance at 4 kHz. It showed an increase with cell spreading and maturation followed by a decrease reflecting changes in cell morphology and size. After 25 days, an automated electrical wound healing assay was performed and subsequent cell migration associated with healing phase was monitored. (d) Immunostaining showing the expression of the transmembrane RPE specific protein Bestrophin(red), Ezrin (green) and DAPI (blue) illustrated markers of mature RPE. (e) RT-PCR revealed that both case and control hiPSC-RPE lines expressed global epithelial and RPE specific markers.

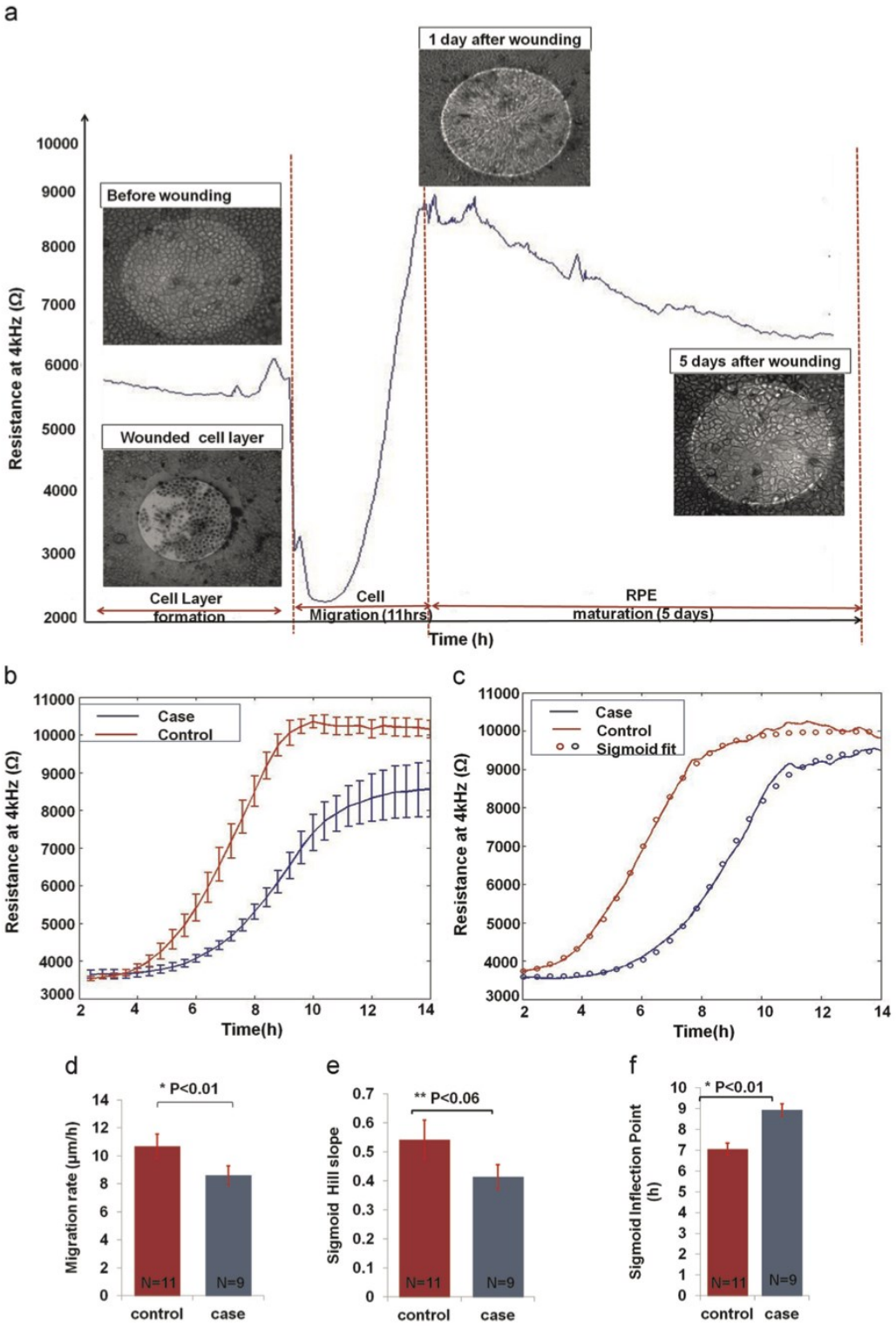

Fig. 2. ECIS Wound Healing Assay of hiPSC-derived RPE. (a) Wounding hiPSC-RPE: The resistance kinetics for one case study after wounding and during healing was monitored. Cells were wounded using wounding parameters of 3 mA, 40 kHz, 30 s. Trypan blue was used to stain dead cells that did not detach from the electrodes. (b) Wounding was a reproducible process, producing a defined wound every time. The control cell line migrated faster than the case cell line to achieve wound healing. (c) Sigmoid fitting: the case and control healing curves were fitted to a sigmoid curve. The parameters of the fitting curve were further analyzed. (d) Migration rate bar graphs: the control migration rate was 10.69 ± 0.21 μm/h while that of the case cell line was 8.6 ± 0.46 μm/h. The two rates were significantly different ($P=0.0046$). (e) Sigmoid hill slope: the difference between the control and case hill slopes were not significantly different. (f) Inflection points were found significantly different.

were cultured in DMEM-F12 (ATCC) with 10% fetal bovine serum (FBS) and 0.01 mg/ml hygromycin B. Cells were seeded with a density of 40,000 cells/well and cultured for two days before starting the migration assay. Culturing medium was changed 3 times per week.

2.4. Impedance sensing

A commercial Electric Cell–Substrate Impedance Sensing instrument (ECIS ZΘ, Applied Biophysics) was used to record multiple frequency impedance measurements (62.5, 125, 250, 500, 1000, 2000, 4000, 8000, 16,000, 32,000 and 64,000 Hz) every 160 s. The measured complex impedance had a resistive and capacitive component which was determined through in-phase and out-of-phase measurements using a lock-in amplifier.

In this study spectroscopic impedance data were presented only at low (4 kHz) and high frequency (64 kHz) for clarity reasons. Following the work of Wegener et al., the resistance at 4 kHz is presented and reflects a combination of intercellular (establishment of cell–cell junctions) and subcellular (cell–substrate adhesion) alterations as well as cell motility (Wegener et al., 2000). In contrast, the capacitance measurements at 64 kHz translate linearly in cell coverage as most of the current is intracellular at this frequency (Wegener et al., 2000).

2.5. Wound healing assay

Generally, impedance sensing with ECIS is achieved with a non-invasive current of 1 μA generated by 1 V, AC signal passing through a 1 MΩ resistor. However, a higher AC voltage (from 100 mV to 3 V) can be applied through a 1 kΩ resistor, thus generating an elevated current (0.1 mA to 3 mA), to wound the cell layer. In this study, an elevated current pulse (3 mA, 40 kHz, 30 s) generated by the ECIS microelectrodes and optimized by trial-and-error experiments was used to wound the confluent cell monolayer. The wounding pulse was mirrored by a drop in impedance to that of the cell free electrode (Fig. 2(a)). The system then switched back to its normal operation to monitor cell repair (Keese et al., 2004). The same wounding parameters were used with all cell lines.

In some cases, trypan blue was used to confirm cell death. 15 min after wounding, the medium was aspirated and 200 μl of diluted trypan blue was added to the well under investigation. After 15 min, trypan blue was removed and the wounded cells were optically observed. Only dead cells were stained blue as their plasma membranes were terminally compromised.

2.6. Quantitative data analysis

2.6.1. Healing kinetics

ECIS data was exported to Matlab for further analysis. The mean and standard errors were calculated for the different cell lines. To better understand the healing kinetics, the healing graphs were fitted to a sigmoid curve in which the hill slope and inflection points were calculated using Eq. (1) shown in Supplementary data, thus providing additional data on the differences between case and control migration.

2.6.2. Average cell migration

The migration rate of the case and control cell lines after electrical wounding was determined according to Eq. (2) in Supplementary data.

2.6.3. Impedance based adhesion assay

Cells were seeded with a high density (typically 100,000 cells/cm^2) and the changes in their impedances were monitored for 1–2 days. The time it takes the cells to attach to the electrode surface and start spreading till they form a confluent layer is an indicator of the cell adhesion properties (Wegener et al., 2000; Heijink et al., 2010) (Fig. 1(d)). Attachment kinetics was fitted to a linear fit and the slope of the case and control curves were determined accordingly. A biochemical adhesion assay was also performed to confirm these results (See Supplementary data).

2.6.4. Cell–substrate adhesion parameter

The built-in ECIS model (Giaever and Keese, 1991) was used to retrieve the cell adhesion parameter (α) to investigate the differences in cell–substrate adhesion between the cell lines under investigation. This model assumes cells as circular disks with radius (r) hovering above the electrode at a distance (h) in a culture medium with resistivity (ρ). The different current pathways (between, under and tough the cells) are then analyzed using differential equations to derive a transfer function defining the complex impedance and the model parameters. The ECIS adhesion parameter (α) is derived according to Eq. (1) and is a reflection of how close the cells are to the electrode. A small cell–electrode distance (h) indicates higher cell–electrode adhesion, i.e. more resistivity against the current flow underneath the cells.

$$\alpha = r\sqrt{\frac{\rho}{h}} \quad (\Omega^{1/2}\mathrm{cm}) \tag{1}$$

A schematic diagram of the ECIS model is shown in Supplementary Fig. 1(c).

2.6.5. Moving variance

Matlab was used to analyze the increase in monitored impedance fluctuations accompanying cell differentiation by the moving variance method (Schneider et al., 2011). First the signal was detrended and normalized. Then the variance was calculated over a total of 512 points (22.75 h) within a 150 point window and a 1 point sliding step, and plotted against time.

2.6.6. Statisitcs

Matlab was also used to perform one-way Anova and Tukey–Kramer multicomparison tests to determine whether the groups under investigation were significantly different from each other. A probability value of $P < 0.01$ was set as significant.

3. Results

3.1. An hiPSC-RPE model on ECIS microelectrode arrays

Induced pluripotent cells were successfully derived from a patient with late-onset retinal macular degeneration (LORMD) and one unaffected sibling. In each case the cells were then differentiated towards RPE cells before being plated on ECIS microelectrode arrays (Fig. 1(a)). Final RPE maturation was completed on the microelectrode arrays using a stepped 25-day protocol that progressively moved towards a serum-free medium (Fig. 1(b)). The hiPSC-RPE control and case cell lines were plated at confluency onto ECIS medusa arrays (Supplementary Fig. 1(a)) with a density of 100,000 cells/well on day 0. Retinal differentiation medium (RDM) was used as the culturing medium with the concentration of fetal bovine serum being changed from 10% to 2% on day 2 and then to 0% from day 6 onwards. Maturation of RPE took place on top of the gold microelectrodes and was evidenced through the changes in ECIS measurements.

Real-time quantitative monitoring of the spectroscopic complex impedance, with a resistive and capacitive component, was performed throughout the RPE maturation phase by acquiring multi-frequency data points at a 160 s interval. The 25-day time-

course maturation process was found to be highly robust and reproducible for both case ($N=9$) and control wells ($N=11$) thus offering a criterion by which to reject faulty in vitro models. Fig. 1(c) shows the changes in the resistance measured at 4 kHz that characterised RPE maturation and was associated with initial cell spreading, morphological changes and barrier formation with an average standard error of 144.6 Ω for the control cell line and 203.2 Ω for the case. The resistance increased with cells attaching and spreading onto the electrodes. First a steep increase in resistance that peaked at 15 kΩ was observed on day 2 of culture and this was followed by a slow decrease over 5.5 days to a plateau with an average value of 8.5 kΩ. The formation of the confluent cell layer and the hiPSC-RPE differentiation stages were also observed under a microscope. It was noticed that the drop in ECIS measurements following the peak in resistance was mirrored by a change in cell morphology from fibroblastic-like cells towards polygonal cobble-stone mature epithelial cells.

Finally, Fig. 1(c) shows that after RPE maturation, an electrical wound healing assay was conducted directly on the chip as schematically described in Supplementary data (Supplementary Fig. 1(b)). An electrical pulse (3 mA, 40 kHz, 30 s) was used to injure the cells on top of the electrode creating a reproducible 250 μm circular wound that mimicked cell loss and damage associated with macular degeneration. A drop in resistance to the level of the cell-free electrode (2600 Ω) was monitored followed by a gradual increase reflecting the migration of RPE cells to repopulate the microelectrodes after wounding.

Before conducting the wound healing assay, the establishment and maturation of the RPE layer on top of the microelectrodes were confirmed. Immunostaining (Fig. 1(d)) and RT-PCR analysis (Fig. 1(e)) were used to identify RPE markers indicating RPE maturation.

RT-PCR showed that both cell lines expressed the global epithelial and RPE specific markers including the phagocytosis marker MERTK, the basal marker BEST1, the apical membrane associated marker Ezrin, the pigmentation marker PEDF(pigment epithelium derived factor), the visual cycle marker RPE65 as well as C1QTNF5 and ACTIN. Moreover, qPCR was used to analyze the relative fold change of expression of the selected mRNA of RPE relative to iPS (Supplementary Fig. 2).

Taken together these data show that an hiPSCs-derived model of the RPE layer can be developed directly on ECIS gold microelectrode arrays and that its robustness, reproducibility and suitability can be quantitatively addressed by real-time impedance sensing before initiating an integrated electrical wound healing assay.

3.2. Electrical wound healing assays of the hiPSC-RPE layer

After 25 days, a mature RPE layer that entirely covered the bottom of the culture well including the gold microelectrodes was established. An RPE injury (analogous to focal RPE loss observed in macular degeneration) was then created as a circular wound with an elevated electrical pulse in the microelectrode area. Then the wound healing process was monitored for both case and control cell lines with ECIS.

Electrical pulse parameters have been optimized through trial and error experiments. A 3 mA current pulse at 40 kHz applied for 30 s was found to cause cell death while preserving the microelectrode integrity. Fig. 2(a) shows the corresponding drop in R_{4kHz} that followed the electrical wound. R_{4kHz} reached a value of 2600 Ω corresponding to a cell-free electrode. This indicated cell death. Light microscopy confirmed that some cells detached from the microelectrode while the few remaining were stained positively with trypan blue indicating irreversible electroporation and death.

Wound healing was then monitored until the RPE layer fully recovered (5 days), and was characterised by two distinct phases (Fig. 2(a)). First, the cells from the wound edges migrated underneath the layer of dead cells in a radial pattern to close the wound. They repopulated the microelectrode with a characteristic steep increase in resistance followed by a plateau that indicated the end of cell migration. Then a maturation phase was observed where the resistance slowly decreased to a second plateau in a similar way to that described for early RPE maturation in Fig. 1(c). Light microscopy indicated that once cell migration was complete, elongated cells switched back to a cuboidal morphology indicating RPE maturation at the end of this phase.

The mean and standard error of the migration phase for all case and control cell lines is shown in Fig. 2(b). It shows that wounding was a reproducible process, producing a defined and concise wound every time. The corresponding capacitance measurements at 64 kHz are shown in Supplementary Fig. 3(a).When calculating the migration rate as the time to repopulate a 250 μm electrode (Fig. 2(d)), we found that the control cell line had a significantly ($P=0.0046$) higher migration rate (10.69 ± 0.21 μm/h) than the case cell line (8.6 ± 0.46 μm/h).

In order to gain more insight into the healing kinetics, R_{4kHz} was fitted to a sigmoid along the migration phase as exemplified for one case and one control cell line in Fig. 2(c). No significant difference ($P=0.057$) was found between the hill slope as shown in Fig. 2(e) of the control (0.54 ± 0.07) and that of the case cell lines (0.41 ± 0.04). However, there was a significant difference between the case and control at the sigmoid inflection point. Fig. 2(f) shows that the inflection point had a significantly ($P=0.0009$) higher value for the case cell line (8.94 ± 0.29 h) than that of the control cell line (7.06 ± 0.27 h).

These results suggested that the case lower migration rate (i.e. the longer time taken by the cells to repopulate the electrodes) of the case cell line might be attributed to a delay in initiating migration. Once the cells rearranged themselves radially and started to move, they migrated with a speed similar to that of the control cell line.

3.3. Observed similarities between healing and maturation processes

During the wound healing process, a transitional stage was observed in which cells showed a change in morphology which was similar to the changes accompanying the early RPE maturation although on a much shorter time scale (Fig. 3(a)). Cells around the wound edge went through a transition from cuboidal to elongated cells before returning to their original polygonal morphology after repopulating the electrodes (Fig. 3(b)). Increased fluctuations were also observed for these transitional phases. A moving variance analysis was applied to the ECIS measurements after wounding following the work of Schneider et al. (2011) (Fig. 3(c)). The analysis clearly shows the transition from a high cellular activity (high variance phase) to a more quiescent state (low variance). No significant differences were found between the case and control cells with an average half-time transition of 11.5 h.

These data suggested that the case cell's ability to go back to the original RPE morphology after completing migration was not affected by the LORMD mutation. Cell morphology and impedance data strongly suggested that cells were able to close the wound through integrin-mediated "mesenchymal" migration (Huttenlocher and Horwitz, 2011).

3.4. Cell–substrate adhesion properties

One of the advantages of the tissue-on-a-chip approach is the ability to exploit the quantitative impedance data collected throughout RPE maturation and wound healing.

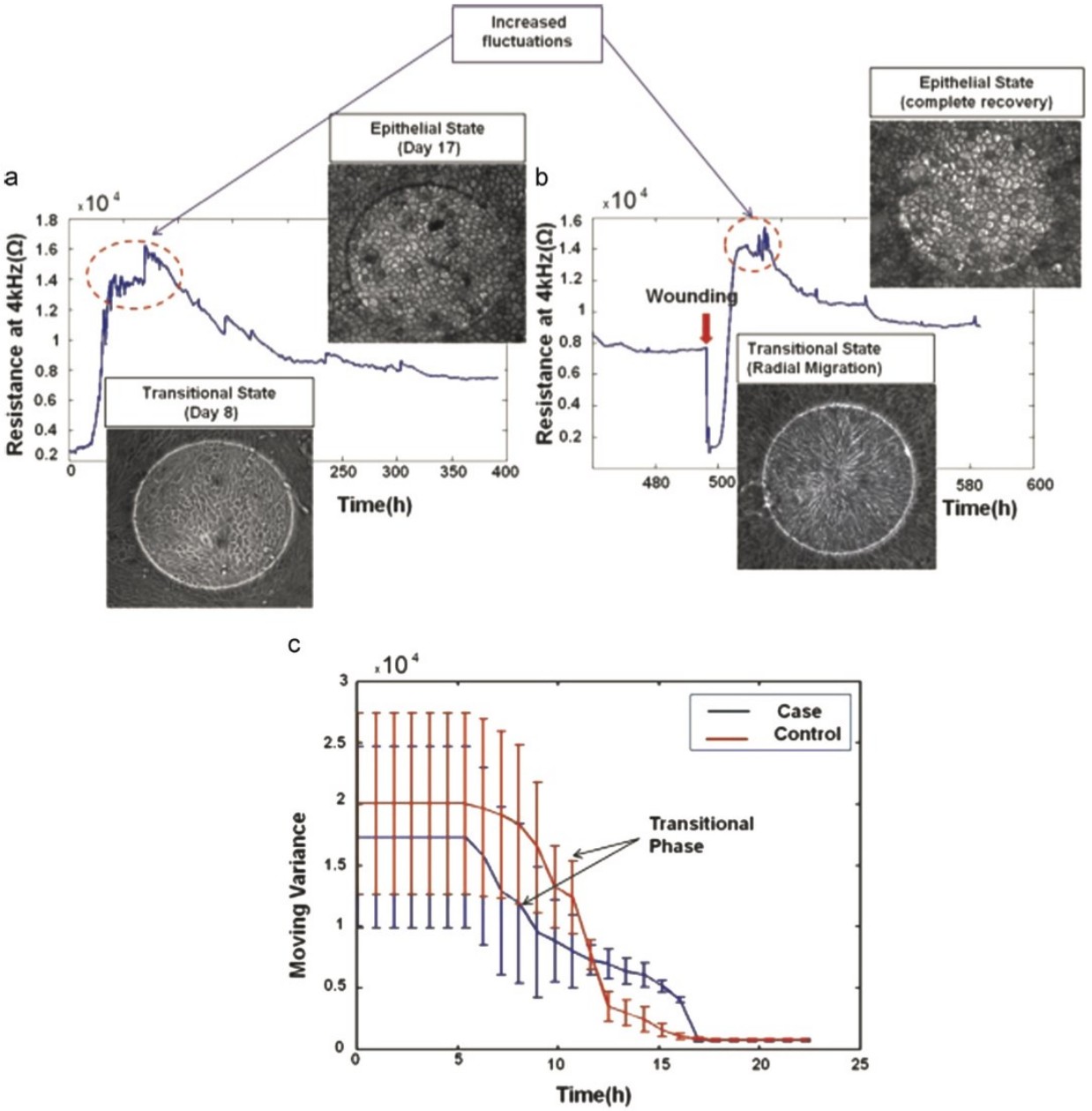

Fig. 3. Similarities between early RPE maturation and healing processes. (a) Differentiation and morphology changes: case and control cell lines changed their morphology from a fibroblastic-like to a cuboidal shape during the differentiation and maturation stage. This was accompanied by an increase in measurement fluctuations. The resistance decreased when the epithelial stage was reached which was attributed to the change in cell size and morphology. (b) Wounding and morphology changes: unwounded cells changed morphology from cuboidal to elongated in order to migrate and repopulate the electrodes. The reverse process then occurred after closing the wound. (c) Moving Variance showed a clear transition phase associated with a transition from an elongated to a cuboidal morphology.

The first monitored difference between the control and case cell lines was at the ECIS attachment and spreading phase during the first 24 h after culture. R_{4kHz} measurements showed that the case cell line attached to the electrodes and spread to form a confluent layer more readily than the control cell line (Fig. 4(a)). The corresponding capacitance measurements during the same period are shown in Supplementary Fig. 3(b).

As the case and control cell lines were seeded at confluency on the microelectrode arrays, the first 24 h of measurements were considered to constitute an impedance-based adhesion assay revealing data on the cell–substrate adhesion. Generally in these types of assays, the microelectrodes are entirely covered with a tight layer of cells that upon attachment to the electrode surface causes a significant increase in the measured resistance. The difference in the measurements between different cell lines can therefore be attributed to cell attachment and adhesion to the substrate (Wegener et al., 2000).

For further analysis, the slope of each of the attachment curves

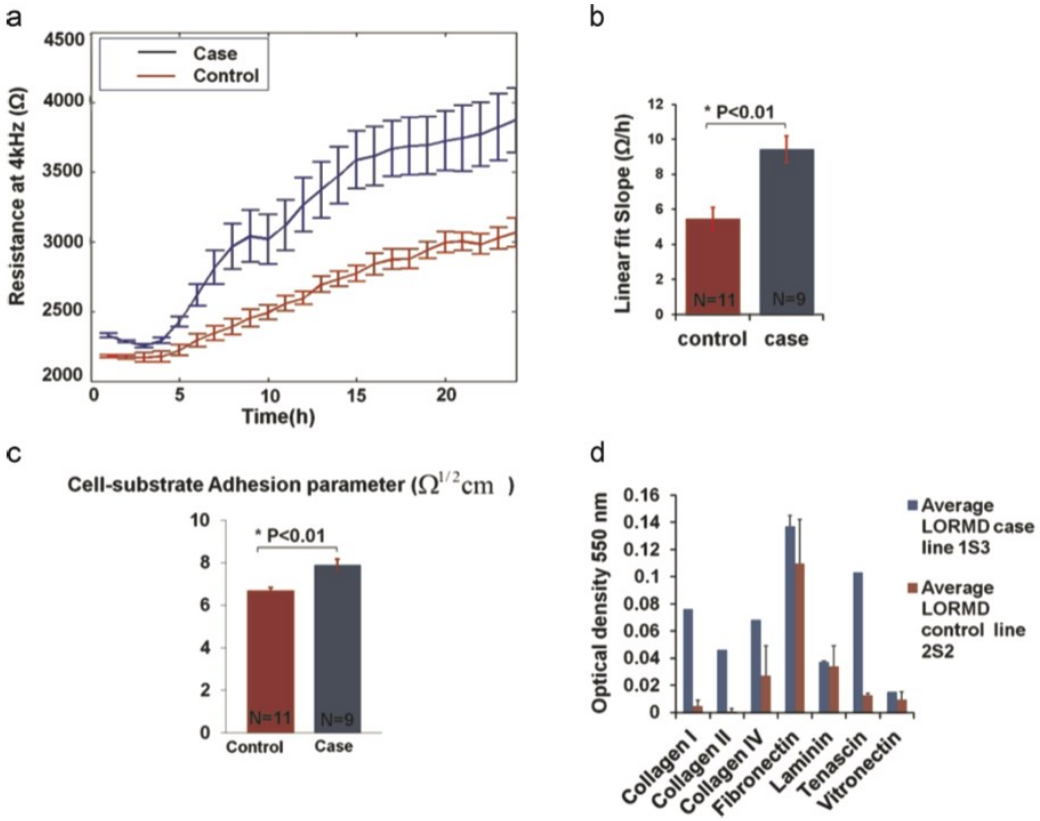

Fig. 4. Case vs. control cell–substrate adhesion. (a) The hiPSC-RPE ECIS adhesion assay: comparing the resistances of the case and control cell lines during the first 24 h of culture, showed how the case cell line attached more quickly to the electrodes and were able to reach a plateau faster than the control cell line. (b) Attachment slope: the slopes of the attachment curves for both case and control cell lines were calculated through a linear fit. The slope was significantly higher for the case cell line ($P < 0.01$) which was consistent with the case cells arriving at a plateau before the control cells. (c) Cell–substrate adhesion parameter (α): ECIS parameter (alpha) of the case cell line was significantly higher than that of the control cell line ($P = 0.002$), indicating that the case cell line obtained a higher cell–substrate adhesion. (d) Adhesion biochemical assay: the case cell line showed stronger adhesion to various ECM proteins than the control cell line.

was fitted to a linear model and they were found to be significantly different ($P < 0.01$) with a value of $5.45 \pm 0.64\ \Omega$/h for the control and $9.43 \pm 0.76\ \Omega$/h for the case cell line (Fig. 4(b)). After this attachment phase however, the case and control cell lines followed similar kinetics throughout the differentiation and maturation phases (see Supplementary Fig 4).

To further investigate the potential role of cell adhesion, the ECIS model was used to define the cell–substrate adhesion parameter (α) (Fig. 4(c)). Again the case cell line showed significantly ($P < 0.01$) higher adhesion ($7.8 \pm 0.28\ \Omega^{1/2}$ cm) than the control cell line ($6.5 \pm 0.15\ \Omega^{1/2}$ cm).

These findings were confirmed by a biochemical adhesion assay (Fig. 4(d)) that showed a clear difference between the adhesion properties of the case and control cell lines. The case line showed a significantly higher adhesion to ECM proteins (including collagen IV and tenascin) than the control cell line. Note that for the case and control cells cultured on ECIS arrays, the microelectrodes were coated with a mixture of proteins present in serum prior to culture.

Finally, to explore further the link between cell adhesion and cell migration, electrical wounding of an additional RPE cell line was conducted (Fig. 5(a)). The immortalized cell line htert-RPE1 were chosen for this study as they are regularly used for in vitro RPE migration assays even with their reported limitations in reflecting in vivo behavior (Alge et al., 2006; Klimanskaya et al., 2004). After htert-RPE1 reached confluency, an ECIS wound healing assay was conducted and its healing rate and adhesion properties were compared to that of the hiPSC-RPE (Fig. 5(b) and (c)). The wounding parameters for htert-RPE1 were the same as that for the hiPSC-RPE case and control cell lines (3 mA, 40 kHz, 30 s). In contrast to the hiPSC-RPE, the wounded cells completely detached leaving a clear electrode, which already suggested that the cells adhered less to the electrodes. Comparing the cell–substrate ECIS parameters of the different cell lines showed that htert-RPE1 were the least adherent to the electrode's surface followed by the control hiPSC-RPE and then by the case cell line having the highest α. This was in turn reflected in the migration rates with the immortalized htert-RPE1 having the highest migration rate of $14.79 \pm 0.39\ \mu$m/h followed by the control cell line ($10.69 \pm 0.21\ \mu$m/h) and then by the case line ($8.6 \pm 0.46\ \mu$m/h) with the slowest migration rate of the three cell lines. These data strongly suggest that the difference observed in cell migration rate between the case and the control cell line may be attributed to a difference in cell adhesion properties.

4. Discussion

In this study, a tissue-on-a chip approach was developed to investigate RPE layer damage and repair in order to mimic retinal macular degeneration. Differences in wound healing between a case and control RPE cell lines associated with an inherited

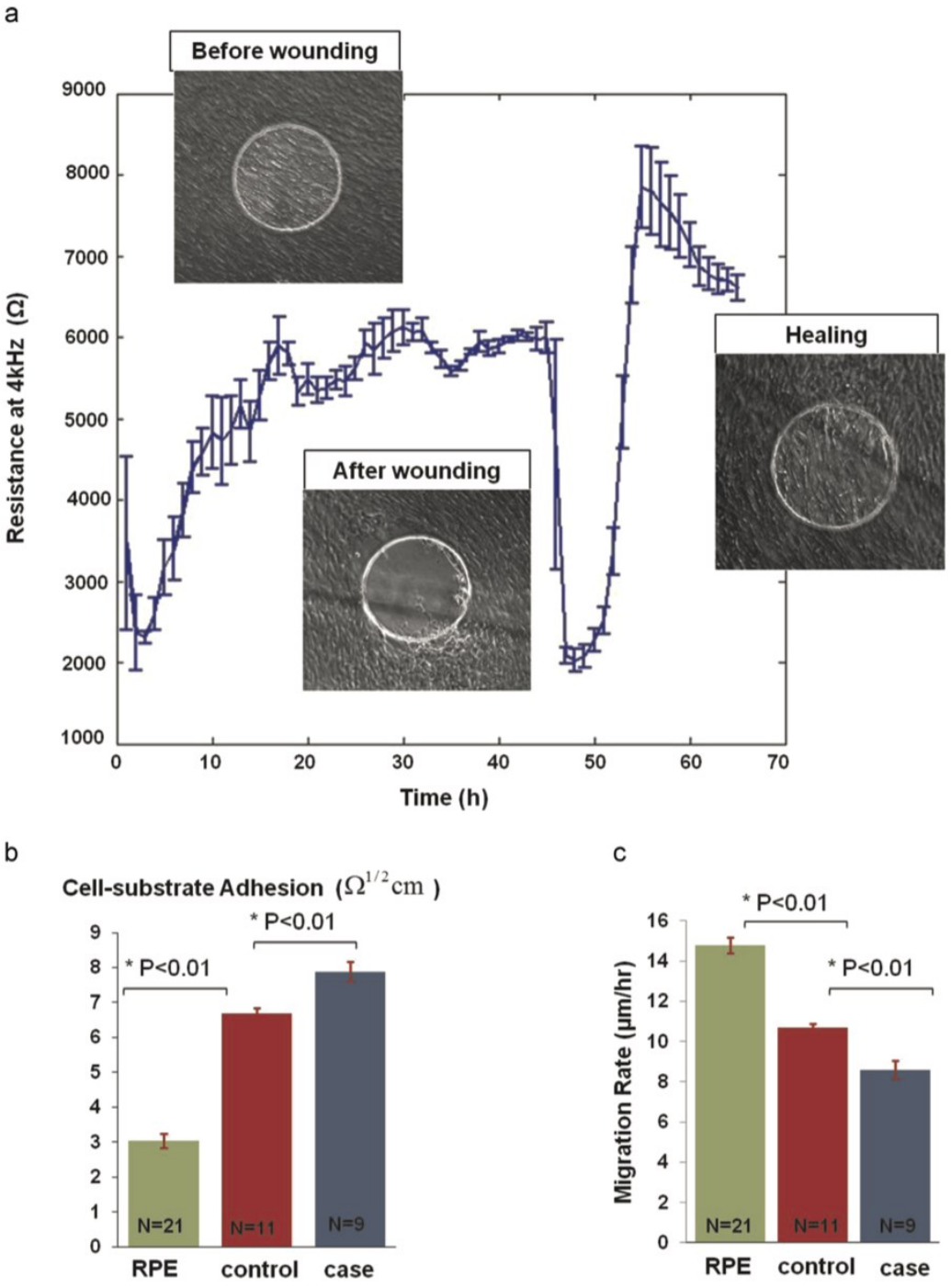

Fig.5. Effect of cell–substrate adhesion on the migration of immortalized and hiPSC-derived RPE (a) Wounding htert-RPE1: wounding parameters used for the migration assay were 3 mA, 40 kHz, 30 s. Wounded cells completely detached from the electrode surface upon wounding leaving clear electrodes. Wound healing was achieved as cells migrated to repopulate the electrode. (b) Cell–substrate adhesion: htert-RPE1 had the lowest adhesion parameter (α), followed by the control cell line and the case line with the highest α. (c) Migration rates: htert-RPE1 had the highest migration rate. It was followed by the control hiPSC-RPE cell line and then by the case cell line.

macular degeneration were reproducibly and quantitatively identified. The obtained results demonstrated that the healing rate was reduced in the case cell line. The differences in healing resulted from a reduced migration rate in the case RPE line when compared to the control RPE line. In addition, the cell lines were found to have different cell–substrate adhesion properties, which may be the reason behind the different cell migration rates. Moreover, the cells undergoing migration adopted a radial pattern of wound healing around the site of damage suggesting a single cell "mesenchymal" migration as opposed to collective "Ameboid"

migration. (Huttenlocher and Horwitz, 2011). "Mesenchymal" migration is integrin dependent and therefore directly linked to cell adhesion properties.

Increased fluctuations in impedance measurements after wounding as well as during maturation were associated with a change in cell morphology from cuboidal to elongated shape. Increased fluctuations monitored by ECIS were reported previously by Schneider et al. (Schneider et al., 2011) and were attributed to the ruffling of cell membranes during EMT (epithelial-to-mesenchymal-transition) process. Taken together, these results point towards an EMT/MET transition post wounding which is known to play a role in development as well as migration in other cell lines (Lane and Jiang, 2012; Lane and Jiang, 2013) and in RPE (Chen et al., 2014). Both the control and case lines went through a morphological change towards a mesenchymal like state during migration before going back to a cuboidal morphology after repopulating the microelectrodes.

Although the central role of cell adhesion in cell migration is established, the relation between migration rate and adhesion level is more subtle. Generally a cell line will have an optimum cell migration rate at intermediate levels of adhesion to allow both an efficient cell–substrate attachment and release (Gupton and Waterman-Storer, 2006). In the presented study, the lower migration rate of the case cell line was found to be associated with a stronger cell–substrate adhesion than that of the control cell line. In this study adhesion and migration parameters were measured separately and thus represent independent, quantitative parameters that will help to achieve a better understanding of the complex relationship between adhesion and migration, and could be used to identify potential therapeutic agents that promote cell migration by modulating cell adhesion (lower or higher).

The case cell line (late onset retinal macular degeneration) results from a mutation in the gene encoding the protein C1QTNF5 (Hayward et al., 2003). C1QTNF5 protein is composed of a C1Q-like globular head, a collagen-like domain and a signal peptide (Tu and Palczewski, 2012). The normal function of C1QTNF5 is currently unknown, however in the eye; it is thought to play a part in interactions between the RPE and the underlying basement membrane since the protein is secreted by the RPE and then attaches to the baso-lateral RPE plasma membrane (Mandal et al., 2006). Previous studies have indicated that mutant C1QTNF5 may affect cellular adhesion. Studies performed by Shu et al. (2006) found that HEK-EBNA cells stably expressing C1QTNF5 had reduced adhesion to laminin coated plates when compared with cells transfected with wild type protein. However, no differences were found when comparing fibronectin coated plates. These differences might have resulted from a number of causes including inherent adhesion differences in the cell lines (Kuschel et al., 2006). ECIS Medusa microarrays in this study were coated only with FCS and not with laminin, which may result in a different cell–substrate adhesion profile. Further studies will need to be performed using other substrates for comparison.

There have been previous studies on the effect of different agents on the adhesion and migration of RPE (Chan et al., 2010; Tsapara et al., 2010). Chan et al. have investigated the role of antioxidants on RPE adhesion and migration using ECIS wound healing assays. They studied the inhibitory effect of (-)-Epigallocatechin gallate (EGCG) (Chan et al., 2010), resveratrol (Chan et al., 2013) and lycopene (Chan et al., 2009) on platelet-derived growth factor (PDGF-BB) induced ARPE19 cell migration and adhesion to fibronectin. They reported that while all the three antioxidants have inhibited PDGF-BB induced RPE migration, only (-)-EGCG had an effect on adhesion to fibronection. Reservatrol and lycopene inhibited migration signaling pathways with no effect on adhesion. In vivo, optical coherence tomography studies in AMD suggested that aberrant adhesion/migration of intraretinal RPE might underlie progression to more advanced disease (Ho et al., 2011).

Finally, it is worth noting that RPE migration can be stimulated by an externally applied electrical field, and electrotaxis has been pointed out as a potential therapeutic strategy (Gamboa et al., 2010). However, RPE stimulated migration was observed at voltages orders of magnitude (50–300 mV) above the voltage used in this study (microvolts). The disease model-on-a-chip approach that have been developed in this study is well suited to investigate further the effect of different agents and drugs on migration and adhesion of both case and control cell lines, and can be adapted to the investigation of other inherited diseases.

Tissue-on-a-chip platforms are an emerging technology in drug discovery, tissue engineering and regenerative medicine (Borooah et al., 2013; Inoue and Yamanaka, 2011). So far, only a few studies restricted to the field of cardio-electrophysiology (Inoue and Yamanaka, 2011; Navarrete et al., 2013) have explored the combination of microelectrodes arrays and iPSC technologies. Human iPSCs-based models-on-a-chip show a new pathway for disease modeling and are beginning to establish a new paradigm for drug development and personalized medicine (Inoue and Yamanaka, 2011; Navarrete et al., 2013).

5. Conclusion

This study has demonstrated a reproducible and robust tissue-on-a-chip approach to quantitatively study a patient-specific retinal macular degeneration disease model. An hiPSC-RPE layer was directly established on ECIS microelectrodes where the platform enabled the label-free, real-time monitoring of hiPSC-RPE maturation in addition to injury and repair through the application of an integrated electrical wounding assay. This method mimicked RPE cell loss accompanying macular degeneration and was used to detect variations in migration rate between a cell line derived from a patient with late-onset retinal macular degeneration versus a control cell line derived from an unaffected siblings. This study points towards the role of cell adhesion in repair and will facilitate further studies to test the efficacy of potential therapeutic agents that modulate cell adhesion.

The tissue-on-a-chip AMD model is a powerful platform for translational studies. Combining hiPSCs technology with impedance sensing, it is amenable to a high throughput thus offering the opportunity to study patient-specific inherited macular degeneration in order to help achieve a better understanding of the disease mechanisms and identify potential therapies.

Acknowledgements

We thank Karen Burr and David Story for assistance with hiPSCs culture, Nina Rzechorzek and Elaine Cleary for technical assistance, Dr. Colin Campbell for providing immortalized RPE cell lines. We would also like to particularly express our gratitude to Dr. Ludovic Vallier and Dr. David Gamm for their guidance and advices. We would like to acknowledge financial support from the College of Science and Engineering, The University of Edinburgh, the Eye Research Fund Edinburgh and Lothian Health Foundation. Shyamanga Borooah acknowledges support from the Royal College of Surgeons of Edinburgh, Eyecare charity, Wellcome Trust STMTI scheme (grant number R42141). Pierre Bagnaninchi and Stewart Smith acknowledge support from RCUK fellowships.

Appendix A. Supplementary material

Supplementary data associated with this article can be found in the online version at http://dx.doi.org/10.1016/j.bios.2015.04.079.

References

Alge, C.S., Hauck, S.M., Priglinger, S.G., Kampik, A.M.U., 2006. Differential protein profiling of primary versus immortalized human RPE cells identifies expression patterns associated with cytoskeletal remodelling and cell survival. J. Proteome Res. 5 (4), 862–878.

Bagnaninchi, P.O., Drummond, N., 2011. Real-time label-free monitoring of adipose-derived stem cell differentiation with electric cell-substrate impedance sensing. Proc. Natl. Acad. Sci. 108 (16), 6462–6467.

Bilican, B., Serio, A., Barmada, S.J., Nishimura, A.L., Carrasco, M., Phatnani, H.P., Puddifoot, C.A., Story, D., Fletcher, J., Park, I.H., Friedman, B.A., Daley, G.Q., Wyllie, D.J., Hardingham, G.E., Wilmut, I., Finkbeiner, S., Maniatis, T., Shaw, C.E., Chandran, S., 2012. Mutant induced pluripotent stem cell lines recapitulate aspects of TDP-43 proteinopathies and reveal cell-specific vulnerability. Proc. Natl. Acad. Sci. 109 (15), 5803–5808.

Borooah, S., Collins, C., Wright, A., Dhillon, B., 2009. Late-onset retinal macular degeneration: clinical insights into an inherited retinal degeneration. Postgrad. Med. J. 85, 495–500.

Borooah, S., Phillips, M.J., Bilican, B., Wright, A.F., Wilmut, I., Chandran, S., Gamm, D., Dhillon, B., 2013. Using human induced pluripotent stem cells to treat retinal disease. Progr. Ret. Eye Res. 37, 163–181.

Cai, H., Del Priore, L.V., 2006. Bruch membrane aging alters the gene expression profile of human retinal pigment epithelium. Curr. Eye Res. 31 (2), 181–189.

Chan, C.M., Chang, H.H., Wang, V.C., Huang, C.L., Hung, C.F., 2013. Inhibitory effects of resveratrol on PDGF-BB-induced retinal pigment epithelial cell migration via PDGFRb,PI3K/Akt and MAPK pathways. PLoS One 8 (2), e56819.

Chan, C.M., Fang, J.Y., Lin, H.H., Yang, C.Y., Hung, C.F., 2009. Lycopene inhibits PDGF-BB-induced retinal pigment epithelial cell migration by suppression of PI3K/Akt and MAPK pathways. Biochem. Biophys. Res. Commun. 388, 172–176.

Chan, C.M., Huang, J.H., Chiang, H.S., Wu, W.B., Lin, H.H., Hong, J.Y., Hung, C.F., 2010. Effects of (-)-epigallocatechin gallate on RPE cell migration and adhesion. Mol. Vis. 16, 586–595.

Chen, X., Xiao, W., Wang, W., Luo, L., Ye, S., Liu, Y., 2014. The complex interplay between ERK1/2, TGFβ/Smad, and Jagged/Notch signaling pathways in the regulation of epithelial-mesenchymal transition in retinal pigment epithelium cells. PLoS One 9 (5), e96365.

David Schneider, D., Tarantola, M., Janshoff, A., 2011. Dynamics of TGF-β induced epithelial-to-mesenchymal transition monitored by Electric Cell–Substrate Impedance Sensing. Biochim. Biophys. Acta 1813 (12), 2099–2107.

Doran, M.R., Mills, R.J., Parker, A.J., Landman, K.A., Cooper-White, J.J., 2009. A cell migration device that maintains a defined surface with no cellular damage during wound edge generation. Lab Chip 9, 2364–2369.

Fronzaa, M., Heinzmann, B., Hamburger, M., Laufer, S., Merfort, I., 2009. Determination of the wound healing effect of Calendula extracts using the scratch assay with 3T3 fibroblasts. J. Ethnopharmacol. 126, 463–467.

Gamboa, O.L., Pu, J., Townend, J., Forrester, J.V., Zhao, M., McCaig, C., Lois, N., 2010. Electrical estimulation of retinal pigment epithelial cells. Exp. Eye Res. 91, 195–204.

Giaever, I., Keese, C.R., 1984. Monitoring fibroblast behaviour in tissue culture with an applied electric field. Proc. Natl. Acad. Sci. USA 81 (12), 3761–3764.

Giaever, I., Keese, C.R., 1991. Micromotion of mammalian cells measured electrically. Proc. Natl. Acad. Sci. 88, 7896–7900.

Gupton, S.L., Waterman-Storer, C.M., 2006. Spatiotemporal feedback between actomyosin and focal-adhesion systems optimizes rapid cell migration. Cell 125, 1361–1374.

Han, J., Liu, G., Profirovic, J., Niu, J., Voyno-Yasenetskaya, T., 2009. Zyxin is involved in thrombin signaling *via* interaction with PAR-1 receptor. FASEB 23, 4193–4206.

Hayward, C., Shu, X., Cideciyan, A., Lennon, A., Barran, P., Zareparsi, S., Sawyer, L., Hendry, G., Dhillon, B., Milam, A., Luthert, P., Swaroop, A., Hastie, N., Jacobson, S., Wright, A., 2003. Mutation in a short-chain collagen gene, CTRP5, results in extracellular deposit formation in late-onset retinal degeneration: a genetic model for age-related macular degeneration. Hum. Mol. Genet. 12 (20), 2657–2667.

Heijink, I.H., Brandenburg, S.M., Noordhoek, J.A., Postma, D.S., Slebos, D.J., van Oosterhout, A.J.M., 2010. Characterisation of cell adhesion in airway epithelial cell types using electric cell–substrate impedance sensing. Eur. Respir. J. 35, 894–903.

Ho, J., Witkin, A.J., Liu, J., Chen, Y., Fujimoto, J.G., Schuman, J.S., Duker, J.S., 2011. Documentation of intraretinal pigment epithelium migration via high-speed ultrahigh-resolution optical coherence tomography. Ophthalmology 118 (4), 687–693.

Huttenlocher, A., Horwitz, A.R., 2011. Integrins in cell migration. Cold Spring Harb. Perspect. Biol. 3, a005074.

Inoue, H., Yamanaka, S., 2011. The use of induced pluripotent stem cells in drug development. Clin. Pharmacol. Ther. 89 (5), 655–661.

Johnson, P.T., Brown, M.N., Pulliam, B.C., Anderson, D.H., Johnson, L.V., 2005. Synaptic pathology, altered gene expression, and degeneration in photoreceptors impacted by drusen. Invest. Ophthalmol. Vis. Sci. 46, 4788–4795.

Keese, C.R., Bhawe, K., Wegener, J., Giaever, I., 2002. Real-time impedance assay to follow the invasive activities of metastatic cells in culture. BioTechniques 33, 842–850.

Keese, C.R., Wegener, J., Walker, S.R., Giaever, I., 2004. Electrical wound-healing assay for cells in vitro. Proc. Natl. Acad. Sci. 101 (6), 1554–1559.

Klimanskaya, I., Hipp, J., Rezai, K.A., West, M., Atala, A.,R.,L., 2004. Derivation and comparative assessment of retinal pigment epithelium from human embryonic stem cells using transcriptomics. Clon. Stem Cells 6 (3), 217–245.

Kuschel, C., Steuer, H., Maurer, A., Kanzok, B., Stoop, R., Angres, B., 2006. Cell adhesion profiling using extracellular matrix protein microarrays. Biotechniques 40 (4), 523–531.

Lane, J., Jiang, W.G., 2012. Epithelial-mesenchymal transition and the use of ECIS. In: Jiang, W.G. (Ed.), Electric Cell-Substrate Impedance Sensing and Cancer Metastasis. Springer, pp. 71–84.

Lane, J., Jiang, W.G., 2013. Metastasis suppressor 1 (MTSS1) and epithelial to mesenchymal transition (EMT) in cancer progression. Eur. J. Cancer 49, S132-S132.

Lee, J., Wang, Y., Ren, F., Lele, T.P., 2010. Stamp wound assay for studying coupled cell migration and cell debris clearance. Langmuir 26 (22), 16672–16676.

Legrand, C., Gilles, C., Zahm, J., Polette, M., Buisson, A., Kaplan, H., Birembaut, P., Tournier, J., 1999. Airway epithelial cell migration dynamics: mmp-9 role in cell-extracellular matrix remodeling. J. Cell Biol. 146 (2), 517–529.

Li, M., Firth, J.D., Putnins, E.E., 2009. An in vitro analysis of mechanical wounding-induced ligand-independent KGFR activation. J. Dermatol. Sci. 53, 182–191.

Lo, C.M., Keese, C.R., Giaever, I., 1995. Impedance analysis of MDCK cells measured by electric cell–substrate impedance sensing. Biophys. J. 69, 2800–2807.

Lovelady, D.C., Friedman, J., Patel, S., Rabson, D.A., Lo, C., 2009. Detecting effects of low levels of cytochalasin B in 3T3 fibroblast cultures by analysis of electrical noise obtained from cellular micromotion. Biosens. Bioelectron. 24, 2250–2254.

Mandal, M., Vasireddy, V., Reddy, G., Wang, X., Moroi, S., Pattnaik, B., Hughes, B., Heckenlively, J., Hitchcock, P., Jablonski, M., Ayyagari, R., 2006. CTRP5 is a membrane-associated and secretory protein in the RPE and ciliary body and the S163R mutation of CTRP5 impairs its secretion. Invest. Ophthalmol. Vis. Sci. 47 (12), 5505–5513.

Meyer, J.S., Shearer, R.L., Capowski, E.E., Wright, L.S., Wallace, K.A., McMillan, E.L., Zhang, S.C., Gamm, D.M., 2009. Modeling early retinal development with human embryonic and induced pluripotent stem cells. Proc. Natl. Acad. Sci. 106, 16698–16703.

Navarrete, E.G., Liang, P., Lan, F., Sanchez-Freire, V., Simmons, C., Gong, T., Sharma, A., Burridge, P.W., Patlolla, B., Lee, A.S., Wu, H., Beygui, R.E., Wu, S.M., Robbins, R. C., Bers, D.M., Wu, J.C., 2013. Screening drug-induced arrhythmia using human induced pluripotent stem cell-derived cardiomyocytes and low-impedance microelectrode arrays. Circulation 128, S3:S13.

Opp, D., Wafula, B., Lim, J., Huang, E., Lo, J., Lo, C., 2009. Use of electric cell-substrate impedance sensing to assess in vitro cytotoxicity. Biosens. Bioelectron. 24, 2625–2629.

Panda-Jonas, S., Jonas, J.B.,M.,J.-Z., 1996. Retinal pigment epithelial cell count, distribution, and correlations in normal human eyes. Am. J. Ophthalmol. 121 (2), 181–189.

Poujade, M., Grasland-Mongrain, E., Hertzog, A., Jouanneau, J., Chavrier, P., Ladoux, B., Buguin, A., Silberzan, P., 2007. Collective migration of an epithelial monolayer in response to a model wound. Proc. Natl. Acad. Sci. 104 (41), 15988–15993.

Shu, X., Tulloch, B., Lennon, A., Vlachantoni, D., Zhou, X., Hayward, C.A.F.W., 2006. Disease mechanisms in late-onset retinal macular degeneration associated with mutation in C1QTNF5. Hum. Mol. Genet. 15 (10), 1680–1689.

Takahashi, K., Tanabe, K., Ohnuki, M., Narita, M., Ichisaka, T., Tomoda, K., Yamanaka, S., 2007. Induction of pluripotent stem cells from adult human fibroblasts by defined factors. Cell 131, 861–872.

Thurman, J.M., Renner, B., Kunchihapautham, K., Ferreira, V.P., Pangburn, M.K., Ablonczy, Z., Tomlinson, S., Holers, V.M., Rohrer, B., 2009. Oxidative stress renders retinal pigment epithelial cells susceptible to complement mediated injury. J. Biol. Chem. 284 (25), 16939–16947.

Tsapara, A., Luthert, P., Greenwood, J., Hill, C.S., Matter, K., Balda, M.S., 2010. The RhoA activator GEF-H1/Lfc is a transforming growth factor-beta target gene and effector that regulates alpha-smooth muscle actin expression and cell migration. Mol. Biol. Cell 21, 860–870.

Tu, X., Palczewski, K., 2012. Crystal structure of the globular domain of C1QTNF5: implications for late-onset retinal macular degeneration. J. Struct. Biol. 180 (3), 439–446.

Varani, J., Orr, W., Ward, P.A., 1978. A comparison of the migration patterns of normal and malignant cells in two assay systems. Am. J. Pathol. 90, 159–172.

Wegener, J., Keese, C.R., Giaever, I., 2000. Electric cell–substrate impedance sensing (ECIS) as a noninvasive means to monitor the kinetics of cell spreading to artificial surfaces. Exp. Cell Res. 259, 158–166.

Yusa, K., Rashid, S.T., Strick-Marchand, H., Varela, I., Liu, P.Q., Paschon, D.E., Miranda, E., Ordóñez, A., Hannan, N.R., Rouhani, F.J., Darche, S., Alexander, G., Marciniak, S.J., Fusaki, N., Hasegawa, M., Holmes, M.C., Di Santo, J.P., Lomas, D.A., Bradley, A., L., V., 2011. Targeted gene correction of α1-antitrypsin deficiency in induced pluripotent stem cells. Nature 478 (7369), 391–394.

Zordan, M.D., Mill, C.P., Riese, D.J., Leary, J.F., 2011. A high throughput, interactive imaging, bright-field wound healing assay. Cytom. Part A 79A, 227–232.